Flavor problem at low and high energy scales

Florentin Jaffredo

université
PARIS-SACLAY

Flavor problem at low and high energy scales

Physique de la saveur aux hautes et basses énergies

Thèse de doctorat de l'université Paris-Saclay

École doctorale n° 564, physique en Île-de-France (PIF)
Spécialité de doctorat: Physique
Graduate School : Physique, Référent : Faculté des sciences d'Orsay

Thèse préparée dans l'unité de recherche IJCLab (Université Paris-Saclay, CNRS), sous la direction de Damir BEČIREVIĆ, Directeur de recherche

Thèse soutenue à Paris-Saclay, le 10 octobre 2022, par

Florentin JAFFREDO

THESE DE DOCTORAT

NNT : 2022UPASP106

Composition du jury

M. Samuel Wallon Professeur, Université Paris-Saclay	Président
Mme Gudrun Hiller Professeur, Technische Universität Dortmund	Rapporteur & Examinatrice
M. Diego Guadagnoli Directeur de recherche, Laboratoire d'Annecy-le-Vieux de Physique Théorique	Rapporteur & Examinateur
M. Dario Buttazzo Professeur, Istituto Nazionale di Fisica Nucleare, Pisa	Examinateur
Mme Dorothea Vom Bruch Chargée de recherche, Centre de Physique des Particules de Marseille	Examinatrice
Damir Bečirević Directeur de recherche, Université Paris-Saclay	Directeur de thèse

université PARIS-SACLAY | ÉCOLE DOCTORALE Physique en Île-de-France (PIF)

Titre: Physique de la saveur aux hautes et basses énergies
Mots clés: Saveur, Chromodynamique quantique (QCD), Modèle Standard, Théorie effective des champs, Grande unification, Leptoquark,

Résumé: Le Modèle Standard de la physique des particules, quoique particulièrement prédictif, est nécessairement incomplet. En effet, de nombreux puzzles restent inexpliqués, tels que le problème de hiérarchie ou le problème de la saveur, qui requièrent une physique au delà de Modèle Standard. De plus, d'apparentes violations de l'universalité de la saveur leptonique ont été observé dans les désintégrations semi-leptoniques des mésons B, suggérant des déviations aussi bien pour les courants neutres que les courants chargés. La physique de la Saveur apparait donc comme un candidat idéal pour rechercher cette nouvelle physique. Dans cette thèse, nous proposons plusieurs observables de saveur dont la mesure pourrait permettre de contraindre cette NP, d'une part dans une approche de théorie effective (EFT), ainsi que dans le cadre de modèle explicites de nouvelle physique impliquant des Leptoquarks à basse énergie. Après avoir résumé les propriétés importantes du Modèle Standard et de ses extensions par les théories effectives permettant de paramétriser de manière générique la nouvelle physique, nous construisons des observables à partir des désintégrations leptoniques et semi-leptoniques des mésons pseudoscalaires via les courants chargés. Un soin particulier est apporté au traitement des incertitudes hadroniques. En utilisant les résultats expérimentaux disponibles pour quelques de ces observables, nous somme en mesure de contraindre plusieurs coefficients de la théorie effective. Nous étudions également en détail les désintégrations semi-leptonique des baryons lourds, et montrons que l'observation de leur distribution angulaire permettrait d'extraire de nombreuses contraintes, en particulier pour la désintégration $\Lambda_b \to \Lambda_c \tau \bar{\nu}$ récemment observé pour la première fois par LHCb. Complémentairement aux processus à basses énergies, nous procédons à une analyse systématique de toutes les observables de saveurs à hautes énergies qui apparaissent dans les queues de distribution de la section efficace de collision $pp \to \ell\ell'$ observée par ATLAS et CMS. Puisque contrairement au modèle standard, la nouvelle physique tend à faire croitre cette section efficace avec l'énergie, les contraintes résultants sont souvent complémentaires, voire meilleures que les observables de précision à basse énergie. Cette analyse a nécessité le développement du programme "HighpT", un outil d'automatisation de la phénoménologie de la saveur au LHC incluant la théorie effective jusqu'aux opérateurs de dimension 8, ainsi que que tout les médiateurs possibles au niveau des arbres, en tenant compte de leur propagation. Ainsi nous pouvons comparer explicitement la validité des théories effectives pour les collisions à haute énergie, et montrons qu'elle amène des erreurs non négligeables, même pour les processus non résonnants. Enfin, nous proposons quelques exemples de scénarios minimaux de nouvelle physique, faisant intervenir des Leptoquarks à une masse $\mathcal{O}(1$ TeV), en cherchant à vérifier toutes les contraintes précédentes. Parmi les 5 Leptoquark considérés, seul le singulet vecteur U_1 est compatible avec l'ensemble des contraintes provenant des expériences à basses énergies, incluant les deux anomalies du B, tout en restant compatible avec les contraintes de recherche directe. Nous proposons également un scénario faisant intervenir une paire de Leptoquarks scalaire, R_2 et S_3, capable d'accommoder ces contraintes, tout en restant renormalisable. Ce modèle a donc l'avantage supplémentaire de permettre la prise en compte d'observables à boucle sans nécessiter de complétion ultraviolette.

université PARIS-SACLAY | ÉCOLE DOCTORALE Physique en Île-de-France (PIF)

Title: Flavor problem at low and high energy scales

Keywords: Flavor physics, Quantum chromodynamics, Standard model, Effective field theory, Grand Unified Theory, Leptoquark,

Abstract: Despite being a very successful theory, the Standard Model (SM) of Particle Physics cannot be the final theory of Nature. Various puzzles remain unexplained, including the issue of hierarchy of scales and the flavor problems, which call for New Physics (NP) beyond the Standard Model. Recent experimental hints of lepton flavor universality violation in semileptonic B-meson decays through charged and neutral currents sealed the flavor sector as a critical laboratory for studying physics beyond the SM. In this work, we propose several new observables the measurement of which could be relevant for flavor physics and set relevant constraints onto NP, both in the model-independent framework via Effective Field Theories (EFT) and with explicit scenarios, involving low-energy Leptoquarks. After pointing out the main features of the SM and the EFTs that we use to parametrize NP, we focus on the semileptonic and leptonic decays of pseudoscalar mesons involving charged currents, and propose observables that are mostly free of hadronic uncertainties and that are independent of the CKM matrix elements. Using available experimental results, we derive bounds on several effective couplings to new physics. We then study in great details the semileptonic decays of heavy baryons, especially the perspectives they offer in terms of new observables that can be extracted from angular distributions. We make several predictions for quantities related to $\Lambda_b \to \Lambda_c \tau \bar{\nu}$ in the SM and its several extensions. That decay is currently studied at LHCb. Complementary to the low-energy processes, we also study the high-energy ones. We systematically analyze the flavor constraints that arise from the tail of the differential cross-section $pp \to \ell\ell'$ at ATLAS and CMS. Due to the energy enhancement of these processes, brought by NP compared to the SM, we find constraints that are often complementary and competitive with low-energy precision observables, and in some cases even better. We create and develop a new package "HighpT", designed to automatize this analysis for a generic EFT up to and including operators of dimension 8. Furthermore, we extend that to any (propagating) tree-level mediator. Comparing the two approaches allows us to explicitly check the validity of the EFT expansion in collider studies, and show that it can introduce uncertainties even for non-resonant processes. Finally, we study some concrete examples of explicit NP scenarios involving $\mathcal{O}(1\,\text{TeV})$ leptoquarks (LQ) than can accommodate all of the available constraints. Among the 3 scalar and 2 vector LQs we consider, we show that only the vector singlet LQ can accommodate a plethora of low-energy experimental data as constraints, including both B-anomalies and remain compatible with direct searches $pp \to \ell\ell'$ high-p_T tails. We also propose and demonstrate that a scenario involving a pair of scalar LQs, R_2 and S_3, can also satisfy all constraints. Such a scenario is even better since it remains renormalizable and no UV-completion needs to be specified to compute the loop effects.

Contents

Remerciements

Je tiens tout particulièrement à remercier les membres de mon jury de thèse pour m'avoir relu et être venus m'écouter lors de ma soutenance. Tout d'abord, Samuel Wallon, pour avoir accepté de présider le jury malgré un délai très bref. Merci ensuite à Diego Guadagnoli et Gudrun Hiller, pour avoir accepté les rôles de rapporteurs et pour leur précieuses relectures de mon manuscrit. Je remercie également Dario Buttazo et Dorothea Vom Bruch d'être venus le jour de ma soutenance, et pour les discussions intéressantes qui y ont eu lieu. Enfin, je remercie particulièrement Asmaa Abada, pour s'être proposée de présider ce jury, même si elle en fut empêchée par les hasards du calendrier.

Je voudrais bien entendu remercier Damir Bečirević, le directeur de thèse qui a su rendre ces trois années de travail merveilleuses. L'attention qu'il porte a ses étudiants est hors du commun, que ce soit sur leur travail ou sur leur carrière. Perfectionniste sans égal, il m'a énormément appris, aussi bien du point de vue humain qu'en ce qui concerne la Physique. Difficile de rêver meilleur encadrant, je ne saurais le remercier suffisamment en quelques lignes.

Je remercie également toutes les personnes avec qui j'ai eu la chance de travailler pendant ma thèse. Notamment Olcyr Sumensari pour ses précieuses contributions à de nombreux projets, et toute l'équipe de Zurich avec Felix Wilsch, Lukas Allwicher et Darius Faroughy. Je remercie aussi très chaleureusement toutes les personnes m'ayant invité malgré les incertitudes pandémiques, en Slovénie grâce à Svetljana Fajfer et Nejc Košnik, en Suisse grâce à Gino Isidori et enfin au Japon avec l'aide inestimable de Minoru Tanaka. Trois voyages que je ne suis pas près d'oublier.

Je voudrais ensuite remercier toutes les personnes que j'ai eu la chance de côtoyer durant ces années à Orsay. Le personnel administratif, Marie-Agnès Poulet et Sarah Même, les membres de mon comité de suivi, Benoit Blossier, Christos Charmousis et Renaud Parentani, et enfin tous les jeunes, pour avoir contribué à la vie du laboratoire : Salva, Gioacchino, Giulia, Elie, Martin, Paul, Donald, Panayotis, Simon, Teseo, Pablo, Héloise, Janne et beaucoup d'autres...

Et enfin je remercie mes amis pour m'avoir occupé pendant les longues soirées de confinement (qui permettent tout de même de belles rencontres), et bien entendu ma famille pour m'avoir soutenu tout au long de cette entreprise.

Introduction

> *The more important fundamental laws and facts of physical science have all been discovered, and these are now so firmly established that the possibility of their ever being supplanted in consequence of new discoveries is exceedingly remote. Nevertheless, it has been found that there are apparent exceptions to most of these laws, and this is particularly true when the observations are pushed to a limit, i. e., whenever the circumstances of experiment are such that extreme cases can be examined. Such examination almost surely leads, not to the overthrow of the law, but to the discovery of other facts and laws whose action produces the apparent exceptions.*
>
> — Albert Abraham Michelson, Light Waves and their Uses, 1899

It would be a crude simplification to assume that physicists from the end of the 19^{th} century considered physics to be solved. After all, Michelson himself was the first to find holes in the classical theory of Ether, but that did not prevent him from depicting the optimistic portrait of human knowledge. Of course, later discoveries of quantum mechanics, relativity, and cosmology would change his interpretation, yet his views stayed surprisingly close to my understanding of modern theoretical physics.

Today, the Standard Model of particle physics is by far the most predictive theory of Nature, both in terms of the number of observables corroborated by experiments and by the precision of its predictions. By the sheer effort that went into it and the quality of its results, the Standard Model shines as one of the overall best successes of the 20^{th} century science. However, we again know that it cannot be the final theory of Nature. It is indeed incompatible with general relativity, for which we have abundant experimental evidence. More importantly, there are *apparent exceptions* mingled in unexpected sectors of the Standard Model, such as the non-zero value of the neutrino masses, the lack of particle candidate constituting dark matter, in addition to the hierarchy and flavor problems. high-energy physics perfectly embodies this idea of *observation pushed to a limit*, be it from the extremely short-range interactions probed in the Large Hadron Collider (LHC) experiment, or through the exceedingly rare interactions in neutrino experiments. Seeking those scarce deviations is key to understanding the shortcomings of the Standard Model.

Just as classical physics is still used in a wide range of applications, the Standard Model is the canvas for any future theory. Whether it emerges as the approximation of a more complete theory or is extended by new particles and new interactions, it would be nothing other than *the discovery of other facts and laws* mentioned by Michelson. In some sense, instead of the common interpretation of a nearly complete 19^{th} century physics, it now feels more like an early foundation for effective theories, almost a century before they were used in high-energy

physics.

In this spirit of exploring the edge of the set of experimental observations in search of New Physics (NP), the work that led to this thesis was focused on finding and constraining new flavor physics observables. While the gauge sector of the Standard Model (SM) is very well understood, by virtue of being constrained by its theoretical simplicity, depending only on a few gauge constants, reflecting the underlying gauge symmetry, this is not the case for the flavor sector. Fermions in the SM appear in three distinct families, that would each obey a $U(3)$ symmetry if they were massless. Not only is this not the case, but fermions also exhibit clear patterns in their masses and mixing. Experimental measurements helped us realize that quark masses span 6 orders of magnitude, each family being heavier than the previous one. The mixing matrix among quarks, the so-call Cabibbo-Kobayashi-Maskawa (CKM) matrix is found to be very hierarchical: composed of 3 rotations between the 3 flavors, such that matrix entries again span 3 orders of magnitude. These curious coincidences already call for a NP explanation of flavor.

In addition to these strange structures, the discovery of hints of Lepton Flavor Universality Violation (LFUV) in semileptonic B meson decays seals the flavor sector as a prime laboratory for discovery of NP. More specifically, since the SM forbids flavor changing neutral currents at tree-level, the so-called "rare B decays" $B \to K^{(*)}\ell^+\ell^-$ ($\ell = e, \mu$) can only happen through purely quantum effects, thus allowing for precision tests of the SM. In particular, because m_e and m_μ are small compared to the other energy scales of this process, the ratio of $R_{K^{(*)}} = \mathcal{B}(B \to K^{(*)}\mu^+\mu^-)/\mathcal{B}(B \to K^{(*)}e^+e^-)$ is expected to be very close to 1. However, LHCb measurements [1, 2] of these observables found significantly smaller values. It is equally surprising that another anomaly appeared in the decay of B mesons through charged currents, which are not suppressed in the SM. In particular the observable $R_{D^{(*)}} = \mathcal{B}(B \to D^{(*)}\tau\bar{\nu})/\mathcal{B}(B \to D^{(*)}\mu\bar{\nu})$ have been measured by B-factories above its SM prediction [3, 4].

There are two main strategies to uncover the potential NP responsible for LFUV. The first is the "top-down" approach, where we start by writing down a NP scenario and then compute quantities that are confronted with experiment. While this opens the possibility for discoveries of new particles, it also requires prior knowledge of the content of NP and a plethora of experimental searches, one for each model. And while it is always possible to push the masses of new particles very high to avoid conflict with all the phenomenological constraints, it becomes hard to explain the anomalies without unnaturally big or fine-tuned couplings. The alternative strategy is a "bottom-up" approach. If we assume that NP happens at a very high energy scale, potentially higher than those probed in experiments, it becomes possible to classify every possible NP contribution within an Effective Field Theory (EFT). Experimental results are then used to constrain the values of the many coefficients of the EFT, in a manner, at least in principle, completely agnostic of the details of the NP.

In this thesis, we will combine these two complementary approaches. Inspired by the B-anomalies, we propose new flavor observables that can be used to further constrain the coefficients of the EFT. Using the constraints we derive, it becomes easier to build explicit models of NP that can satisfy all of the available constraints. We illustrate this point using the extensions of the SM involving one or two low-energy ($\mathcal{O}(1\ \mathrm{TeV})$) Leptoquarks (LQ), a class of scalar or vector bosons that can couple simultaneously to quarks and leptons. The outline of this thesis is as follows:

- In Chapter 1 we briefly introduce the SM Lagrangian in order to fix our notation and conventions, and we discuss some of the motivations for physics beyond the SM in more detail, paying particular attention to the B-anomalies.

- In Chapter 2, we discuss several extensions of the SM considered in this thesis, reflected in 2 Effective Field Theories: the Low-energy EFT (LEFT) used for observable below the electroweak scale and the Standard Model EFT (SMEFT) used when the propagation of the electroweak bosons is required. We also introduce the notation for 5 Leptoquark models that can explain part of the B-anomalies, as well as their matching to the EFTs.

- In Chapter 3 we consider various low-energy flavor observables for charged current processes. In addition to the usual R_D and R_{D^*}, we derive constraints from all the available semileptonic decays of pseudoscalar mesons, while focusing in particular on the observables that are devoid of problematic theoretical uncertainties, such as those coming from the CKM matrix elements or the QCD uncertainties inherent to hadron decays. Finally, we discuss the possibility of extracting constraints from the angular distribution of the semileptonic decays of heavy baryons.

- In Chapter 4, we consider a completely different class of constraints on the NP coefficients: those obtained from study of the tail of the differential cross-section of $pp \to \ell\ell'$ by relying on the data accumulated by CMS and ATLAS collaboration at LHC. While no excess is observed in these processes, the constraints obtained are complementary to the low-energy constraints discussed in Chapter 3. Disentangling the many flavors involved in these collisions led to the development of the package `HighPT`, a new tool for LHC flavor phenomenology. Since the validity of the EFT is not guaranteed in high-energy experiments, we implemented a possibility of both EFT and explicit mediators, thus permitting a comparison between the two approaches.

- Finally, in Chapter 5 we apply all of the previous constraints to our leptoquark scenarios of choice. We first consider single LQ solutions, and then focus on a specific scenario involving two scalar leptoquarks: R_2 and S_3.

Chapter 1

Standard Model

1.1 The SM Lagrangian

The Standard Model (SM) is among the most predictive theories of Nature. It explains the behavior of the content of the universe: particles. Since its formulation (under a simplified form), its validity has continuously been tested experimentally with increasing precision. The final missing piece of the SM has been found in 2012 with the discovery of the predicted Higgs Boson, sealing the success of the theory.

The SM is a quantum field theory (QFT) exhibiting a $SU(3)_C \times SU(2)_L \times U(1)_Y$ gauge invariance. Imposing local invariance of the Lagrangian under each of those 3 groups requires 3 different kinds of gauge bosons. Their interactions will be responsible for 3 fundamental forces: Strong, Weak, and Electromagnetic interaction. In addition to the gauge fields, the theory is populated with fermionic fields forming the matter content of the universe. Some of the gauge fields are observed to be massive but a mass term in the Lagrangian would break gauge invariance. This can be avoided by introducing a scalar Higgs field, whose non-zero vacuum expectation value spontaneously breaks the symmetry. The Higgs field can also explain the mass of fermions via the Yukawa interaction.

The complete SM Lagrangian can thus be decomposed as

$$\mathcal{L}_{\text{SM}} = \mathcal{L}_{\text{Gauge}} + \mathcal{L}_{\text{Higgs}} + \mathcal{L}_{\text{fermions}} + \mathcal{L}_{\text{Yukawa}}. \tag{1.1}$$

In this section, we will introduce our notations by making explicit each component of the SM Lagrangian.

Gauge Sector

The gauge part of the Lagrangian is the sum of 3 Yang-Mill Lagrangians, one for each gauge group. This sector is completely specified by the 3 groups and the 3 gauge coupling constants.

$$\mathcal{L}_{\text{Gauge}} = -\frac{1}{4} G^a_{\mu\nu} G^{\mu\nu,a} - \frac{1}{4} W^i_{\mu\nu} W^{\mu\nu,i} - \frac{1}{4} B_{\mu\nu} B^{\mu\nu}. \tag{1.2}$$

$a = 1 \dots 8$ and $i = 1 \dots 3$ are the adjoint indices of $SU(3)$ and $SU(2)$ respectively. The summation over repeated indices is always implied. The G, W and B are the field strength tensors defined by

$$G^a_{\mu\nu} = \partial_\mu G^a_\nu - \partial_\nu G^a_\mu + g_s f^{abc} G^b_\mu G^c_\nu, \tag{1.3}$$

$$W^a_{\mu\nu} = \partial_\mu W^i_\nu - \partial_\nu W^i_\mu + g\varepsilon^{ijk} W^j_\mu G^k_\nu, \tag{1.4}$$
$$B_{\mu\nu} = \partial_\mu B_\nu - \partial_\nu B_\mu. \tag{1.5}$$

g_s and g are the gauge coupling constants of $SU(3)$ and $SU(2)$ whereas f^{abc} and ε^{ijk} are the structure constants of the $\mathfrak{su}(3)$ and $\mathfrak{su}(2)$ Lie algebras respectively. The $U(1)_Y$ gauge coupling (that doesn't appear here) is denoted g'.

Higgs Sector and Electroweak Symmetry Breaking

If we want to keep the Lagrangian gauge invariant, we cannot directly include mass terms for the gauge fields. This problem is solved by the Brout-Englert-Higgs mechanism. The main idea is to have a theory whose Langrangian is gauge invariant, but with a ground state that breaks the symmetry. This can be achieved by having a scalar field subjected to a potential with many degenerate minima. Falling into one of those minima corresponds to spontaneously breaking the symmetry.

In order to break the $SU(2)$ symmetry, we need our scalar to be a doublet of $SU(2)$. The most generic doublet scalar Lagrangian can be written:

$$\mathcal{L}_{\text{Higgs}} = (D^\mu \Phi)^\dagger (D_\mu \Phi) + \mu^2 \Phi^\dagger \Phi - \lambda (\Phi^\dagger \Phi)^2, \tag{1.6}$$

where the covariant derivative of the scalar field is

$$D_\mu \Phi = \left[\partial_\mu - ig \frac{\sigma^i}{2} W^i_\mu - i \frac{g'}{2} B_\mu \right] \Phi. \tag{1.7}$$

This Higgs potential depends on 2 parameters: μ and λ. When both are positive the potential admits a local maximum in zero, while still being bounded from below thanks to the quadratic term. This leads to a vacuum states with.

$$\left\langle \Phi^\dagger \Phi \right\rangle = \frac{v^2}{2}, \tag{1.8}$$

where $v = \frac{\mu}{\sqrt{\lambda}}$ is the vecuum expectation value (vev) of the Higgs field. Among all the possible vacuum states, we can choose without loss of generality

$$\langle \Phi \rangle = \frac{1}{\sqrt{2}} \begin{pmatrix} 0 \\ v \end{pmatrix}. \tag{1.9}$$

Of the 4 degrees of freedom of the field Φ, 3 are Goldstone bosons that are "eaten" by the gauge bosons to produce their mass. The last one can be expressed in the unitary gauge as

$$\Phi = \frac{1}{\sqrt{2}} \begin{pmatrix} 0 \\ v + H \end{pmatrix}. \tag{1.10}$$

Where H is the physical Higgs fields observed by LHC in 2012. Expanding the covariant derivatives in the Lagrangian (1.6) with this redefinition of Φ, we obtain quadratic terms for gauge bosons. The resulting masses can be diagonalized by the following linear combinations:

$$W^\pm_\mu = \frac{1}{\sqrt{2}} (W^1_\mu \mp i W^2_\mu), \qquad \text{with mass} \quad m_W = \frac{vg}{2}, \tag{1.11}$$
$$Z_\mu = W^3_\mu \cos\theta_W + B_\mu \sin\theta_W, \qquad \text{with mass} \quad m_Z = \frac{vg}{2\cos\theta_W}, \tag{1.12}$$

$$A_\mu = -W^3_\mu \sin\theta_W + B_\mu \cos\theta_W, \qquad \text{with mass} \quad m_A = 0. \tag{1.13}$$

Where θ_W is the Weinberg angle, defined by $\tan\theta_W = \frac{g'}{g}$. These combinations are the physical Z and W bosons, as well as the photon, that remains strictly massless thanks to the residual custodial symmetry. Combined precise electroweak measurements [5,6] give

$$m_W = 80.385(15)\ \text{GeV}, \qquad m_Z = 91.1876(21)\ \text{GeV}. \tag{1.14}$$

The parameters of the Higgs potential can be accessed from the mass of the Higgs boson $m_H = \sqrt{2\mu^2} = 125.25(17)$ GeV [7,8], and the value of the vev v, which can be related to the Fermi constant G_F, usually measured using muon decay:

$$G_F = \frac{1}{\sqrt{2}v^2}. \tag{1.15}$$

The masses of the electroweak gauge bosons being related to the coupling strength and the Higgs VEV is a very strong prediction of the SM, tested with great accuracy.

Fermion sector

The fermionic sector of the theory seems to be populated by 5 fields, all either in the singlet or fundamental representation of the gauge groups. The list of assigned charges is shown in Tab. 1.1. Fields are separated based on their chirality: doublets of $SU(2)_L$ are left-handed while singlets are right-handed fields. In addition, each field exists in 3 *flavors*, i.e. the Lagrangian contains 3 copies of each particle, identical up to the mass, which are given names in Tab. 1.2.

	$SU(3)_C$	$SU(2)_L$	$U(1)_Y$
L	1	2	$-1/2$
ℓ	1	1	-1
Q	3	2	$1/6$
u	3	1	$2/3$
d	3	1	$-1/3$

Table 1.1: *Dimension of the representation of the SM fermionic fields under the gauge group. For $U(1)_Y$ we instead give the hypercharge of the field.*

The Lagrangian for Fermions can be obtained using only the representation and charges of the fields. It is expressed using the following covariant derivatives:

$$D_\mu\Psi = \partial_\mu - i\frac{g_s}{2}\lambda_a G^a_\mu \Psi - i\frac{g}{2}\sigma_i W^i_\mu \Psi - ig' Y B_\mu \Psi, \tag{1.16}$$

where λ_a are the 8 Gell-Mann matrices and σ_i are the 3 Pauli matrices. The second (resp. third) term does not contribute in the case of singlet of $SU(3)$ (resp. $SU(2)$). Using those definitions, we can build a gauge invariant Lagrangian for fermions:

$$\mathcal{L}_{\text{fermions}} = \sum_{\text{flavors}} \sum_{\Psi\in L,Q,u,d,\ell} i\bar{\Psi}\not{D}\Psi. \tag{1.17}$$

In which we can substitute Eqs. (1.11-1.13) to obtain the coupling to the physical gauge bosons.

Since left- and right-handed fermions live in different representations of $SU(2)$ and have different weak hypercharge, a simple mass term in the Lagrangian cannot be gauge invariant. We see that we are always missing a $\pm 1/2$ isospin and a $\pm 1/2$ hypercharge. But since those are exactly the charges of the Higgs doublet we can instead reuse the Higgs field and write a Yukawa interaction:

$$\mathcal{L}_{\text{Yukawa}} = -Y^{\ell}_{\alpha\beta}\bar{L}^{i}_{\alpha}\Phi^{i}\ell_{\beta} - Y^{d}_{\alpha\beta}\bar{Q}^{i}_{\alpha}\Phi^{i}d_{\beta} - Y^{u}_{\alpha\beta}\bar{Q}^{i}_{\alpha}\tilde{\Phi}^{i}d_{\beta} + \text{h.c.}, \tag{1.18}$$

where α and β are flavor indices, i is a $SU(2)$ index, and $\tilde{\Phi} = i\sigma_2\Phi^*$. When Φ acquires a non-zero vev, (1.18) results in mass terms for the fermions. The Yukawa matrices Y^{ℓ}, Y^{d} and Y^{u} can at first be any matrix. Using Singular Value Decomposition, we can diagonalize them by redefining independently the left- and right-handed fermions, rotating them from the “flavor" to the “mass" eigenbasis.

$$\Psi_L^{\text{mass}} = V_L^{\Psi\dagger}\Psi_L^{\text{flavor}}, \qquad \Psi_R^{\text{mass}} = V_R^{\Psi\dagger}\Psi_R^{\text{flavor}}, \tag{1.19}$$

where Ψ can be any fermion. V_L and V_R are unitary matrices. In the mass basis, components are given names based on their flavor index, which are summarized in Tab. 1.2. This redefinition leaves invariant most of SM Lagrangian, except for one part describing the interaction between W, up-type and down-type quarks:

$$\mathcal{L}_{\text{fermions}} \supset -\frac{g}{\sqrt{2}}V^{u}_{L\,ik}V^{d\dagger}_{L\,kj}\bar{u}_i \not{W}^{+} P_L d_j. \tag{1.20}$$

$V = V_L^u V_L^{d\dagger}$ defines the so-called the Cabibbo-Kobayashi-Maskawa (CKM) matrix. It is a unitary 3×3 matrix, and can thus depend on 9 parameters: 3 angles and 6 phases. Since we also have 6 quarks, we can absorb 5 of those 6 phases by redefining the phase of quarks relative to each other. We are left with 3 angles and 1 CP-violating phase. It is convenient for later on to work in the basis in which down-type quarks are diagonal, by setting $V = V_L^u$ and $V_L^d = I$. In other words:

$$Q_i^{\text{mass}} = \begin{pmatrix} (V^{\dagger}u_L^{\text{flavor}})_i \\ d_{L\ \ i}^{\text{flavor}} \end{pmatrix} \tag{1.21}$$

Since the CKM matrix is not diagonal, we see from Eq (1.20) that flavor-changing charged currents (CC) are allowed in the SM at tree-level, through a W exchange. This is not the case for neutral currents, where V_L and V_R cancel.

As a consequence of Eq. (1.20), the charged quark currents in the SM always come with a CKM factor. This is problematic when we want to study precision observables since we need to take into account the uncertainties in the CKM elements determination. For this reason, we often build observables that are free of CKM elements, for example by taking the ratio between two different decays involving the same quark current. Such an example with baryons is investigated in Chapter 3.

1.2 Motivation for Physics Beyond the Standard Model

1.2.1 Incompleteness of the theory

Despite all its successes, we know that the Standard Model cannot be the final theory of Nature. Some of its shortcomings include:

	Gen. 1	Gen. 2	Gen. 3
L	$\begin{pmatrix} \nu_{eL} \\ e_L \end{pmatrix}$	$\begin{pmatrix} \nu_{\mu L} \\ \mu_L \end{pmatrix}$	$\begin{pmatrix} \nu_{\tau L} \\ \tau_L \end{pmatrix}$
ℓ	e_R	μ_R	τ_R
Q	$\begin{pmatrix} u_L \\ d_L \end{pmatrix}$	$\begin{pmatrix} c_L \\ s_L \end{pmatrix}$	$\begin{pmatrix} t_L \\ b_L \end{pmatrix}$
u	u_R	c_R	t_R
d	d_R	s_R	b_R

Table 1.2: *Names of the SM fermions in the mass eigenbasis.*

- The absence of neutrino masses. The absolute values of the Neutrino masses have not yet been measured but the observation of neutrino oscillation requires at least 2 of them to be massive. The current limit on the sum of the 3 neutrinos is $0.06\,\mathrm{eV} < \sum m_\nu < 0.12\,\mathrm{eV}$, where the upper limit comes from cosmology. Since neutrinos are strictly massless, this is definitive proof of the existence of physics beyond the SM.

- The lack of Dark Matter. Cold Dark Matter is a necessary component to explain some of the dynamics of the universe at very large scales, such as the rotational curve of galaxies. For a particle to be a Cold Dark Matter candidate, it needs to be massive and very weekly interacting. The SM contains no such particles (neutrino can only form hot Dark Matter), which again strongly suggests the existence of physics beyond the SM.

- The flavor problem. The masses of the SM fermions exhibit strongly organized patterns. They span 6 orders of magnitude between the lightest (electron, $511\,\mathrm{keV}$) and heaviest fermion (top quark, $173\,\mathrm{GeV}$). In addition to all the masses, the 4 CKM parameters are also very hierarchical, yielding a mostly diagonal matrix. All those parameters arise only from the Yukawa parameters and are not linked through any symmetry. As such they have to be extracted from experiment. Even worse, without the Yukawa interaction, the SM Lagrangian would obey a global $U(3)^5$ flavor symmetry (one for each of L, ℓ, Q, u, and d), which is only broken by the Yukawa interaction. This unsatisfactory situation is referred to as the flavor puzzle, and its resolution calls for physics beyond the SM.

- The Hierarchy problem. The Higgs boson is the only scalar particle of the SM. As such, the quantum corrections to its mass are proportional to Λ, the cutoff scale. This is opposed to all the other particles which receive corrections proportional to their mass. If we assume no NP scale above the SM, the next cutoff is the Planck scale at $10^{19}\,\mathrm{GeV}$. If this is really the case, the cancellation between the mass of the Higgs and its counter-term would have to be abnormally exact to allow for such a light Higgs ($125\,\mathrm{GeV}$). Assuming a more reasonable 1 in 10 fine-tuning, the NP scale is expected to be of the order of a few TeV.

1.2.2 Anomalies in B decays

During the last decade, hints of Lepton Flavor Universality Violation (LFUV) have been observed in B-factories [3] and at LHCb [1, 4]. These experiments observed anomalies in the decay of B mesons compared to their SM prediction.

B decay through neutral currents

The B meson is a QCD bound state composed of a $\bar{b}$ antiquark and another light quark (u or d). In the SM they can decay to various end-products. In particular the decay $B \to K^{(*)}\ell^+\ell^-$ where $\ell = e,\ \mu$ and $K^{(*)}$ is a $\bar{s}d$ bound state, is very suppressed in the SM since it involves a flavor changing neutral current (FCNC): $b \to s\ell^+\ell^-$, which doesn't happen at tree-level in the SM. Instead, it can be mediated via loops, as depicted in Fig. 1.1.

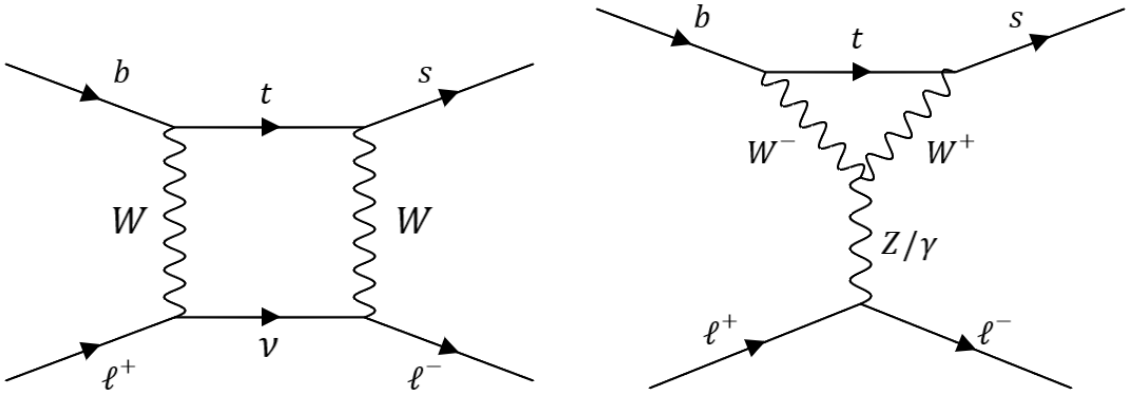

Figure 1.1: *1-loop diagrams contributing to the FCNC in the standard model.*

The theoretical prediction of this decay is complicated by various effects:

- The two quark transitions in the diagrams of Fig. 1.1 are proportional to CKM element, the determination of which comes with experimental uncertainties. Moreover, it is possible that the CKM matrix itself could be affected by NP. We would thus like to use observables that are free of CKM parameters.
- The dominant source of uncertainty by far comes from QCD. The decay amplitude we have to evaluate has to be computed between two bound states of QCD and thus cannot be obtained perturbatively. Instead, we need to use non-perturbative techniques such as Lattice QCD to extract the quark part of the amplitudes. These amplitudes depend on the momentum transfer between the initial and final states and are parameterized in terms of Form Factors. Form factors are obtained along with their uncertainties, which can be of various origins, such as the lattice continuum or high-recoil extrapolation.
- In some regions of phase-space the momentum transfer can be close to the mass of $c\bar{c}$ resonances. This gives the possibility of Non-Local form factors, which will dominate the total decay width since loop-suppressed electroweak effects cannot compete against QCD decays. To prevent those resonances from polluting the results, it is possible to restrict the study of $B \to K^{(*)}\ell^+\ell^-$ to regions of phase-space which are clear of resonances.

To mitigate all three effects, it is convenient to look at the universality ratio $R_K^{\left[q^2_{\rm min},q^2_{\rm max}\right]}$ defined as

$$R_{K^{(*)}}^{[q^2_{\rm min},q^2_{\rm max}]} = \left.\frac{\mathcal{B}\left(B\to K^{(*)}\mu^+\mu^-\right)}{\mathcal{B}\left(B\to K^{(*)}e^+e^-\right)}\right|_{q^2\in\left[q^2_{\rm min},q^2_{\rm max}\right]}, \tag{1.22}$$

where q^2 refers to the square of the momentum transfer between the B and $K^{(*)}$ mesons. $R_{K^{(*)}}$ involves both electrons and muons in the final states, in order for most of the uncertainty (form factors and CKM) to cancel in the ratio. The bounds $\left[q^2_{\rm min}, q^2_{\rm max}\right]$ are chosen in order to avoid any resonances.

Last year, LHCb collaboration presented their new result for R_K [1] which now, combined with their previous data, amounts to

$$R_K^{[1.1,6]} = 0.847 \pm 0.042\,, \tag{1.23}$$

which is 3.1σ lower than predicted in the SM, $R_K^{[1,6]} = 1.00(1)$ [9].

In this work, in addition to the value (1.23), we will also use [2]

$$R_{K*}^{[0.045,1.1]} = 0.68 \pm 0.10\,, \quad R_{K*}^{[1.1,6]} = 0.71 \pm 0.10\,. \tag{1.24}$$

We chose to not use the LHCb measurement of $\Lambda_b \to pK^-\ell^+\ell^-$, involving the same $b\to s\ell^+\ell^-$ semileptonic transition, due to the complicated treatment of theoretical uncertainties. It is however worth mentioning that the universality ratio $R_{pK}^{[0.1,6]}$ has also been measured to be below 1, although with a larger uncertainty [10]:

$$R_{pK}^{[0.1,6]} = \left.\frac{\mathcal{B}\left(\Lambda_b\to pK^-\mu^+\mu^-\right)}{\mathcal{B}\left(\Lambda_b\to pK^-e^+e^-\right)}\right|_{q^2\in[0.1,6]} = 0.86 \pm 14. \tag{1.25}$$

Another related observable involving $b\to s\ell^+\ell^-$ comes from the decay $B_s\to\mu\mu$. The experimental value of $\mathcal{B}(B_s\to\mu\mu)$ has been updated to [11]

$$\mathcal{B}(B_s\to\mu\mu) = (2.70\pm0.36)\times10^{-9}\,, \tag{1.26}$$

to which we include the most recent update of the LHCb result $\mathcal{B}(B_s\to\mu\mu) = (3.09^{+0.48}_{-0.44})\times 10^{-9}$ [12], and by using the prescription of Ref. [13] to build the likelihood functions, the new average value is

$$\mathcal{B}(B_s\to\mu\mu) = (2.85\pm0.33)\times10^{-9}\,, \tag{1.27}$$

thus a little over 2σ lower than predicted in the SM, $\mathcal{B}(B_s\to\mu\mu) = 3.66(14)\times10^{-9}$ [14].

B decay through charged currents

In addition to the anomalies in neutral currents, experimental indications of LFUV have also been observed in the $b\to c\ell\bar\nu_\ell$ charged current (CC) decays. This was surprising considering that this process is allowed at tree-level in the SM through a W exchange, and thus requires a much bigger NP effect compared to the neutral currents, through for example a lower scale of NP [15]. More specifically, we can define the same universality ratio as Eq. (1.22) but involving D mesons in the final state:

$$R_{D^{(*)}} = \left.\frac{\mathcal{B}(B\to D^{(*)}\tau\bar\nu)}{\mathcal{B}(B\to D^{(*)}\ell\bar\nu)}\right|_{\ell\in\{e,\mu\}}. \tag{1.28}$$

Note that since there is no possible resonance in this case, it is not necessary to exclude part of the phase-space in the observable.

Recent measurements by Belle [3], lead to the averages [4],

$$R_D = 0.340 \pm 0.030\,, \quad R_{D^*} = 0.295 \pm 0.014\,, \tag{1.29}$$

which are, due to experimental correlations, about $\approx 3\sigma$ larger than predicted in the SM (see [4] and references therein),

$$R_D^{\rm SM} = 0.293 \pm 0.008\,, \quad R_{D^*}^{\rm SM} = 0.257 \pm 0.003\,. \tag{1.30}$$

A similar deviation, but with less competitive experimental uncertainties, has been observed in a similar $R_{J/\psi}$ ratio [16].

Chapter 2

Beyond the Standard Model

The aforementioned motivations for physics beyond the SM give us little information on its nature, except for the scale of New Physics which has to be around the TeV scale [15]. Thus, we need a way to discuss NP in a model-independent way. This is precisely the framework of Effective Field Theory (EFT). In this work, we will use EFT to present most of our results. This section introduces the notations and conventions we use for the two EFT we will consider: a Low-Energy EFT and the Standard Model EFT.

Since EFT tend to introduce a very large number of parameters, it can also be instructive to introduce explicit scenarios of NP with stronger, minimal assumptions. We discuss here a specific category of scenarios of NP involving Leptoquark states to illustrate the interplay between EFT and explicit models.

2.1 Effective Field Theory

If there is a large separation between the scale of New Physics Λ and the scale of the processes we are studying, we can observe a decoupling between the heavy and light degrees of freedom. This makes it possible to study the low-energy effects of NP without having to completely specify the details of the ultraviolet (UV) completion. By performing an Operator Product Expansion (OPE) we can approximate the complete Lagrangian of NP by a series in $1/\Lambda$, each term composed of a finite number of non-renormalizable operators involving only light (SM) fields. The term Effective Field Theory (EFT) describes the theory we obtain when we allow every possible operator that is allowed by the symmetries of the original theory.

Below the electroweak scale in the broken phase, these symmetries include the Lorentz symmetries, $SU(3)_{\mathrm{color}}$, $U(1)_{\mathrm{charge}}$, and the discrete symmetries of the SM. We consider only operators that contribute to semileptonic transitions, i.e. involving 2 quark and 2 lepton fields, (except for the $\mathcal{O}_7$ operator which involves quarks and photons). Depending on the charge difference between quarks (or equivalently leptons), we separate these operators between the Charged Current (CC) EFT and the Neutral Current EFT (NC).

In the case where we do not want to integrate out the heavy gauge bosons like in Chapter 4, we can instead work in the framework of the Standard Model EFT (SMEFT) by keeping every operator made out of SM fields obeying the same symmetries as the Standard Model: $SU(3)_C \times SU(2)_L \times U(1)_Y$. The added structure can be useful to relate the CC and NC transitions since they will be related through the $SU(2)_L$ symmetry.

In this section, we specify our conventions for the EFT Lagrangians that will be used in this thesis.

2.1.1 Below the electroweak scale: Low-Energy Effective theory

Charged Currents

The most general low-energy effective Lagrangian of dimension-six describing the $d_i \to u_j \ell \bar{\nu}$ transition, with $\ell \in \{e, \mu, \tau\}$, is given by

$$\begin{aligned}\mathcal{L}_{\text{eff}}^{CC} = -2\sqrt{2} G_F V_{ij} \Big[&(1 + g_{V_L}^{ij\,\ell}) \left(\bar{u}_{Li} \gamma_\mu d_{Lj}\right) \left(\bar{\ell}_L \gamma^\mu \nu_L\right) + g_{V_R}^{ij\,\ell} \left(\bar{u}_{Ri} \gamma_\mu d_{Rj}\right) \left(\bar{\ell}_L \gamma^\mu \nu_L\right) \\ &+ g_{S_L}^{ij\,\ell}(\mu) \left(\bar{u}_{Ri} d_{Lj}\right) \left(\bar{\ell}_R \nu_L\right) + g_{S_R}^{ij\,\ell} \left(\bar{u}_{Li} d_{Rj}\right) \left(\bar{\ell}_R \nu_L\right) + g_T^{ij\,\ell}(\mu) \left(\bar{u}_{Ri} \sigma_{\mu\nu} d_{Lj}\right) \left(\bar{\ell}_R \sigma^{\mu\nu} \nu_L\right) \Big] + \text{h.c.}\,,\end{aligned} \tag{2.1}$$

where i, j denote quark-flavor indices, V_{ij} are the CKM matrix elements and $g_\alpha^{ij\,\ell}$ stand for the effective NP couplings, with $\alpha \in \{V_{L(R)}, S_{L(R)}, T\}$. Neutrinos are assumed to be purely left-handed particles and only lepton flavor conserving transitions are considered. In this EFT the scale of NP Λ is supposed to be higher than the electroweak scale and has been hidden into the Fermi constant G_F and the NP couplings $g_\alpha^{ij\,\ell}$. To describe low-energy processes, it is convenient to define effective coefficients with definite parity in the quark current, namely,

$$g_{V(A)}^{ij\,\ell} = g_{V_R}^{ij\,\ell} \pm g_{V_L}^{ij\,\ell}\,, \qquad\qquad g_{S(P)}^{ij\,\ell} = g_{S_R}^{ij\,\ell} \pm g_{S_L}^{ij\,\ell}\,. \tag{2.2}$$

which is useful since the leptonic decays of pseudoscalar mesons will only be sensitive to $g_A^{ij\,\ell}$ and $g_P^{ij\,\ell}$. The remaining effective coefficients, $g_V^{ij\,\ell}$, $g_S^{ij\,\ell}$ and $g_T^{ij\,\ell}$, can be probed by studying the semileptonic processes, $P \to P' \ell \bar{\nu}$, where $P^{(\prime)}$ denote two pseudoscalar mesons.

In the SM, the 5 coefficients appearing in (2.1) are exactly zero, the only SM contribution being the 1 in the left-handed vector operator, obtained from integrating out the W boson (Fermi interaction).

The Effective Lagrangian (2.1) is defined in the broken electroweak phase. However, NP scenarios can only be consistent with the direct search limits from the LHC if the new charged particles arise above the electroweak symmetry breaking scale. Therefore, to reinterpret our results for these scenarios, one should perform the renormalization group evolution from the low-energy scale μ_b up to $\mu_{\text{EW}} \simeq m_W$ [17], and then match Eq. (2.1) to the so-called SMEFT (SM Effective Field Theory) [18, 19]. The concrete ultraviolet scenario can then be matched to the SMEFT after accounting for the running effects above the electroweak scale μ_{EW} [20]. Even though we present our results only in terms of the low-energy effective theory defined in Eq. (2.1), we provide the needed inputs to recast our results to the most general NP scenario in Appendix 2.1.2.

Neutral Currents

In the neutral sector, we restrict ourselves to the quark transition relevant for the B-anomalies. The effective Lagrangian for a generic exclusive decay based on $b \to s \ell_1^- \ell_2^+$, with $\ell_{1,2} \in \{e, \mu, \tau\}$ can be written as

$$\mathcal{L}_{\text{eff}}^{NC} = \frac{4 G_F}{\sqrt{2}} V_{t\alpha} V_{t\beta}^* \sum_i C_i\, \mathcal{O}_i + \text{h.c.}\,, \tag{2.3}$$

where the effective couplings (Wilson coefficients) $C_i \equiv C_i(\mu)$ and the operators $\mathcal{O}_i \equiv \mathcal{O}_i(\mu)$ are defined at the scale μ. The operators relevant to this study are

$$\begin{aligned}
\mathcal{O}_7 &= \frac{e^2}{(4\pi)^2} m_b (\bar{s}\sigma_{\mu\nu} P_R b) F^{\mu\nu} \,, \\
\mathcal{O}_9^{\ell_1\ell_2} &= \frac{e^2}{(4\pi)^2} (\bar{s}\gamma_\mu P_L b)(\bar{\ell}_1 \gamma^\mu \ell_2) \,, \\
\mathcal{O}_{10}^{\ell_1\ell_2} &= \frac{e^2}{(4\pi)^2} (\bar{s}\gamma_\mu P_L b)(\bar{\ell}_1 \gamma^\mu \gamma^5 \ell_2) \,, \\
\mathcal{O}_S^{\ell_1\ell_2} &= \frac{e^2}{(4\pi)^2} (\bar{s} P_R b)(\bar{\ell}_1 \ell_2) \,, \\
\mathcal{O}_P^{\ell_1\ell_2} &= \frac{e^2}{(4\pi)^2} (\bar{s} P_R b)(\bar{\ell}_1 \gamma^5 \ell_2) \,,
\end{aligned} \tag{2.4}$$

in addition to the chirality flipped ones, $\mathcal{O}_i'$, obtained from $\mathcal{O}_i$ by replacing $P_L \leftrightarrow P_R$. The effect of operators $\mathcal{O}_{1-6}$ is included in the redefinition of the effective Wilson coefficients $C_{7,9}$. In what follows we ignore the electromagnetic dipole operators $\mathcal{O}_7^{(\prime)}$ since they do not play a significant role in describing the effects of LFUV.

Contrary to the charged current effective coefficients, the C_i coefficients are not zero in the SM. We thus write all our results in terms of δC_i, the NP contribution to those coefficients.

2.1.2 Above the EW scale: the SM Effective Field Theory

Under the general assumption that NP arises well above the electroweak scale, one should replace Eq. (2.1) with an EFT that is also invariant under $SU(2)_L \times U(1)_Y$, i.e. the SMEFT [18, 19]. The SMEFT Lagrangian can be parameterized as

$$\mathcal{L}_{\text{SMEFT}} \;=\; \mathcal{L}_{\text{SM}} \;+\; \sum_{d,k} \frac{\mathcal{C}_k^{(d)}}{\Lambda^{d-4}} \mathcal{O}_k^{(d)} \;+\; \sum_{d,k} \left[\frac{\mathcal{C}_k^{(d)}}{\Lambda^{d-4}} \widetilde{\mathcal{O}}_k^{(d)} \;+\; \text{h.c.} \right], \tag{2.5}$$

where the first term corresponds to the SM Lagrangian, $\mathcal{O}_i^{(d)}$ and $\widetilde{\mathcal{O}}_k^{(d)}$ respectively denote Hermitian and non-Hermitian operators of dimension $d > 4$, and the UV physics is encoded in the Wilson coefficients $\mathcal{C}_k^{(d)}$. Our conventions for the SMEFT operators are given in appendix E.

To consistently describe a given scattering cross-section at the LHC up to order $\mathcal{O}(1/\Lambda^4)$ in the EFT expansion, it is necessary to include not only the contributions from dimension-6 operators but also the interference terms between dimension-8 operators and the SM contributions since they also appear at the same order,

$$\begin{aligned}
\hat{\sigma} \;\sim\; \int [\mathrm{d}\Phi] \Bigg\{ & |\mathcal{A}_{\text{SM}}|^2 + \frac{v^2}{\Lambda^2} \sum_i 2\,\text{Re}\Big(\mathcal{A}_i^{(6)}\, \mathcal{A}_{\text{SM}}^* \Big) \\
& + \frac{v^4}{\Lambda^4} \left[\sum_{ij} 2\,\text{Re}\Big(\mathcal{A}_i^{(6)}\, \mathcal{A}_j^{(6)\,*} \Big) + \sum_i 2\,\text{Re}\Big(\mathcal{A}_i^{(8)}\, \mathcal{A}_{\text{SM}}^* \Big) \right] + \;\ldots \Bigg\},
\end{aligned} \tag{2.6}$$

where $[\mathrm{d}\Phi]$ denotes the corresponding Lorentz invariant phase-space measure, $\mathcal{A}_{\text{SM}}$ is the SM amplitude, and $\mathcal{A}_i^{(6)}$ and $\mathcal{A}_i^{(8)}$ stand for the New Physics contributions from dimension-6 and dimension-8 operators, respectively. The dependence on the scale Λ is explicitly factorized in each term to emphasize their order in the EFT expansion. The complete classification of

SMEFT operators for $d \leq 8$ can be found in Refs. [18,19,21,22]. In this thesis, we consider the *Warsaw* operator basis at $d=6$ from Ref. [18], as well as its extension to $d=8$ from Ref. [22].

In Chapter 4 we will be interested in the high-energy tails of the momentum-dependent distributions at the LHC. In this regime, only the energy-enhanced terms in eq. (2.6) that are proportional to E/Λ will be relevant, where $E = \sqrt{s}$, while those scaling as powers of v/Λ will be sub-dominant. There are three types of operators that *directly* contribute to the processes $\bar{q}_i q_j \to \ell_\alpha \bar{\ell}_\beta$ and $\bar{u}_i d_j \to \ell_\alpha \bar{\nu}_\beta$ at tree-level which are relevant up to order $\mathcal{O}(1/\Lambda^4)$ in the EFT expansion:

- The semi-leptonic four-fermion operators in the classes $\boldsymbol{\psi^4}$, $\boldsymbol{\psi^4 H^2}$ and $\boldsymbol{\psi^4 D^2}$;
- The Higgs-current operators in the classes $\boldsymbol{\psi^2 H^2 D}$, $\boldsymbol{\psi^2 H^4 D}$ and $\boldsymbol{\psi^2 H^2 D^3}$;
- The dipole operators in the class $\boldsymbol{\psi^2 X H}$.

These operators are defined in appendix E, with the $d = 6$ ones listed in Tables 2, and the $d = 8$ in 3 and 4. The scaling of the New Physics amplitude for large E is shown in Table 2.1 for each class of operators listed above. This scaling is to be compared to the one of the SM amplitude that becomes constant in the $E \gg v$ regime.

Up to dimension $d = 6$, the semi-leptonic four-fermion operators $\boldsymbol{\psi^4}$ give the dominant contributions at large E since they scale quadratically with the energy ($\propto E^2/\Lambda^2$). In particular, the chirality-conserving semi-leptonic operators of this type can also interfere with the SM contributions, giving rise to sizable contributions. Dipole operators $\boldsymbol{\psi^2 X H}$ also induce energy-enhanced contributions at the amplitude level ($\propto vE/\Lambda^2$), but these are suppressed compared to the previous ones since they only increase linearly with E and since they do not interfere with the SM for massless fermions. Moreover, the contributions from Higgs-current operators $\boldsymbol{\psi^2 H^2 D}$ do not increase with E since they only modify the W and Z-couplings, being negligible for the observables we consider. The $d = 8$ operators appear in Table 2.1 with an additional factor of either v^2/Λ^2 or E^2/Λ^2, with respect to the $d = 6$ contributions described above. Since we are interested in the large E region, we will only keep in our numerical analyses the $d = 8$ operators that display an energy enhancement with respect to the SM contributions.

Besides the *direct* contributions to the Drell-Yan cross-sections, there can also be *indirect* contributions arising from the redefinition of the SM inputs by the SMEFT operators. This redefinition induces $\mathcal{O}(v^2/\Lambda^2)$ shifts to the SM contributions in eq. (4.12)–(4.14) depending on

Dimension		$d=6$			$d=8$			
Operator classes		ψ^4	$\psi^2 H^2 D$	$\psi^2 X H$	$\psi^4 D^2$	$\psi^4 H^2$	$\psi^2 H^4 D$	$\psi^2 H^2 D^3$
Amplitude scaling		E^2/Λ^2	v^2/Λ^2	vE/Λ^2	E^4/Λ^4	v^2E^2/Λ^4	v^4/Λ^4	v^2E^2/Λ^4
Parameters	# $\mathbb{Re}$	456	45	48	132	123	48	52
	# $\mathbb{Im}$	399	25	48	18	18	18	12

Table 2.1: *Counting of SMEFT parameters relevant to the high-p_T observables and the corresponding energy scaling of the amplitude for each class of operators. The number of real and imaginary free parameters that contribute to the Drell-Yan cross sections at order $\mathcal{O}(\Lambda^{-4})$ are listed for each type of operator. In total, we find 549 (472) real (imaginary) parameters at $d = 6$ and an additional 355 (66) real (imaginary) parameters at $d = 8$, where for the latter we only consider those parameters that affect the interference of these operators with the SM.*

the chosen scheme for the electroweak parameters [23]. Examples of such operators are the Higgs current $O_{Hl}^{(3)}$ operators or the purely leptonic O_{ll} which can contribute to the muon decay, for specific flavor indices, inducing a finite renormalization of G_F. Similar redefinitions are also needed in the flavor section since the Higgs current and the semi-leptonic operators can induce finite shifts of the CKM parameters that are needed to compute charged-current processes [24]. However, these redefinitions of electroweak and flavor parameters do not lead to energy-enhanced effects at the LHC, thus being negligible in our present analysis.

Lastly, we count the number of independent SMEFT parameters at mass dimension-6 and 8 in Table 2.1. For this counting, it is necessary to separate operators that can contribute to LHC processes including all three quark generations and operators that can contribute only to processes involving the two light quark generations, i.e. operators involving $SU(2)_L$ singlet up-type quarks (u), due to the negligible top quark parton distribution function. We find that there are 549 CP-even and 472 CP-odd parameters that can contribute at $d = 6$ to the Drell-Yan processes. There are additional 355 CP-even and 66 CP-odd parameters that can contribute to these processes when $d = 8$ operators are considered. Note, in particular, that since we truncate the cross-section at order $\mathcal{O}(\Lambda^{-4})$ in the EFT expansion only the interference of the $d = 8$ operators with the SM is relevant for our analysis.

Matching the LEFT to the SMEFT

For completeness, we give here the matching of the SMEFT onto the LEFT. Only five of operators can generate at tree-level the operators in Eq. (2.1), as listed in Table 2.2. To match Eq. (2.1) to (2.5), we assume that down-quark and lepton Yukawa couplings are diagonal, and that right-handed fermions are in the mass basis. The matching relations at $\mu = \mu_{\rm EW}$ are then given by

$$
\begin{aligned}
g_{V_L}^{ij\,\ell}(\mu_{\rm EW}) &= -\frac{v^2}{\Lambda^2}\sum_k \frac{V_{ik}}{V_{ij}}\left(\left[C_{lq}^{(3)}\right]_{\ell\ell kj} + \left[C_{Hq}^{(3)}\right]_{kj} - \delta_{kj}\left[C_{Hl}^{(3)}\right]_{\ell\ell}\right), \\
g_{V_R}^{ij\,\ell}(\mu_{\rm EW}) &= \frac{v^2}{2\Lambda^2}\frac{1}{V_{ij}}\left[C_{Hud}\right]_{ij}, \\
g_{S_L}^{ij\,\ell}(\mu_{\rm EW}) &= -\frac{v^2}{2\Lambda^2}\frac{1}{V_{ij}}\left[C_{lequ}^{(1)}\right]^*_{\ell\ell ji}, \\
g_{S_R}^{ij}(\mu_{\rm EW}) &= -\frac{v^2}{2\Lambda^2}\sum_k \frac{V_{ik}^*}{V_{ij}}\left[C_{ledq}\right]^*_{\ell\ell jk}, \\
g_{T}^{ij\,\ell}(\mu_{\rm EW}) &= -\frac{v^2}{2\Lambda^2}\frac{1}{V_{ij}}\left[C_{lequ}^{(3)}\right]^*_{\ell\ell ji},
\end{aligned}
\tag{2.7}
$$

where we kept only the quark-flavor indices. From these relations, we see that contributions to $g_{V_R}^{ij}$ are necessarily lepton-flavor universal at dimension-6. Furthermore, the operators listed above also induce contributions to the di-lepton transitions $d_i \to d_j\ell\ell$, $d_i \to d_j\nu\nu$, $u_i \to u_j\ell\ell$ and $u_i \to u_j\nu\nu$.

Operator mixing Renormalization group equations (RGEs) are fundamental in order to relate the different scales involved in this problem. First, the running of the semileptonic operators

SMEFT	Definition	LEFT	LFU?
$\left[O_{lq}^{(3)}\right]_{prst}$	$\left(\bar{l}_p\gamma_\mu\tau^I l_r\right)\left(\bar{q}_s\gamma^\mu\tau^I q_t\right)$	g_{V_L}	✗
$\left[O_{ledq}\right]_{prst}$	$\left(\bar{l}_p^j e_r\right)\left(\bar{d}_s q_t\right) + \text{h.c.}$	g_{S_R}	✗
$\left[O_{lequ}^{(1)}\right]_{prst}$	$\left(\bar{l}_p^j e_r\right)\epsilon_{jk}\left(\bar{q}_s^k u_t\right) + \text{h.c.}$	g_{S_L}	✗
$\left[O_{lequ}^{(3)}\right]_{prst}$	$\left(\bar{l}_p^j\sigma_{\mu\nu} e_r\right)\epsilon_{jk}\left(\bar{q}_s^k\sigma^{\mu\nu} u_t\right) + \text{h.c.}$	g_T	✗
$\left[O_{Hl}^{(3)}\right]_{pr}$	$\left(H^\dagger i\overleftrightarrow{D}_\mu^I H\right)\left(\bar{l}_p\gamma^\mu\tau^I l_r\right)$	g_{V_L}	✗
$\left[O_{Hq}^{(3)}\right]_{pr}$	$\left(H^\dagger i\overleftrightarrow{D}_\mu^I H\right)\left(\bar{q}_p\gamma^\mu\tau^I q_r\right)$	g_{V_L}	✓
$\left[O_{Hud}^{(3)}\right]_{pr}$	$\left(\widetilde{H}^\dagger i D_\mu H\right)\left(\bar{u}_p\gamma^\mu d_r\right) + \text{h.c.}$	g_{V_R}	✓

Table 2.2: *SMEFT operators contributing to the low-energy EFT defined in Eq. (2.1). Flavor indices are denoted by $\{p, r, s, t\}$ and $SU(2)_L$ indices by $\{j, k\}$. The operators $O_{Hq}^{(3)}$ and $O_{Hud}^{(3)}$ induce lepton-flavor universal (LFU) contributions. We use the same conventions of Ref. [20].*

from $\mu \approx 1$ TeV down to $\mu_{\text{EW}} \approx m_W$ due to gauge interactions is given by [25]

$$\begin{pmatrix} C_{lq}^{(3)} \\ C_{ledq} \\ C_{lequ}^{(1)} \\ C_{lequ}^{(3)} \end{pmatrix}_{(\mu=m_W)} \approx \begin{pmatrix} 1.00 & 0 & 0 & 0 \\ 0 & 1.19 & 0 & 0 \\ 0 & 0 & 1.20 & -0.185 \\ 0 & 0 & -0.00381 & 0.959 \end{pmatrix} \begin{pmatrix} C_{lq}^{(3)} \\ C_{ledq} \\ C_{lequ}^{(1)} \\ C_{lequ}^{(3)} \end{pmatrix}_{(\mu=1\text{ TeV})} , \tag{2.8}$$

where we have omitted flavor indices and neglected the LFU operators. The $SU(3)_c \times U(1)_{\text{em}}$ running below the EW scale reads [25]

$$\begin{pmatrix} g_{V_L} \\ g_{V_R} \\ g_{S_L} \\ g_{S_R} \\ g_T \end{pmatrix}_{(\mu=m_b)} \approx \begin{pmatrix} 1.00 & 0 & 0 & 0 & 0 \\ 0 & 1.00 & 0 & 0 & 0 \\ 0 & 0 & 1.46 & 0 & -0.0177 \\ 0 & 0 & 0 & 1.46 & 0 \\ 0 & 0 & 0 & 0 & 0.878 \end{pmatrix} \begin{pmatrix} g_{V_L} \\ g_{V_R} \\ g_{S_L} \\ g_{S_R} \\ g_T \end{pmatrix}_{(\mu=m_W)} , \tag{2.9}$$

and

$$\begin{pmatrix} g_{V_L} \\ g_{V_R} \\ g_{S_L} \\ g_{S_R} \\ g_T \end{pmatrix}_{(\mu=2\,\text{GeV})} \approx \begin{pmatrix} 1.00 & 0 & 0 & 0 & 0 \\ 0 & 1.00 & 0 & 0 & 0 \\ 0 & 0 & 1.72 & 0 & -0.02 \\ 0 & 0 & 0 & 1.72 & 0 \\ 0 & 0 & 0 & 0 & 0.82 \end{pmatrix} \begin{pmatrix} g_{V_L} \\ g_{V_R} \\ g_{S_L} \\ g_{S_R} \\ g_T \end{pmatrix}_{(\mu=m_W)} . \tag{2.10}$$

In addition to these RGE effects, there are also the ones induced by the top-quark Yukawa, which mix the four-fermion operators with third-generation couplings into purely leptonic operators such as the ones contributing to $Z \to \ell\ell$ [26] and $H \to \ell\ell$ [27] which are of phenomenological relevance. In summary, the combination of the tree-level matching relations in Eq. (2.7), with the RGE effects in Eq. (2.8)–(2.10), allows us to apply the constraints derived in these thesis to any concrete NP scenario.

2.2 Example of NP scenarios: Leptoquarks

The model-independent approach of EFT is convenient when we do not have any idea of the underlying structure of the NP. In an ideal scenario, we would first obtain numerical values for the Wilson Coefficients through experiment, and would only then search for an explicit realization of the EFT among the many possible NP possibilities. However, it is also possible that the experiment is probing a part of the phase-space where the EFT expansion is not valid, or comes with a sizeable error, see Chapter 4 for an example. In those cases, it is impossible to put truly model-independent constraints on the NP.

Instead, we chose to highlight a small number of explicit NP scenarios involving Leptoquark (LQ) states, which we will introduce briefly in this section. In particular, we focus on the Leptoquarks that have been shown to be compatible with the B-anomalies [28, 29].

Leptoquarks denote massive bosons, scalar or vector, that can couple directly to quarks and leptons in the same interaction. Gauge invariance of the Lagrangian imposes the possible quantum numbers of LQs under SM gauge group $SU(3)_C \times SU(2)_L \times U(1)_Y$. The states we consider here are summarized in table 2.3

	$SU(3)_C$	$SU(2)_L$	$U(1)_Y$
S_1	$\bar{3}$	1	1/3
S_3	$\bar{3}$	3	1/3
R_2	3	2	7/6
U_1	3	1	2/3
U_3	3	3	2/3

Table 2.3: *Quantum number of some Leptoquarks under the SM group* $SU(3)_C \times SU(2)_L \times U(1)_Y$.

In Sect 2.2.1 and 2.2.2 we define the Lagrangian of some scalar and vector Leptoquarks. We neglect the possibility of right-handed neutrinos and we work in the basis with diagonal lepton and down-quark Yukawas, i.e. with left-handed doublets $Q_i = \left((V^\dagger u_L)_i \; d_{Li}\right)^T$ and $L_i = \left(\nu_{Li} \; \ell_{Li}\right)^T$, where V stands for the CKM matrix.

2.2.1 Scalar leptoquarks

- $S_3 = (\bar{\mathbf{3}}, \mathbf{3}, 1/3)$: The weak triplet of LQs is the only scalar boson that can simultaneously accommodate $R_K^{\rm exp} < R_K^{\rm SM}$ and $R_{K^*}^{\rm exp} < R_{K^*}^{\rm SM}$ at tree level [30,31]. The Yukawa Lagrangian

of S_3 can be written as

$$\mathcal{L}_{S_3} = [y_3^L]^{ij}\,\overline{Q_i^C} i\tau_2 (\vec{\tau}\cdot\vec{S_3}) L_j + \text{h.c.}\,, \tag{2.11}$$

where τ_k are the Pauli matrices $(k = 1, 2, 3)$ and $y_3^{L\,ij}$ the generic Yukawa couplings with quark (lepton) indices $i(j)$. LQ couplings to diquarks are neglected in order to guarantee the proton stability [32]. After integrating out the LQ and matching to the low-energy EFT (2.3), we find that the $b \to s\ell_l^-\ell_k^+$ effective coefficients read

$$\delta C_9^{kl} = -\delta C_{10}^{kl} = \frac{\pi v^2}{V_{tb}V_{ts}^*\alpha_{\text{em}}} \frac{[y_3^L]^{bk}\left([y_3^L]^{sl}\right)^*}{m_{S_3}^2}\,, \tag{2.12}$$

As for the charged current transitions, $b \to c\ell\bar{\nu}_{\ell'}$, the S_3 scenario generates at tree level

$$g_{V_L} = -\frac{v^2}{4V_{cb}} \frac{[y_3^L]^{b\ell'}(V[y_3^L])_{c\ell}}{m_{S_3}^2}\,, \tag{2.13}$$

which is strictly negative if we account for the constraints coming from $B \to K^{(*)}\nu\bar{\nu}$ and Δm_{B_s} [28].

- $S_1 = (\bar{\mathbf{3}}, \mathbf{1}, 1/3)$: The weak singlet scalar LQ has the peculiarity of contributing to the $b \to c\tau\bar{\nu}$ transition at tree level, but only at loop level to $b \to s\ell\ell$ [33]. The S_1 Yukawa Lagrangian reads

$$\mathcal{L}_{S_1} = [y_1^L]^{ij}\,\overline{Q_i^C} i\tau_2 L_j\, S_1 + [y_1^R]^{ij}\,\overline{u_{Ri}^C}\ell_{Rj}\, S_1 + \text{h.c.}\,, \tag{2.14}$$

where y_1^L and y_1^R are the LQ Yukawa matrices, and we neglect the diquark couplings for the same reason as in the S_3 case. The coefficients $C_9^{kl} + C_{10}^{kl}$ and $C_9^{kl} - C_{10}^{kl}$ are generated at one-loop by y_1^L and y_1^R, respectively, with the relevant expressions provided in Ref. [33]. This scenario contributes to the $b \to c\ell\bar{\nu}_{\ell'}$ transitions via,

$$g_{V_L} = \frac{v^2}{4V_{cb}} \frac{[y_1^L]^{b\ell'}\left(V[y_1^L]^*\right)_{c\ell}}{m_{S_1}^2}\,, \tag{2.15}$$

$$g_{S_L} = -4g_T = -\frac{v^2}{4V_{cb}} \frac{[y_1^L]^{b\ell'}\left([y_1^R]^{c\ell}\right)^*}{m_{S_1}^2}\,, \tag{2.16}$$

at the matching scale $\mu = m_{S_1}$.

- $R_2 = (\mathbf{3}, \mathbf{2}, 7/6)$: The weak doublet was proposed to separately explain the LFUV effects in the charged [34, 35] and in the neutral current B-decays [36]. This is the only scalar LQ that automatically conserves baryon number [37]. Its Yukawa Lagrangian writes

$$\mathcal{L}_{R_2} = -[y_2^L]^{ij}\,\overline{u}_{Ri} R_2 i\tau_2 L_j + [y_2^R]^{ij}\,\overline{Q}_i R_2 \ell_{Rj} + \text{h.c.}\,, \tag{2.17}$$

with y_2^L and y_2^R being the LQ couplings to fermions. At tree level one gets,

$$\delta C_9^{kl} = \delta C_{10}^{kl} \overset{\text{tree}}{=} -\frac{\pi v^2}{2V_{tb}V_{ts}^*\alpha_{\text{em}}} \frac{[y_2^R]^{sk}\left([y_2^R]^{bl}\right)^*}{m_{R_2}^2}\,. \tag{2.18}$$

We will show in Sec. 3.1 that this pattern is excluded by the observed values of R_K and R_{K^*}, viz. Fig. 3.1. If, however, one sets $y_R = 0$, the leading contribution to $b \to s\mu\mu$

arises at one-loop level and the Wilson coefficients verify $\delta C_9^{\mu\mu} = -\delta C_{10}^{\mu\mu} < 0$, which is a satisfactory scenario [36]. Furthermore, this LQ contributes to the transition $b \to c\ell\bar{\nu}_{\ell'}$, via the effective coupling,

$$g_{S_L} = 4g_T = \frac{v^2}{4V_{cb}} \frac{[y_2^L]^{c\ell'} \left([y_2^R]^{b\ell}\right)^*}{m_{R_2}^2}\,, \tag{2.19}$$

at $\mu = m_{R_2}$.

2.2.2 Vector leptoquarks

- $U_1 = (\mathbf{3}, \mathbf{1}, 2/3)$: A scenario with a weak singlet vector LQ attracted a lot of attention in the literature since it provides the operators needed to explain both the $b \to c\tau\bar{\nu}$ and $b \to s\mu\mu$ anomalies [38–40]. The corresponding interaction Lagrangian can be written as

$$\mathcal{L}_{U_1} = [x_1^L]^{ij}\, \overline{Q}_i \gamma_\mu L_j\, U_1^\mu + [x_1^R]^{ij}\, \overline{d}_{R_i} \gamma_\mu \ell_{Rj} U_1^\mu + \text{h.c.}\,, \tag{2.20}$$

where x_1^L and x_1^R stand for the U_1 couplings to fermions. Notice that the diquark couplings are absent for this state so no additional assumption is needed. In its minimal setup, in which $x_1^R = 0$, and starting from Eq. (2.20), one can easily obtain the contribution to $b \to s\ell_l^-\ell_k^+$,

$$\delta C_9^{kl} = -\delta C_{10}^{kl} = -\frac{\pi v^2}{V_{tb}V_{ts}^* \alpha_{\text{em}}} \frac{[x_1^L]^{sk} \left([x_1^L]^{bl}\right)^*}{m_{U_1}^2}\,, \tag{2.21}$$

while for the $b \to c\ell\bar{\nu}_{\ell'}$ one gets,

$$g_{V_L} = \frac{v^2}{2V_{cb}} \frac{\left(V[x_1^L]\right)_{c\ell'} \left([x_1^L]^{b\ell}\right)^*}{m_{U_1}^2}\,. \tag{2.22}$$

- $U_3 = (\mathbf{3}, \mathbf{3}, 2/3)$: Finally, the interaction of the weak triplet LQ with quarks and leptons is described by

$$\mathcal{L}_{U_3} = [x_3^L]^{ij}\, \overline{Q}_i \gamma_\mu \left(\vec{\tau} \cdot \vec{U}_3^\mu\right) L_j + \text{h.c.}\,, \tag{2.23}$$

where, as before, x_3^L stands for the couplings to fermions. In contrast to U_1 this LQ allows for the dangerous diquark couplings, neglected in the Lagrangian above in order to ensure the proton stability. This scenario contributes to $b \to s\ell_l^-\ell_l^+$ via,

$$\delta C_9^{kl} = -\delta C_{10}^{kl} = -\frac{\pi v^2}{V_{tb}V_{ts}^* \alpha_{\text{em}}} \frac{[x_3^L]^{sk} \left([x_3^L]^{bl}\right)^*}{m_{U_3}^2}\,, \tag{2.24}$$

which, again, can explain R_K and R_{K^*} [41], but it contributes to $b \to c\ell\bar{\nu}_{\ell'}$ through

$$g_{V_L} = -\frac{v^2}{2V_{cb}} \frac{\left(V[x_3^L]\right)_{c\ell'} \left([x_3^L]^{b\ell}\right)^*}{m_{U_3}^2}. \tag{2.25}$$

Alternatively, we give the matching of the 5 leptoquark scenarios to the SMEFT in Tab. 2.4. Note that the matching is given in the flavor basis.

Field	S_1	R_2	U_1	S_3	U_3
Quantum Numbers	$(\bar{\mathbf{3}},\mathbf{1},1/3)$	$(\mathbf{3},\mathbf{2},7/6)$	$(\mathbf{3},\mathbf{1},2/3)$	$(\bar{\mathbf{3}},\mathbf{3},1/3)$	$(\mathbf{3},\mathbf{3},2/3)$
$[\mathcal{C}_{ledq}]_{\alpha\beta ij}$	–	–	$2[x_1^L]^{i\alpha^*}[x_1^R]^{j\beta}$	–	–
$\left[\mathcal{C}^{(1)}_{lequ}\right]_{\alpha\beta ij}$	$\frac{1}{2}[y_1^L]^{i\alpha^*}[y_1^R]^{j\beta}$	$-\frac{1}{2}[y_2^R]^{i\beta}[y_2^L]^{j\alpha^*}$	–	–	–
$\left[\mathcal{C}^{(3)}_{lequ}\right]_{\alpha\beta ij}$	$-\frac{1}{8}[y_1^L]^{i\alpha^*}[y_1^R]^{j\beta}$	$-\frac{1}{8}[y_2^R]^{i\beta}[y_2^L]^{j\alpha^*}$	–	–	–
$[\mathcal{C}_{eu}]_{\alpha\beta ij}$	$\frac{1}{2}[y_1^R]^{j\beta}[y_1^R]^{i\alpha^*}$	–	–	–	–
$[\mathcal{C}_{ed}]_{\alpha\beta ij}$	–	–	$-[x_1^R]^{i\beta}[x_1^R]^{j\alpha^*}$	–	–
$[\mathcal{C}_{\ell u}]_{\alpha\beta ij}$	–	$-\frac{1}{2}[y_2^L]^{i\beta}[y_2^L]^{j\alpha^*}$	–	–	–
$[\mathcal{C}_{qe}]_{ij\alpha\beta}$	–	$-\frac{1}{2}[y_2^R]^{i\beta}[y_2^R]^{j\alpha^*}$	–	–	–
$\left[\mathcal{C}^{(1)}_{lq}\right]_{\alpha\beta ij}$	$\frac{1}{4}[y_1^L]^{i\alpha^*}[y_1^L]^{j\beta}$	–	$-\frac{1}{2}[x_1^L]^{i\beta}[x_1^L]^{j\alpha^*}$	$\frac{3}{4}[y_3^L]^{i\alpha^*}[y_3^L]^{j\beta}$	$\frac{-3}{2}[x_3^L]^{i\beta}[x_3^L]^{j\alpha^*}$
$\left[\mathcal{C}^{(3)}_{lq}\right]_{\alpha\beta ij}$	$-\frac{1}{4}[y_1^L]^{i\alpha^*}[y_1^L]^{j\beta}$	–	$-\frac{1}{2}[x_1^L]^{i\beta}[x_1^L]^{j\alpha^*}$	$\frac{1}{4}[y_3^L]^{i\alpha^*}[y_3^L]^{j\beta}$	$\frac{1}{2}[x_3^L]^{i\beta}[x_3^L]^{j\alpha^*}$

Table 2.4: *Matching of the leptoquarks to the semileptonic operators in the Warsaw basis [18]. In the matching conditions we have set $\Lambda = m_{LQ}$.*

2.2.3 Other potentially constraining observables

The viable leptoquark scenarios mentioned above predict specific combinations of effective semileptonic operators, as shown in Table 2.4. To successfully explain the $b \to c\tau\bar{\nu}$ anomalies, the flavor pattern of the effective coefficients must couple exclusively, or predominantly to the second and third generation of quarks and leptons. The most relevant operators, at the matching scale Λ, in each of these scenarios read

$$S_3 : [\mathcal{C}^{(1)}_{lq}]_{3332} = 3\,[\mathcal{C}^{(3)}_{lq}]_{3332}\,. \tag{2.26}$$

$$S_1 : [\mathcal{C}^{(1)}_{lq}]_{3333} = -[\mathcal{C}^{(3)}_{lq}]_{3333}\,, \qquad [\mathcal{C}^{(1)}_{lequ}]_{3332} = -4\,[\mathcal{C}^{(3)}_{lequ}]_{3332}\,. \tag{2.27}$$

$$R_2 : [\mathcal{C}^{(1)}_{lequ}]_{3332} = 4\,[\mathcal{C}^{(3)}_{lequ}]_{3332}\,. \tag{2.28}$$

$$U_1 : [\mathcal{C}^{(1)}_{lq}]_{3323} = [\mathcal{C}^{(3)}_{lq}]_{3323}\,, \qquad [\mathcal{C}^{(1)}_{lq}]_{3333} = [\mathcal{C}^{(3)}_{lq}]_{3333}\,, \qquad [\mathcal{C}_{ledq}]_{3333}\,. \tag{2.29}$$

$$U_3 : [\mathcal{C}^{(1)}_{lq}]_{3332} = -3\,[\mathcal{C}^{(3)}_{lq}]_{3332}\,. \tag{2.30}$$

These operators contribute not only to the $b \to c\tau\bar{\nu}$ transition but also to many other precision observables that we briefly describe below:

- $B \to K^{(*)}\nu\bar{\nu}$: The $b \to s\nu\bar{\nu}$ transition provides stringent constraints on operators with left-handed leptons [42]. The observables based on this transition are particularly relevant to probe couplings to τ-leptons, which are difficult to assess otherwise. The low-energy

effective Lagrangian describing the $b \to s\nu\nu$ transition can be written as,

$$\mathcal{L}_{\rm eff}^{b\to s\nu\nu} = \frac{4G_F}{\sqrt{2}} V_{tb}V_{ts}^* \frac{\alpha_{\rm em}}{4\pi} \sum_{\alpha\beta} \left(C_L^{\alpha\beta}\, O_L^{\alpha\beta} + C_R^{\alpha\beta}\, O_R^{\alpha\beta} \right) + \text{h.c.}\,, \tag{2.31}$$

with

$$O_L^{\alpha\beta} = (\bar{s}_L\gamma^\mu b_L)(\bar{\nu}_{L\alpha}\gamma_\mu \nu_{L\beta})\,, \qquad O_R^{\alpha\beta} = (\bar{s}_R\gamma^\mu b_R)(\bar{\nu}_{L\alpha}\gamma_\mu \nu_{L\beta})\,, \tag{2.32}$$

where i, j denote flavor indices. The SM contributions are lepton-flavor conserving and they are given by $C_L^{\rm SM} = -13.6(1.2)$, which includes NLO QCD corrections [43–45] and two-loop electroweak contributions [46]. The low-energy Wilson coefficients can be matched to the semileptonic SMEFT operators at $\mu = \mu_{\rm ew}$,

$$C_L^{\alpha\beta} = \delta_{\alpha\beta}\, C_L^{\rm SM} + \frac{2\pi}{\alpha_{\rm em} V_{tb}V_{ts}^*} \frac{v^2}{\Lambda^2} \left(\left[\mathcal{C}_{lq}^{(1-3)}\right]_{\alpha\beta 23} - \delta_{\alpha\beta} \left[\mathcal{C}_{Hq}^{(1-3)}\right]_{23} \right)\,, \tag{2.33}$$

$$C_R^{\alpha\beta} = \frac{2\pi}{\alpha_{\rm em} V_{tb}V_{ts}^*} \frac{v^2}{\Lambda^2} \left(\left[\mathcal{C}_{ld}\right]_{\alpha\beta 23} - \delta_{\alpha\beta} \left[\mathcal{C}_{Hd}\right]_{23} \right)\,, \tag{2.34}$$

where we use the shorthand notation $\mathcal{C}_{lq}^{(1-3)} = \mathcal{C}_{lq}^{(1)} - \mathcal{C}_{lq}^{(3)}$ and $\mathcal{C}_{Hq}^{(1-3)} = \mathcal{C}_{Hq}^{(1)} - \mathcal{C}_{Hq}^{(3)}$. These effective coefficients can be evolved up to the scale Λ by using the one-loop RGEs from Ref. [20, 47, 48]. The $B \to K^{(*)}\nu\bar{\nu}$ branching fractions can be easily computed in terms of the coefficients defined in eq. (2.31) [42]. The most stringent experimental limits are given by $\mathcal{B}(B^+ \to K^+\nu\bar{\nu}) < 1.6 \times 10^{-5}$ and $\mathcal{B}(B^0 \to K^{*0}\nu\bar{\nu}) < 2.7 \times 10^{-5}$ [49–51], which lie just above the SM predictions, namely $\mathcal{B}(B^+ \to K^+\nu\bar{\nu})^{\rm SM} = 4.9(4) \times 10^{-6}$ and $\mathcal{B}(B^0 \to K^{*0}\nu\bar{\nu})^{\rm SM} = 1.00(9) \times 10^{-6}$ [52].

- W and Z-pole observables : The precise determinations of the W and Z couplings at LEP and the LHC can be used to constrain semileptonic interactions at one-loop [26, 53, 54]. The SMEFT operators describing modifications of the Z and W leptonic couplings up to $d = 6$ read

$$\left[\mathcal{O}_{Hl}^{(1)}\right]_{\alpha\beta} = \left(H^\dagger \overleftrightarrow{D}_\mu H\right) \bar{l}_\alpha \gamma^\mu l_\beta\,, \qquad \left[\mathcal{O}_{He}\right]_{\alpha\beta} = \left(H^\dagger \overleftrightarrow{D}_\mu H\right) \bar{e}_\alpha \gamma^\mu e_\beta\,, \tag{2.35}$$

$$\left[\mathcal{O}_{Hl}^{(3)}\right]_{\alpha\beta} = \left(H^\dagger \overleftrightarrow{D}^I_\mu H\right) \bar{l}_\alpha \gamma^\mu \tau^I l_\beta\,. \tag{2.36}$$

  Chirality-conserving semileptonic operators such as $\mathcal{O}_{lq}^{(1)}$ and $\mathcal{O}_{lq}^{(3)}$ mix into these operators at one-loop [20, 47, 48]. In particular, these effects can be sizable for semileptonic couplings to the top quark. In our analysis, we account for these contributions by using a leading-logarithmic approximation and we consider the recent fit to the couplings W and Z couplings from Ref. [55].

- $H \to \tau\tau$: Measurements of the Higgs Yukawa coupling to τ-leptons at the LHC can also provide a useful constraint on specific semileptonic operators at one-loop. This is the case for the chirality-breaking operators $\mathcal{O}_{lequ}^{(1)}$ and $\mathcal{O}_{ledq}$, since they mix at one-loop with the following operator,

$$\left[\mathcal{O}_{eH}\right]_{\alpha\beta} = \left(H^\dagger H\right) \bar{l}_\alpha H e_\beta\,, \tag{2.37}$$

  which induces a shift in the τ-lepton Yukawa after the electroweak-symmetry breaking. This contribution is particularly relevant if the semileptonic operators couple with

third-generation quarks, due to the chirality-enhancement induced via the Yukawa (i.e. $\propto m_t/m_\tau$) [27]. The latest PDG average for the $H \to \tau\tau$ strength signal reads [56],

$$\mu_{\tau\tau}^{\rm exp} = \frac{\sigma(pp \to h) \cdot \mathcal{B}(H \to \tau\tau)}{\sigma(pp \to h)_{\rm SM} \cdot \mathcal{B}(H \to \tau\tau)_{\rm SM}} = 1.15^{+0.16}_{-0.15}\,, \tag{2.38}$$

which is used to constrain the relevant operators at one-loop, with a leading-logarithm approximation, and assuming that the Higgs production cross-section at the LHC is unaffected by New Physics.

Chapter 3

Low Energy Flavor observables

3.1 Previous EFT fits to the B-anomalies

3.1.1 R_K and R_{K^*}

Using the 3 cleanest observables sensitive to neutral current that we introduced in Sec. 1.2.2, namely, R_K, R_{K^*} and $\mathcal{B}(B_s \to \mu\mu)$, we perform a fit in the $C_9 - C_{10}$ plane. The result of our fit is shown in Fig. 3.1 where we see a good agreement among all three observables. Furthermore, we again see that the data are not consistent with the scenario $\delta C_9^{\mu\mu} = +\delta C_{10}^{\mu\mu}$, but instead they are consistent with the solution, $\delta C_9^{\mu\mu} = -\delta C_{10}^{\mu\mu}$. This was to be expected, since the effects of the interference with the SM dominates for small couplings and the SM is lepton-left-handed: $C_9^{SM} \simeq -C_{10}^{SM}$. A scenario involving C_{10} only is also possible. By focussing on the left-handed case, we find

$$\delta C_9^{\mu\mu} = -\delta C_{10}^{\mu\mu} = -0.41 \pm 0.09\,, \tag{3.1}$$

which measures the deviation between the measured and the SM predictions of all three observables combined.

3.1.2 R_D and R_{D^*}

To determine the allowed values of g_i, we assume that NP predominantly contributes to the $b \to c\tau\bar{\nu}$ transition, while being tiny in the case of electron or muon in the final state. In addition to the ratios R_D and R_{D^*}, an important constraint onto $g_P \equiv g_{S_R} - g_{S_L}$ comes from the B_c-meson lifetime [57]. In that respect, we conservatively impose on the still unknown decay rate to be $\mathcal{B}(B_c \to \tau\bar{\nu}) \lesssim 30\%$. That constraint alone already eliminates a possibility of accommodating the $R_{D^{(*)}}^{\rm exp}$ values by solely relying on the (pseudo)scalar operators [57].

To obtain the allowed range of values for g_{S_L} we use the most recent determination of $R_{D^{(*)}}^{\rm SM}$, obtained after combining the lattice QCD results for the relevant form factors in the high q^2-region with those extracted from experimental analysis at low q^2's [58]. Notice also that in this work we use expressions and the values of the ratios of tensor form factors and the (dominant) axial form factor [$A_1(q^2)$] from Ref. [59]. A lattice QCD computation of the tensor form factors would be very welcome.

By using the hadronic input collected in Ref. [28] we make the one-dimensional fits in which one real effective coupling at a time is allowed to take a non-zero value, $g_i(m_b)$, where

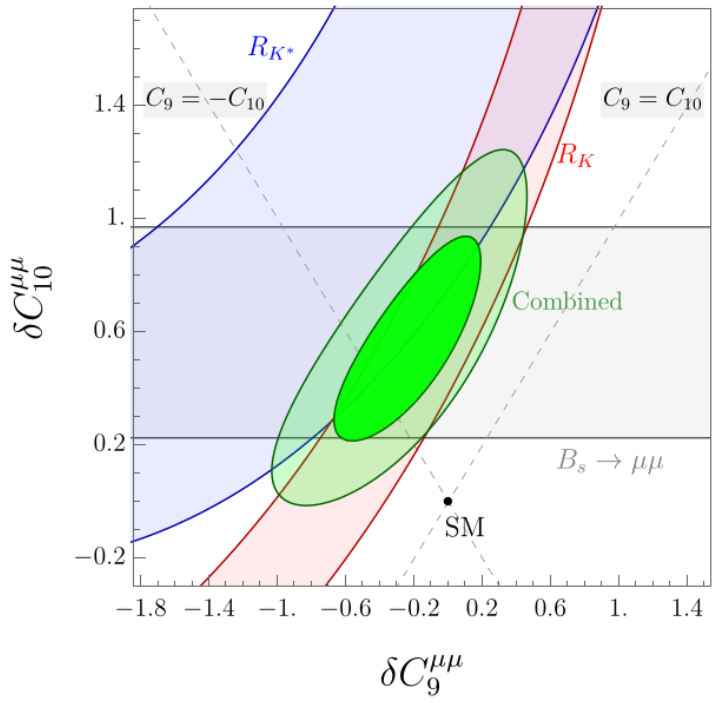

Figure 3.1: *Allowed regions in the plane $\delta C_9^{\mu\mu}$ vs. $\delta C_{10}^{\mu\mu}$ to 1σ accuracy derived by using R_K (red region), R_{K^*} (blue region) and $\mathcal{B}(B_s \to \mu\mu)$ (gray region). Darker (lighter) green regions correspond to the combined fit to 1σ (2σ) accuracy.*

$i \in \{V_L, S_R, S_L, T\}$. We also consider two scenarios motivated by the LQ models and defined by the relations $g_{S_L}(\Lambda) = +4\, g_T(\Lambda)$ and $g_{S_L}(\Lambda) = -4\, g_T(\Lambda)$ at the scale $\Lambda \approx 1$ TeV. After accounting for the renormalization group running from Λ to m_b, these relations become $g_{S_L}(m_b) \approx +8.1\, g_T(m_b)$ and $g_{S_L}(m_b) \approx -8.5\, g_T(m_b)$, respectively. We quote the allowed 1σ ranges for $g_{S_L}(m_b)$ in the latter two scenarios, both for real and for purely imaginary values. The results of all these scenarios are presented in Table 3.1, where we see that only a few scenarios can improve the SM description of $b \to c\tau\bar{\nu}$ data.

In Fig. 3.2, we predict the correlation between $R_{D^*}/R_{D^*}^{\rm SM}$ and $R_D/R_D^{\rm SM}$ within selected EFT scenarios, and we confront these predictions with the current experimental values for these ratios. In this plot, we also illustrate the results presented in Table 3.1 and confirm that the scenarios with $g_{V_L} > 0$, $g_{S_L} = -4g_T > 0$ and $g_{S_L} = \pm 4 g_T \in i\,\mathbb{R}$ are in good agreement with current data. Furthermore, it becomes clear why the scenario $g_{S_L} = 4g_T \in \mathbb{R}$ is excluded, as it cannot simultaneously explain an excess in both $R_D^{\rm exp}$ and $R_{D^*}^{\rm exp}$. In the same Fig. 3.2, we show a similar correlation between $R_{\Lambda_c}/R_{\Lambda_c}^{\rm SM}$ and $R_{D^*}/R_{D^*}^{\rm SM}$, which is perhaps more interesting a prediction, since the value of $R_{\Lambda_c} = \mathcal{B}(\Lambda_b \to \Lambda_c \tau\bar{\nu})/\mathcal{B}(\Lambda_b \to \Lambda_c \mu\bar{\nu})$ has not yet been experimentally established, although the early study has been reported in Ref. [60]. Theoretical expressions for R_{Λ_c} in a general NP scenario (2.1) can be found in Ref. [61] as well as in Sec. 3.3.

3.2 Precision observables of meson decay

Leptonic and semileptonic decays of hadrons in the Standard Model (SM) are described by the weak charged currents and as such, they are useful for extracting the values of the Cabibbo–Kobayashi-Maskawa (CKM) matrix elements. This is done through a comparison of the exper-

Eff. coeff.	1σ range	$\chi^2_{\rm min}/{\rm dof}$
$g_{V_L}(m_b)$	0.07 ± 0.02	$0.02/1$
$g_{S_R}(m_b)$	-0.31 ± 0.05	$5.3/1$
$g_{S_L}(m_b)$	0.12 ± 0.06	$8.8/1$
$g_T(m_b)$	-0.03 ± 0.01	$3.1/1$
$g_{S_L} = +4g_T \in \mathbb{R}$	-0.03 ± 0.07	$12.5/1$
$g_{S_L} = -4g_T \in \mathbb{R}$	0.16 ± 0.05	$2.0/1$
$g_{S_L} = \pm 4g_T \in i\,\mathbb{R}$	0.48 ± 0.08	$2.4/1$

Table 3.1: *Low-energy fit to the $b \to c\tau\bar{\nu}$ effective coefficients defined in Eq. (2.1) by using R_D and R_{D^*}, and by imposing that $\mathcal{B}(B_c \to \bar{\tau}\nu) \lesssim 30\%$. For the individual effective coefficients g_a, we fix the renormalization scale at $\mu = m_b$. For the remaining scenarios with both g_{S_L} and g_T, we impose the conditions $g_{S_L} = \pm 4g_T$ at $\Lambda = 1$ TeV, and provide the allowed range for $g_{S_L}(m_b)$ after accounting for the renormalization-group evolution. The values of $\chi^2_{\rm min}$ for each scenario is to be compared to $\chi^2_{\rm SM} = 12.7$.*

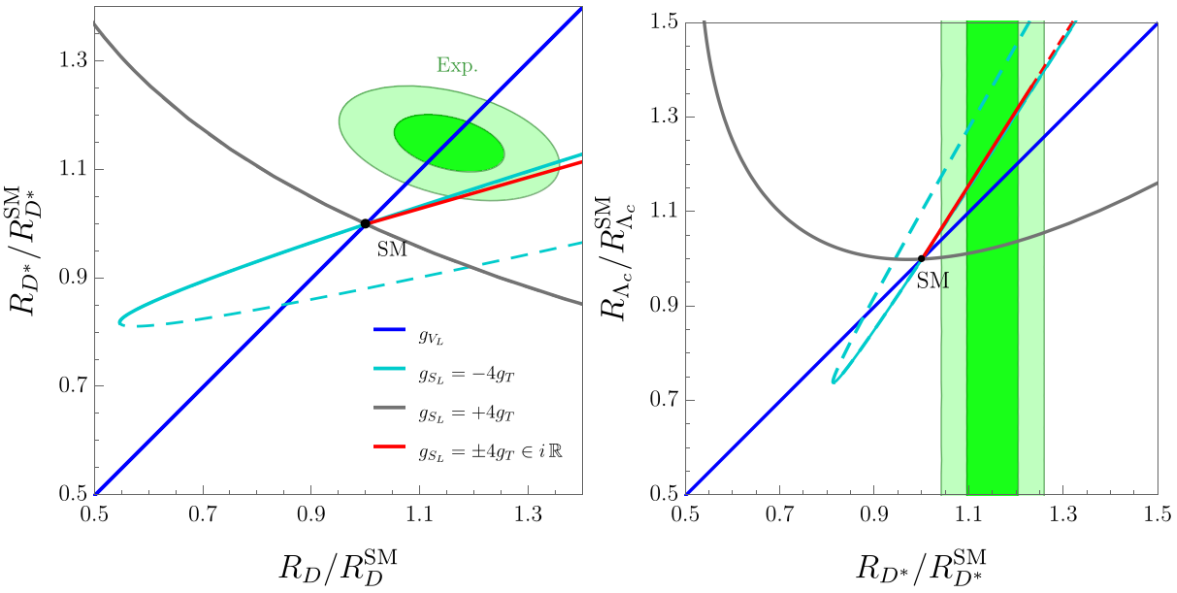

Figure 3.2: *Predictions for $R_{D^*}/R_{D^*}^{\rm SM}$ and $R_{\Lambda_c}/R_{\Lambda_c}^{\rm SM}$ versus $R_D/R_D^{\rm SM}$ in several EFT scenarios, see text for details. Current 1σ (2σ) experimental constraints are depicted by the darker (lighter) green region. Dashed lines correspond to effective couplings that are in tension with the $\mathcal{B}(B_c \to \tau\nu) < 0.3$ constraint.*

imentally established decay rates with the corresponding theoretical expressions. The most difficult problem on the theory side is to reliably estimate the central values and uncertainties attributed to the hadronic matrix elements. In other words, to extract the CKM couplings

with a (sub-)percent accuracy the uncertainties related to the evaluation of the effects of non-perturbative QCD need to be kept at a (sub-)percent level too.

Over the past two decades, we witnessed spectacular progress in taming the hadronic uncertainties by means of numerical simulations of QCD on the lattice (LQCD). In particular, the precision determination of quantities which involve the pseudoscalar mesons (decay constants and form factors) has been radically improved [62]. This is the main reason why we will focus our discussion on the semileptonic decays of one pseudoscalar to another pseudoscalar meson and the leptonic decays of pseudoscalar mesons. Similar semileptonic decays to vector mesons would also be very interesting to consider because they offer a larger set of observables that could be used to probe the effects of New Physics (NP) [63] but the problem is that (i) most of the vector mesons are broad resonances, and (ii) even in the narrow resonance approximation many more hadronic form factors appear in theoretical expressions, making the whole problem much more difficult to handle on the lattice at the level of precision comparable to that achieved with pseudoscalar mesons only. The only exceptions to that pattern are the decays $D_s \to \phi \ell \bar{\nu}$ and $B_c \to J/\psi \ell \bar{\nu}$ which have been studied on the lattice in Ref. [64] and [65], respectively.

In this section, we will therefore use the leptonic and semileptonic decays of pseudoscalar mesons to constrain contributions arising from physics beyond the SM. An important ingredient in such an analysis is the CKM matrix, the entries of which are extracted from various flavor observables, including the same leptonic and semileptonic decays that we consider as probes of the NP couplings [66, 67]. To eliminate this ambiguity in the discussion that follows, we will define suitable observables in which the dependence on the CKM matrix elements cancels out completely. An example of such observables are Lepton Flavor Universality (LFU) ratios, which became popular in recent years owing to the discrepancies observed in semileptonic B-meson decays [68]. However, these are not the only theoretically clean observables that are independent of the CKM matrix elements. Another possibility is to consider ratios of leptonic and semileptonic observables, based on the same quark-level transitions, which allow us to probe the NP couplings without requiring specific assumptions on the non-universality of the leptonic couplings. Furthermore, one can exploit the detailed angular analysis of a given semileptonic decay, which provides us with complementary information on physics beyond the Standard Model (BSM).

3.2.1 $P \to P' \ell \bar{\nu}$

We first focus on $P \to P' \ell \bar{\nu}$, where $P^{(\prime)}$ denotes the pseudoscalar mesons, for which one can build several observables that can be used to test the SM since the hadronic uncertainties in these modes are controlled by LQCD [62]. The differential $P \to P' \ell \bar{\nu}$ decay distribution can be written in general as

$$\frac{\mathrm{d}\mathcal{B}^{\pm}(q^2)}{\mathrm{d}q^2\, \mathrm{d}\cos\theta_\ell} = a^{\pm}(q^2) + b^{\pm}(q^2)\, \cos\theta_\ell + c^{\pm}(q^2)\, \cos^2\theta_\ell \,, \tag{3.2}$$

where $q^2 = (p_\ell + p_\nu)^2$ with $m_\ell^2 < q^2 \leq (m_P - m_{P'})^2$, and θ_ℓ is the angle between ℓ and the P' meson line-of-flight in the rest frame of the lepton pair, cf. Fig. 3.3. The $\pm$ superscript stands for the polarization of the charged lepton, λ_ℓ, and $a^{\pm}(q^2), b^{\pm}(q^2), c^{\pm}(q^2)$ are the q^2-dependent coefficients that are in principle sensitive to NP contributions.

The simplest observable, sensitive to the effective NP couplings, is the differential branching

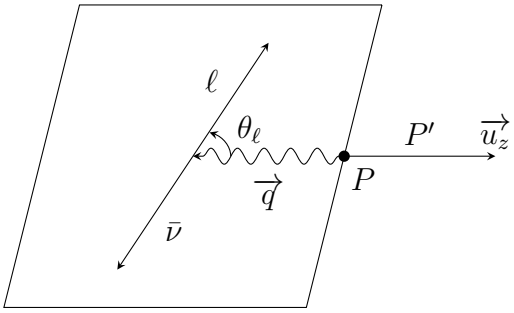

Figure 3.3: *Angular convention for the process $P \to P'\ell\nu$, where $P^{(\prime)}$ are pseudoscalar mesons. The angle θ_ℓ is defined in the rest frame of the meson P.*

fraction,

$$\frac{\mathrm{d}\mathcal{B}(q^2)}{\mathrm{d}q^2} = \int_{-1}^{1} \mathrm{d}\cos\theta_\ell \left[\frac{\mathrm{d}\mathcal{B}^+(q^2)}{\mathrm{d}q^2\,\mathrm{d}\cos\theta_\ell} + \frac{\mathrm{d}\mathcal{B}^-(q^2)}{\mathrm{d}q^2\,\mathrm{d}\cos\theta_\ell}\right] = 2\left[a(q^2) + \frac{c(q^2)}{3}\right], \tag{3.3}$$

where $a(q^2) = a^+(q^2) + a^-(q^2)$, and $c(q^2) = c^+(q^2) + c^-(q^2)$. This observable has already been copiously studied experimentally in the decays of K-, D- and B-mesons [56]. The parameterization in Eq. (3.2) suggests that there is more information that can be in principle extracted from these decays. To this purpose, one should further exploit the angular variables, as well as decays to the specifically polarized outgoing lepton. In the following, we show that four independent observables can be defined and we provide their most general expressions.

Form factors and helicity decomposition

The usual parameterization of the $P \to P'\ell\bar{\nu}$ hadronic matrix elements reads

$$\langle P'(k)|\bar{u}\gamma_\mu d|P(p)\rangle = \left[(p+k)_\mu - \frac{M^2-m^2}{q^2}q_\mu\right] f_+(q^2) + \frac{M^2-m^2}{q^2}q_\mu\, f_0(q^2)\,, \tag{3.4}$$

$$\langle P'(k)|\bar{u}\sigma_{\mu\nu} d|P(p)\rangle = -i(p_\mu k_\nu - p_\nu k_\mu)\frac{2f_T(q^2,\mu)}{M+m}\,, \tag{3.5}$$

where $f_{+,0,T}(q^2)$ are the hadronic form factors evaluated at $q^2 = (p-k)^2$, while $M(m)$ denote the $P(P')$ meson masses. The relevant quark transition is denoted by $d \to u\ell\bar{\nu}$, where flavor indices are omitted for simplicity. The scalar matrix element can be obtained from Eq. (3.4) by using the Ward identity, which amounts to [1]

$$\langle P'(k)|\bar{u}d|P(p)\rangle = \frac{M^2-m^2}{m_d - m_u}\, f_0(q^2)\,. \tag{3.6}$$

With these definitions one can compute the coefficients $a^\pm(q^2)$, $b^\pm(q^2)$ and $c^\pm(q^2)$, defined in Eq. (3.2), as functions of the effective NP couplings, $g_\alpha^{ij\ell}$, introduced in Eq. (2.1). To this purpose, it is convenient to perform a helicity decomposition of the decay amplitude by using the relation,

$$\sum_{n,n'} \varepsilon_V^{*\mu}(n)\varepsilon_V^{\nu}(n') g_{nn'} = g^{\mu\nu}\,, \tag{3.7}$$

[1] In the denominator of the right-hand-side of Eq. (3.6) $m_d - m_u$ should be understood as the quark mass difference between the heavier and the lighter quarks. For instance for the $c \to d$ transition, $m_c - m_d$ should be in the denominator.

where ε_V is the polarization vector of the virtual vector boson, as specified in Appendix 3.2.6, with $n, n' \in \{t, 0, \pm\}$ and $g_{nn'} = \mathrm{diag}(1, -1, -1, -1)$. The decay amplitude can then be decomposed in terms of the helicity amplitudes:

$$h_n(q^2) = \varepsilon_V^{\mu *}(n) \left[(1 + g_V) \langle P' | \bar{u} \gamma_\mu d | P \rangle + g_S \frac{q_\mu}{m_\ell} \langle P' | \bar{u} d | P \rangle \right] , \tag{3.8}$$

$$h_{nm}(q^2) = \varepsilon_V^{\mu *}(n)\, \varepsilon_V^{\nu *}(m)\, g_T \, \langle P' | \bar{u}\, i \sigma_{\mu\nu} d | P \rangle \, , \tag{3.9}$$

which are explicitly given by

$$h_0(q^2) = (1 + g_V) \, \frac{\sqrt{\lambda(q^2, m^2, M^2)}}{\sqrt{q^2}} f_+(q^2) \, , \tag{3.10}$$

$$h_t(q^2) = \left[1 + g_V + g_S \frac{q^2}{m_\ell (m_d - m_u)} \right] \frac{M^2 - m^2}{\sqrt{q^2}} f_0(q^2) \, , \tag{3.11}$$

$$h_{0t}(q^2) = -h_{t0}(q^2) = -\, g_T \frac{\sqrt{\lambda(q^2, m^2, M^2)}}{m + M} f_T(q^2) \, , \tag{3.12}$$

where $\lambda(a^2, b^2, c^2) = [a^2 - (b - c)^2][a^2 - (b + c)^2]$. Other helicity amplitudes actually vanish. In order to express the physical observables defined in Eq. (3.2) in a compact form, we define the following combination of helicity amplitudes

$$h_0^{(+)}(q^2) = h_0(q^2) - \frac{4\sqrt{q^2}}{m_\ell} h_{0t}(q^2) \, , \tag{3.13}$$

$$h_0^{(-)}(q^2) = h_0(q^2) - \frac{4 m_\ell}{\sqrt{q^2}} h_{0t}(q^2) \, , \tag{3.14}$$

which allows us to write

$$a^+(q^2) = \mathcal{B}_0(q^2)\, m_\ell^2 \left| h_t(q^2) \right|^2 , \qquad a^-(q^2) = \mathcal{B}_0(q^2)\, q^2 \left| h_0^{(-)}(q^2) \right|^2 , \tag{3.15}$$

$$b^+(q^2) = \mathcal{B}_0(q^2)\, 2 m_\ell^2 \, \mathrm{Re}\big[h_0^{(+)}(q^2) h_t(q^2)^* \big] , \qquad b^-(q^2) = 0 \, , \tag{3.16}$$

$$c^+(q^2) = \mathcal{B}_0(q^2)\, m_\ell^2 \left| h_0^{(+)}(q^2) \right|^2 , \qquad c^-(q^2) = -\mathcal{B}_0(q^2)\, q^2 \left| h_0^{(-)}(q^2) \right|^2 , \tag{3.17}$$

with

$$\mathcal{B}_0(q^2) = \tau_P \, G_F^2 |V_{ij}|^2 \frac{\sqrt{\lambda(q^2, m^2, M^2)}}{256 \pi^3 M^3} \left(1 - \frac{m_\ell^2}{q^2} \right)^2 , \tag{3.18}$$

where τ_P denotes the P-meson lifetime. From Eqs. (3.15) and (3.17) we see that the following relations hold true,

$$b^-(q^2) = 0 \qquad \text{and} \qquad a^-(q^2) = -c^-(q^2) \, . \tag{3.19}$$

These equalities are respected not only in the SM but also when the NP couplings are considered. An alternative way to derive the above expression is to make a partial-wave decomposition of the matrix elements, combined with selection rules for a left-handed neutrino. In other words, there are only four independent observables that can be constructed at the differential level, instead of six as one would naively infer from Eq. (3.3). These two relations could be a useful consistency check in experimental analyses in which the angular distribution to both polarization states of the charged-lepton is reconstructed. For decays to τ this is possible as the τ-polarization can be reconstructed through its decay to one or three pions, for example. That methodology, however, cannot be applied to the decays to light leptons (μ's or e's).

Physical observables

From the above discussion, we conclude that only four observables are linearly independent. We now list the set of observables that we will use in our subsequent phenomenological discussion.

i) *Branching fraction*: The first observable is the total branching fraction defined in Eq. (3.3), which is the most commonly considered in experimental searches, and which is given by

$$\mathcal{B}_{\rm tot} = \int_{m_\ell^2}^{(M-m)^2} \left(\frac{{\rm d}\mathcal{B}(q^2)}{{\rm d}q^2}\right) dq^2\,, \tag{3.20}$$

with $d\mathcal{B}(q^2)/dq^2$ already given in Eq. (3.3).

ii) *Forward-backward asymmetry*: Another quantity that can be studied experimentally is the forward-backward asymmetry,

$$\frac{{\rm d}A_{\rm fb}(q^2)}{{\rm d}q^2} = \frac{1}{\mathcal{B}_{\rm tot}}\left[\int_0^1 {\rm d}\cos\theta_\ell \frac{{\rm d}\mathcal{B}}{{\rm d}q^2\,{\rm d}\cos\theta_\ell} - \int_{-1}^0 {\rm d}\cos\theta_\ell \frac{{\rm d}\mathcal{B}}{{\rm d}q^2\,{\rm d}\cos\theta_\ell}\right] = \frac{b(q^2)}{\mathcal{B}_{\rm tot}}\,, \tag{3.21}$$

where $\mathcal{B} = \mathcal{B}^+ + \mathcal{B}^-$ and $b(q^2) = b^+(q^2) + b^-(q^2)$, as defined above. This observable is normalized to the total branching fraction, $\mathcal{B}_{\rm tot}$. The above expression refers to the q^2-dependent quantity and its integrated characteristic is obtained after integration over the full q^2 range.

iii) *Lepton-polarization asymmetry*: A study of the decay to the charged lepton with a specific polarization state allows one to measure the lepton-polarization asymmetry defined as,

$$\frac{{\rm d}A_\lambda(q^2)}{{\rm d}q^2} = \frac{1}{\mathcal{B}_{\rm tot}}\left[\frac{{\rm d}\mathcal{B}^+}{{\rm d}q^2} - \frac{{\rm d}\mathcal{B}^-}{{\rm d}q^2}\right]\,, \tag{3.22}$$

which depends on a complementary combination of helicity amplitudes, namely,

$$\frac{{\rm d}A_\lambda(q^2)}{{\rm d}q^2} = \frac{2}{\mathcal{B}_{\rm tot}}\left[a^+(q^2) - a^-(q^2) + \frac{1}{3}\Big(c^+(q^2) - c^-(q^2)\Big)\right]\,. \tag{3.23}$$

iv) *Convexity*: The last independent observable that we consider is defined as follows,

$$\begin{aligned}\frac{{\rm d}A_{\pi/3}(q^2)}{{\rm d}q^2} = \frac{1}{\mathcal{B}_{\rm tot}}\Bigg[&\int_{1/2}^1 {\rm d}\cos\theta_\ell \frac{{\rm d}\mathcal{B}}{{\rm d}q^2{\rm d}\cos\theta_\ell} - \int_{-1/2}^{1/2} {\rm d}\cos\theta_\ell \frac{{\rm d}\mathcal{B}}{{\rm d}q^2\,{\rm d}\cos\theta_\ell} \\ &+ \int_{-1}^{-1/2} {\rm d}\cos\theta_\ell \frac{{\rm d}\mathcal{B}}{{\rm d}q^2\,{\rm d}\cos\theta_\ell}\Bigg]\,,\end{aligned} \tag{3.24}$$

and allows us to single out the "convexity" coefficient $c(q^2) = c^+(q^2) + c^-(q^2)$ i.e.,

$$\frac{{\rm d}A_{\pi/3}(q^2)}{{\rm d}q^2} = \frac{c(q^2)}{2\,\mathcal{B}_{\rm tot}}\,. \tag{3.25}$$

While $A_{\rm fb}$ is defined as the symmetry between events collected in the regions $\theta \in (0, \pi/2)$ and $(\pi/2, \pi)$, the observable $A_{\pi/3}$ measures the difference between events for which $\theta \in (\pi/3, 2\pi/3)$ and those in the complementary angular region, as illustrated in Fig. 3.4.

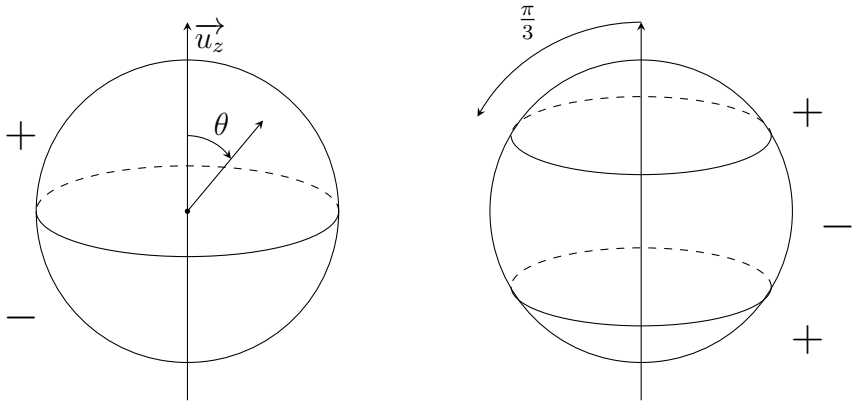

Figure 3.4: *Description to count the events for the angular asymmetry $A_{\rm fb}$ (left panel) and $A_{\pi/3}$ (right panel) as a function of the angle $\theta_\ell \in (0,\pi)$ defined in Fig. 3.3. Both observables are normalized to the total number of events.*

In principle, one could define different sets of observables but, as demonstrated in Eqs. (3.15)–(3.17), these observables would necessarily be a linear combination of the ones defined above. In other words, they do not provide us with any additional information on physics beyond the SM.

3.2.2 $P \to \ell\bar{\nu}$ and $\ell \to P\nu$

As far as the control of the underlying hadronic uncertainties is concerned, the leptonic decays of pseudoscalar mesons are among the cleanest probes of NP. The relevant hadronic matrix elements for these decays in the SM are defined as

$$\langle 0|\bar{u}\gamma^\mu\gamma_5 d|P(p)\rangle = i f_P\, p^\mu\,, \tag{3.26}$$

where f_P is the P-meson decay constant. From Eq. (3.26), after applying the axial Ward identity, the matrix element of the pseudoscalar density reads

$$\langle 0|\bar{u}\gamma_5 d|P(p)\rangle = -i\frac{f_P\, M^2}{m_u + m_d}\,, \tag{3.27}$$

which is also needed to describe the NP contributions. In other words, neglecting QED corrections, the only hadronic quantity needed to describe the leptonic decay mode in the SM and its generic NP extension is the decay constant f_P. It is now straightforward to compute the branching fraction by using the effective Lagrangian (2.1). We have,

$$\mathcal{B}(P\to\ell\bar{\nu}) = \tau_P \frac{G_F^2|V_{ij}|^2 f_P^2 M m_\ell^2}{8\pi}\left(1-\frac{m_\ell^2}{M^2}\right)^2\left|1-g_A+g_P\frac{M^2}{m_\ell(m_u+m_d)}\right|^2\,, \tag{3.28}$$

where M and τ_P denote the mass and the lifetime of P. We remind the reader that the effective coefficients g_A and g_P are related to the effective Lagrangian in Eq. (2.1) via the relations $g_A = g_{V_R} - g_{V_L}$ and $g_P = g_{S_R} - g_{S_L}$. For the τ-lepton and light-quark transitions, it is the inverse process $\tau \to P\nu$ that is kinemetically available, $P = \pi^-, K^-$. These processes can also be computed in terms of f_P and the effective NP couplings $g_{A,P}$,

$$\mathcal{B}(\tau\to P\nu) = \tau_\tau \frac{G_F^2|V_{ij}|^2 f_P^2 m_\tau^3}{16\pi}\left(1-\frac{M^2}{m_\tau^2}\right)^2\left|1-g_A-g_P\frac{M^2}{m_\ell(m_u+m_d)}\right|^2\,, \tag{3.29}$$

where M denotes once again the P-meson mass.

3.2.3 SM phenomenology

Observables

To reduce the theoretical uncertainties, we opt for building observables that are independent of the CKM matrix elements. These observables can be either a ratio of decays with distinct leptons in the final state or a ratio of semileptonic and leptonic decays based on the same quark transition, as we describe in what follows.

- **LFU ratios**: LFU ratios are powerful tests of the validity of the SM, since both theoretical and experimental uncertainties cancel out in these ratios to a large extent. We define,

$$R_P^{(\ell/\ell')} \equiv \frac{\mathcal{B}(P \to \ell\bar{\nu})}{\mathcal{B}(P \to \ell'\bar{\nu})}\,, \qquad R_{PP'}^{(\ell/\ell')} \equiv \frac{\mathcal{B}(P \to P'\ell\bar{\nu})}{\mathcal{B}(P \to P'\ell'\bar{\nu})}\,, \tag{3.30}$$

  where $P^{(\prime)}$ denotes a pseudoscalar meson and $\ell^{(\prime)}$ a charged lepton. Experimental results considered in our analysis are collected in Table 3.4, along with the SM predictions that will be discussed in Section 3.2.3. SM predictions for leptonic decays have no uncertainty when neglecting QED since the decay constant f_P cancels out completely in Eq. (3.30). Moreover, the uncertainties of semileptonic ratios are rather small, since the normalization of $P \to P'$ form factors cancels out in Eq. (3.30), while the remaining uncertainty from the form factor shapes is controlled by the LQCD results, as will be discussed in Sec. 3.2.3.

- **Semileptonic/leptonic ratios:** Another way to eliminate the dependence on the CKM matrix elements is to define the ratios,

$$r_{PP'}^{(\ell)} = \frac{\mathcal{B}(P'' \to \ell\nu)}{\overline{\mathcal{B}}(P \to P'\ell\nu)}\,, \tag{3.31}$$

  where $P'' \to \ell\bar{\nu}$ and $P \to P'\ell\bar{\nu}$ are decays based on the same quark transition. [2] The label in $r_{PP'}^{(\ell)}$ refers to the mesons appearing in the semileptonic process, while P'' is uniquely fixed by the given transition. For instance, $P'' = K$ for the kaon observables $r_{K\pi}^{(\ell)}$, which are based on the transition $s \to u\ell\nu$, and $P'' = B_c$ for $r_{BD}^{(\ell)}$ and $r_{B_sD_s}^{(\ell)}$, which proceed via $b \to c\ell\nu$. The branching fraction in the denominator is defined by combining the semileptonic decays of neutral and charged mesons, as follows,

$$\overline{\mathcal{B}}(P^+ \to P'^0\ell\nu) \equiv \frac{1}{2}\left[\mathcal{B}(P^+ \to P'^0\ell^+\nu) + C_{P'0}^2\,\frac{\tau_{P^+}}{\tau_{P^0}}\,\mathcal{B}(P^0 \to P'^+\ell^-\bar{\nu})\right]\,, \tag{3.32}$$

  where $\tau_{P^+}(\tau_P^0)$ is the lifetime of the meson P with electric charge $+1(0)$, and $C_{P'0}$ is the Clebsch-Gordan coefficient, which is $1/\sqrt{2}$ for $P' = \pi^0$ and 1 otherwise, see e.g. Eq. (3.35) below. [3] The advantage of this definition is to combine meson decays with different lifetimes since the following relation holds, modulo small isospin-breaking corrections,

$$\frac{\mathcal{B}(P^+ \to P'^0\ell^+\nu)}{\mathcal{B}(P^0 \to P'^+\ell^-\bar{\nu})} = C_{P'0}^2\,\frac{\tau_{P^+}}{\tau_{P^0}}\,. \tag{3.33}$$

[2] Similar observables have been defined for the $b \to u\ell\nu$ transition in Ref. [69].

[3] For the decay modes such as $B_s \to D_s\ell\bar{\nu}$, where only one combination of electric charges is possible, the denominator in Eq. (3.31) should be replaced by the standard branching fraction.

The available experimental results for $r_{PP'}^{(\ell/\ell')}$ are collected in Table 3.5, along with our SM predictions that will be discussed in Sec. 3.2.3. The relative hadronic uncertainty of the SM predictions is larger in this case compared to the LFU ratios, also listed in Table 3.4, since they do not cancel out in the ratio. Nonetheless, the current level of accuracy of LQCD determinations for the relevant decay constants and form factors allows us to perform this type of study as well. Notably, these observables are complementary to the ones defined above because they too are sensitive to the LFU contributions from NP which would normally cancel out in Eq. (3.30).

f_P	Value [MeV]	Ref.
f_π	130.2(8)	[62]
f_K	155.7(3)	[62]
f_D	212.0(7)	[62]
f_{D_s}	249.9(5)	[62]
f_B	190.0(1.3)	[62]
f_{B_c}	434(15)	[70]

Table 3.2: *Decay constants obtained by numerical simulations of QCD on the lattice.*

Hadronic inputs and SM predictions

In our analyses, we use the LQCD results for hadronic inputs [62]. The decay constants used in this work are collected in Table 3.2, whereas the publications in which the results for the $P \to P'$ form factors were presented will be appropriately referred to in what follows. The relevant form-factor parameterizations and the needed numerical inputs can be found in the references collected below. In our numerical analysis, we will sample the fit parameters for each transition with a multivariate Gaussian distribution and the covariance matrices provided in the LQCD papers.

- $K \to \pi$: We use the q^2-shape of the $K \to \pi$ form factors $f_0(q^2)$ and $f_+(q^2)$ as reported in Ref. [71] from simulations with $N_f = 2 + 1 + 1$ dynamical quark flavors. Recently, the shapes of these form factors have also been determined in an independent LQCD study [72], but from simulations with $N_f = 2 + 1$ dynamical quarks. The results are fully compatible with those presented in Ref. [71]. Concerning the form factor normalization, i.e. $f_+(0) = f_0(0)$, we use the FLAG average [62],

$$f_+(0) = 0.9706(27)\,, \tag{3.34}$$

  which is dominated by the results reported by MILC/Fermilab [73] and by ETMC [71]. As for the tensor form factor, the only available results come from Ref. [74] which we will use in the following.

- $D \to \pi$ and $D \to K$: The scalar and vector form factors for $D \to \pi$ and $D \to K$ semileptonic decays have been computed in Ref. [75] for all of the physically relevant q^2 values. Similar results for the tensor form factor, for both of these channels, have been presented in Ref. [76].

- $B_{(s)} \to D_{(s)}$: The scalar and vector $B \to D$ form factors have been computed in Refs. [77] and [78], which are combined in our analysis. For the tensor form factor, we use the results for $f_T(q^2)/f_+(q^2)$ evaluated near the zero recoil in Ref. [79] and drive the ratio to low q^2 values by a small slope that we extracted from Ref. [59].

- $B \to \pi$ and $B_s \to K$: The $B \to \pi$ scalar and vector form factors have been computed near zero-recoil in Ref. [80, 81] and combined in Ref. [62], whereas the tensor one has been computed in Ref. [82]. Similarly, the $B_s \to K$ scalar and vector form factors have been recently computed in Ref. [83]. There are no available results for the tensor form factor but since the two decays are similar, we will assume that the ratio $f_T(q^2)/f_+(q^2)$ is the same for both channels, $B \to \pi\ell\bar{\nu}$ and $B_s \to K\ell\bar{\nu}$. Notice that these channels are particularly problematic due to a very large phase-space, which implies rather large theoretical uncertainties when extrapolating the LQCD results for form factors, which are available at large q^2's, all the way down to $q^2 \to 0$. For that reason, these decay modes will be discussed separately in Sec. 3.2.3.

For kaon decays it is also necessary to account for the subleading corrections to match both the experimental precision and the accuracy to which the hadronic matrix elements are evaluated in LQCD. Those subleading corrections are summarized in the following multiplicative factor [84],

$$\mathcal{B}_{K_{\ell 3}} \to \mathcal{B}_{K_{\ell 3}}\, C_\pi^2\, S_{\rm EW} \left(1 + \delta^{K\ell}_{\rm em} + \delta^{K\pi}_{SU(2)}\right)^2 , \tag{3.35}$$

where $S_{\rm EW} = 1.0232(3)$ is the short-distance electroweak correction [85,86], C_π is the Clebsch-Gordan coefficient (1 for decays to $\pi^\pm$ and $1/\sqrt{2}$ for those to π^0), while $\delta^{K\ell}_{\rm em}$ and $\delta^{K\pi}_{SU(2)}$ respectively stand for the channel-dependent electromagnetic and isospin-breaking corrections the values of which are given in Table 3.3. The first lattice QCD results of $\delta^{K\ell}_{\rm em}$ have been presented in Ref. [76], and the reported values fully agree with those given in Table 3.3. Radiative corrections to $K_{\ell 2}$ have been estimated by using chiral perturbation theory (ChPT) and LQCD, leading to the SM prediction [87, 88]

$$\left(\frac{\mathcal{B}_{K_{e2}}}{\mathcal{B}_{K_{\mu 2}}}\right)_{\rm SM} = 2.477(1) \times 10^{-5} . \tag{3.36}$$

The electromagnetic correction to the muonic mode alone can be written as [89–91]

$$\mathcal{B}_{K_{\mu 2}} \to \mathcal{B}_{K_{\mu 2}}(1 + \delta^{K_{\mu 2}}_{\rm em}) , \tag{3.37}$$

where we take $\delta^{K_{\mu 2}}_{\rm em} = 0.0024(10)$, as recently determined in LQCD [88]. While the lattice determination of $\delta^{\pi_{\mu 2}}_{\rm em}$ appeared to be consistent with the one obtained in ChPT, the $\delta^{K_{\mu 2}}_{\rm em}$ value turned out to be much smaller than $\delta^{K_{\mu 2}}_{\rm em} = 0.0107(21)$ as found in ChPT and previously used in phenomenology, cf. Ref. [56] and references therein. As for the ratio of $\mathcal{B}_{K_{\mu 2}}$ and $\mathcal{B}_{\tau_{K2}} \equiv \mathcal{B}(\tau \to K\bar{\nu})$, the radiative corrections are included by [92]

$$\frac{\mathcal{B}_{\tau_{K2}}}{\mathcal{B}_{K_{\mu 2}}} \to \frac{\mathcal{B}_{\tau_{K2}}}{\mathcal{B}_{K_{\mu 2}}} (1 + \delta R_{\tau/K}) , \tag{3.38}$$

with $\delta R_{\tau/K} = 0.90(22) \times 10^{-2}$ [93]. For the observables related to the decays of $D_{(s)}$- and $B_{(s,c)}$-mesons, we do not include the electromagnetic corrections, because the evaluation of these effects is not available from theory yet. In the future, however, and with improved experimental and hadronic uncertainties, it will become necessary to account for these effects as well. Note in particular that such effects are the leading theoretical uncertainties of the LFU ratios of leptonic decays, since the decay constants fully cancel out. [4]

Channel	$\delta_{\rm em}^{K\ell} \times 10^{-2}$	$\delta_{SU(2)}^{K\pi} \times 10^{-2}$
$K^0 \to \pi^+ e\bar{\nu}$	0.49(11)	0
$K^0 \to \pi^+ \mu\bar{\nu}$	0.70(11)	
$K^+ \to \pi^0 e\bar{\nu}$	0.05(13)	2.9(4)
$K^+ \to \pi^0 \mu\bar{\nu}$	0.01(13)	

Table 3.3: *Summary of long-distance electromagnetic* $\left(\delta_{\rm em}^{K\ell}\right)$ *and isospin breaking* $\left(\delta_{SU(2)}^{K\pi}\right)$ *corrections for* $K_{\ell 3}$ *decays [84], see Eq.* (3.35).

With the ingredients described above, we are able to make the SM predictions that are listed in Table 3.4 and 3.5 for the two types of observables that we consider: (i) LFU tests, and (ii) ratios of semileptonic and leptonic decays, based on the same weak process. We find a reasonable agreement between our predictions and the experimental results, with a few exceptions which will be mentioned in the following.

Discussion

$K \to l\nu$, $K \to \pi l\nu$ and $|V_{us}|$: In the kaon sector, we find a good agreement between the SM predictions and experiment for the LFU, as it can be seen in Table 3.4. For the ratios of leptonic and semileptonic decays, we find a reasonable agreement for the electron modes, while for the muonic modes we see a clear discrepancy. More specifically, the SM prediction and the experimental values differ by $3.1\,\sigma$:

$$\frac{\mathcal{B}(K^- \to \mu\nu)^{\rm SM}}{\overline{\mathcal{B}}(K^- \to \pi^0\mu\bar{\nu})^{\rm SM}} = 18.55(16), \qquad \frac{\mathcal{B}(K^- \to \mu\nu)^{\rm exp}}{\overline{\mathcal{B}}(K^- \to \pi^0\mu\bar{\nu})^{\rm exp}} = 19.16(11)\,, \tag{3.39}$$

where in the denominator we use the isospin average according to Eq. (3.32). Also taken separately (without the isospin averaging), the measured values of the ratios are larger than the ones predicted in the SM:

$$\begin{aligned} \frac{\mathcal{B}(K^- \to \mu\nu)^{\rm SM}}{\mathcal{B}(K^- \to \pi^0\mu\bar{\nu})^{\rm SM}} &= 18.26(17), & \frac{\mathcal{B}(K^- \to \mu\nu)^{\rm exp}}{\mathcal{B}(K^- \to \pi^0\mu\bar{\nu})^{\rm exp}} &= 18.9(2)\,, \\ \frac{\mathcal{B}(K^- \to \mu\nu)^{\rm SM}}{\mathcal{B}(K_L \to \pi^+\mu\bar{\nu})^{\rm SM}} &= 2.28(2), & \frac{\mathcal{B}(K^- \to \mu\nu)^{\rm exp}}{\mathcal{B}(K_L \to \pi^+\mu\bar{\nu})^{\rm exp}} &= 2.352(11)\,. \end{aligned} \tag{3.40}$$

[4] Effects from soft-photon emission in semileptonic B-meson decays have been recently considered in Ref. [9, 94, 95], see also Ref. [96].

Observable	Definition	Our SM prediction	Exp. value	Ref.
$R^{(\mu/e)}_{K^-\pi^0}$	$\frac{\mathcal{B}(K^- \to \pi^0 \mu \bar{\nu})}{\mathcal{B}(K^- \to \pi^0 e \bar{\nu})}$	0.663(2)	0.662(3)	[56]
$R^{(\mu/e)}_{K_L\pi^\pm}$	$\frac{\mathcal{B}(K_L \to \pi^\pm \mu \bar{\nu})}{\mathcal{B}(K_L \to \pi^\pm e \bar{\nu})}$	0.666(2)	0.666(4)	[56]
$R^{(e/\mu)}_{K}$	$\frac{\mathcal{B}(K^- \to e \bar{\nu})}{\mathcal{B}(K^- \to \mu \bar{\nu})}$	$2.477(1) \times 10^{-5}$	$2.488(9) \times 10^{-5}$	[56]
$R^{(\tau/\mu)}_{K}$	$\frac{\mathcal{B}(\tau \to K^- \bar{\nu})}{\mathcal{B}(K^- \to \mu \bar{\nu})}$	0.01126(3)	0.0107(4)	[56]
$R^{(\mu/e)}_{D^-\pi^0}$	$\frac{\mathcal{B}(D^- \to \pi^0 \mu \bar{\nu})}{\mathcal{B}(D^- \to \pi^0 e \bar{\nu})}$	0.9864(12)	0.943(45)	[97, 98]
$R^{(\mu/e)}_{D^0\pi^-}$	$\frac{\mathcal{B}(D^0 \to \pi^- \bar{\mu} \nu)}{\mathcal{B}(D^0 \to \pi^- \bar{e} \nu)}$	0.9862(12)	0.915(43)	[99]
$R^{(\mu/e)}_{D}$	$\frac{\mathcal{B}(D^- \to \mu \bar{\nu})}{\mathcal{B}(D^- \to e \bar{\nu})}$	4.24×10^4	> 42.5	[56]
$R^{(\tau/\mu)}_{D}$	$\frac{\mathcal{B}(D^- \to \tau \bar{\nu})}{\mathcal{B}(D^- \to \mu \bar{\nu})}$	2.67	3.21(64)(43)	[100]
$R^{(\mu/e)}_{D^-K^0}$	$\frac{\mathcal{B}(D^- \to K^0 \mu \bar{\nu})}{\mathcal{B}(D^- \to K^0 e \bar{\nu})}$	0.9751(10)	1.003(25)	[56]
$R^{(\mu/e)}_{D^0K^-}$	$\frac{\mathcal{B}(D^0 \to K^- \mu^+ \nu)}{\mathcal{B}(D^0 \to K^- e^+ \nu)}$	0.9751(10)	0.973(14)	[56]
$R^{(\mu/e)}_{D_s}$	$\frac{\mathcal{B}(D_s \to \mu \bar{\nu})}{\mathcal{B}(D_s \to e \bar{\nu})}$	4.25×10^4	> 65.4	[56, 101]
$R^{(\tau/\mu)}_{D_s}$	$\frac{\mathcal{B}(D_s \to \tau \bar{\nu})}{\mathcal{B}(D_s \to \mu \bar{\nu})}$	9.74	10.0(5)	[56, 101]
$R^{(\mu/e)}_{B}$	$\frac{\mathcal{B}(B \to \mu \bar{\nu})}{\mathcal{B}(B \to e \bar{\nu})}$	4.27×10^4	> 0.66	[56, 102]
$R^{(\tau/\mu)}_{B}$	$\frac{\mathcal{B}(B \to \tau \bar{\nu})}{\mathcal{B}(B \to \mu \bar{\nu})}$	2.23×10^2	$1.7(8) \times 10^2$	[56, 102]
$R^{(\mu/e)}_{BD}$	$\frac{\mathcal{B}(B \to D \mu \bar{\nu})}{\mathcal{B}(B \to D e \bar{\nu})}$	0.9960(2)	0.995(22)(39)	[103]
$R^{(\mu/e)}_{B_sD_s}$	$\frac{\mathcal{B}(B_s \to D_s \mu \bar{\nu})}{\mathcal{B}(B_s \to D_s e \bar{\nu})}$	0.9960(2)	–	
$R^{(\tau/\mu)}_{BD}$	$\frac{\mathcal{B}(B \to D \tau \bar{\nu})}{\mathcal{B}(B \to D \mu \bar{\nu})}$	0.295(6)	0.340(27)(13)	[4]
$R^{(\tau/\mu)}_{B_sD_s}$	$\frac{\mathcal{B}(B_s \to D_s \tau \bar{\nu})}{\mathcal{B}(B_s \to D_s \mu \bar{\nu})}$	0.295(6)	–	

Table 3.4: *Experimental results for LFU ratios and SM predictions obtained by using the hadronic inputs described in Sec. 3.2.3. Ratios with semileptonic $B \to \pi(K)$ decays are discussed in Sec. 3.2.3. When quoted, first uncertainty corresponds to the statistical and second to systematic. Upper limits are displayed at 90% C.L.*

Another way to see that problem has been already pointed out when extracting the value of $|V_{us}|$ from leptonic and semileptonic decay respectively [104]. We get:

$$|V_{us}|_{K_{\mu 2}} = 0.2264(6)\,, \qquad |V_{us}|_{K_{\mu 3}} = 0.2228(8)\,, \tag{3.41}$$

with the latter value fully compatible with the one extracted from the electronic mode, $|V_{us}|_{K_{e3}} = 0.2228(7)$. Clearly, the two values in Eq. (3.41) differ by $3.5\,\sigma$. Understanding the origin of that discrepancy requires a proper assessment of the electromagnetic corrections entering the expressions for the $K_{\ell 3}$ decays by means of LQCD.

As a side exercise, one can use the ratio of the accurately measured leptonic decays $K_{\mu 2}/\pi_{\mu 2}$, for which the electromagnetic corrections have been handled by LQCD [105], and combine it with the ratio of decay constants $f_K/f_\pi = 1.193(2)$ [62]. As a result we get $|V_{us}|/|V_{ud}| = 0.2319(5)$. If we neglect $|V_{ub}|$ and impose the CKM unitarity we obtain [5]

$$|V_{us}|^{\rm CKM}_{K_{\mu 2}/\pi_{\mu 2}} = 0.2259(5)\,. \tag{3.42}$$

The same value is obtained if instead of invoking the CKM unitarity we multiply $|V_{us}/V_{ud}|_{K_{\mu 2}/\pi_{\mu 2}}$ by $|V_{ud}|_\beta$, extracted from the nuclear β-decay [106] (see also Ref. [107–110] and references therein). These values are clearly in good agreement with $|V_{us}|_{K_{\mu 2}}$, but not with $|V_{us}|_{K_{\mu 3}}$. Moreover, the discrepancy between $|V_{us}|_{K_{\mu 3}}$ and $|V_{us}|_{K_{\mu 2}}$ is larger if considering the semileptonic decays of charged kaons.

In short, an improved LQCD determination of the $K \to \pi$ form factors, and especially a good control over the electromagnetic corrections is needed in order to clarify this discrepancy. If this discrepancy persists then a viable NP explanation would necessitate introducing the LFU couplings to guarantee consistency with $R_{K\pi}^{(\mu/e)}$, where the SM predictions and the experimental measurements agree very well, cf. Table 3.4.

Before closing this discussion we should emphasize the fact that for the semileptonic decays we took the values for $\mathcal{B}(K^- \to \pi^0 l\bar{\nu})^{\rm exp}$ from Ref. [104]. Had we used the simple averages of the measurements reported in the literature, and listed in PDG Review [56], the abovementioned discrepancy between $|V_{us}|_{K_{\mu 2}}$ and $|V_{us}|_{K_{\ell 3}}$ would increase to $5\,\sigma$. We believe that more discussion in assessing the correct values of the experimental branching fractions in the kaon decays is needed. For example, the value of $\mathcal{B}(K^- \to \pi^0 \mu\bar{\nu})^{\rm exp} = 3.366(30)\ \%$ as suggested in Ref. [104] is very close to the value reported in the PDG Review as "Our Fit", but it is $2.7\,\sigma$ larger than the ordinary average which is heavily dominated by the result reported by the KLOE collaboration, namely $\mathcal{B}(K^- \to \pi^0 \mu\bar{\nu})^{\rm exp} = 3.233(39)\ \%$ [111]. Similar situation is true for $\mathcal{B}(K^- \to \pi^0 e\bar{\nu})^{\rm exp}$.

$D \to \pi l\nu$ and $|V_{cd}|$: As it can be seen in Table 3.4, we also find mild discrepancies between theory and experiment in $D \to \pi l\bar{\nu}$. These are mostly related to the recent BESIII results on $D^0 \to \pi^+ l\bar{\nu}$ decays (with $l = e, \mu$) [99, 112]. To investigate this problem, we compare in Fig. 3.5 the ratio of the $D \to \pi\mu\bar{\nu}$ and $D \to \pi e\bar{\nu}$ differential distributions measured experimentally for both D^+ and D^0 decays [98, 99, 112] with the SM predictions based on the form factors taken from Ref. [75]. While there is a good agreement between theory and experiment for $D^+ \to \pi^0 l\bar{\nu}$ decays, we observe mild discrepancies in several q^2 bins of $D^0 \to \pi^+ l\bar{\nu}$ (see also Ref. [113]). Since these deviations only appear in one of the decay modes, it is likely that they arise from an underestimated theoretical or experimental uncertainty near the

[5] Note that the value of $|V_{ub}|$ is irrelevant for this discussion since its central value is too small compared to the current precision in the determination of $|V_{us}|$ and $|V_{ud}|$.

Observable	Definition	Our SM prediction	Exp. value	Ref.
$r_{K\pi}^{(e)}$	$\frac{\mathcal{B}(K^- \to e\bar{\nu})}{\overline{\mathcal{B}}(K^- \to \pi^0 e\bar{\nu})}$	$3.05(3) \times 10^{-4}$	$3.17(2) \times 10^{-4}$	[104]
$r_{K\pi}^{(\mu)}$	$\frac{\mathcal{B}(K^- \to \mu\bar{\nu})}{\overline{\mathcal{B}}(K^- \to \pi^0 \mu\bar{\nu})}$	18.6(2)	19.2(1)	[104]
$r_{D\pi}^{(e)}$	$\frac{\mathcal{B}(D^- \to e\bar{\nu})}{\overline{\mathcal{B}}(D^- \to \pi^0 e\bar{\nu})}$	$2.79(12) \times 10^{-6}$	$< 2.4 \times 10^{-3}$	[56]
$r_{D\pi}^{(\mu)}$	$\frac{\mathcal{B}(D^- \to \mu\bar{\nu})}{\overline{\mathcal{B}}(D^- \to \pi^0 \mu\bar{\nu})}$	0.120(5)	0.108(7)	[56]
$r_{DK}^{(e)}$	$\frac{\mathcal{B}(D_s \to e\bar{\nu})}{\overline{\mathcal{B}}(D^- \to K^0 e\bar{\nu})}$	$1.41(7) \times 10^{-6}$	$< 9 \times 10^{-4}$	[56]
$r_{DK}^{(\mu)}$	$\frac{\mathcal{B}(D_s \to \mu\bar{\nu})}{\overline{\mathcal{B}}(D^- \to K^0 \mu\bar{\nu})}$	0.061(2)	0.063(2)	[56, 101]
$r_{BD}^{(\mu)}$	$\frac{\mathcal{B}(B_c^- \to \mu\bar{\nu})}{\overline{\mathcal{B}}(B^- \to D^0 \mu\bar{\nu})}$	$4.3(4) \times 10^{-3}$	–	
$r_{BD}^{(\tau)}$	$\frac{\mathcal{B}(B_c^- \to \tau\bar{\nu})}{\overline{\mathcal{B}}(B^- \to D^0 \tau\bar{\nu})}$	3.5(3)	–	

Table 3.5: *Experimental results for ratios of leptonic and semileptonic decays, and SM predictions obtained by using the hadronic inputs described in Sec. 3.2.3. Ratios with semileptonic $B \to \pi(K)$ decays are discussed in Sec. 3.2.3*

zero-recoil. In other words, most NP scenarios would not be able to explain this discrepancy since they would contribute equally to both decay modes. Note that these observables have recently been analyzed in a similar context in Refs. [114, 115].

$D \to Kl\nu$ and $|V_{cs}|$: For the $D \to K$ transition we find a reasonable agreement between theory and experiment. This conclusion is true for both LFU tests, as it can be seen in Table 3.4 and Table 3.5. The plot analogous to those discussed in the $D \to \pi$ case is shown in Fig. 3.6. We observe a good agreement between the SM predictions and the measured LFU ratios in most of the q^2-bins. [6]

$B \to D\ell\nu$ and LFU violation: Lastly, there are hints of LFU violation in the $b \to c\tau\bar{\nu}$ transition. These deviations appear not only in the ratio $R_{BD}^{(\tau/\mu)}$, that shows an $\approx 1.5\sigma$ excess with respect to the SM prediction (cf. Table 3.4) [119, 120], but also in the related decay modes, $B \to D^*\ell\bar{\nu}$ [119–122] and $B_c \to J/\psi\ell\bar{\nu}$ [16], which are $\approx 2.5\sigma$ and $\approx 2\sigma$ above the corresponding SM predictions respectively. This pattern of deviations has triggered an intense activity

[6] See Ref. [116] for a recent study of the related decay mode $D_s \to \phi\ell\bar{\nu}$ with lattice QCD form factors [64].

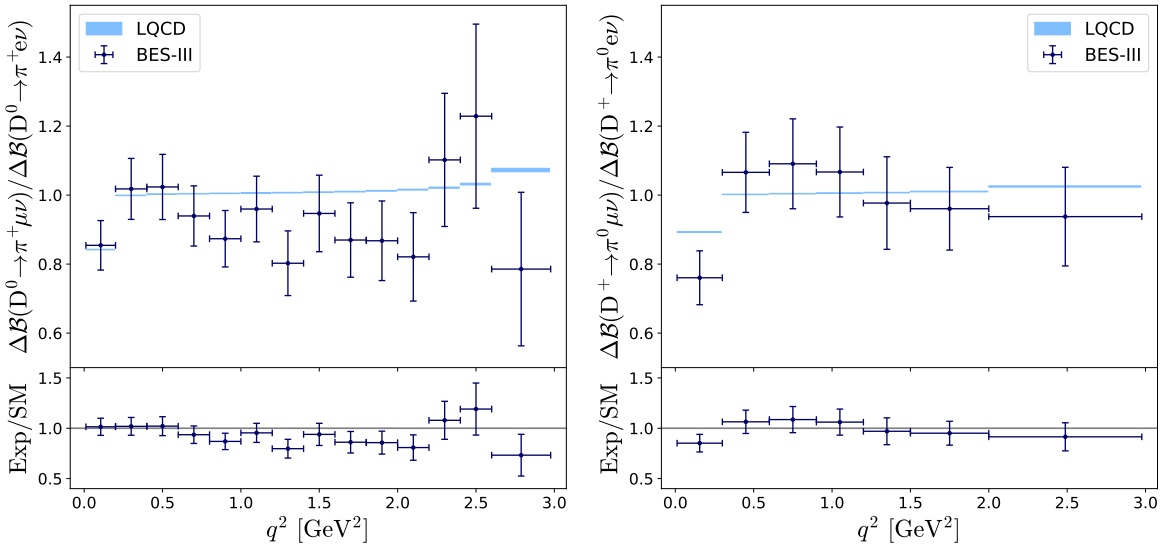

Figure 3.5: *Comparison between the μ/e LFU ratios measured experimentally in different q^2 bins for $D^0 \to \pi^+ l\nu$ [99, 112] (left panel) and $D^+ \to \pi^0 l\nu$ [98, 99] (right panel) with the SM predictions (shaded blue regions).*

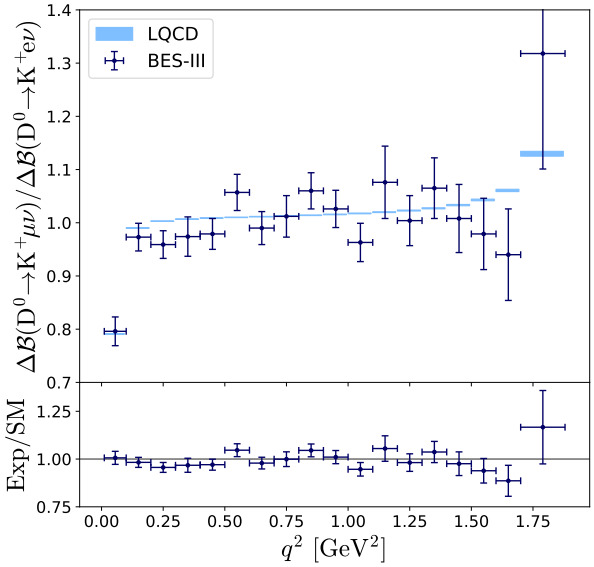

Figure 3.6: *Comparison between the μ/e LFU ratios measured experimentally in different q^2 bins for $D^0 \to K^+\ell\nu$ [112, 117] with the SM predictions (shaded blue regions). The isospin-related decay modes $D^+ \to K^0\ell\nu$ are not shown since the differential data for $D^+ \to K^0\mu\nu$ is not available [118].*

in the theory community which resulted in several viable scenarios beyond the SM capable of accommodating the so-called B-anomalies (see e.g. Ref. [28, 39] and references therein). The SM predictions for the $B \to D^*$ transition are currently made by relying on the differential distributions measured experimentally for $B \to D^*(\to D\pi)l\bar{\nu}$ decays (with $l = e, \mu$) [4], as well as the heavy-quark effective theory combined with the QCD sum rules to evaluate the non-perturbative coefficients entering the heavy quark expansion of the form factors, and in particular to evaluate the f_0 form factor [59]. Although the LQCD results at nonzero recoil are not yet available for this particular transition, there are ongoing lattice studies the results of

which will help clarify the situation, and hopefully in understanding the long-standing disagreement between the $|V_{cb}|$ values as inferred from the exclusive and inclusive semileptonic decays, respectively [123]. For the $B_c \to J/\psi$ transition, the relevant form factors at nonzero recoil have been recently computed by means of LQCD simulations in Ref. [65], which allows us to predict the corresponding LFU ratio $R^{(\tau/\mu)}_{B_c J/\psi}$, with $\mathcal{O}(1\%)$ precision [124], see also Ref. [125].

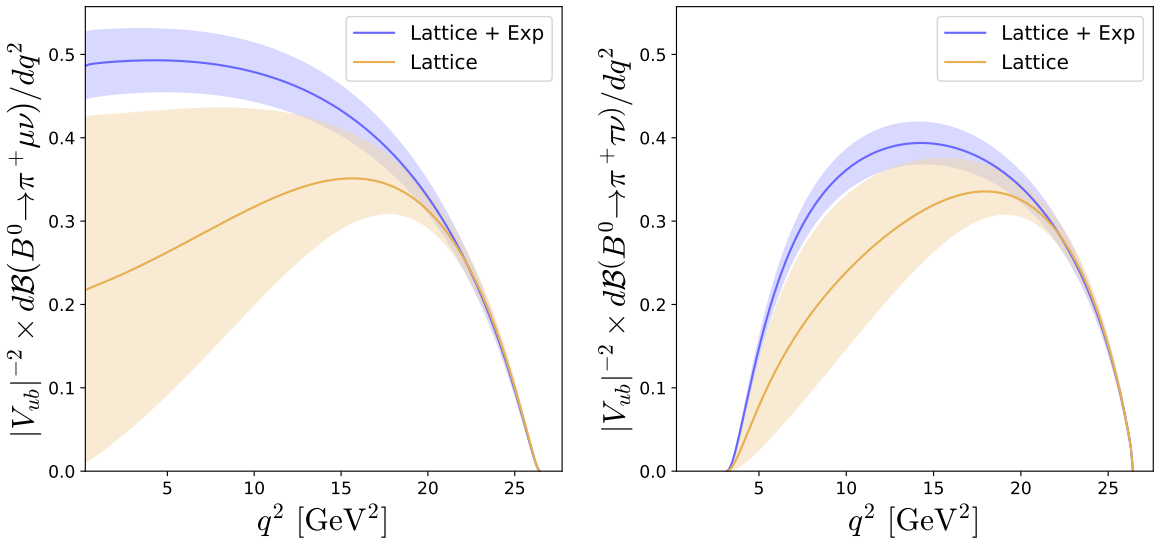

Figure 3.7: *Differential branching fraction for $B \to \pi\mu\bar{\nu}$ (left panel) and $B \to \pi\tau\bar{\nu}$ (right panel) by using only LQCD form factors (orange) [80, 81], and a combined fit to LQCD and experimental data (blue) [62]. The shaded regions correspond to the 1σ predictions.*

$B \to \pi\ell\nu$ with LQCD form factors

The $B \to \pi\ell\nu$ and $B_s \to K\ell\nu$ decays deserve a separate discussion due to the large theoretical uncertainties involved in their SM predictions. For these processes, the form factors obtained in LQCD simulations at large q^2's should be extrapolated to lower q^2's to cover the entire physical region. This extrapolation introduces an ambiguity related to various parameterizations one might use to describe the q^2 dependencies of the form factors. In principle, this issue could be avoided by combining the lattice data with experimental data which are more accurate for low q^2's, but that would be at odds with our goal to solely rely on LQCD to evaluate the hadronic matrix elements. Moreover, for our purpose it is important to avoid using the experimental data to constrain the form factors because such results could already be heavily affected by the NP contributions which we would like to isolate.

The ambiguity related to the form factor parameterization is noticeable for $B \to \pi\ell\nu$ decays. In Fig. 3.7 we compute the $B \to \pi\ell\nu$ differential decay rates by using two different theoretical inputs: (i) the scalar and vector form factors computed on the lattice at high-q^2 values and extrapolated to the rest of the physical region [80, 81]; and (ii) $f_0(q^2)$ and $f_+(q^2)$ obtained by a combined fit of LQCD data with the experimental measurements of $\mathrm{d}\mathcal{B}(B \to \pi l\nu)/\mathrm{d}q^2$ (with $l = e, \mu$), which are more accurate at low q^2-values [62]. Note, in particular, that the second approach allows us to extract $|V_{ub}| = 3.73(14) \times 10^{-3}$ [62], lower than the one extracted from the inclusive decays (see e.g. Ref. [123] for a recent review). Our predictions by using both sets of form factors are shown in Fig. 3.7. Both approaches lead to the same results in the large q^2-region where LQCD data dominate, but they diverge for small q^2 values, due to the

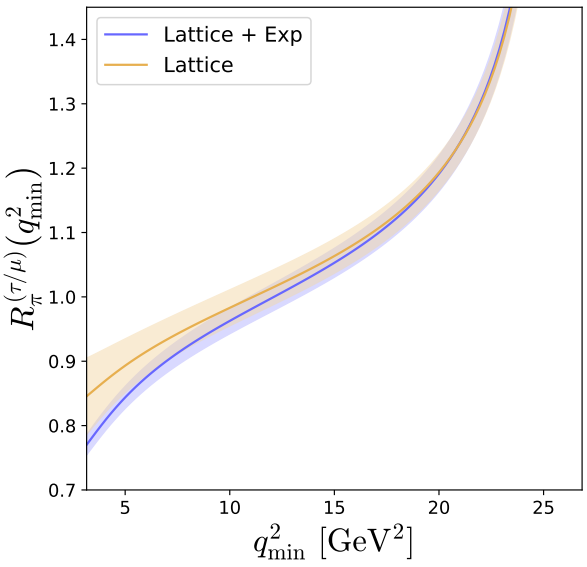

Figure 3.8: *The ratio $\mathcal{R}_{B\pi}^{(\tau/\mu)}(q^2_{\rm min})$, defined in Eq. (3.44), is plotted as a function of the mininum value of the dilepton mass, $q^2_{\rm min}$, which is taken to be the same in the numerator and denominator.*

model-dependent extrapolation of the LQCD form factors. The LFU ratios defined in Eq. (3.30) are then [7]

$$R_{B\pi}^{(\tau/\mu)}\Big|_{\rm LQCD} = 0.78(10)\,, \qquad R_{B\pi}^{(\tau/\mu)}\Big|_{\rm LQCD+exp} = 0.66(2)\,. \tag{3.43}$$

Therefore, it is still not possible to use only LQCD data and have a robust SM prediction for $R_{B\pi}^{(\tau/\mu)}$. To avoid the artifact of the form factor extrapolations, we propose to use, instead of Eq. (3.30), the following observable, [8]

$$\widehat{R}_{PP'}^{(\ell/\ell')}(q^2_{\rm min}) \equiv \frac{\displaystyle\int_{q^2_{\rm min}}^{(M-m)^2} \frac{{\rm d}\mathcal{B}}{{\rm d}q^2}(P\to P'\ell\bar{\nu})\,{\rm d}q^2}{\displaystyle\int_{q^2_{\rm min}}^{(M-m)^2} \frac{{\rm d}\mathcal{B}}{{\rm d}q^2}(P\to P'\ell'\bar{\nu})\,{\rm d}q^2}\,, \tag{3.44}$$

where $q^2_{\rm min} \geq m_\ell^2$ is to be chosen in such a way as to avoid the problematic low q^2-region. This observable is plotted in Fig. 3.8 as a function of $q^2_{\rm min}$, where we see that choosing $q^2_{\rm min} \gtrsim 10\ {\rm GeV}^2$ is already enough to obtain consistent results with both approaches. In order to be conservative, we take $q^2_{\rm min} = 16\ {\rm GeV}^2$, which also corresponds to one of the q^2-bins considered in the experimental measurement of $B\to\pi l\bar{\nu}$ (with $l = e,\mu$) at BaBar [126] and Belle [127]. Experimentally, choosing $q^2_{\rm min} = 16\ {\rm GeV}^2$ (resp. $10\ {\rm GeV}^2$) reduces the branching fraction of $B\to\pi\mu\nu$ to 36% (resp. 64%) of the its full value, while it only reduces the branching fraction of $B\to\pi\tau\nu$ to 51% (resp. 83%). For this choice of integration interval, we obtain the following SM predictions,

$$\widehat{R}_{B\pi}^{(\tau/\mu)}(16\ {\rm GeV}^2)\Big|_{\rm LQCD} = 1.08(3)\,, \qquad R_{B\pi}^{(\tau/\mu)}(16\ {\rm GeV}^2)\Big|_{\rm LQCD+exp} = 1.07(2)\,, \tag{3.45}$$

[7] Note that a similar problem is not present in the μ/e ratios, since the form factors cancel out to a large extent in these observables because $m_e \ll m_\mu \ll m_B$.

[8] A similar proposal has been recently made for the $P\to V\ell\bar{\nu}$ transitions in Ref. [125], where V denotes a vector meson. In this case, the uncertainties related to the pseudoscalar form factor can be substantially reduced by increasing the value of $q^2_{\rm min}$.

Observable	Our SM prediction	Exp. value	Ref.
$\widehat{R}^{(\mu/e)}_{B\pi}(16\ \mathrm{GeV}^2)$	1.0007(1)	–	
$\widehat{R}^{(\mu/e)}_{B_sK}(16\ \mathrm{GeV}^2)$	1.0009(1)	–	
$\widehat{R}^{(\tau/\mu)}_{B\pi}(16\ \mathrm{GeV}^2)$	1.08(3)	< 6.4	[126–128]
$\widehat{R}^{(\tau/\mu)}_{B_sK}(16\ \mathrm{GeV}^2)$	1.10(2)	–	
$\widehat{r}^{(\mu)}_{B\pi}(16\ \mathrm{GeV}^2)$	$2.4(2)\times10^{-2}$	$4(2)\times10^{-2}$	[56, 126, 127]
$\widehat{r}^{(\mu)}_{B_sK}(16\ \mathrm{GeV}^2)$	$1.7(1)\times10^{-2}$	–	
$\widehat{r}^{(\tau)}_{B\pi}(16\ \mathrm{GeV}^2)$	5.4(3)	> 0.44	[56, 128]
$\widehat{r}^{(\tau)}_{B_sK}(16\ \mathrm{GeV}^2)$	3.8(2)	–	

Table 3.6: *Experimental results and our SM predictions for the observables defined in Eq.* (3.44) *and* (3.46) *for* $q^2_{\rm min} = 16\ \mathrm{GeV}^2$.

which are in perfect agreement. By using the same approach, we define the ratio of semileptonic and leptonic decays as

$$\widehat{r}^{(\ell)}_{PP'}(q^2_{\rm min}) \equiv \frac{\mathcal{B}(P''\to\ell\nu)}{\displaystyle\int_{q^2_{\rm min}}^{(M-m)^2}\frac{\mathrm{d}\overline{\mathcal{B}}}{\mathrm{d}q^2}(P\to P'\ell\nu)\,\mathrm{d}q^2}\,, \tag{3.46}$$

where the denominator accounts for the isospin average from Eq. (3.32), and P'' is defined as in Eq. (3.31), i.e. $P'' = B^+$ for $B\to\pi\ell\bar\nu$ and $B_s\to K\ell\bar\nu$. Our predictions for these observables are collected in Table 3.6, along with the existing experimental results. Currently, there is only an experimental limit on the decay mode $\mathcal{B}(B\to\pi\tau\bar\nu) < 2.5\times10^{-4}$ [128], which is expected to be measured soon at Belle-II with a precision of $\mathcal{O}(20\ \%)$ [129]. For the reasons explained above it would be very useful to separate the low and high-q^2 regions. Note also that the ratio of the $B_s\to K$ and $B_s\to D_s$ form factors has been studied in LQCD in Ref. [130]. The first experimental determination of the ratio of branching fractions of these modes has been reported while this paper was in writing [131]. In that paper, the authors indeed make a distinction between the low and high q^2 regions, but with $q^2_{\rm min} = 7\,\mathrm{GeV}^2$ that is perhaps too low.

3.2.4 New Physics Phenomenology

In this section, we use the observables discussed in Sec. 3.2.3 to constrain the effective couplings defined in Eq. (2.1), which are then used to explore the new semileptonic observables proposed in Sec. 3.2.1. In our analysis, we will focus on the LFU ratios of type μ/e and τ/μ, and we will assume that NP couplings affect the decay to the heavier lepton in each ratio (i.e. μ's

for μ/e ratios and τ's for τ/μ). In other words, our analysis is based on the assumption,

$$|g_\alpha^{ij\,e}| \ll |g_\alpha^{ij\,\mu}| \ll |g_\alpha^{ij\,\tau}|\,, \qquad \forall\, i,j \tag{3.47}$$

which holds, for instance, in many NP scenarios aiming at explaining the hierarchy of fermion masses, cf. e.g. Ref. [132,133]. However, the theoretical inputs given in Sec. 3.2.3 are sufficient to recast our results to a more general NP scenario rather than the one defined in Eq. (3.47).

The experimental inputs used in our analysis are

i) The ratios of semileptonic decays $R_{PP'}^{(\ell/\ell')} = \mathcal{B}(P \to P'\ell\bar{\nu})/\mathcal{B}(P \to P'\ell'\bar{\nu})$, which are listed in Table 3.4 for the various transitions.

ii) The ratios of leptonic decays $R_K^{(e/\mu)} = \mathcal{B}(K \to e\bar{\nu})/\mathcal{B}(K \to \mu\bar{\nu})$ and $R_K^{(\tau/\mu)} = \mathcal{B}(\tau \to K\nu)/\mathcal{B}(K \to \mu\bar{\nu})$, which is given in Table 3.4.

iii) The ratios of leptonic and semileptonic decays $r_{PP'}^{(\ell/\ell')} \equiv \mathcal{B}(P \to \ell\bar{\nu})/\mathcal{B}(P \to P'\ell'\bar{\nu})$, are simply the products of $R_{PP'}^{(\ell/\ell')}$ and $r_{PP'}^{(\ell)}$ already presented in Tables 3.4 and 3.5, respectively.

Note that for most transitions we opt for using the ratio $r_{PP'}^{(\ell/\ell')}$, instead of the purely leptonic one, $R_P^{(\ell/\ell')} = \mathcal{B}(P \to \ell\bar{\nu})/\mathcal{B}(P \to \ell'\bar{\nu})$, since the decays $P \to \ell'\bar{\nu}$ (with $\ell' = e,\mu$) are very rare and still unobserved for many transitions. The only exception is the kaon sector, where $R_K^{(e/\mu)}$ and $R_K^{(\tau/\mu)}$ have been precisely measured [56], and in fact used in our analysis. In addition to the observables listed above, we also consider the ones corresponding to $B \to \pi\ell\bar{\nu}$, with the choice of the cut $q^2 \geq 16\ \text{GeV}^2$, as described in Sec. 3.2.3.

Simplified semileptonic expressions

Let us discuss the sensitivity of the different semileptonic observables defined in Sec. 3.2.1 to the NP couplings defined in Eq. (2.1). Starting from the integrated branching fraction, without loss of generality, we can write

$$\begin{aligned}\frac{\mathcal{B}_{\text{tot}}}{\mathcal{B}_{\text{tot}}^{\text{SM}}} &= |1+g_V|^2 + a_S^{\mathcal{B}}\,|g_S|^2 + a_T^{\mathcal{B}}\,|g_T|^2 \\ &\quad + a_{SV}^{\mathcal{B}}\text{Re}\big[(1+g_V)\,g_S^*\big] + a_T^{\mathcal{B}}\,\text{Re}\big[(1+g_V)\,g_T^*\big] + a_{ST}^{\mathcal{B}}\,\text{Re}\big[g_S\,g_T^*\big]\,,\end{aligned} \tag{3.48}$$

where $a_\alpha^{\mathcal{B}}$ are the numerically known coefficients obtained by integrating over the full range of q^2's. Note that the flavor indices in $g_\alpha \equiv g_\alpha^{ij\,\ell}$ are omitted. We evaluated all of $a_\alpha^{\mathcal{B}}$ and collected the results in Table 3.7 for each of the transitions considered in this section. These values can be combined with the SM predictions quoted in Table 3.4 to compute the LFU ratios defined in Eq. (3.30) for the most general NP scenario. For the $B \to \pi\ell\bar{\nu}$ transition, we list the coefficients $a_\alpha^{\mathcal{B}} \equiv a_\alpha^{\mathcal{B}}(q^2_{\text{min}})$ in Table 3.8, as obtained for different values of q^2_{min} and by using the LQCD form factors from Refs. [80, 81]. Notice that the coefficient $a_{ST}^{\mathcal{B}}$ vanishes identically. This particular combination of effective couplings $\propto g_S g_T^*$ can only be probed by using the full angular distribution, as we discuss in the following.

For the semileptonic observables $\mathcal{O} \in \{A_{\text{fb}},\ A_\lambda,\ A_{\pi/3}\}$ defined in Sec. 3.2.1, we can write in full generality,

$$\begin{aligned}\langle\mathcal{O}\rangle\,\frac{\mathcal{B}_{\text{tot}}}{\mathcal{B}_{\text{tot}}^{\text{SM}}} &= \langle\mathcal{O}^{\text{SM}}\rangle\,|1+g_V|^2 + b_S^{\mathcal{O}}\,|g_S|^2 + b_T^{\mathcal{O}}\,|g_T|^2 \\ &\quad + b_{SV}^{\mathcal{O}}\text{Re}\big[(1+g_V)\,g_S^*\big] + b_{TV}^{\mathcal{O}}\,\text{Re}\big[(1+g_V)\,g_T^*\big] + b_{ST}^{\mathcal{O}}\,\text{Re}\big[g_S\,g_T^*\big]\,,\end{aligned} \tag{3.49}$$

Decay	$\lvert V_{ij}\rvert^{-2}\,\overline{\mathcal{B}}(P\to P'\ell\bar\nu)$	$a_S^{\mathcal{B}}$	$a_T^{\mathcal{B}}$	$a_{SV}^{\mathcal{B}}$	$a_{TV}^{\mathcal{B}}$	$a_{ST}^{\mathcal{B}}$
$K^+\to\pi^0\mu\bar\nu$	0.669(6)	15.74(12)	0.152(11)	4.43(3)	0.46(2)	0
$D^+\to\pi^0\mu\bar\nu$	0.066(4)	2.39(12)	1.17(18)	0.435(15)	0.47(4)	0
$D^+\to\overline{K^0}\mu\bar\nu$	0.091(6)	1.69(5)	0.71(10)	0.465(10)	0.45(3)	0
$B^+\to D^0\mu\bar\nu$	14.8(8)	1.13(3)	0.68(6)	0.154(2)	0.188(9)	0
$B^+\to D^0\tau\bar\nu$	4.3(1)	1.076(9)	0.84(8)	1.533(9)	1.09(5)	0

Table 3.7: *Numerical coefficients entering Eq. (3.48) for the different semileptonic transitions. We also quote the values for the SM predictions $\mathcal{B}_{\rm tot}^{\rm SM}=\mathcal{B}(P\to P'\ell\bar\nu)$ after factoring out the CKM matrix elements $|V_{ij}|$. As mentioned in the text, the renormalization scale for all the coefficients is taken to be $\mu=2\,\text{GeV}$, except for the B-meson decays for which $\mu=m_b$.*

where $\mathcal{B}_{\rm tot}\equiv\mathcal{B}_{\rm tot}(g_V,g_S,g_T)$ is the total branching fraction, $b_\alpha^{\mathcal{O}}$ are the known numerical coefficients, and the brackets $\langle\dots\rangle$ denote the integration over the full q^2 range, [9]

$$\langle\mathcal{O}\rangle=\int_{m_\ell^2}^{(M-m)^2}\frac{\mathrm{d}\mathcal{O}}{\mathrm{d}q^2}\,\mathrm{d}q^2\,. \tag{3.50}$$

The values of all coefficients $b_\alpha^{\mathcal{O}}$ are collected in Table 3.9. By comparing Table 3.7 and 3.9, it is evident that $A_{\rm fb}$, A_λ and $A_{\pi/3}$ are complementary to the branching fractions. In particular, $A_{\rm fb}$ is the only observable that depends on $\mathrm{Re}(g_S\,g_T^*)$, with an enhanced sensitivity due to a large numerical coefficients $b_{ST}^{A_{\rm fb}}$, cf. Table 3.9. To assess the potential of these new observables to reveal the presence of NP, we first need to determine the allowed ranges of the effective NP couplings entering Eq. (3.49).

Decay	$q^2_{\rm min}$	$\lvert V_{ub}\rvert^{-2}\,B_{\rm tot}(q^2\geq q^2_{\rm min})$	$a_S^{\mathcal{B}}$	$a_T^{\mathcal{B}}$	$a_{SV}^{\mathcal{B}}$	$a_{TV}^{\mathcal{B}}$	$a_{ST}^{\mathcal{B}}$
$B^+\to\pi^0\mu\bar\nu$	12 GeV^2	2.1(2)	2.8(3)	5(1)	0.13(1)	0.23(3)	0
	16 GeV^2	1.4(1)	3.6(3)	5.2(6)	0.15(1)	0.23(1)	0
	20 GeV^2	0.66(3)	5.2(4)	5.8(5)	0.20(1)	0.23(1)	0
$B^+\to\pi^0\tau\bar\nu$	12 GeV^2	2.2(2)	2.0(1)	4.3(9)	1.5(1)	2.6(3)	0
	16 GeV^2	1.5(1)	2.4(1)	4.5(5)	1.7(1)	2.5(1)	0
	20 GeV^2	0.78(3)	3.3(1)	4.6(4)	2.1(1)	2.4(1)	0

Table 3.8: *Numerical coefficients $a_\alpha^{\mathcal{B}}\equiv a_\alpha^{\mathcal{B}}(q^2_{\rm min})$ appearing in Eq. (3.48) for the decays $B\to\pi\ell\bar\nu$ in the interval $q^2\in(q^2_{\rm min},(m_B-m_\pi)^2)$ with $q^2_{\rm min}$ fixed.*

[9] In this notation the total branching fraction can be written as $B_{\rm tot}=\langle\mathcal{B}(P\to P'\ell\bar\nu)\rangle$.

Decay mode	$\mathcal{O}$	$\langle \mathcal{O}^{\rm SM} \rangle$	$b_S^{\mathcal{O}}$	$b_T^{\mathcal{O}}$	$b_{SV}^{\mathcal{O}}$	$b_{TV}^{\mathcal{O}}$	$b_{ST}^{\mathcal{O}}$
$K^- \to \pi^0 \mu \bar{\nu}$	$A_{\rm fb}$	0.2726(3)	0	0	1.379(2)	0.343(13)	2.15(8)
	$A_{\pi/3}$	−0.1537(6)	0	0.066(5)	0	0	0
	A_λ	−0.091(4)	15.79(11)	0.065(4)	4.43(3)	−0.154(6)	0
$D^- \to \pi^0 \mu \bar{\nu}$	$A_{\rm fb}$	0.0386(11)	0	0	0.160(2)	0.29(3)	2.7(2)
	$A_{\pi/3}$	−0.3455(8)	0	0.84(13)	0	0	0
	A_λ	−0.890(3)	2.40(12)	1.1(2)	0.435(14)	−0.156(14)	0
$D^- \to K^0 \mu \bar{\nu}$	$A_{\rm fb}$	0.0580(8)	0	0	0.1714(15)	0.29(2)	1.78(12)
	$A_{\pi/3}$	−0.3307(7)	0	0.51(7)	0	0	0
	A_λ	−0.833(3)	1.69(5)	0.66(9)	0.465(10)	−0.150(10)	0
$B^- \to D^0 \mu \bar{\nu}$	$A_{\rm fb}$	0.0141(3)	0	0	0.0590(4)	0.116(5)	1.45(7)
	$A_{\pi/3}$	−0.3643(2)	0	0.50(5)	0	0	0
	A_λ	−0.9605(8)	1.13(3)	0.67(6)	0.154(2)	−0.062(3)	0
$B^- \to D^0 \tau \bar{\nu}$	$A_{\rm fb}$	0.3602(8)	0	0	0.4430(8)	0.87(4)	1.14(5)
	$A_{\pi/3}$	−0.0671(3)	0	0.18(2)	0	0	0
	A_λ	0.324(3)	1.076(10)	0.052(5)	1.534(10)	−0.36(2)	0

Table 3.9: *Numerical coefficients for the coefficients $b_i^{\mathcal{O}}$ defined in Eq. (3.49) for the integrated observables $\mathcal{O} \in \{A_{\rm fb}, A_{\pi/3}, A_\lambda\}$ defined in Sec. 3.2.1. Notice that the "magic numbers" are given for the decays of charged mesons, but that they are practically if one considers decays of neutral mesons for the quantities as defined in Eq. (3.49).*

Constraints and predictions

To determine the allowed ranges of the NP effective couplings we consider the observables described above, with the experimental results and SM predictions given in Tables 3.4, 3.5 and 3.6. In addition to these observables, we also require that $\mathcal{B}(B_c \to \ell\bar{\nu}) \lesssim 30\ \%$ in order to avoid the saturation of the B_c-meson lifetime, the value of which is known experimentally [57].These quantities are used in Table 3.10 to constrain the couplings $g_A^{ij\,\ell}$ and $g_P^{ij\,\ell}$ from the leptonic decays, and $g_V^{ij\,\ell}$, $g_S^{ij\,\ell}$ and $g_T^{ij\,\ell}$ from the semileptonic ones. The renormalization scale μ is taken to be $\mu = 2\ \mathrm{GeV}$ for the decays of K and D-mesons, and $\mu = m_b$ for b-decays. [10] Several comments regarding the results are in order:

- First, we note that there are two distinct real solutions for each NP coupling due to the quadratic dependence of the branching fraction on $g_\alpha^{ij\,\ell}$, as it can be seen in Eqs. (3.48). In Table 3.10, we choose the solution closer to the SM, since the other one would correspond to a NP scenario with large NP couplings which is most likely in tension with the direct searches at LHC.

- Our analysis was based on the assumption that the NP couplings to leptons are hierarchical, see Eq. (3.47). The CKM matrix element is eliminated in the ratios of leptonic or semileptonic decays differing in the flavor of the lepton in the final state.

- For the semileptonic decays based on the transitions $s \to u\tau\nu$, $c \to d\tau\nu$ and $c \to s\tau\nu$, there is no available phase space which is why the corresponding $g_V^{ij\,\tau}$, $g_S^{ij\,\tau}$ and $g_T^{ij\,\tau}$ effective couplings are not constrained by the low-energy data.

- The decays $B \to \pi\ell\bar{\nu}$ with $\ell = e, \mu$ are systematically combined in the experimental analyses performed at the B-factories [126, 127]. While this is the best approach to extracting the $|V_{ub}|$ value, it is not straightforward to use these results in order to constrain the NP scenarios in which the LFU is broken, as we assume. For this reason, we prefer not to quote any constraint for this particular transition. We suggest to the future experimental analyses to also quote the value of $R_{B\pi}^{(\mu/e)} = \mathcal{B}(B \to \pi\mu\bar{\nu})/\mathcal{B}(B \to \pi e\bar{\nu})$, as done for instance in certain studies of $B \to D\ell\bar{\nu}$ decays [103].

- The only significant discrepancy between theory and experiment in Table 3.10 is the well-known B-physics LFU deviation in the $B \to D\ell\bar{\nu}$ transition [119, 120]. For this particular transition, the allowed range for the effective couplings would become more constrained if results concerning the $B \to D^*\tau\nu$ transition were also considered, see e.g. Ref. [63]. Note also that the small deviations observed in $D^0 \to \pi^+\mu\bar{\nu}$ decays become less significant when the isospin average is considered, as discussed in Sec. 3.2.3.

We are now in a position to use the constraints obtained in Table 3.10 and predict the value of new observables A_{fb}, A_λ and $A_{\pi/3}$, defined in Sec. 3.2.1, as a function of the allowed ranges for the NP couplings. We first discuss their integrated values, see Eq. (3.50). These quantities are plotted in Fig. 3.9 as functions of the real and imaginary parts of $g_S^{ij\,\alpha}$ and $g_T^{ij\,\alpha}$, for each quark-level transition. The light-colored regions show the dependence of the physical observables on the effective NP couplings, whereas the values allowed by the constraints given in Table 3.10 are highlighted by darker colors. In that plot, we see that the sizeable deviations

[10] For reference, we use the following quark mass values: $m_s^{\overline{\mathrm{MS}}}(2\ \mathrm{GeV}) = 99.6(4.3)\ \mathrm{MeV}$, $m_c^{\overline{\mathrm{MS}}}(2\ \mathrm{GeV}) = 1.176(39)\ \mathrm{GeV}$ [134], and $m_b^{\overline{\mathrm{MS}}}(m_b) = 4.18(4)\ \mathrm{GeV}$ [56].

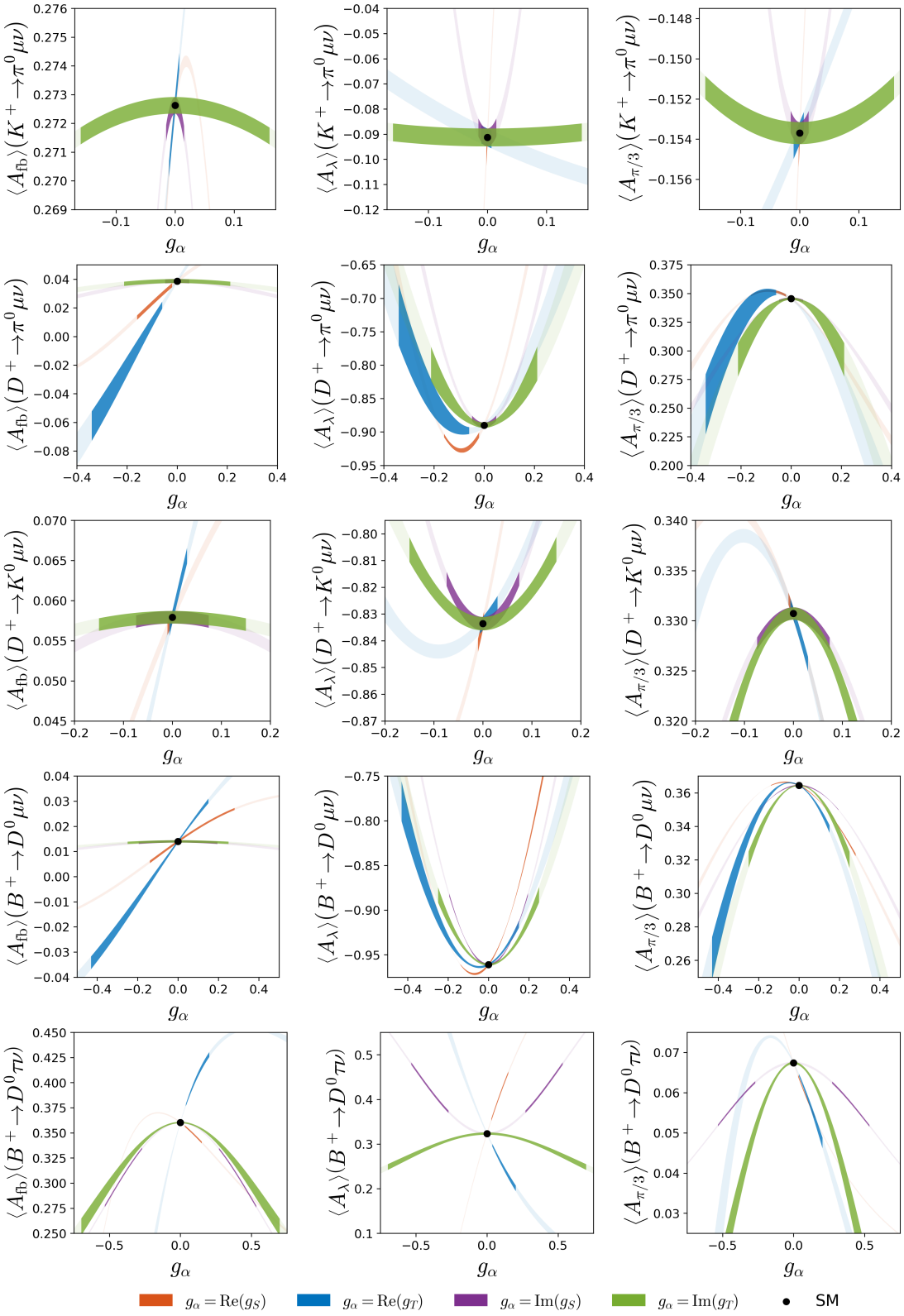

Figure 3.9: *Predictions for the integrated observables $\langle A_{\rm fb}\rangle$, $\langle A_\lambda\rangle$ and $\langle A_{\pi/3}\rangle$, defined in Eq. (3.50), as a function of the Wilson coefficients $g_i \in \{\mathrm{Re}(g_S), \mathrm{Re}(g_T), \mathrm{Im}(g_S), \mathrm{Im}(g_T)\}$. The darker regions are allowed by existing experimental constraints collected in Table 3.4.*

$u_i\, d_j\, \ell$	$\mathrm{Re}(g_V^{ij\,\ell})$	$\mathrm{Re}(g_A^{ij\,\ell})$	$\mathrm{Re}(g_S^{ij\,\ell})$	$\mathrm{Re}(g_P^{ij\,\ell})$	$\mathrm{Re}(g_T^{ij\,\ell})$
$u\,s\,\mu$	$(0 \pm 2) \times 10^{-3}$	$(2.2 \pm 1.8) \times 10^{-3}$	$(-2 \pm 9) \times 10^{-4}$	$(-9 \pm 8) \times 10^{-5}$	$(-2 \pm 9) \times 10^{-3}$
$u\,s\,\tau$	–	$(2.2 \pm 1.7) \times 10^{-2}$	–	$(1.6 \pm 1.1) \times 10^{-2}$	–
$c\,d\,\mu$	$(-3.0 \pm 1.6) \times 10^{-2}$	$(7 \pm 4) \times 10^{-2}$	$(-9 \pm 7) \times 10^{-2}$	$(-2.6 \pm 1.3) \times 10^{-3}$	$(-2.0 \pm 1.4) \times 10^{-1}$
$c\,d\,\tau$	–	$(-0.1 \pm 1.1) \times 10^{-1}$	–	$(1 \pm 7) \times 10^{-2}$	–
$c\,s\,\mu$	$(3 \pm 6) \times 10^{-3}$	$(-2 \pm 4) \times 10^{-2}$	$(-1 \pm 2) \times 10^{-2}$	$(0.7 \pm 1.4) \times 10^{-3}$	$(1.2 \pm 1.8) \times 10^{-2}$
$c\,s\,\tau$	–	$(-3 \pm 4) \times 10^{-2}$	–	$(2 \pm 2) \times 10^{-2}$	–
$u\,b\,\mu$	–	–	–	–	–
$u\,b\,\tau$	-1 ± 2	$(-1 \pm 2) \times 10^{-1}$	-0.3 ± 1.5	$(3 \pm 7) \times 10^{-2}$	-0.3 ± 1.1
$c\,b\,\mu$	$(0 \pm 2) \times 10^{-2}$	–	$(1 \pm 2) \times 10^{-1}$	$(0 \pm 8) \times 10^{-1}$	$(-1 \pm 3) \times 10^{-1}$
$c\,b\,\tau$	$(7 \pm 5) \times 10^{-2}$	1 ± 4	$(9 \pm 6) \times 10^{-2}$	$(-2 \pm 8) \times 10^{-1}$	$(1.2 \pm 0.8) \times 10^{-1}$

Table 3.10: *1σ constraints on the real part of the coefficients $g_\alpha^{ij\,\ell} = g_\alpha^{ij\,\ell}(\mu)$, with $\alpha \in \{V, A, S, P, T\}$), derived from the observables collected in Table 3.4. The scale μ is taken to be $\mu = 2$ GeV for K and D-meson observables, and $\mu = m_b$ for B-meson decays.*

from the SM are indeed possible. For instance, $\langle A_{\rm fb}\rangle(D \to \pi\mu\bar{\nu})$ can be modified by varying the NP coupling g_T in the interval allowed by the data. Its value could not only change the sign but its absolute value could be $\approx 2\times$ larger than its SM value. Significant deviations for $A_{\rm fb}$ and $A_{\pi/3}$, are also possible in $D \to K\mu\bar{\nu}$, $B \to D\mu\bar{\nu}$ and $B \to D\tau\bar{\nu}$. It is therefore clear that studying the angular distribution of these decays experimentally could offer a fertile ground for searching the NP effects.

For decays to τ-leptons, such as $B_{(s)} \to D_{(s)}\tau\bar{\nu}$, $B_s \to K\tau\bar{\nu}$ and $B \to \pi\tau\bar{\nu}$, the τ-polarization is also experimentally accessible, since it can be reconstructed from the kinematics of its decay products [135, 136]. From Fig. 3.9 we see that the lepton-polarization asymmetry $\langle A_\lambda\rangle(B \to D\tau\bar{\nu})$ is very sensitive to the NP couplings, which can be increased (decreased) by a pronounced NP coupling to the scalar (tensor) operator. For the processes involving muons, it is not clear how the lepton polarization can be determined since muons are stable for the length scales probed in most particle colliders. For these decays, the only observables that can be reconstructed with known techniques are $A_{\rm fb}$ and $A_{\pi/3}$, and the predictions for A_λ are less relevant, being given in Fig. 3.9 only for the sake of completeness.

Finally, we also explore the impact of NP effects on the differential distributions of the quantities (observables) discussed above. We focus on $B \to D\tau\bar{\nu}$, as motivated by the discrepancies observed in B-meson decays [119–122]. For simplicity, we consider the scenarios in which the SM is extended by a $\mathcal{O}(1\,\mathrm{TeV})$ leptoquark boson $S_1 = (\bar{\mathbf{3}}, \mathbf{1}, 1/3)$ or $R_2 = (\mathbf{3}, \mathbf{2}, 7/6)$, where in the parentheses are the SM quantum numbers. These scenarios can accommodate the observed LFU discrepancies and remain consistent with numerous low and high-energy constraints [28]. [11] Moreover, in these models the NP couplings satisfy $g_{S_L}(\Lambda) = -4\, g_T(\Lambda)$ and

[11] Another viable solution to the problem of B-anomalies is given by the vector LQ $U_1 = (\bar{3}, 1, 2/3)$, see e.g. Ref. [28] and references therein. Even though this scenario can also allow for a nonzero $g_{S_R}^{cb\,\tau}$, the dominant coupling to explain the anomalies is $g_{V_L}^{cb\,\tau}$ which does not affect the asymmetries considered

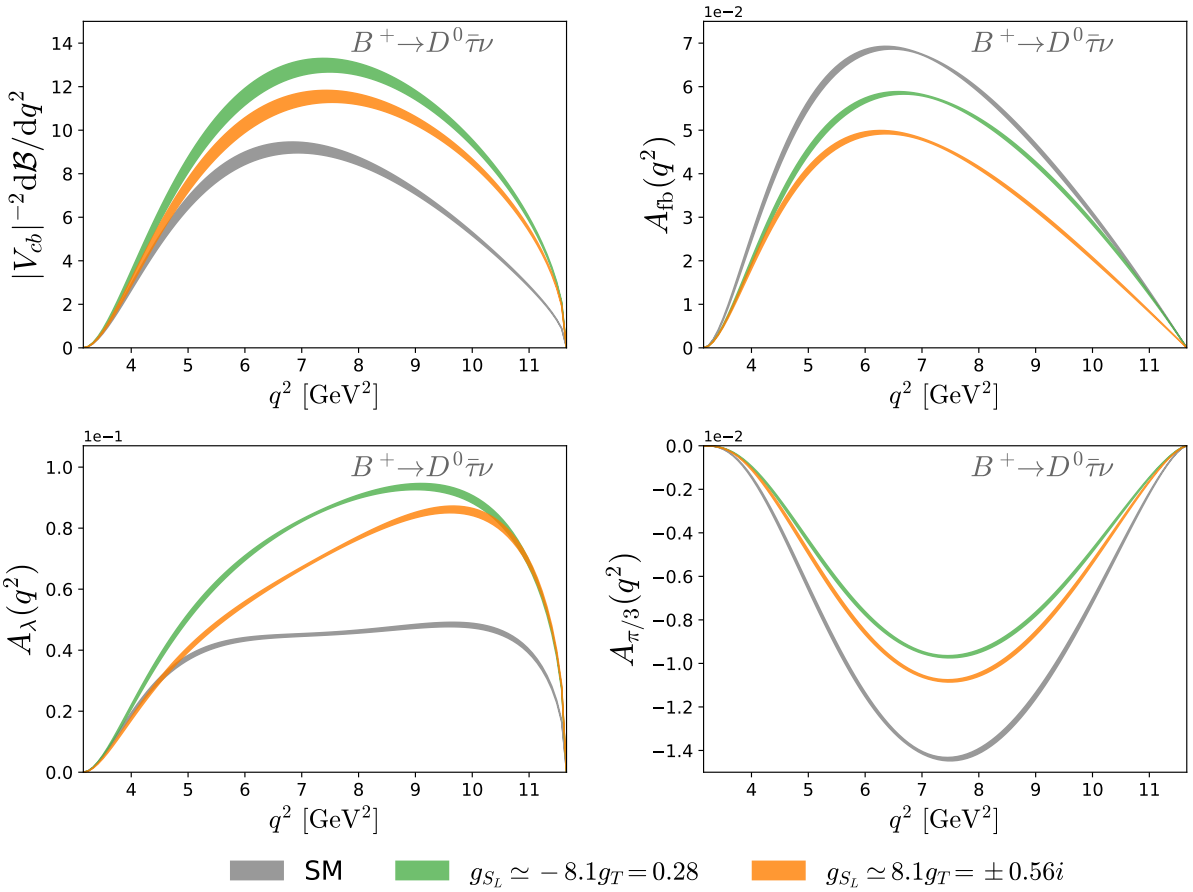

Figure 3.10: *Predictions for the differential distributions of $A_{\mathrm{fb}}(q^2)$, $A_\lambda(q^2)$ and $A_{\pi/3}(q^2)$ for the $B \to D\tau\bar{\nu}$ transition. The benchmark values for the NP scenarios are motivated by the LQ scenarios that can accommodate the discrepancies observed in $B \to D^{(*)} l\bar{\nu}$ [28]. See text for details.*

$g_{S_L}(\Lambda) = +4\, g_T(\Lambda)$, respectively, at the matching scale Λ. After accounting for the running effects from $\Lambda \approx 1$ TeV down to $\mu_b = m_b$, these relations become $g_{S_L}(\mu_b) \approx -8.5\, g_T(\mu_b)$ and $g_{S_L}(\mu_b) \approx 8.14\, g_T(\mu_b)$, respectively. We use the best-fit values for the NP couplings obtained in Ref. [28] for these two leptoquark scenarios and plot the differential q^2-distributions of different observables. The results are shown in Fig. 3.10. We find that the overall normalization of A_{fb} and A_λ, as well as the branching fraction, can change by about 20% (S_1) and by about 50 % (R_2), which are possibly large enough to be testable at the LHCb and Belle-II. Even more significant are the predictions for $A_{\pi/3}$, which can be strongly modified by the plausible values of the NP couplings, especially in the region of intermediate q^2's.

Therefore, measuring the observables discussed in this section and their q^2 shapes can indeed be revelatory of the non-zero value of one of the NP couplings.

3.2.5 Conclusion

In this section, we made a comprehensive phenomenological analysis of the leptonic and semileptonic decays of pseudoscalar mesons in the framework of a general low-energy ef-

above [28].

fective theory which includes all possible interactions BSM, except for possible contributions arising from the right-handed neutrinos.

One of our main goals was to derive the constraints on the NP couplings by relying only on the decay modes for which the non-perturbative QCD uncertainties are fully under control, i.e. which are handled through extensive numerical simulations of QCD on the lattice. In this regard, the decay of pseudoscalar mesons offers the most precise predictions. By switching on the NP couplings, one at a time, we were able to derive constraints by comparing the accurate theoretical determination with the experimentally available results for the (partial) branching fractions. To eliminate the dependence on the CKM matrix elements we combined similar decay channels in suitable ratios.

The obtained constraints on the NP couplings are then used to predict the possible departure of the angular observables with respect to their SM values. To that effect, we showed that one can construct at most four independent observables from the detailed study of the angular distribution of the semileptonic pseudoscalar-to-pseudoscalar meson decays. Our results show that these observables can indeed reveal the presence of physics BSM both through their values integrated over the available phase space or through modification of their q^2-dependence compared to the SM. Clearly more experimental work in this direction is very much needed.

Besides turning one NP coupling at a time, we also discussed the possibility of simultaneously including two non-zero couplings. Such a situation is realized in the scenarios in which the SM is extended by a low-energy scalar leptoquark, such as R_2 or S_1, for which the scalar and tensor couplings are both nonzero but the ratio of the two is fixed.

The future analyses along the one presented in this section should be updated and extended to include the decays to vector mesons in the final state, as long as the vector meson is sufficiently narrow, as well as the semi-leptonic decay of baryons, which we will discuss is Sect. 3.3. For that to be done one also needs reliable LQCD results for the form factors, obtained by more than one LQCD collaboration. If these results were available, we would end up with far more restrictive constraints on the New Physics couplings and many more observables to predict. With the further improvement in the accuracy of the experimental results and the hadronic matrix elements, one also has to start accounting for the electromagnetic corrections. Such a situation is already present in the case of the kaon leptonic and semileptonic decays for which we included electromagnetic corrections as estimated by means of chiral perturbation theory with the low energy constants fixed from phenomenology. The strategies to control the electromagnetic corrections through LQCD studies exist and the first results for the leptonic decays of kaon appeared very recently in Ref. [137] and the result is compatible with what we used in this paper.

3.2.6 Appendix

Angular conventions

Kinematics Our conventions for the decay $P(p) \to P'(k)\ell(k_1)\bar{\nu}(k_2)$ are summarized in Fig. 3.3. In the P rest-frame, the leptonic and hadronic four-vectors $q = p - k$ and k are given by

$$q^\mu = (q_0, 0, 0, q_z)\,, \qquad\qquad k^\mu = (q_0, 0, 0, -q_z)\,, \tag{3.51}$$

where

$$q_0 = \frac{M^2 + q^2 - m^2}{2M}\,, \qquad k_0 = \frac{M^2 - q^2 + m^2}{2M}\,, \quad \text{and} \quad q_z = \frac{\lambda^{1/2}(M^2, q^2, m^2)}{2M}\,. \tag{3.52}$$

In the dilepton rest-frame, the leptonic four-vectors read

$$k_1^\mu = (E_\ell, |p_\ell| \sin\theta_\ell, 0, |p_\ell| \cos\theta)\,, \qquad k_2^\mu = (E_\nu, -|p_\ell| \sin\theta_\ell, 0, -|p_\ell| \cos\theta)\,, \tag{3.53}$$

where

$$E_\ell = \frac{q^2 + m_\ell^2}{2\sqrt{q^2}}\,, \tag{3.54}$$

and $E_\nu = |p_\ell| = \sqrt{q^2} - E_\ell$.

Polarization vectors In the P-meson rest-frame, we choose the polarization vectors of the virtual boson V to be

$$\varepsilon^\mu(\pm) = \frac{1}{\sqrt{2}}(0, \pm 1, i, 0)\,, \tag{3.55}$$

$$\varepsilon^\mu(0) = \frac{1}{\sqrt{q^2}}(q_z, 0, 0, q_0)\,, \tag{3.56}$$

$$\varepsilon^\mu(t) = \frac{1}{\sqrt{q^2}}(q_0, 0, 0, q_z)\,, \tag{3.57}$$

where q_0 and q_z are given in Eq. (3.52). These four-vectors are orthonormal and satisfy the completeness relation (3.7).

3.3 Usefulness of baryons: The case of $\Lambda_b \to \Lambda_c \ell\bar{\nu}$

Ever since the first indication of the lepton flavor universality violation (LFUV), reported by BaBar in Refs. [119, 138], we witnessed a growing interest in the high energy physics community with a goal to clarify the situation and assess whether or not the LFUV is a real effect in the decay modes based on $b \to c\ell\bar{\nu}_\ell$ decays, mediated by the charged currents that occur at tree level in the Standard Model (SM). The BaBar collaboration was the first to measure

$$R_{D^{(*)}} = \left.\frac{\mathcal{B}(B \to D^{(*)}\tau\bar{\nu})}{\mathcal{B}(B \to D^{(*)}l\bar{\nu})}\right|_{l\in\{e,\mu\}}\,, \tag{3.58}$$

and they found that both R_D and R_{D^*} are larger than predicted in the SM. Since $\mathcal{B}(B \to D^{(*)}l\bar{\nu})$ are known to be rather consistent with expectations, it has been inferred that $\mathcal{B}(B \to D^{(*)}\tau\bar{\nu})^{\rm exp}$ is larger than its SM prediction. To make that assessment clearer the lattice QCD community has been working on computing the relevant form factors so that the hadronic uncertainties could be minimized. While this has been achieved in the case of $B \to D\ell\bar{\nu}$ decays [62, 77, 139], the first results regarding the $B \to D^*\ell\bar{\nu}_\ell$ decay need more clarification [58, 140, 141]. On the experimental side, after combining significant contributions from various experiments [121, 122, 142–144], the HFLAV collaboration reported the following average values [145]:

$$R_D = 0.340(30)\,, \qquad R_{D^*} = 0.295(14)\,, \tag{3.59}$$

which, together, are more than 3σ larger than evaluated in the SM. Another exclusive $b \to c\ell\bar{\nu}_\ell$ channel, in which a similar test of LFUV could be made, has been experimentally studied by the LHCb collaboration in Ref. [16], and the result

$$R_{J/\psi} = \frac{\mathcal{B}(B_c \to J/\psi\tau\bar{\nu})}{\mathcal{B}(B \to J/\psi\mu\bar{\nu})} = 0.71 \pm 0.25\,, \tag{3.60}$$

again appears to be a little less than 2σ larger than its SM value [124].

The above observations have motivated many physicists to build scenarios that go beyond the SM (BSM) in order to accommodat the effects of LFUV while keeping a large plethora of other processes compatible both with the SM and with experiment. Clearly, while the LFUV ratios $R_{D^{(*)}}$ and $R_{J/\psi}$ provide us with valuable information, they alone are insufficient to select among various possible BSM contributions to $b \to c\tau\bar{\nu}$. Indeed, much more information about the effects of physics BSM can be extracted from the angular distributions of the above-mentioned decay modes [146–151], some of which will be possible to study in the years to come, at the Belle II and the LHC experiments.

Another exclusive channel, which is yet to be experimentally explored in the case of heavy lepton in the final state, is $\Lambda_b \to \Lambda_c \ell\bar{\nu}$. So far the LHCb collaboration presented the results concerning the q^2-shape of the differential decay rate, $d\Gamma(\Lambda_b \to \Lambda_c \mu\bar{\nu})/dq^2$ [152], without a normalization factor. This year, LHCb reported the first measurement of R_{Λ_c} and found [153]

$$R_{\Lambda_c} = \frac{\mathcal{B}(\Lambda_b \to \Lambda_c \tau\bar{\nu})}{\mathcal{B}(\Lambda_b \to \Lambda_c \mu\bar{\nu})} = 0.242 \pm 0.076\,, \tag{3.61}$$

which is consistent with the SM prediction [154]. That measurement can be improved in multiple ways. In this Chapter we will provide the expressions for the full angular distribution of this decay, including the subsequent decay $\Lambda_c \to \Lambda\pi$. We will then combine various coefficients to construct the observables which could provide us with valuable information concerning the BSM physics. While deriving the relevant expressions we separately show the results for spin up and spin $down$ of the outgoing lepton and/or baryon. In such a way we could propose new quantities, including the well known lepton polarization asymmetry. To illustrate the power of measuring angular observables relevant to $\Lambda_b \to \Lambda_c \tau\bar{\nu}$, we monitor their integrated characteristics in several scenarios in which the BSM couplings are required to be consistent with $R^{\rm exp}_{D^{(*)}}$. Since the uncertainty of $R^{\rm exp}_{J/\psi}$ is large the BSM couplings selected from compatibility with $R^{\rm exp}_{D^{(*)}}$ are automatically consistent with $R^{\rm exp}_{J/\psi}$ as well. We should also mention the constraints on the effective NP couplings arising from the studies of the high-p_T tails of the differential cross section of $pp \to \ell\nu$ at LHC. Such constraints in this case are not yet competitive with those obtained from the low-energy observables, but in the future they might play an ever more important role, cf. Refs. [155–160].

3.3.1 Effective Theory, Matrix Elements, Decay Amplitude

To account for both the SM and the effects of physics BSM, we describe the $b \to c\ell\bar{\nu}$ process by the following low-energy effective field theory:

$$\begin{aligned}
\mathcal{L}_{\rm eff} =& -2\sqrt{2}G_F V_{cb}\Big[(1+g_{V_L})\,(\bar{c}_L\gamma_\mu b_L)(\bar{\ell}_L\gamma^\mu\nu_L) + g_{V_R}\,(\bar{c}_R\gamma_\mu b_R)(\bar{\ell}_L\gamma^\mu\nu_L)\\
&+ g_{S_L}(\mu)\,(\bar{c}_R b_L)(\bar{\ell}_R\nu_L) + g_{S_R}(\mu)\,(\bar{c}_L b_R)(\bar{\ell}_R\nu_L) + g_T(\mu)\,(\bar{c}_R\sigma_{\mu\nu}b_L)(\bar{\ell}_R\sigma^{\mu\nu}\nu_L)\Big] + \text{h.c.}\,,\\
=& -\frac{G_F}{\sqrt{2}}V_{cb}\Big[(1+g_V)\,(\bar{c}\gamma_\mu b)\big(\bar{\ell}\gamma^\mu(1-\gamma_5)\nu\big) - (1-g_A)\,(\bar{c}\gamma_\mu\gamma_5 b)\big(\bar{\ell}\gamma^\mu(1-\gamma_5)\nu\big)\\
&+ g_S(\mu)\,(\bar{c}b)\big(\bar{\ell}(1-\gamma_5)\nu\big) + g_P(\mu)\,(\bar{c}\gamma_5 b)\big(\bar{\ell}(1-\gamma_5)\nu\big)\\
&+ g_T(\mu)\,\big(\bar{c}\sigma_{\mu\nu}(1-\gamma_5)b\big)\big(\bar{\ell}\sigma^{\mu\nu}(1-\gamma_5)\nu\big)\Big] + \text{h.c.}\,,
\end{aligned} \tag{3.62}$$

written in both commonly used bases of operators. The two sets of the New Physics (NP) couplings are related via, $g_{V,A} = g_{V_R} \pm g_{V_L}$, $g_{S,P} = g_{S_R} \pm g_{S_L}$. After setting all of the NP couplings to zero one obviously retrieves the SM Fermi theory.

The main stumbling point in the discussion of the weak interaction processes of hadrons is the theoretical treatment of hadronic uncertainties. For the $\Lambda_b \to \Lambda_c \ell \bar{\nu}$ decay, however, all of the relevant form factors have already been computed on the lattice [154, 161]. In this Chapter we will use the same decomposition of the hadronic matrix elements as in the papers in which the form factors have been computed, namely:

$$\langle \Lambda_c | \bar{c} \gamma^\mu b | \Lambda_b \rangle = \overline{u}_{\Lambda_c} \Bigg[F_0(q^2)(M_{\Lambda_b} - M_{\Lambda_c}) \frac{q^\mu}{q^2} + F_\perp(q^2) \left(\gamma^\mu - \frac{2M_{\Lambda_c}}{Q_+} p^\mu - \frac{2M_{\Lambda_b}}{Q_+} k^\mu \right) + F_+(q^2) \frac{M_{\Lambda_b} + M_{\Lambda_c}}{Q_+} \left(p^\mu + k^\mu - (M^2_{\Lambda_b} - M^2_{\Lambda_c}) \frac{q^\mu}{q^2} \right) \Bigg] u_{\Lambda_b}, \tag{3.63}$$

$$\langle \Lambda_c | \bar{c} \gamma^\mu \gamma_5 b | \Lambda_b \rangle = -\overline{u}_{\Lambda_c} \Bigg[G_0(q^2)(M_{\Lambda_b} + M_{\Lambda_c}) \frac{q^\mu}{q^2} + G_\perp(q^2) \left(\gamma^\mu - \frac{2M_{\Lambda_c}}{Q_-} p^\mu - \frac{2M_{\Lambda_b}}{Q_-} k^\mu \right) + G_+(q^2) \frac{M_{\Lambda_b} - M_{\Lambda_c}}{Q_-} \left(p^\mu + k^\mu - (M^2_{\Lambda_b} - M^2_{\Lambda_c}) \frac{q^\mu}{q^2} \right) \Bigg] u_{\Lambda_b}, \tag{3.64}$$

which, by virtue of the vector and axial Ward identities, imply:

$$\langle \Lambda_c | \bar{c} b | \Lambda_b \rangle = F_0(q^2) \frac{M_{\Lambda_b} - M_{\Lambda_c}}{m_b - m_c} \overline{u}_{\Lambda_c} u_{\Lambda_b}, \tag{3.65}$$

$$\langle \Lambda_c | \bar{c} \gamma_5 b | \Lambda_b \rangle = G_0(q^2) \frac{M_{\Lambda_b} + M_{\Lambda_c}}{m_b + m_c} \overline{u}_{\Lambda_c} \gamma_5 u_{\Lambda_b}. \tag{3.66}$$

Regarding the matrix element of the tensor density,

$$\begin{aligned} \langle \Lambda_c | \bar{c} i\sigma^{\mu\nu} b | \Lambda_b \rangle = -\overline{u}_{\Lambda_c} \Bigg[& 2h_+(q^2) \frac{p^\mu k^\nu - p^\nu k^\mu}{Q_+} \\ & + h_\perp(q^2) \left(\frac{M_{\Lambda_b} + M_{\Lambda_c}}{q^2} (q^\mu \gamma^\nu - q^\nu \gamma^\mu) - 2 \left(\frac{1}{q^2} + \frac{1}{Q_+} \right) (p^\mu k^\nu - p^\nu k^\mu) \right) \\ & + \widetilde{h}_+(q^2) \left(i\sigma^{\mu\nu} - \frac{2}{Q_-} \left(M_{\Lambda_b} (k^\mu \gamma^\nu - k^\nu \gamma^\mu) - M_{\Lambda_c} (p^\mu \gamma^\nu - p^\nu \gamma^\mu) + p^\mu k^\nu - p^\nu k^\mu \right) \right) \\ & + \widetilde{h}_\perp(q^2) \frac{M_{\Lambda_b} - M_{\Lambda_c}}{q^2 Q_-} \Big(\left(M^2_{\Lambda_b} - M^2_{\Lambda_c} - q^2 \right) (\gamma^\mu p^\nu - \gamma^\nu p^\mu) \\ & - \left(M^2_{\Lambda_b} - M^2_{\Lambda_c} + q^2 \right) (\gamma^\mu k^\nu - \gamma^\nu k^\mu) + 2(M_{\Lambda_b} - M_{\Lambda_c})(p^\mu k^\nu - p^\nu k^\mu) \Big) \Bigg] u_{\Lambda_b}, \end{aligned} \tag{3.67}$$

from which one can also obtain $\langle \Lambda_c | \bar{c} i\sigma^{\mu\nu} \gamma_5 b | \Lambda_b \rangle$ by simply using the relation

$$\sigma^{\mu\nu} \gamma_5 = -\frac{i}{2} \epsilon^{\mu\nu\alpha\beta} \sigma_{\alpha\beta}, \tag{3.68}$$

with the convention $\epsilon_{0123} = +1$. In the above decomposition matrix elements, p and k are the four-momenta of Λ_b and Λ_c, respectively, while $q^2 = (p-k)^2$, and $Q_\pm = (M_{\Lambda_b} \pm M_{\Lambda_c})^2 - q^2$. Kinematics and the explicit forms of spinors in the convenient reference frames are specified in Appendix. The polarization of the virtual vector boson, $\eta^\mu(\lambda)$ satisfies the completeness relation:

$$\sum_{\lambda \in \{\pm, 0, t\}} \eta^{*\mu}(\lambda) \eta^\nu(\lambda) \delta_\lambda = g^{\mu\nu}, \qquad \delta_0 = -\delta_{\pm,t} = 1\,. \tag{3.69}$$

With all of the above ingredients in hand we can write the $\Lambda_b \to \Lambda_c \ell \bar{\nu}$ amplitude as:

$$\frac{\mathcal{M}^{\lambda_b}_{\lambda_c \lambda_\ell}}{G_F V_{cb}/\sqrt{2}} = H^{\mathrm{S-P},\lambda_b}_{\lambda_c} L^{\mathrm{S-P}}_{\lambda_\ell} + \sum_{\lambda} \delta_\lambda H^{\mathrm{V-A},\lambda_b}_{\lambda_c \lambda} L^{\mathrm{V-A}}_{\lambda_\ell \lambda} + \sum_{\lambda,\lambda'} \delta_\lambda \delta_{\lambda'} H^{\mathrm{T-T5},\lambda_b}_{\lambda_c \lambda \lambda'} L^{\mathrm{T-T5}}_{\lambda_\ell \lambda \lambda'}, \tag{3.70}$$

where λ_b, λ_c, λ_ℓ and $\lambda^{(\prime)}$ are the polarization states of Λ_b, Λ_c, the outgoing lepton and the virtual vector boson, respectively. The hadronic parts in the above decomposition are evaluated by using the explicit expressions for spinors, cf. Appendix. We get:

$$\begin{aligned}
H^{\mathrm{S-P},\lambda_b}_{\lambda_c} &= g_S(\mu)\, \langle \Lambda_c | \bar{c} b | \Lambda_b \rangle + g_P(\mu)\, \langle \Lambda_c | \bar{c} \gamma_5 b | \Lambda_b \rangle, \\
H^{\mathrm{V-A},\lambda_b}_{\lambda_c \lambda} &= (1+g_V)\, \eta^*_\mu(\lambda)\, \langle \Lambda_c | \bar{c} \gamma^\mu b | \Lambda_b \rangle - (1-g_A)\, \eta^*_\mu(\lambda)\, \langle \Lambda_c | \bar{c} \gamma^\mu \gamma_5 b | \Lambda_b \rangle, \\
H^{\mathrm{T-T5},\lambda_b}_{\lambda_c \lambda \lambda'} &= g_T(\mu)\, \eta^*_\mu(\lambda) \eta^*_\mu(\lambda')\, \langle \Lambda_c | \bar{c} \sigma^{\mu\nu} b | \Lambda_b \rangle - g_T(\mu)\, \eta^*_\mu(\lambda) \eta^*_\mu(\lambda')\, \langle \Lambda_c | \bar{c} \sigma^{\mu\nu} \gamma_5 b | \Lambda_b \rangle.
\end{aligned} \tag{3.71}$$

In a more explicit form, after using the hadronic matrix elements listed in Eq. (3.63–3.67), the above expressions read:

$$\begin{aligned}
H^{\mathrm{S-P},\pm}_{\pm} &= g_S \sqrt{Q_+} \frac{M_{\Lambda_b} - M_{\Lambda_c}}{m_b - m_c} F_0(q^2) \mp g_P \sqrt{Q_-} \frac{M_{\Lambda_b} + M_{\Lambda_c}}{m_b + m_c} G_0(q^2), \\
H^{\mathrm{V-A},\pm}_{\pm 0} &= (1+g_V)\, (M_{\Lambda_b} + M_{\Lambda_c}) \frac{\sqrt{Q_-}}{\sqrt{q^2}} F_+(q^2) \mp (1-g_A)\, (M_{\Lambda_b} - M_{\Lambda_c}) \frac{\sqrt{Q_+}}{\sqrt{q^2}} G_+(q^2), \\
H^{\mathrm{V-A},\pm}_{\pm t} &= (1+g_V)\, (M_{\Lambda_b} - M_{\Lambda_c}) \frac{\sqrt{Q_+}}{\sqrt{q^2}} F_0(q^2) \mp (1-g_A)\, (M_{\Lambda_b} + M_{\Lambda_c}) \frac{\sqrt{Q_-}}{\sqrt{q^2}} G_0(q^2), \\
H^{\mathrm{V-A},\mp}_{\pm \pm} &= -(1+g_V) \sqrt{2Q_-}\, F_\perp(q^2) \pm (1-g_A) \sqrt{2Q_+}\, G_\perp(q^2), \\
H^{\mathrm{T-T5},\pm}_{\pm +-} &= -g_T \left[\sqrt{Q_-}\, h_+(q^2) \mp \sqrt{Q_+}\, \widetilde{h}_+(q^2) \right], \\
H^{\mathrm{T-T5},\pm}_{\pm t 0} &= g_T \left[\sqrt{Q_-}\, h_+(q^2) \pm \sqrt{Q_+}\, \widetilde{h}_+(q^2) \right], \\
H^{\mathrm{T-T5},\mp}_{\pm t \pm} &= -g_T \left[(M_{\Lambda_b} + M_{\Lambda_c}) \frac{\sqrt{2Q_-}}{\sqrt{q^2}} h_\perp(q^2) \mp (M_{\Lambda_b} - M_{\Lambda_c}) \frac{\sqrt{2Q_+}}{\sqrt{q^2}} \widetilde{h}_\perp(q^2) \right], \\
H^{\mathrm{T-T5},\mp}_{\pm \pm 0} &= g_T \left[\pm (M_{\Lambda_b} + M_{\Lambda_c}) \frac{\sqrt{2Q_-}}{\sqrt{q^2}} h_\perp(q^2) + (M_{\Lambda_b} - M_{\Lambda_c}) \frac{\sqrt{2Q_+}}{\sqrt{q^2}} \widetilde{h}_\perp(q^2) \right],
\end{aligned} \tag{3.72}$$

where, for notational simplicity, we omit the renormalization scale dependence of the BSM couplings $g_{S,P,T}$. In what follows we assume that scale to be $\mu = m_b$. Note also that $H^{\mathrm{T-T5},\lambda_b}_{\lambda_c \lambda \lambda'} = -H^{\mathrm{T-T5},\lambda_b}_{\lambda_c \lambda' \lambda}$. As for the leptonic parts,

$$\begin{aligned}
L^{\mathrm{S-P}}_{\lambda_\ell} &= \langle\, \ell \overline{\nu}\, | \overline{u}(\lambda_\ell) v(\lambda_\nu) | 0 \rangle, \\
L^{\mathrm{V-A}}_{\lambda_\ell, \lambda} &= \eta^\mu(\lambda)\, \langle\, \ell \overline{\nu}\, | \overline{u}(\lambda_\ell) \gamma_\mu v(\lambda_\nu) | 0 \rangle, \\
L^{\mathrm{T-T5}}_{\lambda_\ell, \lambda \lambda'} &= i \eta^\mu(\lambda) \eta^\nu(\lambda') \langle\, \ell \overline{\nu}\, | \overline{u}(\lambda_\ell) \sigma_{\mu\nu} v(\lambda_\nu) | 0 \rangle.
\end{aligned} \tag{3.73}$$

The non-zero contributions read:

$$
\begin{aligned}
L_{+}^{\mathrm{S-P}} &= 2\sqrt{q^2}\beta, & L_{+,t}^{\mathrm{V-A}} &= 2\beta m_\ell, \\
L_{+,0}^{\mathrm{V-A}} &= -2\beta m_\ell \cos\theta, & L_{+,\pm}^{\mathrm{V-A}} &= \pm\sqrt{2}\beta m_\ell \sin\theta, \\
L_{-,0}^{\mathrm{V-A}} &= 2\sqrt{q^2}\beta \sin\theta, & L_{-,\pm}^{\mathrm{V-A}} &= \sqrt{2q^2}\beta(\pm\cos\theta + 1), \\
L_{+,0\pm}^{\mathrm{T-T5}} &= -\sqrt{2q^2}\beta \sin\theta, & L_{+,0t}^{\mathrm{T-T5}} &= 2\sqrt{q^2}\beta\cos\theta, \\
L_{+,-+}^{\mathrm{T-T5}} &= 2\sqrt{q^2}\beta\cos\theta, & L_{+,\pm t}^{\mathrm{T-T5}} &= \mp\sqrt{2q^2}\beta\sin\theta, \\
L_{-,0\pm}^{\mathrm{T-T5}} &= -\sqrt{2}\beta m_\ell(\cos\theta \pm 1), & L_{-,0t}^{\mathrm{T-T5}} &= -2\beta m_\ell \sin\theta, \\
L_{-,-+}^{\mathrm{T-T5}} &= -2\beta m_\ell \sin\theta, & L_{-,\pm t}^{\mathrm{T-T5}} &= \sqrt{2}\beta m_\ell(\mp\cos\theta - 1),
\end{aligned}
\tag{3.74}
$$

where $\beta = \sqrt{1 - m_\ell^2/q^2}$. Similarly to the hadronic parts, also here $L^{\mathrm{T-T5}}_{\lambda_\ell,\lambda\lambda'} = -L^{\mathrm{T-T5}}_{\lambda_\ell,\lambda'\lambda}$. Moreover, we find that the leptonic amplitudes satisfy the following relations:

$$
L^{\lambda_\ell}_{\mathrm{S-P}} = \frac{\sqrt{q^2}}{m_\ell} L^{\lambda_\ell}_{\mathrm{V-A,t}}, \qquad L^{+1/2,0t}_{\mathrm{T-T5}} = -\frac{\sqrt{q^2}}{m_\ell} L^{+1/2,0}_{\mathrm{V-A}}, \qquad L^{-1/2,0t}_{\mathrm{T-T5}} = -\frac{m_\ell}{\sqrt{q^2}} L^{-1/2,0}_{\mathrm{V-A}}. \tag{3.75}
$$

In other words, all of the leptonic amplitudes are proportional to $L^{\mathrm{V-A}}_{\lambda_\ell,\lambda}$, and we can therefore redefine the hadronic contributions to

$$
\begin{aligned}
\widetilde{H}^{\lambda_b +}_{\lambda_c \pm} &= -H^{\mathrm{V-A},\lambda_b}_{\lambda_c \pm} + \frac{2\sqrt{q^2}}{m_l}\left(\pm H^{\mathrm{T-T5},\lambda_b}_{\lambda_c \pm 0} + H^{\mathrm{T-T5},\lambda_b}_{\lambda_c \pm t}\right), \\
\widetilde{H}^{\lambda_b +}_{\lambda_c 0} &= -H^{\mathrm{V-A},\lambda_b}_{\lambda_c 0} + \frac{2\sqrt{q^2}}{m_l}\left(H^{\mathrm{T-T5},\lambda_b}_{\lambda_c +-} + H^{\mathrm{T-T5},\lambda_b}_{\lambda_c 0t}\right), \\
\widetilde{H}^{\lambda_b +}_{\lambda_c t} &= H^{\mathrm{V-A},\lambda_b}_{\lambda_c t} + \frac{\sqrt{q^2}}{m_l} H^{\mathrm{S-P},\lambda_b}_{\lambda_c}, \\
\widetilde{H}^{\lambda_b -}_{\lambda_c \pm} &= -H^{\mathrm{V-A},\lambda_b}_{\lambda_c \pm} + \frac{2m_l}{\sqrt{q^2}}\left(\pm H^{\mathrm{T-T5},\lambda_b}_{\lambda_c \pm 0} + H^{\mathrm{T-T5},\lambda_b}_{\lambda_c \pm t}\right), \\
\widetilde{H}^{\lambda_b -}_{\lambda_c 0} &= -H^{\mathrm{V-A},\lambda_b}_{\lambda_c 0} + \frac{2m_l}{\sqrt{q^2}}\left(H^{\mathrm{T-T5},\lambda_b}_{\lambda_c +-} + H^{\mathrm{T-T5},\lambda_b}_{\lambda_c 0t}\right), \\
\widetilde{H}^{\lambda_b -}_{\lambda_c t} &= H^{\mathrm{V-A},\lambda_b}_{\lambda_c t} + \frac{m_l}{\sqrt{q^2}} H^{\mathrm{S-P},\lambda_b}_{\lambda_c}.
\end{aligned}
\tag{3.76}
$$

The relations (3.75), therefore, help simplifying drastically the expression for the full decay amplitude (3.70), which now becomes

$$
\mathcal{M}^{\lambda_b\lambda_\ell}_{\lambda_c} = \frac{G_F V_{cb}}{\sqrt{2}} \sum_{\lambda\in\{\pm,0,t\}} \widetilde{H}^{\lambda_b\lambda_\ell}_{\lambda_c\lambda} L^{\mathrm{V-A}}_{\lambda_\ell\lambda}, \tag{3.77}
$$

just like in the SM, except that the whole set of NP contribution is now collected in $\widetilde{H}^{\lambda_b\lambda_\ell}_{\lambda_c\lambda}$. Of all of the 32 terms, only the following 12 are nonzero:

$$
\mathcal{M}^{++}_{+} = \frac{G_F V_{cb}}{\sqrt{2}}\, 2\beta m_\ell \left(\widetilde{H}^{++}_{+t} - \cos\theta\, \widetilde{H}^{++}_{+0}\right), \qquad \mathcal{M}^{++}_{-} = -\frac{G_F V_{cb}}{\sqrt{2}}\, \sqrt{2}\beta m_\ell \sin\theta\, \widetilde{H}^{++}_{--},
$$

$$\mathcal{M}_+^{-+} = \frac{G_F V_{cb}}{\sqrt{2}}\,\sqrt{2}\beta m_\ell \sin\theta\;\widetilde{H}_{++}^{-+}, \qquad \mathcal{M}_-^{-+} = \frac{G_F V_{cb}}{\sqrt{2}}\,2\beta m_\ell \left(\widetilde{H}_{-t}^{-+} - \cos\theta\;\widetilde{H}_{-0}^{-+}\right),$$
$$\mathcal{M}_+^{+-} = \frac{G_F V_{cb}}{\sqrt{2}}\,2\sqrt{q^2}\beta \sin\theta\;\widetilde{H}_{+0}^{+-}, \qquad \mathcal{M}_-^{+-} = -\frac{G_F V_{cb}}{\sqrt{2}}\,\sqrt{2q^2}\beta(1-\cos\theta)\;\widetilde{H}_{--}^{+-},$$
$$\mathcal{M}_+^{--} = \frac{G_F V_{cb}}{\sqrt{2}}\,\sqrt{2q^2}\beta(1+\cos\theta)\;\widetilde{H}_{++}^{--}, \qquad \mathcal{M}_-^{--} = -\frac{G_F V_{cb}}{\sqrt{2}}\,2\sqrt{q^2}\beta \sin\theta\;\widetilde{H}_{-0}^{--}. \tag{3.78}$$

This, to our knowledge, is a new result and represents the most compact way to express the full $\Lambda_b \to \Lambda_c \ell\nu$ decay amplitude in a generic BSM scenario.

3.3.2 $\Lambda_b \longrightarrow \Lambda_c(\to \Lambda\pi)\ell\nu$

Using the above expressions, we can now write the angular distribution of the $\Lambda_b \longrightarrow \Lambda_c\ell\nu$ decay, $\ell \in \{e, \mu, \tau\}$. In this Section we discuss such a distribution for various polarization states of the outgoing Λ_c and ℓ. That will allow us to introduce the polarization asymmetries. We will then consider the subsequent decay of $\Lambda_c \to \Lambda\pi$ and give the expression for the full angular distribution of $\Lambda_b \longrightarrow \Lambda_c(\to \Lambda\pi)\ell\nu$, again separating the rates according to the polarization states of the outgoing ℓ and Λ.

Detailed $\Lambda_b \to \Lambda_c\ell\nu$ Decay Rate

We average over the polarizations of the initial state (Λ_b) and write the decay rate for each combination of λ_c and λ_ℓ. After inspection, we see that each such a differential decay rate can be written as

$$\frac{d^2\Gamma_{\lambda_c}^{\lambda_\ell}}{dq^2 d\cos\theta} = a_{\lambda_c}^{\lambda_\ell}(q^2) + b_{\lambda_c}^{\lambda_\ell}(q^2)\cos\theta + c_{\lambda_c}^{\lambda_\ell}(q^2)\cos^2\theta. \tag{3.79}$$

The full decay rate is then obviously obtained by summing over λ_c and λ_ℓ. The explicit expressions for the coefficients $a_{\lambda_c}^{\lambda_\ell}$, $b_{\lambda_c}^{\lambda_\ell}$ and $c_{\lambda_c}^{\lambda_\ell}$ are:

$$a_+^+(q^2) = \mathcal{N} m_\ell^2 \left(2\left|\widetilde{H}_{+t}^{++}\right|^2 + \left|\widetilde{H}_{++}^{-+}\right|^2\right), \qquad a_-^+(q^2) = \mathcal{N} m_\ell^2 \left(2\left|\widetilde{H}_{-t}^{-+}\right|^2 + \left|\widetilde{H}_{--}^{++}\right|^2\right),$$
$$a_+^-(q^2) = \mathcal{N} q^2 \left(2\left|\widetilde{H}_{+0}^{+-}\right|^2 + \left|\widetilde{H}_{++}^{--}\right|^2\right), \qquad a_-^-(q^2) = \mathcal{N} q^2 \left(2\left|\widetilde{H}_{-0}^{--}\right|^2 + \left|\widetilde{H}_{--}^{+-}\right|^2\right),$$
$$b_+^+(q^2) = -4\mathcal{N} m_\ell^2 \,\mathrm{Re}\left(\overline{\widetilde{H}_{+0}^{++}}\widetilde{H}_{+t}^{++}\right), \qquad b_-^+(q^2) = -4\mathcal{N} m_\ell^2 \,\mathrm{Re}\left(\overline{\widetilde{H}_{-0}^{-+}}\widetilde{H}_{-t}^{-+}\right),$$
$$b_+^-(q^2) = 2\mathcal{N} q^2 \left|\widetilde{H}_{++}^{--}\right|^2, \qquad b_-^-(q^2) = -2\mathcal{N} q^2 \left|\widetilde{H}_{--}^{+-}\right|^2,$$
$$c_+^+(q^2) = \mathcal{N} m_\ell^2 \left(2\left|\widetilde{H}_{+0}^{++}\right|^2 - \left|\widetilde{H}_{++}^{-+}\right|^2\right), \qquad c_-^+(q^2) = \mathcal{N} m_\ell^2 \left(2\left|\widetilde{H}_{-0}^{-+}\right|^2 - \left|\widetilde{H}_{--}^{++}\right|^2\right),$$
$$c_+^-(q^2) = \mathcal{N} q^2 \left(-2\left|\widetilde{H}_{+0}^{+-}\right|^2 + \left|\widetilde{H}_{++}^{--}\right|^2\right), \qquad c_-^-(q^2) = \mathcal{N} q^2 \left(-2\left|\widetilde{H}_{-0}^{--}\right|^2 + \left|\widetilde{H}_{--}^{+-}\right|^2\right), \tag{3.80}$$

where

$$\mathcal{N} \equiv \mathcal{N}(q^2) = \frac{G_F^2 |V_{cb}|^2 \sqrt{\lambda_{\Lambda_b\Lambda_c}(q^2)}}{1024\pi^3 M_{\Lambda_b}^3}\left(1 - \frac{m_\ell^2}{q^2}\right)^2, \tag{3.81}$$

and $\lambda_{\Lambda_b\Lambda_c}(q^2) = (q^2 - M_{\Lambda_b}^2)(q^2 - M_{\Lambda_c}^2)$. Using the above expressions we are now able to write the polarization asymmetry with respect to the outgoing lepton ℓ and with respect to Λ_c, the observables which we will come back to in the next Section.

Before continuing, it is interesting to note that, based on the above formulas, we have:

$$b_+^-(q^2) = a_+^-(q^2) + c_+^-(q^2), \qquad b_-^-(q^2) = -a_-^-(q^2) - c_-^-(q^2). \tag{3.82}$$

Since there are 4 angular distributions of the differential rate (3.79), each with 3 coefficients, it means that one could construct at most 12 observables. That number reduces to 10, thanks to the identities in Eq. (3.82). Notice also that the form (3.79) is similar to what one gets for the semileptonic decays of the pseudoscalar mesons, such as $B \to D\ell\nu$. It can be shown that Eq. (3.82) also holds true for $B \to D\ell\nu$, with an extra condition that $b^-(q^2) = 0$, which comes from the fact that $L_{-t}^{V-A} = 0$. [12]

Inclusion of $\Lambda_c \to \Lambda\pi$

In experiments, one reconstructs Λ_c from its decay products. This may give us access to new observables. Here we focus on $\Lambda_c \to \Lambda\pi$ with a charged pion in the final state, and work in the narrow width approximation in which we can use the Breit-Wigner distribution:

$$BW(k^2) = \frac{1}{k^2 - M_{\Lambda_c}^2 + iM_{\Lambda_c}\Gamma_{\Lambda_c}} \quad \Longrightarrow \quad |BW(k^2)|^2 \simeq \frac{\pi}{M_{\Lambda_c}\Gamma_{\Lambda_c}}\delta\left(k^2 - M_{\Lambda_c}^2\right). \tag{3.83}$$

In that way we can decompose the 4-body amplitude in terms of the 3-body ones as

$$\mathcal{M}_{\lambda_\Lambda}^{(4)\lambda_b\lambda_\ell} = \sum_{\lambda_c=\pm} \langle \Lambda^{\lambda_\Lambda}\pi|\Lambda_c^{\lambda_c}\rangle\, \mathcal{M}_{\lambda_c}^{\lambda_b\lambda_\ell}\, BW(k^2). \tag{3.84}$$

A convenient parametrization of the matrix element $\langle \Lambda^{\lambda_\Lambda}\pi|\Lambda_c^{\lambda_c}\rangle$ is,

$$\begin{aligned}
\langle \Lambda^+\pi|\Lambda_c^+\rangle &= h_+ \cos\left(\frac{\theta_\Lambda}{2}\right), & \langle \Lambda^+\pi|\Lambda_c^-\rangle &= h_- e^{i\phi} \sin\left(\frac{\theta_\Lambda}{2}\right), \\
\langle \Lambda^-\pi|\Lambda_c^+\rangle &= -h_+ e^{-i\phi} \sin\left(\frac{\theta_\Lambda}{2}\right), & \langle \Lambda^-\pi|\Lambda_c^-\rangle &= h_- \cos\left(\frac{\theta_\Lambda}{2}\right).
\end{aligned} \tag{3.85}$$

where θ_Λ is the angle between the z-axis and the direction of flight of Λ in the Λ_c rest frame, while the parameters h_+ and h_- can be extracted from the total decay rate $\Gamma_{\Lambda_c\to\Lambda\pi}$ and the Λ_c-polarization asymmetry α, viz.

$$\begin{aligned}
\Gamma_{\Lambda_c\to\Lambda\pi} &= \Gamma^+_{\Lambda_c\to\Lambda\pi} + \Gamma^-_{\Lambda_c\to\Lambda\pi} = \frac{\sqrt{\lambda_{\Lambda_c\Lambda\pi}}}{32\pi M_{\Lambda_c}^3}\Big(|h_+|^2 + |h_-|^2\Big), \\
\alpha &= \frac{\Gamma^+_{\Lambda_c\to\Lambda\pi} - \Gamma^-_{\Lambda_c\to\Lambda\pi}}{\Gamma^+_{\Lambda_c\to\Lambda\pi} + \Gamma^-_{\Lambda_c\to\Lambda\pi}} = \frac{|h_+|^2 - |h_-|^2}{|h_+|^2 + |h_-|^2},
\end{aligned} \tag{3.86}$$

where $\lambda_{\Lambda_c\Lambda\pi} = \lambda_{\Lambda\pi}(M_{\Lambda_c}^2)$. The measurement of α has been recently improved at BES III [162], and now its world average is $\alpha = -0.84(9)$ [56]. The sum $|h_+|^2 + |h_-|^2$, is traded for a parameter κ,

$$\kappa = |h_+|^2 + |h_-|^2 = \frac{32\pi M_{\Lambda_c}^3}{\sqrt{\lambda_{\Lambda_c\Lambda\pi}}}\Gamma_{\Lambda_c\to\Lambda\pi}, \tag{3.87}$$

[12] Note that in the case of $B \to D\ell\nu$ there is only one index, referring to the polarization state of the outgoing lepton.

so that

$$|h_+|^2\cos^2\left(\frac{\theta_\Lambda}{2}\right)+|h_-|^2\sin^2\left(\frac{\theta_\Lambda}{2}\right)=(1+\alpha\cos\theta_\Lambda)\frac{\kappa}{2},$$

$$|h_+|^2\cos^2\left(\frac{\theta_\Lambda}{2}\right)-|h_-|^2\sin^2\left(\frac{\theta_\Lambda}{2}\right)=(\alpha+\cos\theta_\Lambda)\frac{\kappa}{2}.$$

Using κ and α, we can describe $\Lambda_c\to\Lambda\pi$ and write the full angular distribution for the decay $\Lambda_b\to\Lambda_c(\to\Lambda\pi)\ell\bar{\nu}_\ell$, which now involves 3 angles: θ, θ_Λ and ϕ, cf. Appendix. Similarly to what we did in Eq. (3.77), in order to simplify the expression for the decay rate, we write

$$\mathcal{M}^{(4)\lambda_b\lambda_\ell}_{\lambda_\Lambda}=\frac{G_F V_{cb}}{\sqrt{2}}\sum_{\lambda\in\{\pm,0,t\}}\widehat{H}^{\lambda_b\lambda_\ell}_{\lambda_\Lambda\lambda}L^{\mathrm{V-A}}_{\lambda_\ell\lambda}\,BW(k^2),\tag{3.88}$$

where $\widehat{H}^{\lambda_b\lambda_\ell}_{\lambda_\Lambda\lambda}$ are obtained from $\widetilde{H}^{\lambda_b\lambda_\ell}_{\lambda_c\lambda}$, given in Eq. (3.76), by

$$\begin{pmatrix}\widehat{H}^{\lambda_b\lambda_\ell}_{+\lambda}\\ \widehat{H}^{\lambda_b\lambda_\ell}_{-\lambda}\end{pmatrix}=\begin{pmatrix}h_+\cos\left(\frac{\theta_\Lambda}{2}\right) & -h_+e^{-i\phi}\left(\frac{\theta_\Lambda}{2}\right)\\ h_-e^{i\phi}\sin\left(\frac{\theta_\Lambda}{2}\right) & h_-\cos\left(\frac{\theta_\Lambda}{2}\right)\end{pmatrix}\begin{pmatrix}\widetilde{H}^{\lambda_b\lambda_\ell}_{+\lambda}\\ \widetilde{H}^{\lambda_b\lambda_\ell}_{-\lambda}\end{pmatrix}.\tag{3.89}$$

The resulting 8 amplitudes read:

$$\begin{aligned}
\mathcal{M}^{(4)++}_{\lambda_\Lambda}&=BW(k^2)\sqrt{2}\beta m_\ell\left(\sqrt{2}\widehat{H}^{++}_{\lambda_\Lambda t}-\sqrt{2}\cos\theta\widehat{H}^{++}_{\lambda_\Lambda 0}-\sin\theta\widehat{H}^{++}_{\lambda_\Lambda -}\right),\\
\mathcal{M}^{(4)-+}_{\lambda_\Lambda}&=BW(k^2)\sqrt{2}\beta m_\ell\left(\sqrt{2}\widehat{H}^{-+}_{\lambda_\Lambda t}-\sqrt{2}\cos\theta\widehat{H}^{-+}_{\lambda_\Lambda 0}+\sin\theta\widehat{H}^{-+}_{\lambda_\Lambda -}\right),\\
\mathcal{M}^{(4)+-}_{\lambda_\Lambda}&=BW(k^2)\sqrt{2q^2}\beta\left((1-\cos\theta)\widehat{H}^{+-}_{\lambda_\Lambda +}+\sqrt{2}\sin\theta\widehat{H}^{+-}_{\lambda_\Lambda 0}\right),\\
\mathcal{M}^{(4)--}_{\lambda_\Lambda}&=BW(k^2)\sqrt{2q^2}\beta\left((1+\cos\theta)\widehat{H}^{--}_{\lambda_\Lambda +}+\sqrt{2}\sin\theta\widehat{H}^{--}_{\lambda_\Lambda 0}\right),
\end{aligned}\tag{3.90}$$

where the superscript "(4)" indicates that we deal with the 4-body decay. By combining the vector defined in Eq. (3.89) with its conjugate and by using Eq. (3.88) we obtain two useful expressions, namely,

$$\begin{aligned}
\overline{\widehat{H}^{\lambda_b\lambda_\ell}_{+\lambda}}\widehat{H}^{\lambda'_b\lambda'_\ell}_{+\lambda'}+\overline{\widehat{H}^{\lambda_b\lambda_\ell}_{-\lambda}}\widehat{H}^{\lambda'_b\lambda'_\ell}_{-\lambda'}&=\frac{\kappa}{2}\left(\overline{\widetilde{H}^{\lambda_b\lambda_\ell}_{+\lambda}}\widetilde{H}^{\lambda'_b\lambda'_\ell}_{+\lambda'}+\overline{\widetilde{H}^{\lambda_b\lambda_\ell}_{-\lambda}}\widetilde{H}^{\lambda'_b\lambda'_\ell}_{-\lambda'}\right)\\
&+\frac{\alpha\kappa\cos\theta_\Lambda}{2}\left(\overline{\widetilde{H}^{\lambda_b\lambda_\ell}_{+\lambda}}\widetilde{H}^{\lambda'_b\lambda'_\ell}_{+\lambda'}-\overline{\widetilde{H}^{\lambda_b\lambda_\ell}_{-\lambda}}\widetilde{H}^{\lambda'_b\lambda'_\ell}_{-\lambda'}\right)\\
&-\frac{\alpha\kappa\sin\theta_\Lambda}{2}\left(e^{-i\phi}\overline{\widetilde{H}^{\lambda_b\lambda_\ell}_{+\lambda}}\widetilde{H}^{\lambda'_b\lambda'_\ell}_{-\lambda'}+e^{i\phi}\overline{\widetilde{H}^{\lambda_b\lambda_\ell}_{-\lambda}}\widetilde{H}^{\lambda'_b\lambda'_\ell}_{+\lambda'}\right),\\
\overline{\widehat{H}^{\lambda_b\lambda_\ell}_{+\lambda}}\widehat{H}^{\lambda'_b\lambda'_\ell}_{+\lambda'}-\overline{\widehat{H}^{\lambda_b\lambda_\ell}_{-\lambda}}\widehat{H}^{\lambda'_b\lambda'_\ell}_{-\lambda'}&=\frac{\alpha\kappa}{2}\left(\overline{\widetilde{H}^{\lambda_b\lambda_\ell}_{+\lambda}}\widetilde{H}^{\lambda'_b\lambda'_\ell}_{+\lambda'}+\overline{\widetilde{H}^{\lambda_b\lambda_\ell}_{-\lambda}}\widetilde{H}^{\lambda'_b\lambda'_\ell}_{-\lambda'}\right)\\
&+\frac{\kappa\cos\theta_\Lambda}{2}\left(\overline{\widetilde{H}^{\lambda_b\lambda_\ell}_{+\lambda}}\widetilde{H}^{\lambda'_b\lambda'_\ell}_{+\lambda'}-\overline{\widetilde{H}^{\lambda_b\lambda_\ell}_{-\lambda}}\widetilde{H}^{\lambda'_b\lambda'_\ell}_{-\lambda'}\right)\\
&-\frac{\kappa\sin\theta_\Lambda}{2}\left(e^{-i\phi}\overline{\widetilde{H}^{\lambda_b\lambda_\ell}_{+\lambda}}\widetilde{H}^{\lambda'_b\lambda'_\ell}_{-\lambda'}+e^{i\phi}\overline{\widetilde{H}^{\lambda_b\lambda_\ell}_{-\lambda}}\widetilde{H}^{\lambda'_b\lambda'_\ell}_{+\lambda'}\right).
\end{aligned}\tag{3.91}$$

The first of the above formulas shows that the summation over the spin projections of Λ allows us to trade h_+ and h_-, for the overall factors κ and $\alpha\kappa$. The same holds true in the second

formula, which is useful when considering the polarization asymmetry with respect to Λ. Furthermore, we see that the last line in both of the above formulas is vanishing when $\lambda_b = \lambda_b'$, $\lambda_c = \lambda_c'$ and $\lambda = \lambda'$, or when $\lambda = 0$ and $\lambda' = t$.

The final missing ingredient is the 4-body phase space which we write as

$$\mathrm{dLIPS} = \frac{1}{64(2\pi)^6} \frac{\sqrt{\lambda_{\Lambda_b\Lambda_c}(q^2)}}{2M_{\Lambda_b}^2} \frac{\sqrt{\lambda_{\Lambda_c\Lambda\pi}}}{2M_{\Lambda_c}^2} \left(1 - \frac{m_\ell^2}{q^2}\right) dq^2 dk^2 d\cos\theta d\cos\theta_\Lambda d\phi, \tag{3.92}$$

and the full angular distribution reads:

$$\frac{d^4\Gamma}{dq^2 d\cos\theta d\cos\theta_\Lambda d\phi} = \frac{1}{64(2\pi)^6} \frac{\sqrt{\lambda_{\Lambda_b\Lambda_c}(q^2)}}{2M_{\Lambda_b}^3} \frac{\sqrt{\lambda_{\Lambda_c\Lambda\pi}}}{2M_{\Lambda_c}^2} \left(1 - \frac{m_\ell^2}{q^2}\right) \frac{1}{4} \sum_{\lambda_\ell\lambda_b\lambda_\Lambda} \int dk^2 \left|\mathcal{M}_{\lambda_\Lambda}^{(4)\lambda_b\lambda_\ell}\right|^2. \tag{3.93}$$

Before closing this Section we need to emphasize that $\Lambda_c \to \Lambda\pi$ as the secondary decay is our choice. One could equally choose $\Lambda_c \to pK_S$, since both of them have nearly equal branching fractions $\mathcal{B}(\Lambda_c \to \Lambda\pi) = 1.30(7)\%$ and $\mathcal{B}(\Lambda_c \to pK_S) = 1.59(8)\%$ [56]. Currently, however, $\Lambda_c \to \Lambda\pi$ is more advantageous because its asymmetry parameter $\alpha = -0.84(9)$ [56] has been experimentally determined more accurately than in the case of $\Lambda_c \to pK_S$, for which $\alpha = 0.2(5)$ [56]. We should also add that in some special cases we were able to compare our expressions with those that are available in the literature and we agree with them [61, 161, 163–166].

3.3.3 Angular distribution and observables

If we do not sum over λ_ℓ in Eq. (3.93) we can use the formulas given in Eq. (3.91), which appear to be particularly useful when combining the coefficients of the angular distribution in order to define various observables. Concerning the spin projections of Λ we can either sum over them or take their difference. In this way we arrive to the angular distribution of the full decay,

$$\begin{aligned}
\frac{d^4\Gamma^{\lambda_\ell}}{dq^2 d\cos\theta d\cos\theta_\Lambda d\phi} &= A_1^{\lambda_\ell} + A_2^{\lambda_\ell}\cos\theta_\Lambda \\
&+ \left(B_1^{\lambda_\ell} + B_2^{\lambda_\ell}\cos\theta_\Lambda\right)\cos\theta \\
&+ \left(C_1^{\lambda_\ell} + C_2^{\lambda_\ell}\cos\theta_\Lambda\right)\cos^2\theta \\
&+ \left(D_3^{\lambda_\ell}\sin\theta_\Lambda\cos\phi + D_4^{\lambda_\ell}\sin\theta_\Lambda\sin\phi\right)\sin\theta \\
&+ \left(E_3^{\lambda_\ell}\sin\theta_\Lambda\cos\phi + E_4^{\lambda_\ell}\sin\theta_\Lambda\sin\phi\right)\sin\theta\cos\theta,
\end{aligned} \tag{3.94}$$

and the angular distribution of the Λ-polarization asymmetry:

$$\begin{aligned}\frac{d^4\mathcal{A}_{\lambda_\Lambda}}{dq^2 d\cos\theta d\cos\theta_\Lambda d\phi} &= \widetilde{A}_1^{\lambda_\ell} + \widetilde{A}_2^{\lambda_\ell}\cos\theta_\Lambda \\ &+ \left(\widetilde{B}_1^{\lambda_\ell} + \widetilde{B}_2^{\lambda_\ell}\cos\theta_\Lambda\right)\cos\theta \\ &+ \left(\widetilde{C}_1^{\lambda_\ell} + \widetilde{C}_2^{\lambda_\ell}\cos\theta_\Lambda\right)\cos^2\theta \\ &+ \left(\widetilde{D}_3^{\lambda_\ell}\sin\theta_\Lambda\cos\phi + \widetilde{D}_4^{\lambda_\ell}\sin\theta_\Lambda\sin\phi\right)\sin\theta \\ &+ \left(\widetilde{E}_3^{\lambda_\ell}\sin\theta_\Lambda\cos\phi + \widetilde{E}_4^{\lambda_\ell}\sin\theta_\Lambda\sin\phi\right)\sin\theta\cos\theta.\end{aligned} \tag{3.95}$$

The q^2-dependent coefficients entering Eq. (3.94) read:

$$\begin{aligned}
A_1^+ &= \kappa\beta^2\mathcal{N}' m_\ell^2\left(\left|\widetilde{H}_{--}^{++}\right|^2 + 2\left|\widetilde{H}_{+t}^{++}\right|^2 + \left|\widetilde{H}_{++}^{-+}\right|^2 + 2\left|\widetilde{H}_{-t}^{-+}\right|^2\right), \\
A_2^+ &= \alpha\kappa\beta^2\mathcal{N}' m_\ell^2\left(-\left|\widetilde{H}_{--}^{++}\right|^2 + 2\left|\widetilde{H}_{+t}^{++}\right|^2 + \left|\widetilde{H}_{++}^{-+}\right|^2 - 2\left|\widetilde{H}_{-t}^{-+}\right|^2\right), \\
B_1^+ &= -4\kappa\beta^2\mathcal{N}' m_\ell^2\,\mathrm{Re}\left(\overline{\widetilde{H}_{-t}^{-+}}\widetilde{H}_{-0}^{-+} + \overline{\widetilde{H}_{+t}^{++}}\widetilde{H}_{+0}^{++}\right), \\
B_2^+ &= 4\alpha\kappa\beta^2\mathcal{N}' m_\ell^2\,\mathrm{Re}\left(\overline{\widetilde{H}_{-t}^{-+}}\widetilde{H}_{-0}^{-+} - \overline{\widetilde{H}_{+t}^{++}}\widetilde{H}_{+0}^{++}\right), \\
C_1^+ &= \kappa\beta^2\mathcal{N}' m_\ell^2\left(-\left|\widetilde{H}_{--}^{++}\right|^2 + 2\left|\widetilde{H}_{+0}^{++}\right|^2 - \left|\widetilde{H}_{++}^{-+}\right|^2 + 2\left|\widetilde{H}_{-0}^{-+}\right|^2\right), \\
C_2^+ &= \alpha\kappa\beta^2\mathcal{N}' m_\ell^2\left(\left|\widetilde{H}_{--}^{++}\right|^2 + 2\left|\widetilde{H}_{+0}^{++}\right|^2 - \left|\widetilde{H}_{++}^{-+}\right|^2 - 2\left|\widetilde{H}_{-0}^{-+}\right|^2\right), \\
D_3^+ &= 2\sqrt{2}\alpha\kappa\beta^2\mathcal{N}' m_\ell^2\,\mathrm{Re}\left(\overline{\widetilde{H}_{+t}^{++}}\widetilde{H}_{--}^{++} - \overline{\widetilde{H}_{++}^{-+}}\widetilde{H}_{-t}^{-+}\right), \\
D_4^+ &= 2\sqrt{2}\alpha\kappa\beta^2\mathcal{N}' m_\ell^2\,\mathrm{Im}\left(\overline{\widetilde{H}_{+t}^{++}}\widetilde{H}_{--}^{++} - \overline{\widetilde{H}_{++}^{-+}}\widetilde{H}_{-t}^{-+}\right), \\
E_3^+ &= 2\sqrt{2}\alpha\kappa\beta^2\mathcal{N}' m_\ell^2\,\mathrm{Re}\left(\overline{\widetilde{H}_{++}^{-+}}\widetilde{H}_{-0}^{-+} - \overline{\widetilde{H}_{+0}^{++}}\widetilde{H}_{--}^{++}\right), \\
E_4^+ &= 2\sqrt{2}\alpha\kappa\beta^2\mathcal{N}' m_\ell^2\,\mathrm{Im}\left(\overline{\widetilde{H}_{++}^{-+}}\widetilde{H}_{-0}^{-+} - \overline{\widetilde{H}_{+0}^{++}}\widetilde{H}_{--}^{++}\right), \\
A_1^- &= \kappa\beta^2\mathcal{N}' q^2\left(\left|\widetilde{H}_{++}^{--}\right|^2 + 2\left|\widetilde{H}_{-0}^{--}\right|^2 + \left|\widetilde{H}_{--}^{+-}\right|^2 + 2\left|\widetilde{H}_{+0}^{+-}\right|^2\right), \\
A_2^- &= \alpha\kappa\beta^2\mathcal{N}' q^2\left(\left|\widetilde{H}_{++}^{--}\right|^2 - 2\left|\widetilde{H}_{-0}^{--}\right|^2 - \left|\widetilde{H}_{--}^{+-}\right|^2 + 2\left|\widetilde{H}_{+0}^{+-}\right|^2\right), \\
B_1^- &= 2\kappa\beta^2\mathcal{N}' q^2\left(\left|\widetilde{H}_{++}^{--}\right|^2 - \left|\widetilde{H}_{--}^{+-}\right|^2\right), \\
B_2^- &= 2\alpha\kappa\beta^2\mathcal{N}' q^2\left(\left|\widetilde{H}_{++}^{--}\right|^2 + \left|\widetilde{H}_{--}^{+-}\right|^2\right), \\
C_1^- &= \kappa\beta^2\mathcal{N}' q^2\left(\left|\widetilde{H}_{++}^{--}\right|^2 - 2\left|\widetilde{H}_{-0}^{--}\right|^2 + \left|\widetilde{H}_{--}^{+-}\right|^2 - 2\left|\widetilde{H}_{+0}^{+-}\right|^2\right), \\
C_2^- &= \alpha\kappa\beta^2\mathcal{N}' q^2\left(\left|\widetilde{H}_{++}^{--}\right|^2 + 2\left|\widetilde{H}_{-0}^{--}\right|^2 - \left|\widetilde{H}_{--}^{+-}\right|^2 - 2\left|\widetilde{H}_{+0}^{+-}\right|^2\right), \\
D_3^- &= -2\sqrt{2}\alpha\kappa\beta^2\mathcal{N}' q^2\,\mathrm{Re}\left(\overline{\widetilde{H}_{-0}^{--}}\widetilde{H}_{++}^{--} + \overline{\widetilde{H}_{--}^{+-}}\widetilde{H}_{+0}^{+-}\right), \\
D_4^- &= 2\sqrt{2}\alpha\kappa\beta^2\mathcal{N}' q^2\,\mathrm{Im}\left(\overline{\widetilde{H}_{-0}^{--}}\widetilde{H}_{++}^{--} + \overline{\widetilde{H}_{--}^{+-}}\widetilde{H}_{+0}^{+-}\right),
\end{aligned}$$

$$E_3^- = 2\sqrt{2}\alpha\kappa\beta^2\mathcal{N}' q^2\,\mathrm{Re}\left(-\overline{\widetilde{H}_{-0}^{--}}\,\widetilde{H}_{++}^{--} + \overline{\widetilde{H}_{--}^{+-}}\,\widetilde{H}_{+0}^{+-}\right),$$
$$E_4^- = 2\sqrt{2}\alpha\kappa\beta^2\mathcal{N}' q^2\,\mathrm{Im}\left(\overline{\widetilde{H}_{-0}^{--}}\,\widetilde{H}_{++}^{--} - \overline{\widetilde{H}_{--}^{+-}}\,\widetilde{H}_{+0}^{+-}\right). \tag{3.96}$$

Once again $\beta = \sqrt{1 - m_\ell^2/q^2}$, and

$$\kappa\beta^2\mathcal{N}' = \frac{G_F^2|V_{cb}|^2}{4096\pi^4}\frac{\sqrt{\lambda_{\Lambda_b\Lambda_c}(q^2)}}{M_{\Lambda_b}^3}\left(1 - \frac{m_\ell^2}{q^2}\right)^2 \mathcal{B}\left(\Lambda_c \to \Lambda\pi\right). \tag{3.97}$$

The coefficients entering the angular distribution of the Λ-polarization asymmetry, cf. Eq. (3.95), are not independent. More specifically, we find:

$$\begin{aligned}
\widetilde{A}_1^\pm &= \alpha A_1^\pm, & \widetilde{A}_2^\pm &= A_2^\pm/\alpha,\\
\widetilde{B}_1^\pm &= \alpha B_1^\pm, & \widetilde{B}_2^\pm &= B_2^\pm/\alpha,\\
\widetilde{C}_1^\pm &= \alpha C_1^\pm, & \widetilde{C}_2^\pm &= C_2^\pm/\alpha,\\
\widetilde{D}_3^\pm &= D_3^\pm/\alpha, & \widetilde{D}_4^\pm &= D_4^\pm/\alpha,\\
\widetilde{E}_3^\pm &= E_3^\pm/\alpha, & \widetilde{E}_4^\pm &= E_4^\pm/\alpha.
\end{aligned} \tag{3.98}$$

This means that measuring the asymmetry with respect to the polarization of the outgoing Λ would not bring us any new information about the BSM physics with respect to Eq. (3.94). If one of these quantities becomes experimentally accessible, it can be used as another determination of the α parameter, and then both options for the secondary decay, $\Lambda_c \to pK_S$ and $\Lambda_c \to pK_S$ would become equally interesting to study.

As we can see from the expressions for the differential decay width, for each polarization of the outgoing lepton (3.94) there are 10 q^2-dependent coefficients corresponding to $\lambda_\ell = +1/2$, and 10 coefficients corresponding to $\lambda_\ell = -1/2$. In the latter case, however, it is easy to see that not all the coefficients are linearly independent. Instead, one can express $B_{1,2}^-$ in terms of $A_{1,2}^-$ and $C_{1,2}^-$. If we normalize each coefficient by the full differential decay rate, we get a total of 18 observables which we discuss in the next Section.

3.3.4 Observables

We already counted the number of independent coefficients in the angular distributions. We found that the angular analysis of the 3-body decay, $\Lambda_b \to \Lambda_c\ell\nu$, can yield 10 independent observables, while a detailed angular analysis of the 4-body decay, $\Lambda_b \to \Lambda_c(\to \Lambda\pi)\ell\nu$, allows us to define 18 observables. Let us denote by O_i one of the angular coefficients, $O_i^\pm \in \{A_{1,2}^\pm, B_{1,2}^\pm, C_{1,2}^\pm, D_{3,4}^\pm, E_{3,4}^\pm\}$, and define $O_i = O_i^+ + O_i^-$ and $O_i^{\mathcal{A}} = O_i^+ - O_i^-$, where the superscript $\mathcal{A}$ indicates that we deal with asymmetry with respect to the lepton polarization. [13]

Integrated observables, R_{Λ_c} and more

Each of the above-mentioned coefficients (observables), entering the full angular distribution of $\Lambda_b \longrightarrow \Lambda_c(\to \Lambda\pi)\ell\nu$, is a q^2-dependent function. To get the integrated characteristic of each

[13] We reiterate that the separation of the amplitudes with respect to the polarization of Λ does not lead to any new interesting physics information. Instead, the separation of the amplitudes with respect to the lepton polarization does provide us with new information.

a_i	$a_{\rm S}$	$a_{\rm VS}$	$a_{\rm P}$	$a_{\rm AP}$	$a_{\rm V}$	$a_{\rm TV}$	$a_{\rm A}$	$a_{\rm TA}$	$a_{\rm T}$
Central Value	0.1011	0.1414	0.0105	−0.0272	0.1061	0.2947	0.2270	1.3289	3.4734
Error	0.0048	0.0071	0.0005	0.0013	0.0055	0.0156	0.0093	0.0528	0.1448

Table 3.11: *Central values and uncertainty on each of the nine magic numbers a_i entering the expression for R_{Λ_c} given in Eq. (3.103). Their correlation matrix is given in the text.*

one of them, we will integrate over the available phase space, $q^2 \in [m_\ell^2, (M_{\Lambda_b} - M_{\Lambda_c})^2]$, and normalize by the full decay width which is otherwise given by:

$$\frac{d\Gamma(\Lambda_b \to \Lambda_c \ell \nu)}{dq^2} = 8\pi \left(A_1 + \frac{C_1}{3} \right). \tag{3.99}$$

In other words we define,

$$\langle O_i \rangle = \frac{8\pi}{\Gamma} \int_{m_\ell^2}^{(M_{\Lambda_b} - M_{\Lambda_c})^2} O_i \, dq^2, \tag{3.100}$$

where the factor 8π is chosen for convenience so that $\langle A_1 \rangle + \langle C_1 \rangle / 3 = 1$.

Furthermore, for the quantities that are non-zero in the SM, we also introduce the ratios,

$$\mathcal{R}(O_i^{(\mathcal{A})}) = \frac{\langle O_i^{(\mathcal{A})} \rangle}{\langle O_i^{(\mathcal{A})} \rangle^{\rm SM}}, \tag{3.101}$$

which is a convenient way to measure the deviation of any given observable with respect to its SM value.

Using the definition similar to Eq. (3.61), we write

$$R_{\Lambda_c} = \left. \frac{\mathcal{B}(\Lambda_b \to \Lambda_c \tau \nu)}{\mathcal{B}(\Lambda_b \to \Lambda_c l \nu)} \right|_{l \in \{e,\mu\}}, \tag{3.102}$$

and we follow a common practice to assume that the New Physics affects only the decay with τ in the final state, i.e. $g^{\tau}_{V,A,S,P,T} \neq 0$, while $g^{\mu,e}_{V,A,S,P,T} = 0$. The generic expression for R_{Λ_c} can be conveniently written in terms of the NP couplings, $g_{V,A,S,P,T} \equiv g^{\tau}_{V,A,S,P,T}$, and the "magic numbers" a_i as:

$$\begin{aligned} R_{\Lambda_c} =& a_{\rm S} \left| g_S \right|^2 + a_{\rm VS} \, {\rm Re} \left[(1 + g_{\rm V}) g_{\rm S}^* \right] + a_{\rm P} \left| g_P \right|^2 + a_{\rm AP} \, {\rm Re} \left[(g_A - 1) g_P^* \right] + a_{\rm V} \left| 1 + g_V \right|^2 \\ &+ a_{\rm TV} \, {\rm Re} \left[g_T (1 + g_V{}^*) \right] + a_{\rm A} \left| 1 - g_A \right|^2 + a_{\rm TA} \, {\rm Re} \left[g_T (g_A{}^* - 1) \right] + a_{\rm T} \left| g_T \right|^2 . \end{aligned}$$

Since the parameter α does not enter the expression for the decay rate, the errors on the values of a_i are practically entirely due to form factors. We computed all of the magic numbers a_i and their values are given in Tab. 3.11. The correlation matrix has the following form

$$\mathrm{Corr}_a = \begin{pmatrix} 1 & 0.993 & 0.6985 & -0.7 & 0.9492 & 0.764 & 0.8137 & 0.816 & 0.7969 \\ \cdot & 1 & 0.6695 & -0.6741 & 0.9666 & 0.7611 & 0.777 & 0.7784 & 0.7669 \\ \cdot & \cdot & 1 & -0.9987 & 0.7091 & 0.7203 & 0.8545 & 0.7893 & 0.7408 \\ \cdot & \cdot & \cdot & 1 & -0.7159 & -0.7237 & -0.8554 & -0.7892 & -0.7402 \\ \cdot & \cdot & \cdot & \cdot & 1 & 0.8389 & 0.7555 & 0.7464 & 0.754 \\ \cdot & \cdot & \cdot & \cdot & \cdot & 1 & 0.7229 & 0.7295 & 0.8344 \\ \cdot & \cdot & \cdot & \cdot & \cdot & \cdot & 1 & 0.9703 & 0.877 \\ \cdot & \cdot & \cdot & \cdot & \cdot & \cdot & \cdot & 1 & 0.9483 \\ \cdot & \cdot & \cdot & \cdot & \cdot & \cdot & \cdot & \cdot & 1 \end{pmatrix} ,$$

where the order of rows and columns corresponds to the order of the magic numbers in Tab. 3.11. Obviously, if we set all of the NP couplings to zero we obtain:

$$R_{\Lambda_c}^{\rm SM} = 0.333 \pm 0.013 \,. \tag{3.103}$$

Before closing this Section, we also give the Standard Model values for all $\langle O_i^{(\mathcal{A})} \rangle$, in the case of τ in the final state. We find:

$$\begin{aligned} &\langle A_1 \rangle_{\rm SM} = 1.035(1) \,, \quad \langle A_2 \rangle_{\rm SM} = 0.658(6) \,, \quad \langle B_1 \rangle_{\rm SM} = 0.049(8) \,, \quad \langle B_2 \rangle_{\rm SM} = -0.093(9) \,, \\ &\langle C_1 \rangle_{\rm SM} = -0.106(3) \,, \quad \langle C_2 \rangle_{\rm SM} = -0.095(2) \,, \quad \langle D_3 \rangle_{\rm SM} = 0.189(8) \,, \quad \langle D_4 \rangle_{\rm SM} = 0 \,, \\ &\langle E_3 \rangle_{\rm SM} = 0.069(2) \,, \quad \langle E_4 \rangle_{\rm SM} = 0 \,, \end{aligned} \tag{3.104}$$

and

$$\begin{aligned} &\langle A_1^{\mathcal{A}} \rangle_{\rm SM} = -0.405(6) \,, \quad \langle A_2^{\mathcal{A}} \rangle_{\rm SM} = -0.261(4) \,, \quad \langle B_1^{\mathcal{A}} \rangle_{\rm SM} = 0.667(6) \,, \quad \langle B_2^{\mathcal{A}} \rangle_{\rm SM} = 0.761(2) \,, \\ &\langle C_1^{\mathcal{A}} \rangle_{\rm SM} = 0.293(7) \,, \quad \langle C_2^{\mathcal{A}} \rangle_{\rm SM} = 0.300(7) \,, \quad \langle D_3^{\mathcal{A}} \rangle_{\rm SM} = -0.492(8) \,, \quad \langle D_4^{\mathcal{A}} \rangle_{\rm SM} = 0 \,, \\ &\langle E_3^{\mathcal{A}} \rangle_{\rm SM} = -0.172(6) \,, \quad \langle E_4^{\mathcal{A}} \rangle_{\rm SM} = 0 \,. \end{aligned} \tag{3.105}$$

We should add, once again, that due to the fact that $\alpha(A_1^- + C_1^-) = B_2^-$ and $(A_2^- + C_2^-) = \alpha B_1^-$, two of the above observables are not independent, so that the final number is indeed 18, as discussed before.

3.3.5 Illustration and Phenomenology

We made an extensive analysis of all of the observables mentioned so far, and found that the following 6 exhibit more pronounced sensitivity to the presence of physics BSM:

- Ratio R_{Λ_c}, which in the SM is predicted to be $R_{\Lambda_c}^{\rm SM} = 0.333(13)$.
- Forward-backward asymmetry, $\langle \mathcal{A}_{\rm fb} \rangle = \langle B_1 \rangle / 2$, which in the SM is expected to be $\langle \mathcal{A}_{\rm fb} \rangle^{\rm SM} = 0.049(8)$.
- Lepton polarization asymmetry, $\langle \mathcal{A}_\tau \rangle = \langle A_1^{\mathcal{A}} \rangle + \langle C_1^{\mathcal{A}} \rangle / 3$. In the SM, $\langle \mathcal{A}_\tau \rangle^{\rm SM} = -0.307(7)$.
- Asymmetry "$\pi/3$", $\langle \mathcal{A}_{\pi/3} \rangle = \langle C_1 \rangle / 4$; [14]

[14] From the full angular distribution (3.94), after integrating over q^2, θ_Λ and ϕ, $\mathcal{A}_{\pi/3}$ is obtained by selecting the events as follows:

$$\mathcal{A}_{\pi/3} = \frac{1}{\Gamma} \left[\int_0^{\pi/3} + \int_{2\pi/3}^{\pi} - \int_{\pi/3}^{2\pi/3} \right] \frac{d\Gamma}{d\cos\theta} \sin\theta \, d\theta . \tag{3.106}$$

	$g_i \in \mathbb{C}$	$g_i \in \mathbb{R}$	$g_i \in \mathbb{C}$ and $\mathrm{Re}[g_i] = 0$
g_{V_L}	0.074	0.074	$\pm 0.39\, i$
g_{S_L}	$-0.76 \pm 0.80\, i$	0.12	$\pm 0.48\, i$
g_T	$0.10 \pm 0.17\, i$	-0.032	$\pm 0.10\, i$
$g_{S_L} = +8.1\, g_T$	$-0.094 \pm 0.51\, i$	N.A.	$\pm 0.48\, i$
$g_{S_L} = -8.5\, g_T$	0.16	0.16	$\pm 0.48\, i$

Table 3.12: *Best fit values for the couplings obtained by requiring R_D and R_{D^*} to be consistent with the experimental values. Apart from g_{V_L}, all the couplings are scale-dependent. The above results refer to the scale $\mu = m_b$. Notice that the last two scenarios verify $g_{S_L} = \pm 4 g_T$ at $\mu \simeq 1\,\mathrm{TeV}$.*

- $\langle D_4 \rangle$, which is strictly zero in the SM, $\langle D_4 \rangle^{\mathrm{SM}} = 0$.

- $\langle E_4^{\mathcal{A}} \rangle$, which is also zero in the SM, $\langle E_4^{\mathcal{A}} \rangle^{\mathrm{SM}} = 0$.

The last two quantities become non-zero only if the imaginary part of one of the NP couplings is different from zero.

We reiterate that we assume that the LFUV in the $b \to c\ell\bar{\nu}$ decays originates from the pronounced NP coupling to τ, $g^{(\tau)}_{V,A,S,P,T} \neq 0$, while we keep $g^{(e,\mu)}_{V,A,S,P,T} = 0$. In order to select the plausible values of the couplings $g_{V,A,S,P,T} \equiv g^{(\tau)}_{V,A,S,P,T}$ we use the current experimental values of R_D and R_{D^*}, and extract the allowed ranges of each of the couplings by using the expressions presented in Ref. [28, 29]. Obviously, since we have only two experimental input values, we cannot simultaneously vary all of the BSM couplings. Instead, we restrain our attention to four scenarios of physics BSM that have been actively investigated in recent years. More specifically, we either allow only g_{V_L} or only g_{S_L} to be non-zero, or we consider a peculiar combination of two BSM couplings which satisfy $g_{S_L} = \pm 4 g_T$ at the high energy scale, $\mu = \mathcal{O}(1\ \mathrm{TeV})$. Due to the renormalization group running, at the $\mu = m_b$ this last relation becomes $g_{S_L} \simeq 8.1 g_T$, and $g_{S_L} \simeq -8.5 g_T$ [25]. In Tab. 3.12 we present the best fit values for each of the scenarios. We first allow the couplings to be complex, and then impose them to be either fully real or fully imaginary. Notice that in the scenario with $g_{S_L} = +4 g_T$ there is no real solution that would accommodate both R_D^{exp} and $R_{D^*}^{\mathrm{exp}}$ [29].

For each of the values of the couplings given in Tab. 3.12 we compute the observables mentioned above and compare them with their SM values, following Eq. (3.101). For the quantities which are zero in the SM, such as $\langle D_4 \rangle$ and $\langle E_4^{\mathcal{A}} \rangle$, we just give the values which are non-zero in the presence of NP. The response of the observables mentioned above to the non-zero BSM couplings is given in Tab. 3.13.

Observable		$\mathcal{R}(R_{\Lambda_c})$	$\mathcal{R}(\mathcal{A}_{\rm fb})$	$\mathcal{R}(\mathcal{A}_\tau)$	$\mathcal{R}(\mathcal{A}_{\pi/3})$	$\langle D_4 \rangle$	$\langle E_4^{\mathcal{A}} \rangle$
g_{V_L}	cplx	1.153(0)	1	1	1	0	0
g_{S_L}	cplx	1.147(3)	-0.77(25)	0.45(1)	0.87(0)	0.12(0)	0
	real	1.046(1)	1.24(4)	0.81(1)	0.96(0)	0	0
	im	1.077(1)	0.93(0)	0.70(1)	0.93(0)	0.08(0)	0
g_T	cplx	1.095(8)	2.92(39)	0.50(1)	1.38(2)	0.10(0)	-0.25(1)
	real	1.110(2)	1.51(15)	0.99(0)	0.91(0)	0	0
	im	1.104(2)	1.83(17)	0.88(0)	1.02(1)	0.06(0)	-0.15(0)
$g_{S_L} = 4g_T$	cplx	1.137(1)	2.02(22)	0.74(1)	0.93(1)	0.11(0)	-0.09(0)
	im	1.114(1)	1.91(19)	0.66(1)	0.94(0)	0.11(0)	-0.08(0)
$g_{S_L} = -4g_T$	cplx	1.006(3)	1.17(32)	0.72(1)	1.00(0)	0	0
	im	1.114(1)	0.53(7)	0.66(1)	0.94(0)	0.04(0)	0.09(0)

Table 3.13: *Illustration of the change of the observable with respect to its SM value for different choices of the New Physics couplings chosen as discussed in the text and explicitly given in Tab. 3.12. Notice that we separate the cases in which $g_i \in \mathbb{C}$, $g_i \in \mathbb{R}$ or purely imaginary. The error on D_4 and $E_4^{\mathcal{A}}$ only takes into account the error on the form factors, not on α, which is taken to be $\alpha = 0.82$ [61].*

Therefore measuring the angular observables entering the $\Lambda_b \to \Lambda_c \tau \nu$ can give us access to four of the above quantities which in turn can be very helpful for identifying the Lorentz structure of the BSM contribution.To figure out whether or not there is a BSM phase, one needs to go beyond and consider the secondary decay $\Lambda_b \to \Lambda_c(\to \Lambda\pi)\tau\nu$ which then gives a possibility to get a non-zero contribution to $\langle D_4 \rangle$ and $\langle E_4^{\mathcal{A}} \rangle$.

We now go through various scenarios to further illustrate the usefulness of the quantities mentioned above.

Only $g_{V_L} \neq 0$

Considering the scenarios in which the only BSM coupling different from zero is g_{V_L}, practically all of the observables are SM-like, because $1+g_{V_L}$ enters as an overall factor with respect to the SM Lagrangian, cf. Eq. (3.62). Since the angular observables are normalized to the decay rate, the effect of this coupling is not changing the SM predictions. The only exception is precisely R_{Λ_c}, the value of which does change, as we show in Fig. 3.11. An example of the explicit BSM

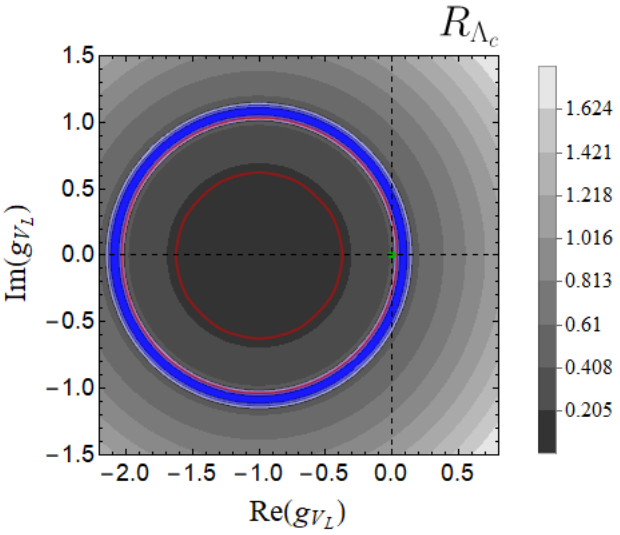

Figure 3.11: *R_{Λ_c} is plotted in the plane of $\mathrm{Re}(g_{V_L})$ - $\mathrm{Im}(g_{V_L})$. The blue circle corresponds to the values of g_{V_L} allowed by simultaneously requiring R_D and R_{D^*} to be compatible with R_D^{exp} and $R_{D^*}^{\mathrm{exp}}$. We also show the 2σ region defined by $R_{\Lambda_c}^{\mathrm{exp}}$ (between the two red circles). The green dot corresponds to the SM value. Various values of R_{Λ_c} are shown by the graded gray regions.*

model that falls into this category is the one with a light [$\mathcal{O}(1\,\mathrm{TeV})$] vector leptoquark [167–174].

$g_{S_L,T} \neq 0$

In the case in which only the $g_{S_L} \neq 0$ is allowed, we find that a particularly sensitive quantity is $\langle \mathcal{A}_{\pi/3} \rangle$ and the τ-polarization asymmetry, $\langle \mathcal{A}_\tau \rangle$. However, since the preferred values of g_{S_L} by R_D^{exp} and $R_{D^*}^{\mathrm{exp}}$ have a large imaginary part, also $\langle D_4 \rangle$ becomes significantly different from zero, cf. Tab. 3.13. A representative example of such a scenario would be the extension of the SM with two Higgs doublets (2HDM), which provides a new tree-level mediator for the $B \to D^{(*)}\tau\bar{\nu}_\tau$, namely a charged Higgs boson. The complex coupling, selected by R_D^{exp} and $R_{D^*}^{\mathrm{exp}}$, is however unusual and in particular inconsistent with a Type II 2HDM [151, 175, 176]. Note also that a purely real g_{S_L} is inconsistent with R_D^{exp} and $R_{D^*}^{\mathrm{exp}}$ to almost 3σ.

Another possibility is to only allow $g_T \neq 0$. Such a scenario could be built up from the scalar leptoquarks $R_2 = (3, 2, 7/6)$ and $S_1 = (\bar{3}, 1, 1/3)$, coupled in such a way that their respective non-zero g_{S_L} cancel, in which case only $g_T \neq 0$ would survive. [15] In such a scenario, from the requirement of compatibility with R_D^{exp} and $R_{D^*}^{\mathrm{exp}}$, we again obtain a possibility of $\mathrm{Im}(g_T) \neq 0$, which could be verified by measuring $\langle D_4 \rangle$ or $\langle E_4^{\mathcal{A}} \rangle$. Otherwise, $\langle \mathcal{A}_{\mathrm{fb}} \rangle$ appears to be more sensitive to this scenario than the other observables mentioned in this Section.

We now consider the scenarios that are often invoked when trying to accommodate R_D^{exp} and $R_{D^*}^{\mathrm{exp}}$ in a minimalistic NP scenario. In the first one, one allows for the $\mathcal{O}(1\,\mathrm{TeV})$ scalar leptoquark R_2 [35, 177–179] in which, at the high energy scale we have $g_{S_L} = 4g_T$ which arises after applying the Fierz identities in order to match with the effective theory (3.62). That relation becomes $g_{S_L} \simeq 8.1 g_T$ at the $\mu = m_b$, to which we refer in the following. A peculiarity of this scenario is that the g_{S_L} resulting from compatibility with R_D^{exp} and $R_{D^*}^{\mathrm{exp}}$ has a large imaginary

[15] Note that the leptoquarks are specified by their SM gauge group quantum numbers.

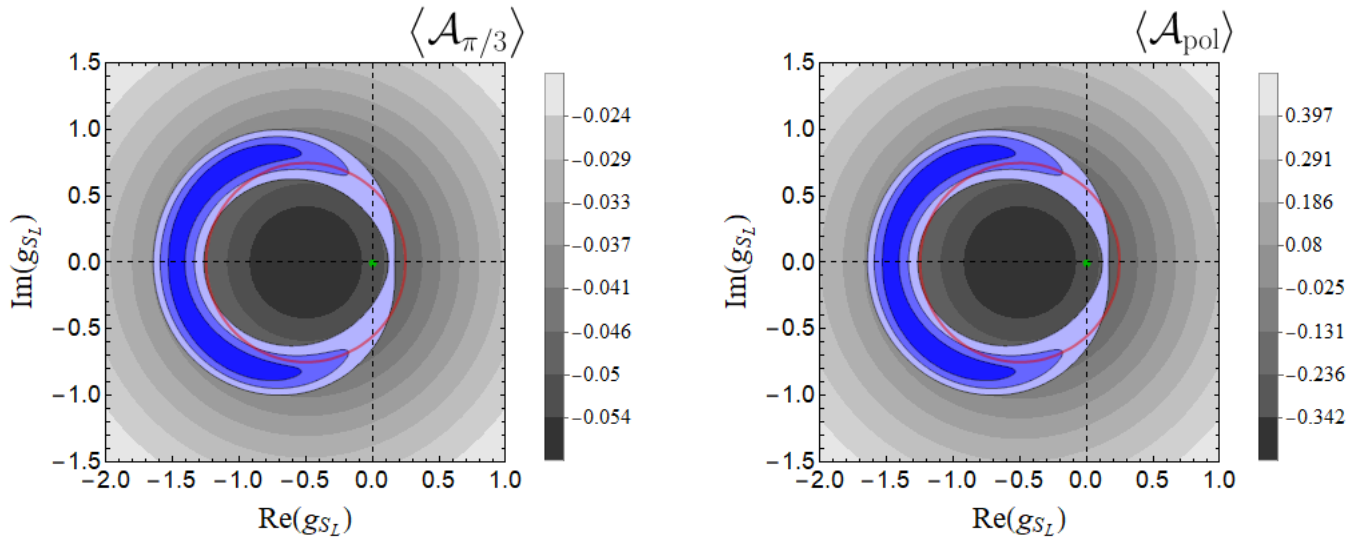

Figure 3.12: *Scenario with only $g_{S_L} \neq 0$ shows that the only $\mathrm{Re}(g_{S_L})$ and $\mathrm{Im}(g_{S_L})$, allowed by $R_D^{\rm exp}$ and $R_{D^*}^{\rm exp}$, are complex and large (blue regions). The gray regions correspond to various values of $\langle \mathcal{A}_{\pi/3} \rangle$ and to $\langle \mathcal{A}_\tau \rangle$ in the left and right panel respectively. Both quantities are smaller than their SM counterparts, denoted by green dots in the plots. Red circles correspond to g_{S_L} consistent with the current $R_{\Lambda_c}^{\rm exp}$.*

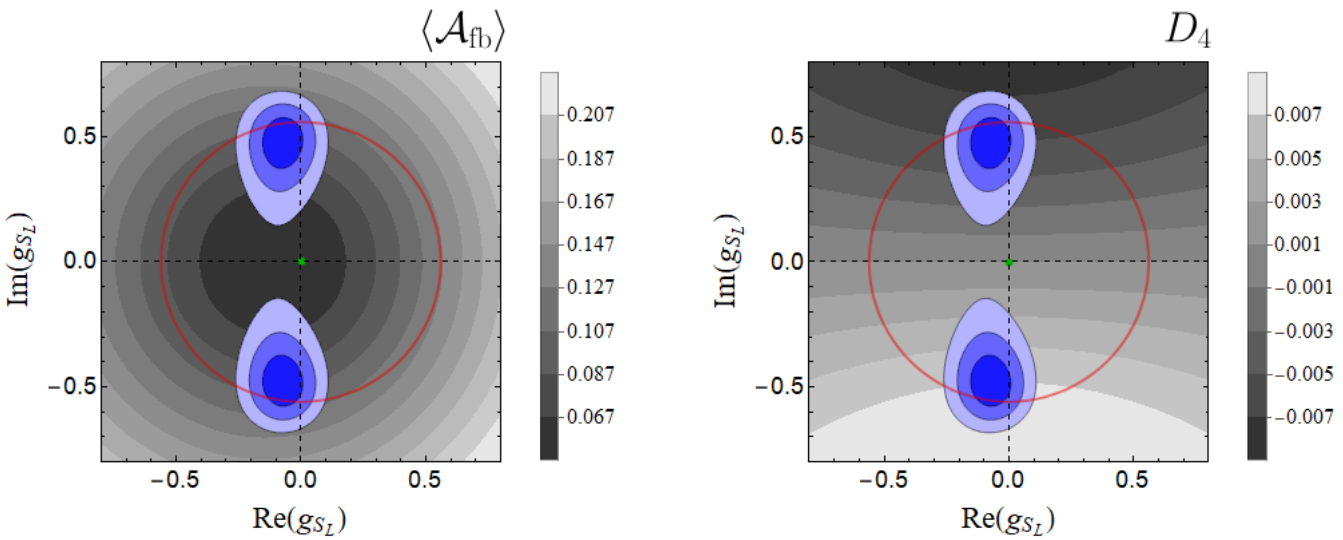

Figure 3.13: *Scenario with non-zero NP couplings satisfying $g_{S_L} = 4g_T$ is shown in the $\mathrm{Re}(g_{S_L})$-$\mathrm{Im}(g_{S_L})$ plane. The blue regions are selected by $R_D^{\rm exp}$ and $R_{D^*}^{\rm exp}$ to 1, 2 and 3 σ. The gray regions correspond to various values of $\langle \mathcal{A}_{\rm fb} \rangle$ and to $\langle D_4 \rangle$ in the left and right panel respectively. Their SM values are indicated by green dots while the red circles limit the domain of g_{S_L} consistent with $R_{\Lambda_c}^{\rm exp}$.*

part, and different from zero to more than 3σ. In order to check for the validity of this scenario, it is therefore of major importance to get $\langle D_4 \rangle$ or $\langle E_4 \rangle$. Other quantities are also important to measure as all of them, $\langle \mathcal{A}_{\rm fb} \rangle$, $\langle \mathcal{A}_{\pi/3} \rangle$, $\langle \mathcal{A}_\tau \rangle$, are likely to be smaller than their respective SM values. In Fig. 3.13 we illustrate the situation for $\langle \mathcal{A}_{\rm fb} \rangle$ and for $\langle D_4 \rangle$. Since the sign of the phase

is not constrained, the available values of $\langle D_4 \rangle$ are symmetric.

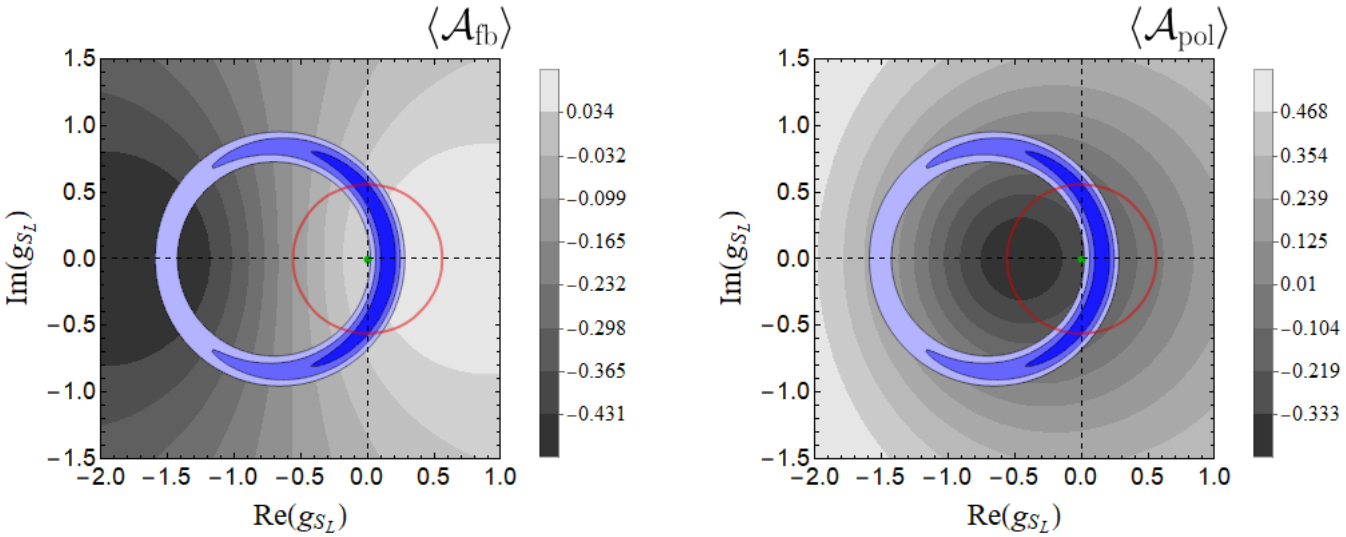

Figure 3.14: *Scenario with non-zero NP couplings satisfying* $g_{S_L} = -4g_T$*. The values of* $\mathrm{Re}(g_{S_L})$-$\mathrm{Im}(g_{S_L})$ *in the blue regions are selected by* $R_D^{\rm exp}$ *and* $R_{D^*}^{\rm exp}$ *to* 1*,* 2 *and* 3 σ*. The gray regions correspond to various values of* $\langle \mathcal{A}_{\rm fb} \rangle$ *and to* $\langle \mathcal{A}_\tau \rangle$ *in the left and right panel respectively. The SM values are indicated by green dots while the red circles limit the domain consistent with* $R_{\Lambda_c}^{\rm exp}$*.*

The second scenario in which $g_{S_L,T} \neq 0$, and which can explain $R_D^{\rm exp}$ and $R_{D^*}^{\rm exp}$ is the minimal extension of the SM by a low energy S_1 scalar leptoquark [33,39,180–182]. In that scenario the two non-zero effective couplings are related as $g_{S_L} = -4g_T$, a relation that at the low energy scale $\mu = m_b$ becomes $g_{S_L} \approx -8.5 g_T$. Like in the previous cases, one would obviously prefer all the observables to be measured. None of the observables exhibits more pronounced sensitivity with respect to the others.. We select to show in Fig. 3.14 how $\langle \mathcal{A}_{\rm fb} \rangle$ and $\langle \mathcal{A}_\tau \rangle$ vary with respect to the SM when $g_{S_L} \neq 0$.

More comments on the $g_{S_L} = +4g_T$ scenario

As we showed above, the model in which the SM is extended by a presence of the $\mathcal{O}(1\,\mathrm{TeV})$ scalar leptoquark R_2 is peculiar because the compatibility with the measured $R_D^{\rm exp}$ and $R_{D^*}^{\rm exp}$ necessitates the NP coupling to have a large imaginary part. We show in Fig. 3.15 how the measurement of three quantities, R_{Λ_c}, $\langle \mathcal{A}_{\rm fb} \rangle$ and $\langle D_4 \rangle$, can help distinguishing this scenario from the SM.

Another point, which was abundantly discussed in the literature regarding $B \to K^* \ell^+ \ell^-$, is the interest in defining the forward-backward asymmetry in one half of the physics q^2-region allowed in this decay. The situation with several observables, including the forward-backward asymmetry, is that they change the sign when moving from the low to large q^2's. [16] As a result their integrated characteristics, cf. Eq. (3.100), become small due to significant cancellations. It would be therefore beneficiary for this research if one could split the data into high and low q^2-regions, so that the absolute values of the resulting observables become larger. Note also

[16] To be more specific, we find that $\mathcal{A}_{\rm fb}(q^2)$, $B_2(q^2)$, $\mathcal{A}_\tau(q^2)$ are the observables which change the sign when going from low to high q^2 regions.

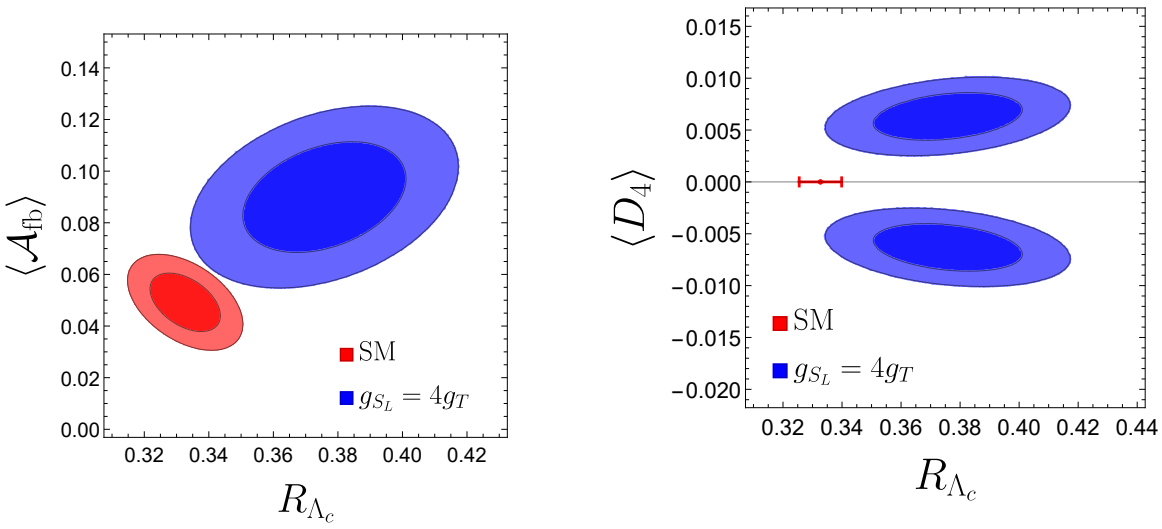

Figure 3.15: *Scenario of NP with a low energy scalar leptoquark R_2 verifying $g_{S_L} = +4g_T$. We show the regions of predicted values of R_{Λ_c}, $\langle \mathcal{A}_{\rm fb} \rangle$ and $\langle D_4 \rangle$, which clearly differ from SM, so that the measurement of these quantities can help (in)validating this model. Note that the couplings are selected in such a way as to ensure the compatibility with $R_D^{\rm exp}$ and $R_{D^*}^{\rm exp}$ to 1 and 2 σ.*

that the shape of $D_4(q^2)$ is somewhat skewed towards the larger q^2's when $\mathrm{Im}(g_{S_L}) \neq 0$, cf. Fig. 3.16.

Finally, looking for the point q_0^2 at which a given observable changes the sign could provide us with helpful information as well. In particular, in the SM, we find that,

$$\mathcal{A}_{\rm fb}^{\rm SM}(q_0^2) = 0, \quad \text{for} \quad q_0^2 = 8.0(1)\ \mathrm{GeV}^2\,. \tag{3.107}$$

However, when switching on $\mathrm{Im}(g_{S_L}) = 0.48$, which is consistent with the scenario discussed in this subsection, that zero is shifted to a larger $q_0^2 = 8.6(1)\ \mathrm{GeV}^2$, see Fig. 3.16.

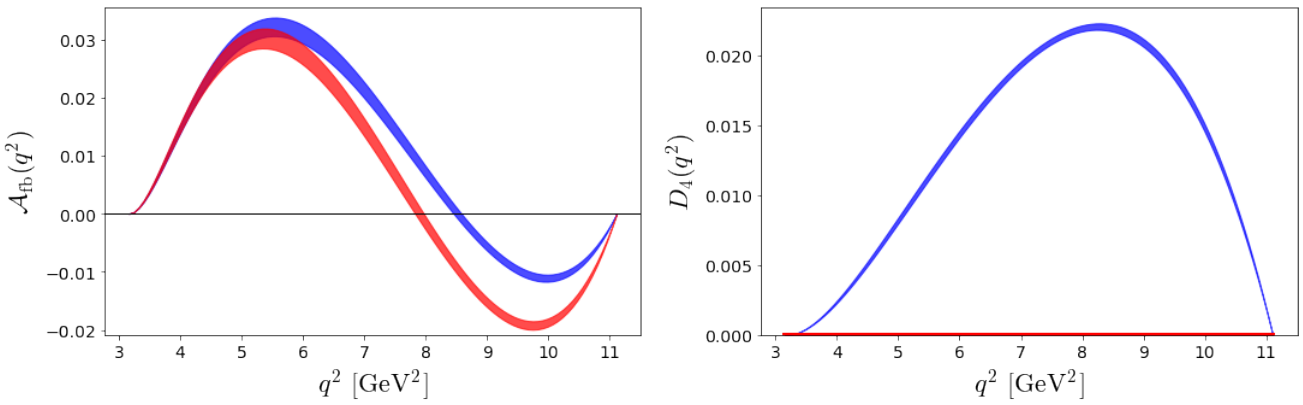

Figure 3.16: *Displayed are the q^2 shapes of $\mathcal{A}_{\rm fb}(q^2)$ and $D_4(q^2)$, in the SM (red curves) and in the scenario with $g_{S_L} = 4g_T$ where we choose the purely imaginary, $\mathrm{Im}(g_{S_L}) = 0.48$ (blue curve). Notice that the zero of $\mathcal{A}_{\rm fb}(q^2)$ is larger in this NP scenario with respect to the SM value.*

3.3.6 Summary on baryons

In this work we revisited the problem of distinguishing the NP scenario in the exclusive $b \to c\ell\bar{\nu}$ decays, by focusing on the $\Lambda_b \longrightarrow \Lambda_c \ell\nu$ decay mode. This mode has received considerable attention in recent years, it is being studied at the LHCb, and more importantly the hadronic matrix elements relevant to the SM operators and those arising in the BSM scenarios have all been computed by means of numerical simulations of QCD on the lattice.

By working in a general low energy effective theory, in which we included all of the possible NP contributions (without considering the right-handed neutrinos), we first provided the expression for the angular distribution of this decay. In doing so we separated the contributions arising from various polarization states of the outgoing baryon and lepton. In that way we were able to show that one can at most build 10 different observables. That number rises to 18, if one considers the secondary decay, which we choose to be $\Lambda_c \to \Lambda\pi$. Notice that we can have extra 18 observables if we also include the coefficients that would come with the polarization asymmetries regarding the final Λ. However, those extra observables would not be informative, as far as NP is concerned but it would lead to yet another determination of the polarization asymmetry parameter of Λ, referred to as α.

In an ideal scenario, one would obviously prefer to have as many observables in order to test the viability of various scenarios of physics BSM. In our phenomenological analysis we restrained our attention to a subset of 6 observables which we find to exhibit more pronounced sensitivity to the non-zero couplings to NP. In simplified scenarios, used to accommodate $R^{\rm exp}_{D^{(*)}}$, one is turning on one coupling at a time.

If we assume NP to arise from the g_{V_L} coupling, we find that all our observables remain SM-like, except for the ratio $R_{\Lambda_c} = |1 + g_{V_L}|^2 R^{\rm SM}_{\Lambda_c}$.

Other simplified scenarios arise from the extensions of the SM by including an $\mathcal{O}(1\,\mathrm{TeV})$ scalar leptoquark, giving rise to two NP couplings, g_{S_L} and g_T, couplings to the (left) scalar and tensor quark operators respectively. These couplings are, due to Fierz identities, related to each other as $g_{S_L} = \pm 4 g_T$, at the high energy scale. In these scenarios all observables can be very different from their SM counterparts. We isolated a few such observables to show how they can be used to validate or to refute the scenarios that are currently used in order to describe the deviations of $R^{\rm exp}_{D^{(*)}}$ with respect to their SM values, $R^{\rm SM}_{D^{(*)}}$. In particular, to accommodate those discrepancies in the scenario with $g_{S_L} = +4 g_T$, the NP coupling must have a non-zero complex phase, in which case some of the observables (such as $\langle D_4 \rangle$) would be a clear test of validity because $\langle D_4 \rangle \neq 0$ only if $\mathrm{Im}(g_{S_L}) \neq 0$.

We also discuss the impact of the recently reported $R^{\rm exp}_{\Lambda_c}$, the result which can and should be improved. Importantly, however, we must emphasize that the observables arising from the angular distribution, such as those discussed in this Chapter, represent a fine and powerful check of the presence of NP at low energy scales. One can, for example, easily build a scenario in which $R_{D^{(*)}}$, $R_{J/\psi}$ and R_{Λ_c} are consistent with their SM values but that several of the angular observables have values very different from SM. It is therefore important to measure these quantities. Throughout our phenomenological discussion we referred to the quantities integrated over the available q^2's. Needless to say that in some cases, such as the forward-backward asymmetry with respect to the outgoing lepton, the q^2-dependence of the observables could provide us with very interesting information and potentially reveal the presence of physics BSM.

We should also stress that the hadronic form factors for all of the operators needed for the full NP analysis of this decay have been computed on the lattice, which is not the case with

the modes involving mesons, such as $B \to D^{(*)}\ell\bar{\nu}$, for which the tensor form factors have not been computed on the lattice. It should be kept in mind, however, that the hadronic matrix elements relevant to $\Lambda_b \to \Lambda_c\ell\bar{\nu}$ have been computed by only one lattice group and it is of major importance for this research that another lattice QCD study is made, preferably by using a different discretization of QCD.

Appendix

In this appendix we give additional details which might be important for a reader willing to repeat the computation the results of which are presented in the body of this Chapter. To discuss the kinematics of $\Lambda_b(p) \to \Lambda_c(k)\ell(k_1)\bar{\nu}(k_2)$, we introduce $q = k_1 + k_2 = p - k$, and choose a z-axis along the flight of Λ_c. Angle θ is defined in the frame in which $|\vec{q}| = 0$ between the z-axis and the direction of flight of ℓ.

In the Λ_b rest frame we then have: $M_{\Lambda_b} = E_{\Lambda_c} + q_0$. By combining $M^2_{\Lambda_b} = M^2_{\Lambda_c} + q^2 + 2k \cdot q$ with $k \cdot q = E_{\Lambda_c} q_0 + q_z^2 = M_{\Lambda_b} q_0 - q^2$ we get

$$q_0 = \frac{M^2_{\Lambda_b} - M^2_{\Lambda_c} + q^2}{2M_{\Lambda_b}}, \quad E_{\Lambda_c} = \frac{M^2_{\Lambda_b} + M^2_{\Lambda_c} - q^2}{2M_{\Lambda_b}}, \quad q_z = \sqrt{q_0^2 - q^2} = \frac{\sqrt{\lambda_{\Lambda_b\Lambda_c}(q^2)}}{2M_{\Lambda_b}}, \tag{3.108}$$

where we use

$$\lambda_{\Lambda_b\Lambda_c}(q^2) = M^4_{\Lambda_b} + M^4_{\Lambda_c} + q^4 - 2M^2_{\Lambda_b}M^2_{\Lambda_c} - 2M^2_{\Lambda_b}q^2 - 2M^2_{\Lambda_c}q^2 = Q_+Q_-, \tag{3.109}$$

where

$$Q_\pm = (M_{\Lambda_b} \pm M_{\Lambda_c})^2 - q^2\,, \tag{3.110}$$

which we already used in Sec. 3.3.1.

In the dilepton rest frame:

$$\begin{pmatrix} \sqrt{q^2} \\ 0 \\ 0 \\ 0 \end{pmatrix} = \begin{pmatrix} E_\nu \\ -p_\ell \sin\theta \\ 0 \\ -p_\ell \cos\theta \end{pmatrix} + \begin{pmatrix} E_\ell \\ p_\ell \sin\theta \\ 0 \\ p_\ell \cos\theta \end{pmatrix}, \tag{3.111}$$

and

$$k_1 \cdot k_2 = \frac{q^2 - m_\ell^2}{2}, \quad E_\ell = \frac{q^2 + m_\ell^2}{2\sqrt{q^2}}, \quad E_\nu = \frac{q^2 - m_\ell^2}{2\sqrt{q^2}}. \tag{3.112}$$

To go from the first frame to the other, we use a Lorentz boost, $\sqrt{q^2} = \gamma q_0 + \beta\gamma q_z$, $0 = \beta\gamma q_0 + \gamma q_z$, so that the boost parameters are $\beta = -q_z/q_0$ and $\gamma = q_0/\sqrt{q^2}$, and therefore the components of the momenta of hadrons in the second frame are:

$$p = \frac{1}{\sqrt{q^2}}\left(M_{\Lambda_b} q_0, 0, 0, M_{\Lambda_b} q_z\right) = \frac{1}{2\sqrt{q^2}}\left(M^2_{\Lambda_b} - M^2_{\Lambda_c} + q^2, 0, 0, \sqrt{\lambda_{\Lambda_b\Lambda_c}(q^2)}\right), \tag{3.113}$$

$$k = \frac{1}{\sqrt{q^2}}\left(q_0(M_{\Lambda_b} - q_0) + q_z^2, 0, 0, q_z^2\right) = \frac{1}{2\sqrt{q^2}}\left(M^2_{\Lambda_b} - M^2_{\Lambda_c} - q^2, 0, 0, \sqrt{\lambda_{\Lambda_b\Lambda_c}(q^2)}\right), \tag{3.114}$$

from which one can compute other scalar products.

For completeness, we also give the expression for the spinors in the Dirac basis:

$$u(\lambda_\ell = \pm 1/2) = \sqrt{E_\ell + m_\ell}\begin{pmatrix} \xi_\pm \\ \frac{\vec{\sigma}\cdot\vec{p}_\ell}{E_\ell + m_\ell}\xi_\pm \end{pmatrix}, \quad v(\lambda_\ell = \pm 1/2) = \sqrt{E_\ell + m_\ell}\begin{pmatrix} \frac{\vec{\sigma}\cdot\vec{p}_\ell}{E_\ell + m_\ell}\xi_\mp \\ \xi_\mp \end{pmatrix}, \tag{3.115}$$

where $\vec{\sigma}$ are the Pauli matrices and the spinors $\xi_\pm$ are given by

$$\xi_+ = \exp\left(i\frac{\vec{\sigma}\cdot\vec{\theta}}{2}\right)\begin{pmatrix}1\\0\end{pmatrix}, \qquad \xi_- = \exp\left(i\frac{\vec{\sigma}\cdot\vec{\theta}}{2}\right)\begin{pmatrix}0\\1\end{pmatrix}. \tag{3.116}$$

Explicitly, for the lepton in the dilepton rest-frame, we have

$$\xi_+ = \begin{pmatrix} \cos\frac{\theta}{2} \\ \sin\frac{\theta}{2} \end{pmatrix}, \qquad \xi_- = \begin{pmatrix} -\sin\frac{\theta}{2} \\ \cos\frac{\theta}{2} \end{pmatrix}, \tag{3.117}$$

and

$$u_{\ell,+1/2} = \sqrt{E_\ell + m_\ell} \begin{pmatrix} \cos\frac{\theta}{2} \\ \sin\frac{\theta}{2} \\ \frac{p_\ell}{E_l+m_\ell}\cos\frac{\theta}{2} \\ \frac{p_\ell}{E_\ell+m_\ell}\sin\frac{\theta}{2} \end{pmatrix}, \qquad u_{\ell,-1/2} = \sqrt{E_\ell + m_\ell} \begin{pmatrix} -\sin\frac{\theta}{2} \\ \cos\frac{\theta}{2} \\ \frac{p_\ell}{E_\ell+m_\ell}\sin\frac{\theta}{2} \\ -\frac{p_\ell}{E_\ell+m_\ell}\cos\frac{\theta}{2} \end{pmatrix}. \tag{3.118}$$

For the neutrino in the dilepton rest-frame, we take $\theta \to \theta + \pi$:

$$v_{\nu,+1/2} = \sqrt{E_\nu} \begin{pmatrix} \cos\frac{\theta}{2} \\ \sin\frac{\theta}{2} \\ -\cos\frac{\theta}{2} \\ -\sin\frac{\theta}{2} \end{pmatrix}. \tag{3.119}$$

As for the baryons, in the Λ_b rest frame, $|\vec{\theta}| = 0$, we simply have

$$u_{\Lambda_b,+1/2} = \sqrt{2M_{\Lambda_b}} \begin{pmatrix} 1 \\ 0 \\ 0 \\ 0 \end{pmatrix}, \quad u_{\Lambda_b,-1/2} = \sqrt{2M_{\Lambda_b}} \begin{pmatrix} 0 \\ 1 \\ 0 \\ 0 \end{pmatrix},$$

$$u_{\Lambda_c,+1/2} = \sqrt{M_{\Lambda_c} + E_{\Lambda_c}} \begin{pmatrix} 1 \\ 0 \\ \frac{q_z}{M_{\Lambda_c}+E_{\Lambda_c}} \\ 0 \end{pmatrix}, \quad u_{\Lambda_c,-1/2} = \sqrt{M_{\Lambda_c} + E_{\Lambda_c}} \begin{pmatrix} 0 \\ 1 \\ 0 \\ \frac{-q_z}{M_{\Lambda_c}+E_{\Lambda_c}} \end{pmatrix}. \tag{3.120}$$

Finally, the spinors for Λ_c and Λ in the Λ_c rest frame, $\vec{\theta} = \phi\vec{e}_z + \theta_\Lambda\vec{e}_x$, read:

$$\xi_+ = \begin{pmatrix} e^{\frac{i\phi}{2}}\cos\frac{\theta_\Lambda}{2} \\ \sin\frac{\theta_\Lambda}{2} \end{pmatrix}, \qquad \xi_- = \begin{pmatrix} -\sin\frac{\theta_\Lambda}{2} \\ e^{\frac{-i\phi}{2}}\cos\frac{\theta_\Lambda}{2} \end{pmatrix}, \tag{3.121}$$

and

$$u_{\Lambda_c,+1/2} = \sqrt{2M_{\Lambda_c}} \begin{pmatrix} 1 \\ 0 \\ 0 \\ 0 \end{pmatrix}, \qquad u_{\Lambda_c,-1/2} = \sqrt{2M_{\Lambda_c}} \begin{pmatrix} 0 \\ 1 \\ 0 \\ 0 \end{pmatrix},$$

$$u_{\Lambda,+1/2} = \sqrt{E_\Lambda + M_\Lambda} \begin{pmatrix} \cos\frac{\theta_\Lambda}{2}\, e^{\frac{i\phi}{2}} \\ \sin\frac{\theta_\Lambda}{2} \\ \frac{p_\ell}{E_\Lambda+M_\Lambda}\cos\frac{\theta_\Lambda}{2}\, e^{\frac{i\phi}{2}} \\ \frac{p_\ell}{E_\Lambda+M_\Lambda}\sin\frac{\theta_\Lambda}{2} \end{pmatrix}, \quad u_{\Lambda,-1/2} = \sqrt{E_\Lambda + M_\Lambda} \begin{pmatrix} -\sin\frac{\theta_\Lambda}{2} \\ \cos\frac{\theta_\Lambda}{2}\, e^{-\frac{i\phi}{2}} \\ \frac{p_\ell}{E_\Lambda+M_\Lambda}\sin\frac{\theta_\Lambda}{2} \\ -\frac{p_\ell}{E_\Lambda+M_\Lambda}\cos\frac{\theta_\Lambda}{2}\, e^{-\frac{i\phi}{2}} \end{pmatrix}. \tag{3.122}$$

Chapter 4

Flavor Physics in High-p_T collisions at the LHC

4.1 Introduction

Even though low-energy flavor observables provide the most stringent constraints on semileptonic transitions, their sensitivity strongly depends on the (unknown) flavor structure beyond the SM. Scenarios based on Minimal Flavor Violation (MFV) [183], or on the $U(2)^5$ flavor symmetry [132] can be fully compatible with current flavor data for much lower Λ values, in the $\mathcal{O}(1\ \mathrm{TeV})$ range, which is currently being probed at the LHC. With a more agnostic approach to the flavor structure of New Physics, it is also clear that there are specific semileptonic transitions that remain unconstrained or that can only be weakly constrained by low-energy processes. Therefore, it is fundamental to devise strategies to probe semileptonic transitions that are complementary to the low-energy flavor probes in the quest for New Physics.

The measurement of the tails of mono-lepton and di-lepton production at the LHC has been proven to be particularly useful as a complementary probe of flavor physics. EFT contributions to the Drell-Yan partonic cross-sections can be energy enhanced, as long as the EFT approach is valid, being potentially larger than the SM expectation in the tails of the distributions [184]. Moreover, the parton content of the proton includes five different quark flavors that can be used to indirectly probe various semileptonic transitions in high-energy proton collisions. A recent example concerns the discrepancies observed in the $b \to c\tau\nu$ transition, for which $pp \to \tau\tau$ data at high-p_T was used to discard a few New Physics explanations of these anomalies, see e.g. Ref. [185] and following works.

There have been many studies that derive constraints on flavor-physics scenarios by using the processes $pp \to \ell\ell$ [185–191], $pp \to \ell\nu$ [157, 159, 160, 189, 191–194] and $pp \to \ell\ell'$ (with $\ell \neq \ell'$) [195] at the LHC. However, these studies typically consider either specific types of processes or impose a given ansatz to the flavor pattern of the New Physics couplings. The complete combination of the LHC constraints on semileptonic transitions in a single framework was not available thus far. In this work, we aim to amend this gap by combining the most recent LHC data on all possible mono-lepton and di-lepton productions channels, without any assumption about the flavor of the colliding quarks. This combination will be done for the Standard Model Effective Field Theory (SMEFT) [18, 19], with a consistent EFT expansion up to $\mathcal{O}(\Lambda^{-4})$ in the cross-section [196], as well as for models with concrete mediators, which should be used if the experimental regime in a given channel is not sufficient to justify the EFT approach.

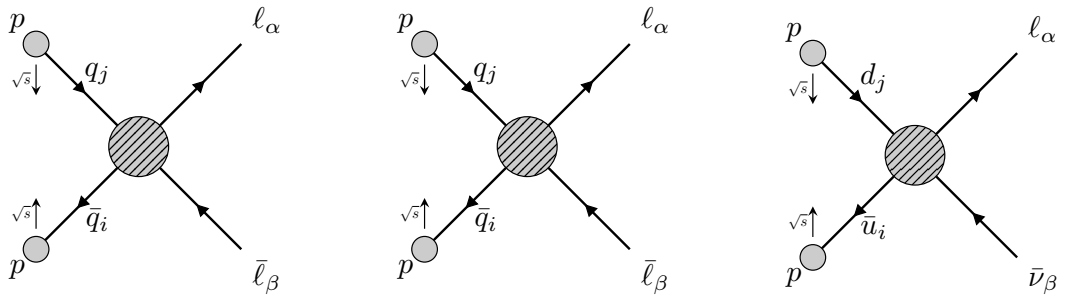

Figure 4.1: *Neutral and charged Drell-Yan production processes at proton-proton colliders.*

As an important by-product of our work, we developed the `Mathematica` package `HighPT` [197] that provides the complete SMEFT likelihood for semileptonic operators at the LHC. This package complements the ongoing effort to provide tools for the SMEFT phenomenology of low-energy flavor observables [198, 199], as well as electroweak and Higgs data [200]. Future releases of `HighPT` will also provide the likelihood for specific models of interest such as leptoquarks [32, 201] based on the framework presented in this work. The comparison of the constraints derived for both EFT and concrete models will allow the users to directly assess the validity of the EFT description for a given high-p_T process.

This chapter is organized as follows. In Sec. 4.2, we provide the most general description of mono-lepton and di-lepton production in hadron colliders. In Sec. 4.3, we apply this description to two specific scenarios, namely to the SMEFT and to simplified models with a tree-level exchange of new bosonic mediators. In Sec. 4.4, we recast the most recent LHC searches in the mono-lepton and di-lepton channels, with all possible lepton flavors in the final state. In Sec. 4.5, discuss important aspects of the validity of EFT in colliders studies. We summarize our findings and discuss the outlook for our study in Sec. 4.6.

4.2 Drell-Yan production at hadron colliders

In this Section, we provide a general description of the processes $pp \to \ell_\alpha^- \ell_\beta^+$ and $pp \to \ell_\alpha^- \bar{\nu}_\beta$, in terms of generic form-factors, where α, β are generic lepton-flavor indices. This description has the advantage of covering both the EFT case, as well as scenarios containing new bosonic mediators that propagate at tree-level, as will be discussed in Sec. 4.3. In Sec. 4.2.1, we write the most general scattering amplitudes consistent with Lorentz invariance and the $SU(3)_c \times U(1)_{\rm em}$ gauge symmetry, and we compute the differential partonic cross-section. In Sec. 4.2.2, we discuss a general tree-level parameterization of the form factors that encapsulates both the EFT and the concrete mediator contributions, which will be considered in the following Sections.

4.2.1 Amplitude decomposition

First, we consider the scattering amplitude for the neutral Drell-Yan process $\bar{q}_i q_j \to \ell_\alpha^- \ell_\beta^+$ given by the first two diagrams in fig. 4.1, with $q_i = \{u_i, d_i\}$, where quark and lepton flavor indices are denoted by Latin letters ($i, j = 1, 2, 3$) and Greek letters ($\alpha, \beta = 1, 2, 3$), respectively[1]. The

[1]For up-type quarks the the indices run as $i, j = 1, 2$ because of the negligible top-quark content of the proton at LHC energies.

most general decomposition of the four-point scattering amplitude that is Lorentz and gauge invariant is given by

$$\begin{aligned}\mathcal{A}(\bar{q}_i q_j \to \ell^-_\alpha \ell^+_\beta) \;=\; \frac{1}{v^2}\sum_{XY}\Big\{ & \left(\bar{\ell}_\alpha \gamma^\mu \mathbb{P}_X \ell_\beta\right)\left(\bar{q}_i \gamma_\mu \mathbb{P}_Y q_j\right)\, [\mathcal{F}_V^{XY,\,qq}(\hat{s},\hat{t})]_{ij}^{\alpha\beta} \\ & + \left(\bar{\ell}_\alpha \mathbb{P}_X \ell_\beta\right)\left(\bar{q}_i \mathbb{P}_Y q_j\right)\, [\mathcal{F}_S^{XY,\,qq}(\hat{s},\hat{t})]_{ij}^{\alpha\beta} \\ & + \left(\bar{\ell}_\alpha \sigma_{\mu\nu} \mathbb{P}_X \ell_\beta\right)\left(\bar{q}_i \sigma^{\mu\nu} \mathbb{P}_X q_j\right)\, [\mathcal{F}_T^{X,\,qq}(\hat{s},\hat{t})]_{ij}^{\alpha\beta} \\ & + \left(\bar{\ell}_\alpha \gamma_\mu \mathbb{P}_X \ell_\beta\right)\left(\bar{q}_i \sigma^{\mu\nu} \mathbb{P}_Y q_j\right)\, \frac{ik_\nu}{v}\, [\mathcal{F}_{D_q}^{XY,\,qq}(\hat{s},\hat{t})]_{ij}^{\alpha\beta} \\ & + \left(\bar{\ell}_\alpha \sigma^{\mu\nu} \mathbb{P}_X \ell_\beta\right)\left(\bar{q}_i \gamma_\mu \mathbb{P}_Y q_j\right)\, \frac{ik_\nu}{v}\, [\mathcal{F}_{D_\ell}^{XY,\,qq}(\hat{s},\hat{t})]_{ij}^{\alpha\beta} \Big\}\,, \end{aligned} \tag{4.1}$$

where $X, Y \in \{L, R\}$ are the chiralities of the anti-lepton and anti-quark fields, $\mathbb{P}_{R,L} = (1 \pm \gamma^5)/2$ are the chirality projectors, $v = (\sqrt{2} G_F)^{-1/2}$ stands for the electroweak vacuum-expectation-value (vev) and fermion masses have been neglected. Here it is understood that q ($\bar{q}$) and ℓ ($\bar{\ell}$) denote the Dirac spinors of the incoming quark (anti-quark) and outgoing anti-lepton (lepton) fields, respectively. The four-momentum of the dilepton system is defined by $k = p_q + p_{\bar{q}}$, and we take the Mandelstam variables to be $\hat{s} = k^2 = (p_q + p_{\bar{q}})^2$, $\hat{t} = (p_q - p_{\ell^-})^2$ and $\hat{u} = (p_q - p_{\ell^+})^2 = -\hat{s} - \hat{t}$ for massless external states. For each of the five components in eq. (4.1) we define the neutral current form-factor $\mathcal{F}_I^{XY,\,qq}(\hat{s},\hat{t})$ where $I \in \{V, S, T, D_\ell, D_q\}$ labels the corresponding *vector*, *scalar*, *tensor*, *lepton-dipole* and *quark-dipole* Lorentz structures, respectively. These form-factors are dimensionless functions of the Mandelstam variables that describe the underlying local and non-local semi-leptonic interactions between fermions with fixed flavors and chiralities. Note, in particular, that the tensor form-factor is non-vanishing only for $X = Y$. [2]

Similarly, the most general scattering amplitude for the charged current Drell-Yan process can be written as

$$\begin{aligned}\mathcal{A}(\bar{u}_i d_j \to \ell^-_\alpha \bar{\nu}_\beta) \;=\; \frac{1}{v^2}\sum_{XY}\Big\{ & \left(\bar{\ell}_\alpha \gamma^\mu \mathbb{P}_X \nu_\beta\right)\left(\bar{u}_i \gamma_\mu \mathbb{P}_Y d_j\right)\, [\mathcal{F}_V^{XY,\,ud}(\hat{s},\hat{t})]_{ij}^{\alpha\beta} \\ & + \left(\bar{\ell}_\alpha \mathbb{P}_X \nu_\beta\right)\left(\bar{u}_i \mathbb{P}_Y d_j\right)\, [\mathcal{F}_S^{XY,\,ud}(\hat{s},\hat{t})]_{ij}^{\alpha\beta} \\ & + \left(\bar{\ell}_\alpha \sigma_{\mu\nu} \mathbb{P}_X \nu_\beta\right)\left(\bar{u}_i \sigma^{\mu\nu} \mathbb{P}_X d_j\right)\, [\mathcal{F}_T^{X,\,ud}(\hat{s},\hat{t})]_{ij}^{\alpha\beta} \\ & + \left(\bar{\ell}_\alpha \gamma_\mu \mathbb{P}_X \nu_\beta\right)\left(\bar{u}_i \sigma^{\mu\nu} \mathbb{P}_Y d_j\right)\, \frac{ik_\nu}{v}\, [\mathcal{F}_{D_q}^{XY,\,ud}(\hat{s},\hat{t})]_{ij}^{\alpha\beta} \\ & + \left(\bar{\ell}_\alpha \sigma^{\mu\nu} \mathbb{P}_X \nu_\beta\right)\left(\bar{u}_i \gamma_\mu \mathbb{P}_Y d_j\right)\, \frac{ik_\nu}{v}\, [\mathcal{F}_{D_\ell}^{XY,\,ud}(\hat{s},\hat{t})]_{ij}^{\alpha\beta} \Big\}\,, \end{aligned} \tag{4.2}$$

where the dilepton four-momenta is defined in a similar way by $k = p_d + p_{\bar{u}}$, and where we take the Mandelstam variables to be $\hat{s} = k^2 = (p_d + p_{\bar{u}})^2$, $\hat{t} = (p_d - p_{\ell^-})^2$ and $\hat{u} = (p_d - p_\nu)^2$. The charged current form-factors are denoted by $\mathcal{F}_I^{XY,\,ud}(\hat{s},\hat{t})$, with the same possible Lorentz structures as in the previous case[3]. The above equation is also valid for $X = R$ in the presence of a light right-handed neutrino field ν_R that is a singlet under the SM gauge group. The amplitudes in Eqs. (4.1, 4.2) are written in the mass basis. Similar expressions in the weak interaction basis can be recovered by rotating the quark fields accordingly, as described in appendix B.

[2] This can be shown e.g. by using the identity $\sigma^{\mu\nu}\gamma_5 = i\varepsilon^{\mu\nu\alpha\beta}\sigma_{\alpha\beta}/2$.

[3] Note that the charge-conjugate process can be described by a similar expression to eq. (4.2). The relations between the $\bar{d}_j u_i \to \ell^+_\alpha \nu_\beta$ and the $d_j \bar{u}_i \to \ell^-_\alpha \bar{\nu}_\beta$ form-factors are spelled out in appendix 2.1.2.

Related processes

We briefly comment on two other semi-leptonic processes at hadron colliders that are closely related to Drell-Yan production. The first of these are the *quark-lepton fusion* processes $q_i l_\alpha^\mp \to q_j \ell_\beta^\mp$ and $d_i l_\alpha^\mp \to u_j \bar{\nu}_\beta$. These probe the same semi-leptonic transitions entering Drell-Yan production. In this case, the initial lepton is taken as a partonic constituent of the proton with a PDF that is suppressed by $\alpha_{\rm em}$ [202]. By using crossing symmetry, it is straightforward to express the amplitudes in terms of the Drell-Yan form factors described above,

$$\mathcal{A}(u_j \ell_\alpha^+ \to u_i \ell_\beta^+) \;=\; \mathcal{A}(\bar{u}_i u_j \to \ell_\alpha^- \ell_\beta^+)|_{\,s\to -t,\, t\to -s}\,, \tag{4.3}$$

$$\mathcal{A}(d_j \ell_\alpha^+ \to d_i \ell_\beta^+) \;=\; \mathcal{A}(\bar{d}_i d_j \to \ell_\alpha^- \ell_\beta^+)|_{\,s\to -t,\, t\to -s}\,, \tag{4.4}$$

$$\mathcal{A}(d_j \ell_\alpha^+ \to u_i \bar{\nu}_\beta) \;=\; \mathcal{A}(\bar{u}_i d_j \to \ell_\alpha^- \bar{\nu}_\beta)|_{\,s\to -t,\, t\to -s}\,. \tag{4.5}$$

Another relevant probe for semi-leptonic transitions, also related to Drell-Yan production, are the *quark-gluon fusion* processes $q_j g \to q_i \ell_\alpha^- \ell_\beta^+$ and $q_j g \to q_i \ell_\alpha^\mp \bar{\nu}_\beta$. Since these are $2 \to 3$ scatterings they will suffer from an additional phase-space suppression when compared to the $2 \to 2$ Drell-Yan process. Given that both the quark-lepton and quark-gluon fusions are generically less powerful New Physics probes [4], in the following, we will focus exclusively on the Drell-Yan production modes as they are currently the most relevant ones for phenomenology.

4.2.2 Form-factor parametrization

In this section, we discuss a general parametrization of the Drell-Yan form-factors that is useful for describing tree-level contributions from generic New Physics. For this purpose, we perform an analytic continuation of the scattering amplitudes to the complex $\hat{s}$ and $\hat{t}$ Mandelstam variables. Furthermore, we assume that the form-factors are analytic functions within some radius $|\hat{s}|, |\hat{t}| < \Lambda^2$ except for a finite set of simple poles in the $\hat{s}$, $\hat{t}$ and $\hat{u}$ complex planes. This assumption captures all possible tree-level physics entering high-p_T Drell-Yan production at collider energies below the scale Λ.[5] We decompose each form-factor into a "regular" term and a "pole" term,

$$\mathcal{F}_I(\hat{s},\hat{t}) \;=\; \mathcal{F}_{I,\,\rm Reg}(\hat{s},\hat{t}) \;+\; \mathcal{F}_{I,\,\rm Poles}(\hat{s},\hat{t})\,, \tag{4.6}$$

each encoding underlying local and non-local semi-leptonic interactions, respectively. To simplify the notation we drop the XY and qq' superscripts wherever the equations hold true for any form-factor, and only keep the dependence on $I \in \{V, S, T, D_\ell, D_q\}$.

The regular term $\mathcal{F}_{I,\,\rm Reg}$ is an analytic function that describes local interactions, e.g. four-point contact interactions, that arise from heavy unresolved degrees of freedom living at the scale Λ beyond the characteristic energy of the scattering process. Within the radius Λ^2, this function admits a power series expansion of the form

$$\mathcal{F}_{I,\,\rm Reg}(\hat{s},\hat{t}) \;=\; \sum_{n,m=0}^{\infty} \mathcal{F}_{I\,(n,m)} \left(\frac{\hat{s}}{v^2}\right)^n \left(\frac{\hat{t}}{v^2}\right)^m \tag{4.7}$$

[4] A notable exception is the quark-gluon fusion processes $gb \to b\ell\ell$ and $gc \to b\ell\nu$. The enhancement of the gluon over the bottom PDF and the background reduction from the additional b-tagged jet makes this process an important probe for New Physics entering third-generation semi-leptonic transitions. See [159] for more details.

[5] This assumption leaves out scenarios with loop-level contributions from light degrees of freedom where e.g. branch cuts can appear.

where $\mathcal{F}_{I\,(n,m)}$ are dimensionless expansion coefficients. The series in eq. (4.7) is not to be confused with the complete EFT expansion in $1/\Lambda$, since each coefficient $\mathcal{F}_{I\,(n,m)}$ can receive contributions from an infinite tower of non-renormalizable operators, as will be discussed for the SMEFT in Sec. 4.3. This expression, however, provides a convenient separation of contributions with different dependencies on $\hat{s}$ and $\hat{t}$ and, in particular, those that become dominant in the tails of the Drell-Yan distributions.

The pole term $\mathcal{F}_{I,\,\text{Poles}}$ is a non-analytic function with simple poles describing non-local tree-level interactions. We adopt the following parametrization,

$$\mathcal{F}_{I,\,\text{Poles}}(\hat{s},\hat{t}) \;=\; \sum_a \frac{v^2\,\mathcal{S}_{I\,(a)}}{\hat{s}-\Omega_a} \;+\; \sum_b \frac{v^2\,\mathcal{T}_{I\,(b)}}{\hat{t}-\Omega_b} \;-\; \sum_c \frac{v^2\,\mathcal{U}_{I\,(c)}}{\hat{s}+\hat{t}+\Omega_c}\,, \tag{4.8}$$

where the poles $\Omega_k = m_k^2 - i m_k \Gamma_k$ belong to each of the corresponding complex Mandelstam planes, with the last term representing the poles in the u-channel. The pole residues $\mathcal{S}_{I\,(a)}$, $\mathcal{T}_{I\,(b)}$ and $\mathcal{U}_{I\,(c)}$ in the numerators are taken to be dimensionless parameters. Each term in eq. (4.8) describes the tree-level exchange of degrees of freedom in the s-channel, t-channel and u-channel, respectively, i.e. these are the propagators for various bosons a, b, c with masses $m_{a,b,c}$ and widths $\Gamma_{a,b,c}$ that can be resolved at the energy scales involved in the scattering.

In principle, the simple pole assumption for the form-factor singularities allows for the numerators in eq. (4.8) to be general analytic functions of the form $\mathcal{S}_{I\,(a)}(\hat{s})$, $\mathcal{T}_{I\,(b)}(\hat{t})$ and $\mathcal{U}_{I\,(c)}(\hat{u})$, where each describes generic three-point local interactions. However, the dependence of these residues on the Mandelstam variables can be completely removed from each pole by applying the identity,

$$\frac{\mathcal{Z}_I(\hat{z})}{\hat{z}-\Omega} \;=\; \frac{\mathcal{Z}_I(\Omega)}{\hat{z}-\Omega} \;+\; f(\hat{z},\Omega)\,, \tag{4.9}$$

where $f(\hat{z},\Omega)$ is an analytic function of $\hat{z} = \{\hat{s},\hat{t},\hat{u}\}$ that can be reabsorbed into the regular form-factor by a redefinition of $\mathcal{F}_{I,\,\text{Reg}}$. The identity in eq. (4.9) can be shown by power expanding the numerator $\mathcal{Z}_I(\hat{z})$ and decomposing in partial fractions each of the resulting terms as

$$\frac{\hat{z}^n}{\hat{z}-\Omega} \;=\; \frac{\Omega^n}{\hat{z}-\Omega} \;+\; \Omega^{n-1} \sum_{k=0}^{n-1} \left(\frac{\hat{z}}{\Omega}\right)^k\,, \tag{4.10}$$

or in diagrammatic form:

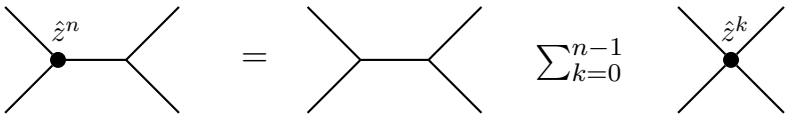

Therefore, from now on the residues $\mathcal{S}_{I\,(a)}$, $\mathcal{T}_{I\,(b)}$ and $\mathcal{U}_{I\,(c)}$ in (4.8) are taken to be independent of $\hat{s}$, $\hat{t}$ and $\hat{u}$. When discussing the SMEFT, we will see that decomposing into partial fractions turns out to be useful for disentangling the effects from different operator classes within different dimensions d.

In the SM, the gauge bosons contribute to the Drell-Yan amplitudes in Eqs. (4.1) and (4.2) through the s-channel poles of the vector form-factors. It is therefore convenient to separate the effects of the SM from potential BSM effects by defining the s-channel vector residues in (4.8) as

$$\mathcal{S}_{V\,(a)} \;=\; \mathcal{S}_{(a,\,\text{SM})} \;+\; \delta\mathcal{S}_{(a)}\,, \tag{4.11}$$

with $a \in \{\gamma, W, Z\}$, and where the $\delta\mathcal{S}_{(a)}$ parametrize potential modifications of the SM gauge couplings to fermions. The SM pole residues at leading order read

$$\mathcal{S}^{XY,\,qq}_{(\gamma,\,\mathrm{SM})} = 4\pi\alpha_{\mathrm{em}}\, Q_\ell\, Q_q\, \mathbb{1}_\ell \mathbb{1}_q\,, \tag{4.12}$$

$$\mathcal{S}^{XY,\,qq}_{(Z,\,\mathrm{SM})} = \frac{4\pi\alpha_{\mathrm{em}}}{c_W^2 s_W^2}\, g_\ell^X g_q^Y\,, \tag{4.13}$$

$$\mathcal{S}^{LL,\,ud}_{(W,\,\mathrm{SM})} = \frac{1}{2} g_2^2\, \mathbb{1}_\ell V\,, \tag{4.14}$$

where $g_\psi^X \equiv (T^3_{\psi_X} - s_W^2 Q_\psi)\,\mathbb{1}_\psi$ denote the Z-boson couplings to a fermion ψ, with electric charge Q_ψ and weak isospin $T^3_{\psi_X}$, and $c_W \equiv \cos\theta_W$ and $s_W = \sin\theta_W$, where θ_W denotes the Weinberg angle. V stands for the 3×3 CKM matrix, and $\mathbb{1}_{\ell(q)}$ correspond to the 3×3 unit matrices in lepton (quark) flavor-space with components $\delta_{\alpha\beta}$ (δ_{ij}). See appendix 2.1.2 for our conventions. The New Physics contributions to the form-factors $\mathcal{S}_{(a)}$, $\mathcal{T}_{(a)}$ and $\mathcal{U}_{(a)}$ will be discussed in Sec. 4.3.

4.2.3 Cross-sections

The general amplitudes given in eq. (4.1) and (4.2) can be used to compute the neutral- and charged-current cross-sections. After integrating over the azimuthal angle, the differential partonic cross-section for the Drell-Yan process is given by

$$\frac{\mathrm{d}\hat{\sigma}}{\mathrm{d}\hat{\mathrm{t}}}(\bar{q}_i q'_j \to \ell_\alpha \overline{\ell'}_\beta) = \frac{1}{48\pi\, v^4} \sum_{XY} \sum_{IJ} M_{IJ}^{XY}(\hat{s},\hat{t}) \left[\mathcal{F}_I^{XY,\,qq'}(\hat{s},\hat{t})\right]^{\alpha\beta}_{ij} \left[\mathcal{F}_J^{XY,\,qq'}(\hat{s},\hat{t})\right]^{\alpha\beta\,*}_{ij}, \tag{4.15}$$

where neutral and charged currents are described by the same expression, where $q^{(\prime)} \in \{u, d\}$ can be either a down- or up-type quark, and $\ell' \in \{\ell, \nu\}$ denotes both neutral and charged leptons, depending on the specific process. The indices $I, J \in \{V, S, T, D_\ell, D_q\}$ account for the different contributions and M^{XY} are 5×5 symmetric matrices that take the form

$$M^{XY}(\hat{s},\hat{t}) = \begin{pmatrix} M_{VV}^{XY}(\hat{t}/\hat{s}) & 0 & 0 & 0 & 0 \\ 0 & M_{SS}^{XY}(\hat{t}/\hat{s}) & M_{ST}^{XY}(\hat{t}/\hat{s}) & 0 & 0 \\ 0 & M_{ST}^{XY}(\hat{t}/\hat{s}) & M_{TT}^{XY}(\hat{t}/\hat{s}) & 0 & 0 \\ 0 & 0 & 0 & \frac{\hat{s}}{v^2} M_{DD}^{XY}(\hat{t}/\hat{s}) & 0 \\ 0 & 0 & 0 & 0 & \frac{\hat{s}}{v^2} M_{DD}^{XY}(\hat{t}/\hat{s}) \end{pmatrix} \tag{4.16}$$

where the different M_{IJ}^{XY} entries are polynomials in the angular variable $\omega \equiv \hat{t}/\hat{s}$ defined by

$$M_{VV}^{XY}(\omega) = (1+2\omega)\delta^{XY} + \omega^2\,, \tag{4.17}$$

$$M_{SS}^{XY}(\omega) = 1/4\,, \tag{4.18}$$

$$M_{TT}^{XY}(\omega) = 4(1+2\omega)^2\delta^{XY}\,, \tag{4.19}$$

$$M_{ST}^{XY}(\omega) = -(1+2\omega)\delta^{XY}\,, \tag{4.20}$$

$$M_{DD}^{XY}(\omega) = -\omega(1+\omega)\,. \tag{4.21}$$

The quantity $\omega = -(1-\cos\theta_\ell)/2$ is a function of the emission angle θ_ℓ of the lepton ℓ^- with respect to the incoming quark in the center-of-mass frame. At the differential level, there is an interference term only between the scalar and tensor structures that vanishes for the full cross-section after integration over $\hat{t} \in (-\hat{s}, 0)$.

Hadronic cross-sections

The hadronic cross-section σ at a proton-proton collider can be written, following the conventions of Ref. [203], as the convolution of the partonic cross-section $\hat{\sigma}(\bar{q}_i q_j \to \ell_\alpha \bar{\ell}'_\beta)$ with the parton distribution functions (PDFs) $f_{\bar{q}_i}(x, \mu_F)$ and $f_{q_j}(x, \mu_F)$, summed over all possible incoming quark flavor combinations,

$$\sigma(pp \to \ell_\alpha \bar{\ell}'_\beta) = \sum_{ij} \int_0^1 \mathrm{d}x_1 \, \mathrm{d}x_2 \left[f_{\bar{q}_i}(x_1, \mu) f_{q_j}(x_2, \mu) \, \hat{\sigma}(\bar{q}_i q_j \to \ell_\alpha \bar{\ell}'_\beta) + (\bar{q}_i \leftrightarrow q_j) \right] , \tag{4.22}$$

where $x_{1,2}$ are the fractions of momenta that the scattering quarks carry relative to the momenta of the corresponding protons. We set the factorization and renormalization scales equal to the scale of the hard scattering $\mu = \sqrt{\hat{s}}$. The hadronic cross-section can be more conveniently expressed as

$$\sigma\left(pp \to \ell_\alpha \bar{\ell}'_\beta\right) = \sum_{ij} \int \frac{\mathrm{d}\hat{s}}{s} \, \mathcal{L}_{ij}\left(\hat{s}\right) \hat{\sigma}(\bar{q}_i q_j \to \ell_\alpha \bar{\ell}'_\beta) \, , \tag{4.23}$$

where $\sqrt{s} = 13$ TeV is the proton-proton center-of-mass energy for the LHC searches considered in this paper, and where $\mathcal{L}_{ij}(\hat{s})$ are the dimensionless parton-parton luminosity functions [203, 204] defined as

$$\mathcal{L}_{ij}(\hat{s}) \equiv \int_{\frac{\hat{s}}{s}}^1 \frac{\mathrm{d}x}{x} \left[f_{\bar{q}_i}\left(x, \mu\right) f_{q_j}\left(\frac{\hat{s}}{sx}, \mu\right) + (\bar{q}_i \leftrightarrow q_j) \right] . \tag{4.24}$$

In Sec. 4.4, we will confront the predictions for Drell-Yan production from different New Physics models with the LHC run-II measurements of the high-p_T tails of various momentum-dependent distributions. For the neutral Drell-Yan process, we compute in terms of the form-factors introduced in Eqs. (4.1), the particle-level distribution of the invariant mass $m_{\ell\ell}$ of the dilepton system. Combining the previous results we find the expression for the hadronic cross-sections restricted to a specific invariant mass bin $B \equiv [m_{\ell\ell_0}, m_{\ell\ell_1}]$ to be given by

$$\sigma_B(pp \to \ell^-_\alpha \ell^+_\beta) = \frac{1}{48\pi v^2} \sum_{XY,\, IJ} \sum_{ij} \int_{m^2_{\ell\ell_0}}^{m^2_{\ell\ell_1}} \frac{\mathrm{d}\hat{s}}{s} \int_{-\hat{s}}^0 \frac{\mathrm{d}\hat{t}}{v^2} \, M^{XY}_{IJ} \, \mathcal{L}_{ij} \left[\mathcal{F}^{XY,qq}_I\right]^{\alpha\beta}_{ij} \left[\mathcal{F}^{XY,qq}_J\right]^{\alpha\beta\,*}_{ij} , \tag{4.25}$$

where summing over up and down-type quarks $q \in \{u, d\}$ is implied and where we have integrated over the full azimuthal angle. Similarly, for the charged Drell-Yan process we compute the particle-level distribution of the transverse momentum of the charged lepton $p_T(\ell^\pm)$. In this case the cross-section $\sigma_B(pp \to \ell^\pm_\alpha \nu_\beta)$ restricted to a specific high-p_T bin $B \equiv [p_{T_0}, p_{T_1}]$ takes the same form as in eq. (4.25) but with the integration boundaries changed to[6]

$$\int_{m^2_{\ell\ell_0}}^{m^2_{\ell\ell_1}} \mathrm{d}\hat{s} \;\longrightarrow\; \int_{4p^2_{T_0}}^{s} \mathrm{d}\hat{s} \quad \text{and} \quad \int_{-\hat{s}}^0 \mathrm{d}\hat{t} \;\longrightarrow\; \left(\int_{\hat{t}^+_0}^{\hat{t}^+_1} \mathrm{d}\hat{t} \, + \int_{\hat{t}^-_1}^{\hat{t}^-_0} \mathrm{d}\hat{t} \right) , \tag{4.26}$$

where

$$\hat{t}^\pm_i(\hat{s}) = -\frac{\hat{s}}{2} \left(1 \pm \sqrt{1 - \min\left\{1, \frac{4p^2_{T_i}}{\hat{s}}\right\}} \right) . \tag{4.27}$$

[6] Notice that for $\hat{s} < 4p^2_{T_1}$ we find $\hat{t}^-_2 = \hat{t}^+_2$, whereas for $\hat{s} < 4p^2_{T_0}$ the cross-section vanishes. Taking the limit $p_{T_0} \to 0$ and $p_{T_1} \to \infty$ yields again the integration boundaries for the full angular integration.

For the sake of presentation, we have not explicitly expanded the squared form-factors in Eqs. (4.15) and (4.25) in terms of the various regular and pole form-factors defined in (4.7) and (4.8). Complete expressions for the hadronic cross-sections in terms of these parameters can be easily extracted for any bin using the Mathematica package `HighPT`.

4.2.4 High-p_T Tails

The high-energy regime of the dilepton invariant-mass or the monolepton transverse-mass are known to be very sensitive probes for a variety of New Physics models affecting semi-leptonic transitions [159, 160, 185, 195]. In the SM, the partonic cross-section scales as $\sim 1/E^2$ at high-energies, leading to a smoothly falling tail for the kinematic distributions of any momentum-dependent observable. The presence of new particles coupling to quarks and leptons or new semi-leptonic interactions beyond the SM can modify the shapes of these tails substantially.

The most obvious BSM effect is the appearance of a resonant feature on top of the smoothly falling SM background, i.e. a peak in the dilepton invariant mass spectrum, or an edge in the monolepton transverse mass spectrum. This indicates that a heavy colorless particle has been produced on-shell in the s-channel. Non-resonant effects from contact interactions or on-shell leptoquarks exchanged in the t/u-channels, on the other hand, lead to more subtle non-localized features in the tails. Indeed, energy-enhanced interactions coming from non-renormalizable operators will modify the energy scaling of the distributions leading to an apparent violation of unitarity in the tails. The effects from leptoquarks exchanged in the t/u-channels will lead to a similar behavior [187, 205]. After convoluting with the quark PDFs, the non-resonant features are more difficult to uncover than a resonance peak, but can still be used to set competitive limits on many relevant NP scenarios entering semi-leptonic transitions.

Finally, we remark that for the quark-lepton fusion process $q_i \ell_\alpha^+ \to q_j \bar{\ell}'_\beta$, leptoquarks are exchanged in the s-channel, leading to a resonance peak in the jet-lepton invariant mass distribution [206–209], while the colorless mediators, now exchanged in the t/u-channels, will produce non-resonant effects in the tails of the distribution. The lepton PDFs have been recently computed in Ref. [207] and could be used to give a robust estimation of event yields.

4.3 Semi-leptonic transitions beyond the SM

Form-factors in the SMEFT

In the SMEFT the Drell-Yan amplitude can be written as a double perturbative expansion in the small parameters $\hat{s}/\Lambda^2$ and v^2/Λ^2. This EFT expansion can be matched to eq. (4.7) in order to determine the regular form-factor coefficients $\mathcal{F}_{I\,(n,m)}$. These are given by an infinite perturbative series in the parameter v^2/Λ^2 of the form

$$\mathcal{F}_{I\,(n,m)} = \sum_{d \geq 2(n+m+3)}^{\infty} c_I^{(d)} \left(\frac{v}{\Lambda}\right)^{d-4} . \tag{4.28}$$

For example, the dimension-6 operators only maps to the leading coefficient $\mathcal{F}_{I\,(0,0)}$, whereas dimension-8 operators map to $\mathcal{F}_{I\,(0,0)}$ as well as the next-to-leading coefficients $\mathcal{F}_{I\,(1,0)}$ and $\mathcal{F}_{I\,(0,1)}$, and so on.

In order to write down the Drell-Yan form factors in terms of the SMEFT Wilson coefficients, it is convenient to recast the general parametrization given in sec. 4.2.2 to a simpler truncated

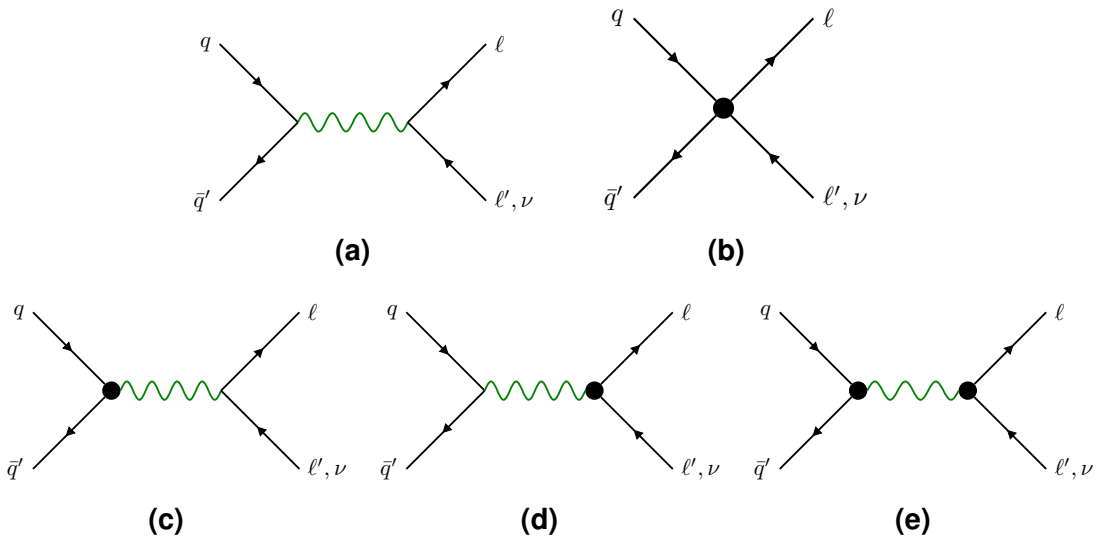

Figure 4.2: *Representation of the leading contributions in the SM (a) and in the SMEFT (b)-(e) to the partonic processes $q\bar{q}' \to \ell\ell'$ and $u\bar{d}' \to \ell\nu$ with an EFT expansion up to $\mathcal{O}(\Lambda^{-4})$. The green mediator represents the exchange of the SM gauge bosons $V \in \{\gamma, Z, W\}$ and the black dots are insertions of the SMEFT effective interaction.*

form more suitable for the SMEFT to order $d \leq 8$. First, it is sufficient truncate the power expansion of the regular form-factors $\mathcal{F}_{I,\,\mathrm{Ref}}$ in eq. (4.7) to order $n, m \leq 1$. The regular pieces of the scalar and tensor form-factors can be further truncated to order $n = m = 0$ because when squaring the amplitude, the terms with $n+m = 1$ generated at dimension-8 do not interfere with the SM poles and will only lead to higher-order effects in the cross-section beyond $\mathcal{O}(1/\Lambda^4)$. In the SMEFT, the dipole interactions only arise from non-local interactions involving the SM gauge bosons, so we can set the regular terms $\mathcal{F}_{D_\ell,\,\mathrm{Reg}}$ and $\mathcal{F}_{D_q,\,\mathrm{Reg}}$ to zero. For the singular form-factors $\mathcal{F}_{I,\,\mathrm{Poles}}$, we only need to consider the vector poles and dipoles arising from the s-channel exchange of the SM gauge bosons. The s-channel scalar pole $\mathcal{F}_{S,\,\mathrm{Poles}}$ generated from the exchange of the SM Higgs boson is completely negligible because of the small fermion Yukawa couplings of the external states. When putting all this together we end up with the following form-factor parametrization for the SMEFT:

$$\mathcal{F}_S = \mathcal{F}_{S\,(0,0)}\,, \tag{4.29}$$

$$\mathcal{F}_T = \mathcal{F}_{T\,(0,0)}\,, \tag{4.30}$$

$$\mathcal{F}_V = \mathcal{F}_{V\,(0,0)} + \mathcal{F}_{V\,(1,0)}\,\frac{\hat{s}}{v^2} + \mathcal{F}_{V\,(0,1)}\,\frac{\hat{t}}{v^2} + \sum_a \frac{v^2\left[\mathcal{S}_{(a,\,\mathrm{SM})} + \delta\mathcal{S}_{(a)}\right]}{\hat{s} - m_a^2 + i m_a \Gamma_a}\,, \tag{4.31}$$

$$\mathcal{F}_{D_\ell} = \sum_a \frac{v^2\,\mathcal{S}_{D_\ell\,(a)}}{\hat{s} - m_a^2 + i m_a \Gamma_a}\,, \tag{4.32}$$

$$\mathcal{F}_{D_q} = \sum_a \frac{v^2\,\mathcal{S}_{D_q\,(a)}}{\hat{s} - m_a^2 + i m_a \Gamma_a}\,, \tag{4.33}$$

where $a \in \{\gamma, Z\}$ when describing neutral Drell-Yan processes $\bar{q}_i q_j \to \ell_\alpha^- \ell_\beta^+$, and $a \in \{W^\pm\}$ when describing the charged Drell-Yan processes $\bar{d}_i u_j \to \ell_\alpha^- \bar{\nu}_\beta$ ($\bar{u}_i d_j \to \ell_\alpha^+ \nu_\beta$), and $\mathcal{S}_{(a,\mathrm{SM})}$ are defined in eq. (4.12)-(4.14). This parametrization is enough to capture all possible effects to order $\mathcal{O}(1/\Lambda^4)$ in semileptonic transitions.

Given that the scalar and tensor form-factors are independent of $\hat{s}$ and $\hat{t}$, the coefficients $\mathcal{F}_{S\,(0,0)}$ and $\mathcal{F}_{T\,(0,0)}$ will directly map to the Wilson coefficients of the dimension-6 scalar and tensor operators in class $\boldsymbol{\psi^4}$, respectively, as shown in appendix C.1. On the other hand, for the vector form-factor, the dimension-8 operators will give rise to effects of order $\mathcal{O}(1/\Lambda^4)$ in the squared amplitude via interference with the SM s-channel contributions. The leading coefficient $\mathcal{F}_{V\,(0,0)}$ receives contributions from contact operators in the classes $\boldsymbol{\psi^4}$ and $\boldsymbol{\psi^4 H^2}$ at dimension-6 and dimension-8, respectively, as well as from modified interactions between fermions and the SM gauge bosons generated by the dimension-8 operators in class $\boldsymbol{\psi^2 H^2 D^3}$. The higher-order coefficients $\mathcal{F}_{V\,(1,0)}$ and $\mathcal{F}_{V\,(0,1)}$ receive contributions from the dimension-8 operators in class $\boldsymbol{\psi^4 D^2}$. The SM coefficients $\delta\mathcal{S}_{(a)}$ receive contributions from modified fermion interaction generated by dimension-6 operators in class $\boldsymbol{\psi^2 H^2 D}$ and dimension-8 operators in class $\boldsymbol{\psi^2 H^2 D^3}$. Schematically, the matching between SMEFT Wilson coefficients and the form factors take the following form:

$$\mathcal{F}_{V\,(0,0)} = \frac{v^2}{\Lambda^2}\mathcal{C}^{(6)}_{\psi^4} + \frac{v^4}{\Lambda^4}\mathcal{C}^{(8)}_{\psi^4 H^2} + \frac{v^2 m_a^2}{\Lambda^4}\mathcal{C}^{(8)}_{\psi^2 H^2 D^3} + \cdots, \tag{4.34}$$

$$\mathcal{F}_{V\,(1,0)} = \frac{v^4}{\Lambda^4}\mathcal{C}^{(8)}_{\psi^4 D^2} + \cdots, \tag{4.35}$$

$$\mathcal{F}_{V\,(0,1)} = \frac{v^4}{\Lambda^4}\mathcal{C}^{(8)}_{\psi^4 D^2} + \cdots, \tag{4.36}$$

$$\delta\mathcal{S}_{(a)} = \frac{m_a^2}{\Lambda^2}\mathcal{C}^{(6)}_{\psi^2 H^2 D} + \frac{v^2 m_a^2}{\Lambda^4}\left(\left[\mathcal{C}^{(6)}_{\psi^2 H^2 D}\right]^2 + \mathcal{C}^{(8)}_{\psi^2 H^4 D}\right) + \frac{m_a^4}{\Lambda^4}\mathcal{C}^{(8)}_{\psi^2 H^2 D^3} + \cdots, \tag{4.37}$$

where the squared term $[\mathcal{C}^{(6)}_{\psi^2 H^2 D}]^2$ in eq. (4.37) corresponds to double vertex insertions of the corresponding dimension-6 operators, as depicted in diagram (e) of Fig. 4.2. The ellipses $\cdots$ indicate contributions from the neglected dimension-10 operators. The precise matching of the SMEFT to the vector form-factors can be found in appendix C.2. Notice that the operators in class $\boldsymbol{\psi^2 H^2 D^3}$ contribute to both $\mathcal{F}_{V\,(0,0)}$ and $\delta\mathcal{S}_{(a)}$. This can be understood by analyzing one of the operator in this class, say $\mathcal{O}^{(1)}_{q^2 H^2 D^3} = (\bar{q}_i\gamma^\mu D^\nu q_j) D_{(\mu} D_{\nu)} H^\dagger H$. After spontaneous symmetry breaking, this operator gives rise to a modified coupling between the Z boson and quarks that is proportional to $(\hat{s}\, m_Z v/\Lambda^4)\, Z_\mu(\bar{q}_i\gamma^\mu q_j)$. This interaction contributes to neutral Drell-Yan production with an amplitude that scales as $\mathcal{A}(\bar{q}_i q_j \to \ell^-_\alpha \ell^+_\beta) \propto \hat{s}/(\hat{s} - m_Z^2)$. This amplitude can be brought to the form eq. (4.31) by using the partial fraction decomposition in eq. (4.10), which in diagrammatic form reads:

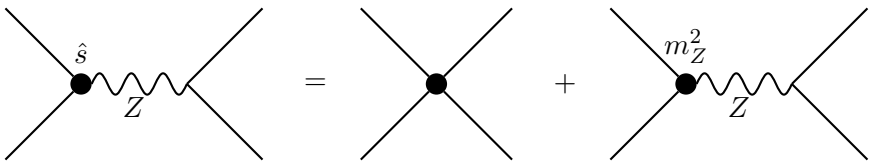

The first contact diagram appearing above on the right-hand side of the equality corresponds to the last term in (4.34), while the second diagram corresponds to the last term in (4.37). Finally, the dipole residues $\mathcal{S}_{D\,(a)}$ match trivially to the $d = 6$ SMEFT dipole operators in class $\boldsymbol{\psi^2 X H}$, as shown in appendix C.3.

4.3.1 Concrete UV Mediators

In this section, we discuss the effects of new heavy bosonic states mediating Drell-Yan processes at tree level. These states can be classified in terms of their SM quantum numbers

	SM rep.	Spin	$\mathcal{L}_{\rm int}$
Z'	$(\mathbf{1},\mathbf{1},0)$	1	$\mathcal{L}_{Z'} = \sum_\psi [g_1^\psi]^{ab}\, \bar\psi_a \not{Z}' \psi_b \ , \ \ \psi \in \{u,d,e,q,l\}$
W'	$(\mathbf{1},\mathbf{3},0)$	1	$\mathcal{L}_{W'} = [g_3^q]^{ij}\, \bar q_i \not{W}' q_j + [g_3^l]^{\alpha\beta}\, \bar l_\alpha \not{W}' l_\beta$
$\widetilde{Z}$	$(\mathbf{1},\mathbf{1},1)$	1	$\mathcal{L}_{\widetilde{Z}} = [\widetilde{g}_1^q]^{ij}\, \bar u_i \not{\widetilde{Z}} d_j + [\widetilde{g}_1^\ell]^{\alpha\beta}\, \bar e_\alpha \not{\widetilde{Z}} N_\beta$
$\Phi_{1,2}$	$(\mathbf{1},\mathbf{2},1/2)$	0	$\mathcal{L}_{\rm 2HDM-I} = [\lambda_I^u]^{ij} \bar q_i u_j \Phi_2^c + [\lambda_I^d]^{ij} \bar q_i d_j \Phi_2 + [\lambda_I^e]^{\alpha\beta} \bar l_\alpha e_\beta \Phi_2 + \text{h.c.}$
			$\mathcal{L}_{\rm 2HDM-II} = [\lambda_{II}^u]^{ij} \bar q_i u_j \Phi_2^c + [\lambda_{II}^d]^{ij} \bar q_i d_j \Phi_1 + [\lambda_{II}^e]^{\alpha\beta} \bar l_\alpha e_\beta \Phi_1 + \text{h.c.}$
			$\mathcal{L}_{\rm 2HDM-X} = [\lambda_X^u]^{ij} \bar q_i u_j \Phi_2^c + [\lambda_X^d]^{ij} \bar q_i d_j \Phi_2 + [\lambda_X^e]^{\alpha\beta} \bar l_\alpha e_\beta \Phi_1 + \text{h.c.}$
			$\mathcal{L}_{\rm 2HDM-Y} = [\lambda_Y^u]^{ij} \bar q_i u_j \Phi_2^c + [\lambda_Y^d]^{ij} \bar q_i d_j \Phi_1 + [\lambda_Y^e]^{\alpha\beta} \bar l_\alpha e_\beta \Phi_2 + \text{h.c.}$
S_1	$(\bar{\mathbf{3}},\, \mathbf{1},\, 1/3)$	0	$\mathcal{L}_{S_1} = [y_1^L]^{i\alpha}\, S_1 \bar q_i^c \epsilon l_\alpha + [y_1^R]^{i\alpha}\, S_1 \bar u_i^c e_\alpha + \ [\bar y_1^R]^{i\alpha}\, S_1 \bar d_i^c N_\alpha + \text{h.c.}$
$\widetilde{S}_1$	$(\bar{\mathbf{3}},\, \mathbf{1},\, 4/3)$	0	$\mathcal{L}_{\widetilde{S}_1} = [\widetilde{y}_1^R]^{i\alpha}\, \widetilde{S}_1 \bar d_i^c e_\alpha + \text{h.c.}$
U_1	$(\mathbf{3},\, \mathbf{1},\, 2/3)$	1	$\mathcal{L}_{U_1} = [x_1^L]^{i\alpha}\, \bar q_i \not{U}_1 l_\alpha + [x_1^R]^{i\alpha}\, \bar d_i \not{U}_1 e_\alpha + [\bar x_1^R]^{i\alpha}\, \bar u_i \not{U}_1 N_\alpha + \text{h.c.}$
$\widetilde{U}_1$	$(\mathbf{3},\mathbf{1},5/3)$	1	$\mathcal{L}_{\widetilde{U}_1} = [\widetilde{x}_1^R]^{i\alpha}\, \bar u_i \not{\widetilde{U}}_1 e_\alpha + \text{h.c.}$
R_2	$(\mathbf{3},\mathbf{2},7/6)$	0	$\mathcal{L}_{R_2} = -[y_2^L]^{i\alpha}\, \bar u_i R_2 \epsilon l_\alpha + [y_2^R]^{i\alpha}\, \bar q_i e_\alpha R_2 + \text{h.c.}$
$\widetilde{R}_2$	$(\mathbf{3},\mathbf{2},1/6)$	0	$\mathcal{L}_{\widetilde{R}_2} = -[\widetilde{y}_2^L]^{i\alpha}\, \bar d_i \widetilde{R}_2 \epsilon l_\alpha + [\widetilde{y}_2^R]^{i\alpha}\, \bar q_i N_\alpha \widetilde{R}_2 + \text{h.c.}$
V_2	$(\bar{\mathbf{3}},\, \mathbf{2},\, 5/6)$	1	$\mathcal{L}_{V_2} = [x_2^L]^{i\alpha}\, \bar d_i^c \not{V}_2 \epsilon l_\alpha + [x_2^R]^{i\alpha}\, \bar q_i^c \epsilon \not{V}_2 e_\alpha + \text{h.c.}$
$\widetilde{V}_2$	$(\bar{\mathbf{3}},\, \mathbf{2},\, -1/6)$	1	$\mathcal{L}_{\widetilde{V}_2} = [\widetilde{x}_2^L]^{i\alpha}\, \bar u_i^c \not{\widetilde{V}}_2 \epsilon l_\alpha + [\widetilde{x}_2^R]^{i\alpha}\, \bar q_i^c \epsilon \not{\widetilde{V}}_2 N_\alpha + \text{h.c.}$
S_3	$(\bar{\mathbf{3}},\, \mathbf{3},\, 1/3)$	0	$\mathcal{L}_{S_3} = [y_3^L]^{i\alpha}\, \bar q_i^c \epsilon S_3 l_\alpha + \text{h.c.}$
U_3	$(\mathbf{3},\, \mathbf{3},\, 2/3)$	1	$\mathcal{L}_{U_3} = [x_3^L]^{i\alpha}\, \bar q_i \not{U}_3 l_\alpha + \text{h.c.}$

Table 4.1: *Possible bosonic mediators contributing at tree level to Drell-Yan production classified by their SM quantum numbers and spin. In the last column we provide the interaction Lagrangian where $\epsilon \equiv i\tau_2$, $\psi^c \equiv i\gamma_2\gamma_0\bar\psi^T$, $\Phi_i^c = i\tau_2\Phi_i^*$, the RH fermion fields as $u \equiv u_R$, $d \equiv d_R$, $e \equiv \ell_R$, $N \equiv \nu_R$, and LH fermion fields as $q \equiv (u_L, d_L)^T$, $l \equiv (\nu_L, \ell_L)^T$. For the Leptoquark states we adopt the symbols from Ref. [32].*

$(SU(3)_c,\, SU(2)_L,\, U(1)_Y)$ with $Q = Y + T_3$, and their spin. The possible semileptonic mediators are displayed in Table 4.1, where we also provide the relevant interaction Lagrangians with generic couplings in the last column. For completeness, we also include three[7] right-handed neutrinos $N_\alpha \sim (\mathbf{1},\mathbf{1},0)$ with $\alpha = 1,2,3$. Furthermore, we assume that the masses of these SM singlets are negligible compared to the collider energies and if produced, can escape the LHC detectors as missing energy.

The possible mediators fall into two broad categories with similar phenomenology: (i) color-singlets exchanged in the s-channel, and (ii) leptoquarks, i.e. color-triplets, exchanged in the t/u-channels. If the masses of these states are at the $\mathcal{O}(\text{TeV})$ scale, their propagators will

[7] For simplicity we assume three RH neutrinos, but this need not be the case.

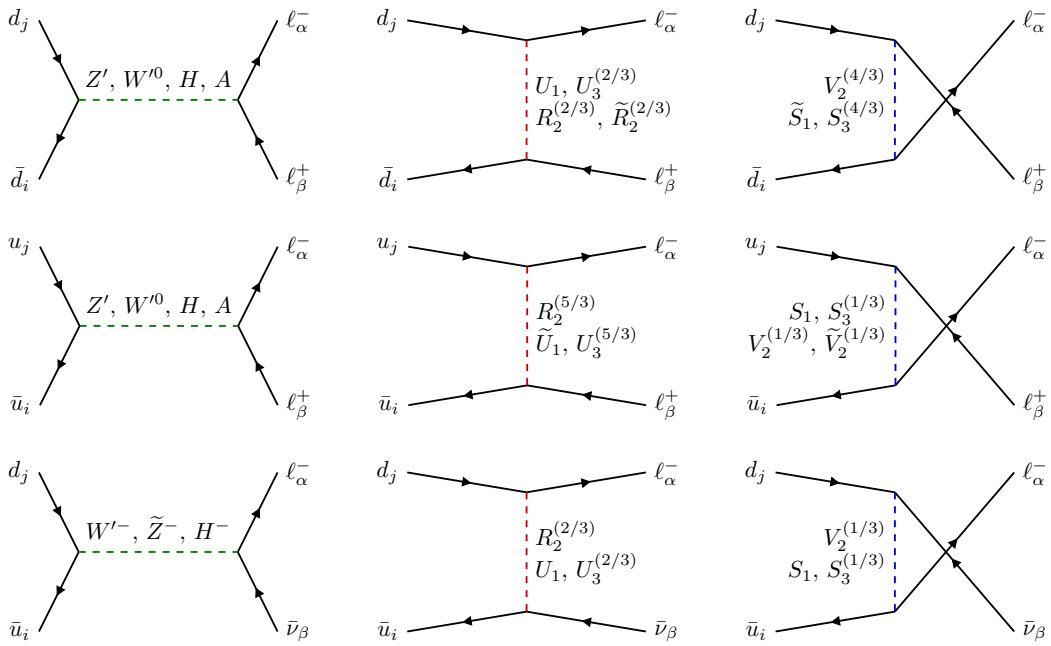

Figure 4.3: *Contributions to dilepton transitions $\bar{d}d \to l^+l^-$ (upper row), $\bar{u}u \to l^+l^-$ (middle row) and $\bar{u}d \to l^\pm\nu$ (lower row), from the tree-level exchange of the mediators displayed in table 4.1 via the s-channel (left column), t-channel (middle column) and u-channel (right column).*

contribute to the pole residues $\mathcal{S}_{I\,(a)}$, $\mathcal{T}_{I\,(b)}$, $\mathcal{U}_{I\,(c)}$ of the pole form-factor, (4.8).

In the broken phase of the SM, the $SU(2)_L$ multiplets decompose into charge eigenstates as: $\Phi_2 \sim (\phi^+, \phi_R^0 + i\phi_I^0)$, $R_2 \sim (R_2^{5/3}, R_2^{2/3})$, $\widetilde{R}_2 \sim (\widetilde{R}_2^{2/3}, \widetilde{R}_2^{-1/3})$, $V_2 \sim (V_2^{4/3}, V_2^{1/3})$, $\widetilde{V}_2 \sim (\widetilde{V}_2^{1/3}, \widetilde{V}_2^{-2/3})$ for doublets, and $W_\mu'^a \sim (W_\mu'^+, W_\mu'^0, W'^-)$, $S_3 \sim (S_3^{4/3}, S_3^{1/3}, S_3^{-2/3})$, $U_3 \sim (U_3^{5/3}, U_3^{2/3}, U_3^{-1/3})$ for triplets. The superscripts denote the electric charge of each component.

Form-factors in concrete models

The complete matching of the pole form-factors to concrete models is given in appendix D where the flavor structure of the residues of the pole form-factors takes the following form:

$$[\mathcal{S}_{I\,(a)}]_{ij}^{\alpha\beta} = [g_a^*]^{ij}[g_a^*]^{\alpha\beta}\,, \tag{4.38}$$

$$[\mathcal{T}_{I\,(b)}]_{ij}^{\alpha\beta} = [g_b^*]^{i\alpha}[g_b^*]^{j\beta}\,, \tag{4.39}$$

$$[\mathcal{U}_{I\,(c)}]_{ij}^{\alpha\beta} = [g_c^*]^{i\beta}[g_c^*]^{j\alpha}\,, \tag{4.40}$$

for $I \in \{V, S, T\}$, where $g_{a,b,c}^*$ denote generic couplings of the mediators to fermions of a given chirality and each index a, b, c labels the possible mediators contributing to the s, t and u channels, respectively, as displayed in the Feynman diagrams in Fig. 4.3.

4.4 Collider limits

At hadron colliders, the detectors are complex and imperfect environments with a finite resolution and limited acceptance. When dealing with di-lepton and mono-lepton searches at the LHC, differential distributions are measured from the reconstructed four-momenta of high-level

objects such as isolated leptons, τ-tagged jets, and missing transverse energy $\not{E}_T$. These objects are meant to approximate the underlying final state leptons produced in the hard scattering. Theoretical predictions, on the other hand, are typically computed from the experimentally inaccessible final state leptons. This mismatch between the predicted distribution of a particle-level observable x and the observed distribution of the corresponding observable $x_{\rm obs}$ is described by the convolution

$$\frac{\mathrm{d}\sigma}{\mathrm{d}x_{\rm obs}} = \int \mathrm{d}x\; K(x_{\rm obs}|x)\,\frac{\mathrm{d}\sigma}{\mathrm{d}x}\,, \tag{4.41}$$

where $K(x_{\rm obs}|x)$ is a *kernel function* that parametrizes the detector response[8] [211]. In practice, for a given LHC search, both the measured and particle-level distributions are binned into histograms leading to the discretization of eq. (4.41). For binnings $\mathcal{A}$ of $x_{\rm obs}$ and $\mathcal{B}$ of x, the expected number of signal events $\mathcal{N}_A$ in a bin $A \in \mathcal{A}$ is given by

$$\mathcal{N}_A = \sum_{B\,\in\,\mathcal{B}} \mathcal{L}_{\rm int}\cdot K_{AB}\cdot \sigma_B\,, \tag{4.42}$$

where $\mathcal{L}_{\rm int}$ is the integrated luminosity used in the search, σ_B is the particle-level cross-section restricted to a bin $B \in \mathcal{B}$, and K is a $N\times M$ *response matrix*, where N and M are the number of bins in $\mathcal{A}$ and $\mathcal{B}$, respectively. The response matrix represents the probability that an event produced in a bin B of x passes all event selections of the search and is measured in bin A of $x_{\rm obs}$. When estimating the event yields $\mathcal{N}_A$ of a BSM signal, each independent term contributing to the computation of the cross-section σ_B (e.g. see eq. (4.42)) needs to be convoluted with a different K_{AB} matrix since each term can respond differently to the selection cuts and the detector. Therefore, in full generality, the response matrices entering eq. (4.42) are quantities depending on the chiralities (X, Y) and flavors (α, β, i, j) of the external leptons and quarks, as well as the shape of the New Physics, i.e. the regular and pole form-factors that are involved $(I, J, n, m, \Omega_a, \Omega_b, \Omega_c)$. It is clearly not possible to compute the entries of each response matrix from first principles. These must be estimated numerically for each LHC search using Monte Carlo event generators and detector simulators.

4.4.1 LHC searches in di-leptons and mono-leptons

The experimental searches considered in our analysis are collected in Table 4.2. These correspond to data sets from the full Run-II ATLAS and CMS searches for heavy resonances in di-lepton and mono-lepton production at the LHC. In the last two columns, we display the observables measured in each search ($x_{\rm obs}$) serving as proxies for the particle-level observables (x) used to compute the signal cross-sections. Specific details concerning the definition of the measured observables, selection cuts and any other inputs used in these experimental analyses are available in the respective ATLAS and CMS papers listed in Table 4.2. Limits on the SMEFT and on mediator models are extracted with the `HighPT` package [197] where

[8] For example, the particle-level observable relevant for resonance searches in di-tau production at the LHC [210] is the invariant mass $x = m_{\tau\tau}$ of the di-tau system. Given that τ-leptons always decay into neutrinos, a precise experimental reconstruction of $m_{\tau\tau}$ is challenging. Therefore, what is actually measured is the quantity $x_{\rm obs} = m_T^{\rm tot}$ known as the *total transverse mass*, which serves as a proxy for $m_{\tau\tau}$. This observable is computed from the two leading τ-tagged jets coming from the visible part of the hadronic decay of each underlying tau-lepton (τ_h) and the missing transverse energy of the event which accounts for the undetected neutrinos.

Process	Experiment	Luminosity	Ref.	$x_{\rm obs}$	x
$pp \to \tau\tau$	ATLAS	$139\,\text{fb}^{-1}$	[210]	$m_T^{\rm tot}(\tau_h^1, \tau_h^2, \not{E}_T)$	$m_{\tau\tau}$
$pp \to \mu\mu$	CMS	$140\,\text{fb}^{-1}$	[212]	$m_{\mu\mu}$	$m_{\mu\mu}$
$pp \to ee$	CMS	$137\,\text{fb}^{-1}$	[212]	m_{ee}	m_{ee}
$pp \to \tau\nu$	ATLAS	$139\,\text{fb}^{-1}$	[213]	$m_T(\tau_h, \not{E}_T)$	$p_T(\tau)$
$pp \to \mu\nu$	ATLAS	$139\,\text{fb}^{-1}$	[214]	$m_T(\mu, , \not{E}_T)$	$p_T(\mu)$
$pp \to e\nu$	ATLAS	$139\,\text{fb}^{-1}$	[214]	$m_T(e, \not{E}_T)$	$p_T(e)$
$pp \to \tau\mu$	CMS	$137.1\,\text{fb}^{-1}$	[215]	$m^{\rm col}_{\tau_h\mu}$	$m_{\tau\mu}$
$pp \to \tau e$	CMS	$137.1\,\text{fb}^{-1}$	[215]	$m^{\rm col}_{\tau_h e}$	$m_{\tau e}$
$pp \to \mu e$	CMS	$137.1\,\text{fb}^{-1}$	[215]	$m_{\mu e}$	$m_{\mu e}$

Table 4.2: *Experimental searches by the ATLAS and CMS collaborations that have been recast in the* `HighPT` *package [197]. The last two columns refer to the observables considered in our analyses.*

each Drell-Yan search has been repurposed for generic New Physics scenarios. For each signal hypothesis, we compute the 95% confidence intervals using the χ^2 likelihood function `ChiSquareLHC` which we then minimize using the native `Mathematica` routines for numerical minimization. In order for the χ^2 to give reliable limits, beforehand we made sure to combine the data between neighboring experimental bins until $\mathcal{N}_A \geq 10$ for any bin (background errors are added in quadrature when combining).

Internally, for each search in Table. 4.2, the `HighPT` function `ChiSquareLHC` extracts the number of signal events $\mathcal{N}_A(\theta)$ in a bin $A \in \mathcal{A}$ of $x_{\rm obs}$ by convoluting the relevant response matrix K_{AB} with the analytical expressions for σ_B. These are computed with the PDF set `PDF4LHC15_nnlo_mc` [216]. We denote by θ the parameters of the New Physics model that we wish to constrain, e.g. form-factor parameters or specific model parameters such as Wilson coefficients or mediator masses and couplings. The χ^2 is then built from the number of background events $\mathcal{N}^b$, background uncertainties $\delta\mathcal{N}^b$ and observed events $\mathcal{N}^{\rm obs}$ provided by the experimental collaborations:

$$\chi^2(\theta) = \sum_{A\in\mathcal{A}} \left(\frac{\mathcal{N}_A(\theta) + \mathcal{N}_A^b - \mathcal{N}_A^{\rm obs}}{\Delta_A} \right)^2 , \tag{4.43}$$

where the uncertainty Δ is given by adding in quadrature the background and observed uncertainties, $\Delta^2 = (\delta\mathcal{N}^b)^2 + \mathcal{N}^{\rm obs}$. The response matrices K_{AB} have been provided in the `HighPT` package for each LHC search. These were obtained from MC simulations using the following pipeline: first, all relevant semileptonic operators in the SMEFT with $d \leq 8$ and all mediator Lagrangians in Table. (4.1) were implemented with `FeynRules` [217]. The resulting `UFO` model files [218] were then imported into `Madgraph5` [219] and used to simulate statistically significant event samples for the dilepton and monolepton processes with all possible initial quark flavors. Samples were then showered and hadronized using `Pythia8` [220], and the final-state object reconstruction and detector simulation were performed using `Delphes3` [221] tuned to match the experimental searches. After applying the same event selections as in each experiment, the events were binned into $x_{\rm obs}$ histograms. The simulation pipeline outlined above was used to produce a $x_{\rm obs}$ histogram from each bin $B \in \mathcal{B}$ of x. The rows of the matrix K_{AB} were then extracted from the resulting histograms.

4.4.2 Constraints on the SMEFT

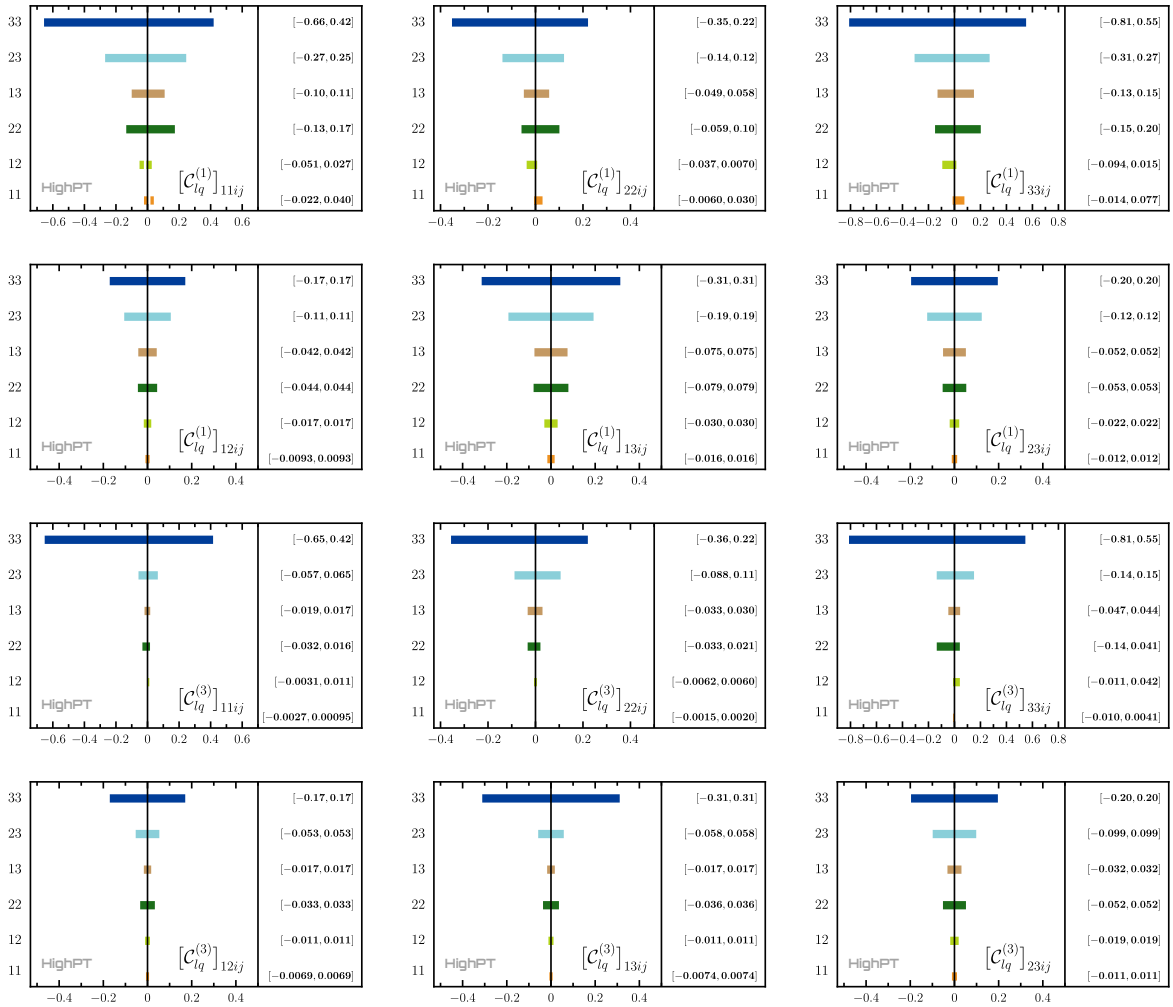

Figure 4.4: *LHC constraints on the SMEFT Wilson $\mathcal{C}_{lq}^{(1,3)}$ coefficients with different flavor indices to 2σ accuracy, where a single coefficient is turned on at a time. Quark flavor indices are denoted by ij and are specified on the left-hand side of each plot. All coefficients are assumed to be real and contributions to the cross-section up to and including $\mathcal{O}(1/\Lambda^4)$ are considered. The NP scale is chosen as $\Lambda = 1\,\text{TeV}$.*

In this section, we report on numerical results for the SMEFT operators up to $d = 6$, by considering a single effective coefficient at a time, which is assumed to be real, and with the New Physics scale fixed to $\Lambda = 1$ TeV. These constraints are presented in Appendix F of Ref. [222] for semileptonic operators with fixed leptonic indices, namely ee, $\mu\mu$, $\tau\tau$, $e\mu$, $e\tau$ and $\mu\tau$, and for all possible quark-flavor indices that can be probed at the LHC. From these plots, we find that the most constrained operators are the ones with valence quarks, but we also derive useful constraints for operators with c-, s- and b-quarks despite the PDF suppression. The only semileptonic operators that cannot be probed at leading order with the processes that we consider are the ones with right-handed top quarks.

In addition to semileptonic operators, we show the constraints on lepton and quark dipole-operators in Fig. 4.5, with the most general flavor indices, and assuming once again CP conser-

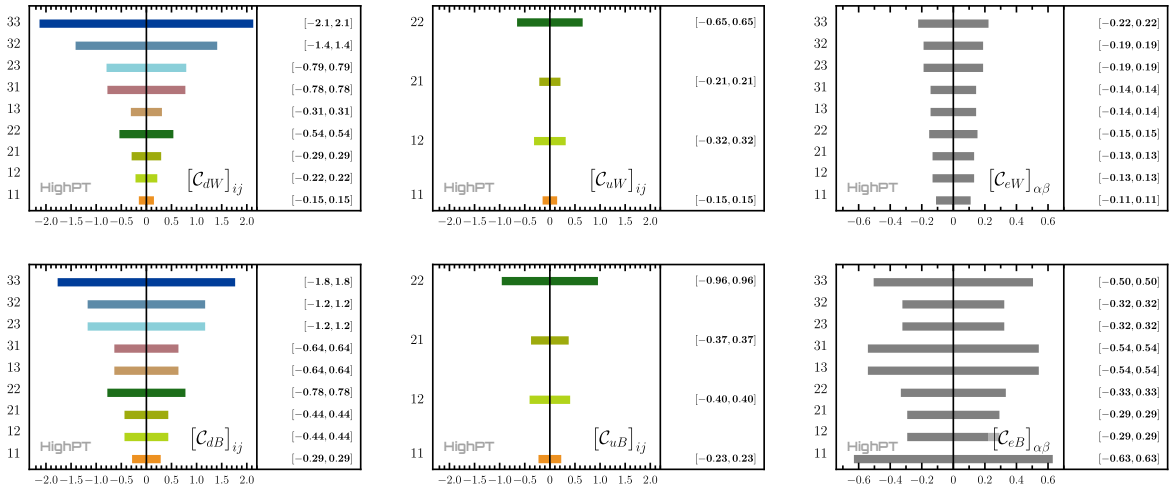

Figure 4.5: *LHC constraints on the SMEFT dipole Wilson coefficients with different flavor indices to 2σ accuracy, where a single coefficient is turned on at a time. Quark (lepton) flavor indices are denoted by ij ($\alpha\beta$) and are specified on the left-hand side of each plot. All coefficients are assumed to be real and contributions to the cross-section at order $\mathcal{O}(1/\Lambda^4)$ are considered. The NP scale is chosen as $\Lambda = 1\,\text{TeV}$.*

vation. These constraints are much weaker than the ones obtained for semileptonic operators, since these operators induce a mild energy enhancement of the cross-section and since their interference with the SM contributions is highly suppressed by the external fermion masses.

Finally, we note that in scenarios with several effective operators there are correlations among these coefficients if they contribute to the same process at the LHC. These correlations are relevant for phenomenology and they can be obtained in full generality by using the `HighPT` package, as illustrated in Ref. [52]. Furthermore, even though we do not present numerical results for the $d = 8$ operators, the complete likelihood including these effects can be obtained with the `HighPT` package, as shown in Ref. [52].

4.4.3 Numerical results

In this section, we combine the LHC constraints derived in Sec. 4.4 with the flavor and electroweak precision observables discussed above. To illustrate the main features of the `HighPT` package, which provides constraints for both EFT and concrete model scenarios, we perform a two-step analysis. In a first step, we will consider the minimal set of SMEFT operators that can accommodate $R_{D^{(*)}}$ in the viable scenarios described in eq. (2.29)–(2.28). In a second step, we directly consider the leptoquark models that predict these Wilson coefficients, including their propagation effects in the LHC observables. The comparison of the results obtained for the EFTs and the concrete models will allow us to directly assess the validity of the EFT approach for the high-p_T observables that we have considered. Using the leptoquark models will also allow us to correlate the effective coefficients entering flavor processes in different sectors, as shown in Table 2.4. The code input needed to extract these LHC constraints with the `HighPT` package will be given in Ref. [52].

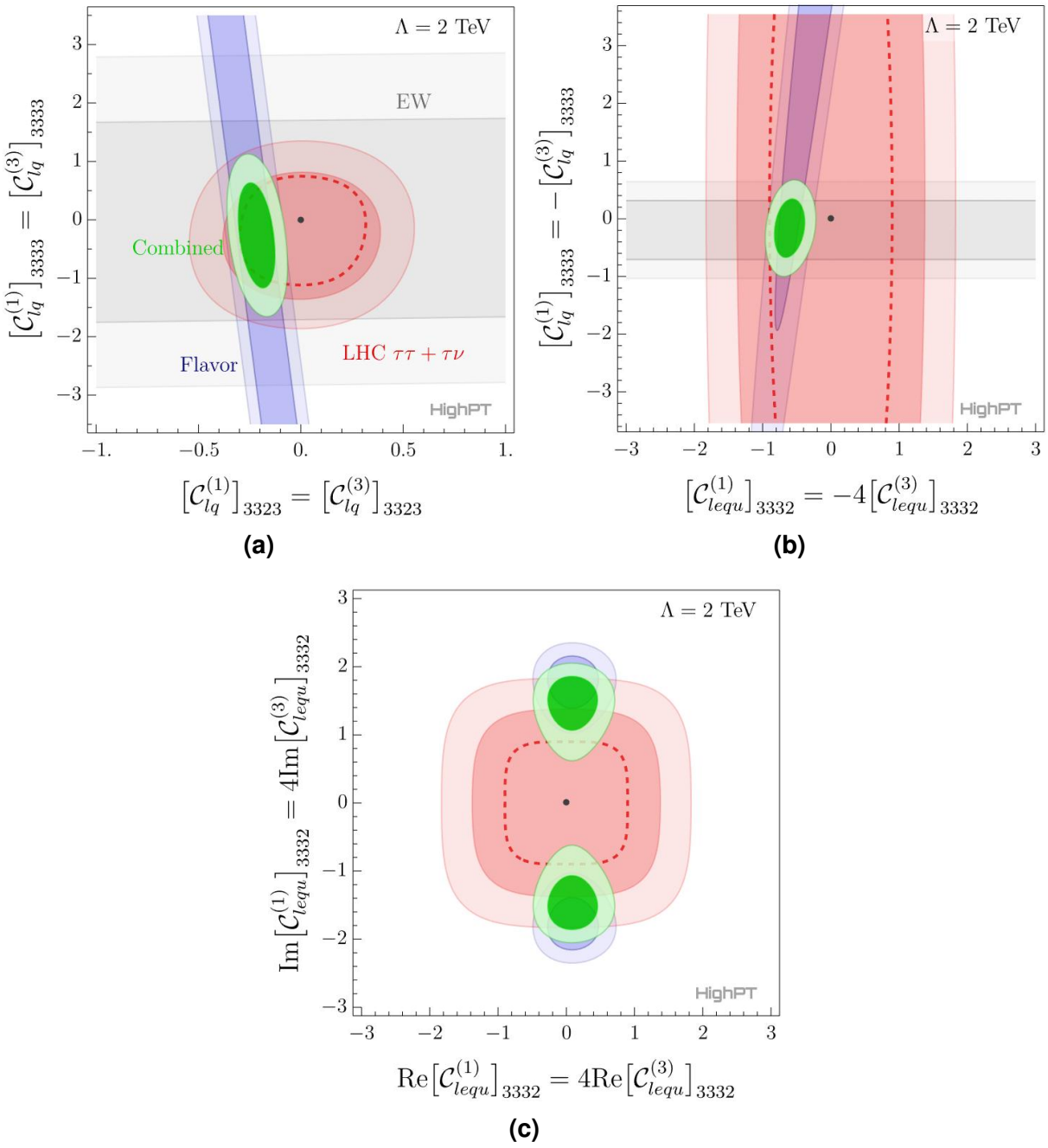

Figure 4.6: *Constraints on the SMEFT coefficients from flavor-physics (blue region), electroweak-precision (gray) and high-p_T observables (red). The combined fit is shown in green. For each type of observables, we show the 1σ (2σ) regions with lighter (darker) colors. Three effective scenarios are considered which are motivated by different leptoquark models, as explained in the text. The EFT cutoff is set to be $\Lambda = 2$ TeV.*

EFT approach

Starting with the EFT scenarios inspired by the viable leptoquarks, we consider the effective coefficients $\mathcal{C}_{lq}^{(1)} = \mathcal{C}_{lq}^{(3)}$, which are predicted at tree-level by the vector leptoquark U_1 with purely

left-handed couplings, see Table 2.4. [9] In the top left panel of Fig. 4.6, we show the allowed Wilson coefficients with flavor indices that contribute directly to the $b \to c\tau\bar{\nu}$. The flavor constraints, in this case, are dominated by $R_{D^{(*)}}$ (blue region), which are combined with electroweak (gray) and LHC constraints (red). In this case, the LHC constraints are dominated by $pp \to \tau\tau$, whereas $pp \to \tau\nu$ give weaker bounds. From Fig. 4.6, we see that low- and high-energy observables are complementary, and the synergy of the different searches is fundamental to restricting the allowed region of the effective coefficients.

In a similar way, the scenario with $\mathcal{C}^{(1)}_{lequ} = -4\,\mathcal{C}^{(3)}_{lequ}$ and $\mathcal{C}^{(1)}_{lq} = -\mathcal{C}^{(1)}_{lq}$ is considered in Fig. 4.6(b). This pattern of effective coefficients is predicted by the S_1 leptoquark at tree-level. For simplicity, we assume real couplings and focus on the flavor indices 3332 and 3333 for the scalar/tensor and vector operators, respectively. [10] In this case, we find that the most relevant constraints arise from flavor observables, which are once again dominated by $R_{D^{(*)}}$, and from electroweak observables. In particular, the latter prevent an explanation of the $b \to c\tau\bar{\nu}$ anomalies in this scenario if only left-handed couplings are considered. In this particular case, LHC constraints turn out to be practically irrelevant, at the EFT level, since the contributions to $pp \to \tau\tau$ are CKM suppressed.

The last scenario we consider is $\mathcal{C}^{(1)}_{lequ} = 4\,\mathcal{C}^{(3)}_{lequ}$, which is predicted by the R_2 leptoquark. The corresponding constraints are shown in Fig. 4.6(c) for the flavor indices entering the $b \to c\tau\bar{\nu}$ transition, with the same color code as before. This scenario is peculiar since purely real effective coefficients would induce contributions to R_D and R_{D^*} with different signs, which is incompatible with current data [34, 35, 224]. In other words, an imaginary part of the scalar/tensor coefficients is needed to simultaneously explain the deviations observed in R_D and R_{D^*}, as shown in Fig. 4.6. Electroweak and Higgs constraints are not shown in this plot since they turn out to be weak in comparison to flavor bounds at the EFT level. LHC constraints are dominated by $pp \to \tau\nu$ and they appear to probe a small portion of the favored flavor region. However, this conclusion should be taken with caution since the propagation effects of the leptoquark have a non-negligible effect in the LHC observables.

Concrete models

From the EFT examples discussed above, it is clear that the Drell-Yan tails provide complementary information to low-energy observables, being particularly useful to single out the viable solutions of the $R_{D^{(*)}}$ anomalies. However, there are limitations of the EFT approach that must be kept in mind. First of all, there can be non-negligible corrections to the EFT description of the LHC observables if the EFT cutoff Λ is not sufficiently larger than the partonic center-of-mass energy. Moreover, there are correlations among low- and high-energy observables that are only manifest within the concrete models.

The constraints on the concrete models are shown in Fig. 4.7 for the leptoquarks U_1 (upper left), S_1 (upper right) and R_2 (bottom), with the leptoquark masses fixed to 2 TeV, in agreement with current constraints from leptoquark pair-production at the LHC [29]. For each scenario, a minimal set of two Yukawa couplings has been chosen to induce the SMEFT operators needed to explain $R_{D^{(*)}}$ in Fig. 4.6. The leptoquark Lagrangians are defined in Table 4.1, with their tree-level matching to the SMEFT given in Table 2.4.

[9] Notice that the presence of right-handed U_1 couplings is also allowed by current constraints, which would predict a different pattern of low- and high-energy observables [223].

[10] Note that the effective coefficients $\mathcal{C}^{(1)}_{lq} = -\mathcal{C}^{(3)}_{lq}$ with flavor indices 3323 also contribute to $R_{D^{(*)}}$, but these effective coefficients are subject to stringent constraints from $B \to K\nu\bar{\nu}$.

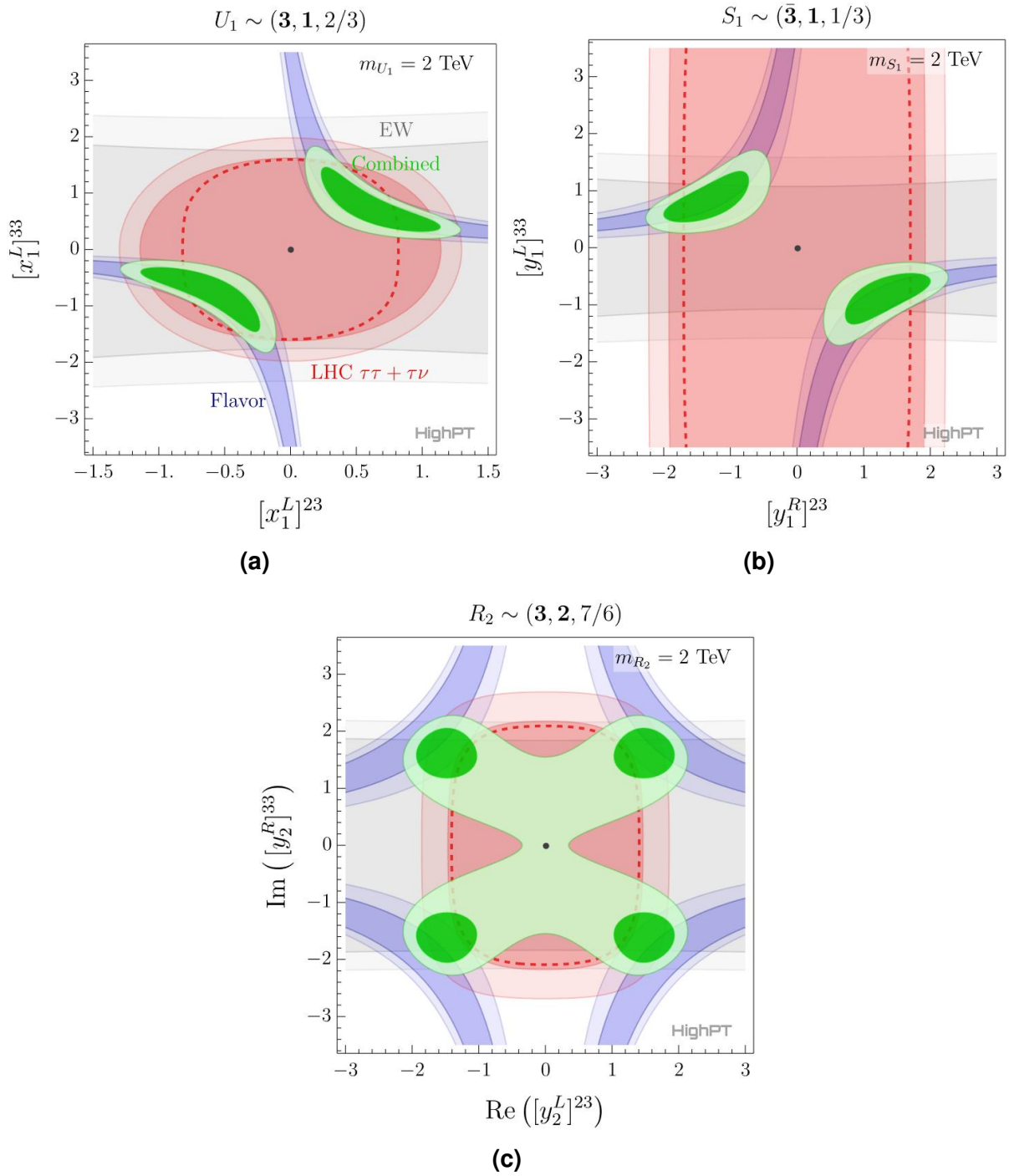

Figure 4.7: *Bounds on the LQ couplings from low-energy (blue), electroweak pole (gray) and high-p_T (red) observables. The combined fit is shown in green. For every bound we show the 1σ and 2σ regions. The LQ mass is set to be $\Lambda = 2$ TeV.*

From Fig. 4.7 we see that the three models are viable explanations of $R_{D^{(*)}}$ and we confirm that there is a complementarity of the low- and high-energy constraints. The high-p_T constraints turn out to be slightly relaxed in all cases in comparison to the EFT computation, due to the propagation effects of the leptoquarks,

$$\frac{1}{(t-m^2)^2} \simeq \frac{1}{m^4}\left(1 + \frac{2t}{m^2} + \dots\right), \qquad t \in (-s, 0)\,, \tag{4.44}$$

where m denotes the leptoquark mass and we assume without loss of generality that the leptoquark is exchanged in the t-channel. The first power-correction on t/m^2 comes with a relative negative sign which reduces the cross-section estimated with the EFT. This difference is particularly relevant for the R_2 model, where the LHC constraints seem to exclude the favored region in the EFT approach, but this is no longer true once the leptoquark propagator is considered, as recently noted in Ref. [157].

Going from the EFT description to concrete models also allows us to obtain additional constraints arising from the correlation of the different SMEFT operators. An example is given by the electroweak constraints for the R_2 model in Fig. 4.7(c), which are not present for the minimal set of operators contributing to the charged currents in Fig. 4.6(c). This correlation is also the reason why LHC constraints seem to be weak in Fig. 4.6(b), but become relevant for the full S_1 models in Fig. 4.7(b).

4.5 On the validity of the EFT approach in collider observables

It is well-known that the EFT approach is not always valid to describe LHC processes, since the collision energies can be in certain cases of the same order or even above the EFT cutoff, thus not justifying the truncation of the EFT expansion. One possible alternative to reduce this problem is to give the constraints coming from the analyses as a function of a mass scale M_{cut}, representing an upper value in some kinematical variable relevant for the considered process, above which all data are discarded [225]. This would, in principle, allow for a more robust interpretation of the bounds. However, such an approach is not ideal for the searches we consider, since the last bin is typically the one with the largest S/B. In other words, the sensitivity of the EFT coefficients would dramatically decrease.

Another important issue, which we try to address in this section in two explicit examples, is the contribution of dimension-eight operators in the SMEFT. In many cases, the current precision of the experiments requires keeping the $1/\Lambda^4$ terms in the squared amplitude. This is especially the case when dimension-six operators do not interfere with the SM amplitude. At the same order in the expansion, however, also the interference terms of dimension-eight operators with the SM appear, opening the question of whether these can be neglected or not. While this is mainly the case, it has been pointed out that there are classes of operators that might even lead to new kinds of effects, e.g. in angular distributions. In our case, we have mentioned operators ($\psi^4 D^2$) that have an additional energy enhancement, thus being potentially important in the tails of the distributions.

4.5.1 Limit comparison

In order to illustrate the difference between the limit obtained with an EFT and with concrete scenarios, we focus on a single specific experimental search: the latest mono-tau resonance search by ATLAS [213].

Due to the energy enhancement in the EFT partonic cross-section the most significant events in the analysis will be located at the high energy end of the spectrum, i.e. in the tail of the distribution. For obtaining the results presented in Sections 4.4.2, as well as in Refs. [158–160],

the most constraining events are indeed those above $1\,\mathrm{TeV}$. [11] If we assume NP to be mediated by a t- or u-channel particle with a mass around $1\,\mathrm{TeV}$, the partonic cross-section will be greatly overestimated if we do not account for the propagation of the NP state. This can be easily seen if we write the propagator

$$\frac{1}{t-m^2} \simeq -\frac{1}{m^2}\left(1+\frac{t}{m^2}+\dots\right), \qquad t\in[-s,0]. \tag{4.45}$$

Obviously, if the negative t/m^2 correction is neglected the cross-section would be much larger than the one obtained by using the usual EFT approach. This effect becomes even worse due to the energy enhancement in the cross-section and the fact that the size of the t/m^2 correction is enhanced by the cuts in the analysis.

To illustrate the effect of propagation of the mediator we shall compare the recast results of the R_2 leptoquark with and without the use of EFT.

Framework

For convenience we copy the R_2 Lagrangien here:

$$\mathcal{L}_{R_2} = [y_2^R]^{ij}\bar{Q}_i R_2 l_{Rj} + [y_2^L]^{i,j}\bar{u}_{Ri}\widetilde{R}_2^\dagger L_j + h.c. \tag{4.46}$$

where, as usual, Q and L are the left-handed doublets of quarks and leptons, while u_R and l_R are the right-handed singlets. We work in the basis where down-quark Yukawa couplings are diagonal. In Eq. (4.46) we use the notation with $\widetilde{R}_2 = i\tau_2 R_2^*$, where τ_2 is the usual Pauli matrix. As for the Yukawa couplings, i.e. between the R_2 leptoquark and the lepton and quark flavors, we use:

$$[y_2^L] = \begin{pmatrix} 0 & 0 & 0 \\ 0 & 0 & y_L^{c\tau} \\ 0 & 0 & 0 \end{pmatrix}, \qquad [y_2^R] = \begin{pmatrix} 0 & 0 & 0 \\ 0 & 0 & 0 \\ 0 & 0 & y_R^{b\tau} \end{pmatrix}. \tag{4.47}$$

This is the minimal set of couplings needed to explain the charged current B-anomalies [29,35], see also Ref. [158]. We take the mass $m_{R_2} = 1.3\ \mathrm{TeV}$ as our benchmark point, which is consistent with current limits derived from direct searches [29,35]. After neglecting the fermion masses, the partonic cross-section reads

$$\frac{\mathrm{d}\hat{\sigma}\left(c\bar{b}\to\tau^+\nu_\mu\right)}{\mathrm{d}\hat{t}} = \frac{1}{64N_c\pi\hat{s}^2}\frac{\left|[y_2^L]^{c\tau}\right|^2\left|[y_2^R]^{b\tau}\right|^2\hat{u}^2}{\left(\hat{u}-m_{R_2}^2\right)^2}. \tag{4.48}$$

This can be easily integrated since in the same limit $\hat{s}+\hat{t}+\hat{u}=0$. We get

$$\hat{\sigma}(\hat{s}) \simeq \frac{\left|[y_2^L]^{c\tau}\right|^2\left|[y_2^R]^{b\tau}\right|^2}{192\pi m_{R_2}^2}\left[\frac{x+2}{x(1+x)}-\frac{2\log(1+x)}{x^2}\right], \tag{4.49}$$

where $x=\hat{s}/m_{R_2}^2$.

We recast the latest ATLAS searches [213], using the same selection of events as in the previous Section, again by allowing at most one extra jet in the final state.

[11] Note that in the new ATLAS data [213] 60 events are found above 1 TeV.

Results

Like in the previous Section, we use the CLs method to constraint the two non-zero couplings appearing in Eq. (4.46, 4.47). The resulting limit can be expressed as

$$\boxed{\left|[y_2^L]^{c\tau}[y_2^R]^{b\tau}\right| < 2.44} \qquad \text{for} \quad m_{R_2} = 1.3\,\text{TeV}\,. \tag{4.50}$$

This inequality translates to a bound on the Wilson coefficient $g_{S_L} \equiv g_{S_L}(m_b)$ as

$$|g_{S_L}| = 8.1\,|g_T| \;<\; 0.88\,,$$

which is to be compared with $|g_{S_L}| < 0.55$ as given in Refs. [157] using the exact same analysis, and which was also previously obtained in Refs. [158–160].

We see that the latter constraint on g_{S_L} is approximately $60\ \%$ weaker than the one obtained by using EFT alone. This statement is dependent on the leptoquark mass and the difference should decrease as m_{R_2} increases (see Fig. 4.8).

An important observation is that despite the total cross-section being only $10\ \%$ smaller when considering the propagation of the mediator the difference in the limits on Wilson coefficients can be much larger. This is because the ratio of cross-sections depends on p_T^{min}, the value starting from which the high-p_T tail is defined to derive desired constraints. For a smaller p_T^{min}, the t/m^2 term in Eq. (4.45) is large only in a small part of the phase space, whereas for larger values of p_T^{min} this term remains always large. In Fig. 4.8 we show how the two constraints compare for various p_T^{min} and various values of leptoquark masses. Indeed for heavier LQs, the constraints on couplings derived from EFT and propagating leptoquarks become closer to each other. Already at $m_{R_2} \simeq 5\,\text{TeV}$, we find that the two constraints are within $20\ \%$ from each other. One should keep in mind, however, that the bound on $|g_{S_L}|$ is stronger for larger p_T^{min} because the events larger than $1\ \text{TeV}$ provide the most significant constraints.

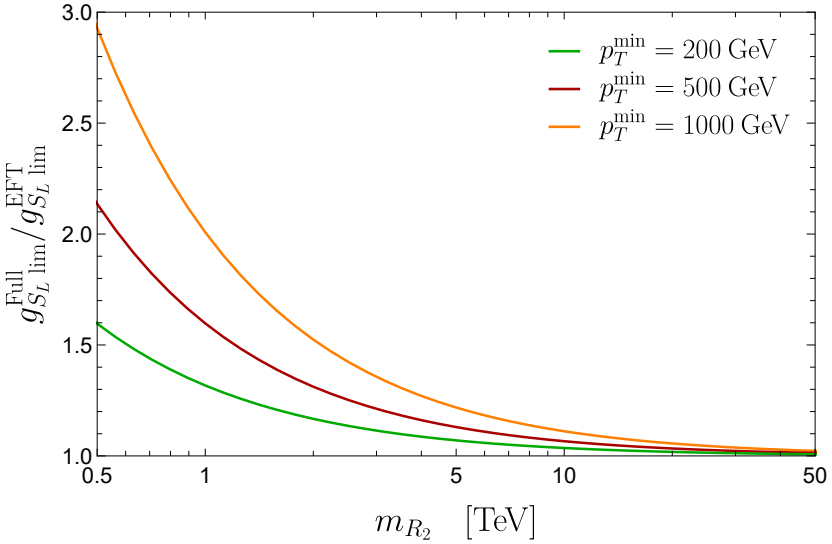

Figure 4.8: *Ratio of the limits obtained with the full model and the EFT for various p_T cuts, in the limit of infinite luminosity.*

In Fig. 4.9 we plot the limit on the average coupling $\sqrt{y_{c\tau}^L y_{b\tau}^R}$, that we obtain from the ATLAS data. We see that we can only probe the region under $3.5\ \text{TeV}$ because the couplings would

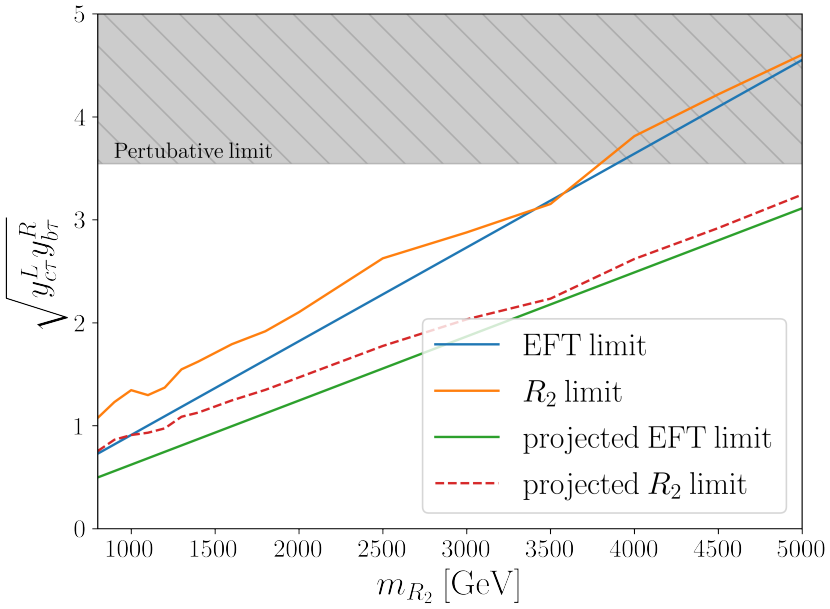

Figure 4.9: 95 % *exclusion limit on* $\sqrt{y^L_{c\tau} y^R_{b\tau}}$ *as a function of the* R_2 *mass (orange). The equivalent EFT result is shown in blue. We also include the projected limits with* 3 ab^{-1} *of integrated luminosity.*

otherwise become nonperturbative, i.e. larger than $\sim \sqrt{4\pi}$. However, with a further increase in luminosity, the slope of the curves shown in Fig. 4.9 would become smaller, thus opening a possibility to probe heavier leptoquarks. We also tried to include the effect of the leptoquark width in this analysis, and we found that the effect is insignificant in the perturbative regime, $|y^L_{c\tau}|, |y^R_{b\tau}| < \sqrt{4\pi}$.

4.5.2 Convergence of the EFT

A definite answer about the weight of dimension-eight operators can be only given with further assumptions on the UV structure generating the EFT in the first place. For this reason, we study the bounds obtained with and without the dimension-eight effects within two concrete examples of simplified NP mediators, corresponding to the extension of the SM field content by a Z' boson and a U_1 vector leptoquark, respectively. In the first case, the Z' being exchanged in the s-channel in Drell-Yan processes, we expect to see a larger effect, with the EFT essentially failing to describe the data in the proximity of the resonance. The leptoquark, on the contrary, being a t-channel mediator, should suffer less from this problem. We then compare the results with what we obtain without integrating out the mediator. The whole analysis has been performed within `HighPT`.

$Z' \sim (1,1,0)$: The general lagrangian for the Z' is given in Table 4.1, which we report here for convenience:

$$\mathcal{L}_{Z'} = \sum_{\psi} [g_1^{\psi}]^{ab} \bar{\psi}_a \not{Z}' \psi_b \,, \;\; \psi \in \{u, d, e, q, l\} \,. \tag{4.51}$$

We choose to switch on only the three couplings $[g_1^l]^{22}$, $[g_1^q]^{11}$ and $[g_1^q]^{22}$, matching only onto the following two effective coefficients in the SMEFT at dimension six[12],

$$\frac{\left[\mathcal{C}_{lq}^{(1)}\right]_{1122}}{\Lambda^2} = -\frac{[g_1^l]^{22}[g_1^q]^{11}}{m_{Z'}^2}\,, \qquad \frac{\left[\mathcal{C}_{lq}^{(1)}\right]_{2222}}{\Lambda^2} = -\frac{[g_1^l]^{22}[g_1^q]^{22}}{m_{Z'}^2}\,, \tag{4.52}$$

our constraints will therefore derive from the parton-level transitions of the type $q\bar{q} \to \mu^+\mu^-$, with $q \in \{u, d, s, c\}$. Going one step forward in the EFT matching, we find the following tree-level contribution to dimension-eight operators,

$$\frac{\left[\mathcal{C}_{l^2q^2D^2}^{(1)}\right]_{2211}}{\Lambda^4} = -\frac{[g_1^l]^{22}[g_1^q]^{11}}{m_{Z'}^4}\,, \qquad \frac{\left[\mathcal{C}_{l^2q^2D^2}^{(1)}\right]_{2222}}{\Lambda^4} = -\frac{[g_1^l]^{22}[g_1^q]^{22}}{m_{Z'}^4}\,, \tag{4.53}$$

where we have neglected operators without derivatives, since they are suppressed with respect to the dimension-six contributions.

$U_1 \sim (3, 1, 2/3)$: The Lagrangian of the U_1 leptoquark is

$$\mathcal{L}_{U_1} = [x_1^L]^{i\alpha}\,\bar{q}_i \not{\psi}_1 l_\alpha + [x_1^R]^{i\alpha}\,\bar{d}_i \not{\psi}_1 e_\alpha + \text{h.c.}\,. \tag{4.54}$$

By considering only the left-handed couplings x_1^L, the following dimension-six operators are generated at tree-level,

$$\frac{\left[\mathcal{C}_{lq}^{(1)}\right]_{\alpha\beta ij}}{\Lambda^2} = \frac{\left[\mathcal{C}_{lq}^{(3)}\right]_{ijkl}}{\Lambda^2} = -\frac{[x_1^L]^{\alpha j}[x_1^L]^{\beta i*}}{2m_{U_1}^2}\,. \tag{4.55}$$

Several operators appear at the next order in the EFT matching. However, only a few of these induce energy-enhanced contributions to Drell-Yan tails (see Table 2.1). These effective coefficients are given by

$$-\frac{\left[\mathcal{C}_{l^2q^2D^2}^{(1)}\right]_{\alpha\beta ij}}{\Lambda^4} = \frac{\left[\mathcal{C}_{l^2q^2D^2}^{(2)}\right]_{\alpha\beta ij}}{\Lambda^4} = -\frac{\left[\mathcal{C}_{l^2q^2D^2}^{(3)}\right]_{\alpha\beta ij}}{\Lambda^4} = \frac{\left[\mathcal{C}_{l^2q^2D^2}^{(4)}\right]_{\alpha\beta ij}}{\Lambda^4} = -\frac{[x_1^L]^{\alpha j}[x_1^L]^{\beta i*}}{4m_{U_1}^4}\,, \tag{4.56}$$

with flavor indices α, β, i, j, as above. The $d = 6$ and $d = 8$ have the same numerator and their contribution to the cross-sections will only differ by $t/m_{U_1}^2$, as one could expect from expanding the leptoquark propagator in the t-channel (see Fig. XX).

As an illustration, we choose to switch on the couplings with flavor indices 12 and 22, giving effects in mono-muon and di-muon final states. Even without looking at the actual constraints, it is useful to look at the differential Drell-Yan cross-section in the three cases (Figure 4.10) for a mediator mass of $2\ \text{TeV}$, where we see that the interference of dimension-6 SMEFT is indeed not sufficient to describe the model correctly, and that the dimension-8 terms only bring a small correction compared to the squared dimension-6 terms. In the example chosen here, the dimension-8 term is bringing the EFT cross-section closer to the full model, but this doesn't have to be the case, since the opposite value for one of the coupling would have resulted in a destructive interference with the SM.

We can thus expect the effects of dimension-8 operators to be small for most explicit scenarios of NP. We decided to include them in this work anyways in order to make fully consistent the EFT expansion to the order $1/\Lambda^4$, to no almost no additional computational cost, since our form-factor parameterization 4.1 and 4.2 are capable of encapsulating such effects.

[12] Note that we set $\Lambda = M_{Z'}$

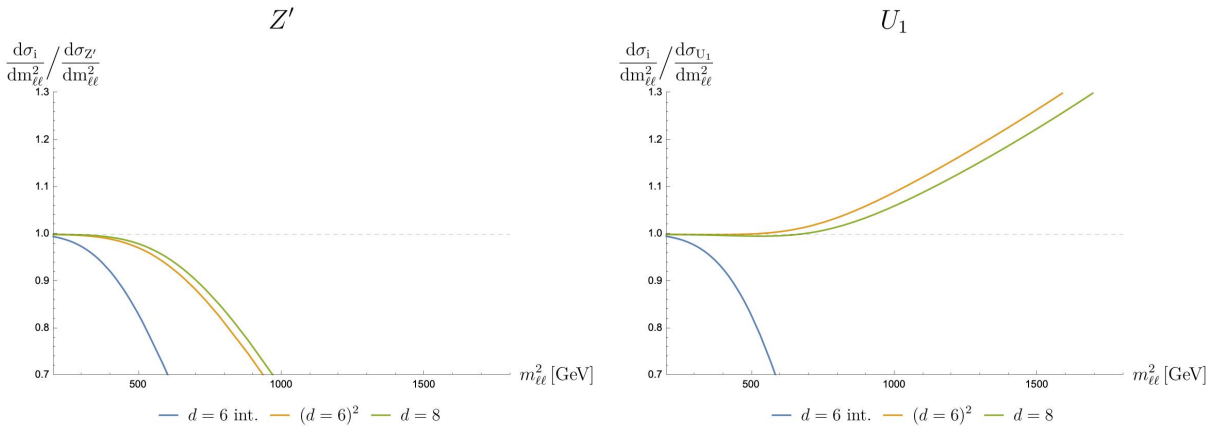

(a) **(b)**

Figure 4.10: *Differential cross-sections normalized to the cross-section computed with the mediators. For both cases* $\Lambda = m = 2$ *TeV.*

4.6 Summary and outlook

We have presented an analysis of semileptonic transitions in charged- and neutral current Drell-Yan processes at the LHC. Starting with a general description of the scattering amplitude in terms of form factors, we have computed the relevant hadronic cross-sections with the Mathematica package `HighPT` that we have developed for the phenomenology of these processes at high-p_T [52]. These form-factors have been matched to the SMEFT with a consistent EFT expansion up to $\mathcal{O}(\Lambda^{-4})$ at the cross-section level, making distinctions between the contributions which are energy-enhanced and those which lead to an overall shift of the SM cross-section, as well as to explicit concrete models with new bosonic mediators that contribute at tree-level to these processes. In particular, the comparison of these results allowed us to directly assess the range of validity of the EFT description of LHC data in certain scenarios.

Our computations have been compared to LHC data, through appropriate recasts of the experimental searches made by ATLAS and CMS. We have provided, for the first time, the complete likelihood for semileptonic operators, with general flavor indices of quarks and leptons, derived from the processes $pp \to \ell\nu$ and $pp \to \ell\ell'$ at high-p_T. To illustrate these results, we have provided the constraints on all possible SMEFT semileptonic effective coefficients up to dimension-6 by assuming a single coefficient at a time. The impact of dimension-8 in our constraints has also been explored by considering a few illustrative scenarios.

Finally, we have considered the explicit leptoquark scenarios needed to explain the charged-current B-anomalies as an example. These models have been explored by combining our limits with the constraints arising from low-energy observables and electroweak precision measurements. For the viable models, we have confirmed that the high-p_T observables are complementary to the low-energy ones and that they provide fundamental information to identify the viable solutions to these anomalies. Furthermore, we have discussed the impact of the leptoquark propagation effects on the LHC bounds that could be derived by naively recasting the EFT results.

Several extensions and improvements of our analysis are foreseen for the future, which will be accompanied by updates of the `HighPT` package:

- We plan to include all relevant flavor observables, as well as the relevant electroweak

and Higgs observables, into a unified framework for flavor-physics phenomenology.

- The input-scheme used for the gauge parameters of the SM receives corrections from New Physics parametrized with dimension-six operators, see e.g. Ref. [23]. The modification of these inputs therefore needs to be taken into account when computing the SM expectation for any observable, leading to correlations between different sectors. This applies, in particular, to G_F and the CKM matrix [24]. These contributions were irrelevant in the examples considered here, as they do not induce energy-enhanced contributions to the cross-section. However, they must be carefully taken into account to combine low-energy and high-energy observables in full generally.

- We plan to implement a complete list of concrete mediators in the code, in addition to the leptoquark models which already are available, with arbitrary values for the mass and width of these particles.

- We plan to directly implement a more robust statistical approach to analyze LHC data in the bins with few events, such as the CLs method [226].

- Lastly, it is possible to extend both our EFT and concrete-mediator analyses to scenarios with light right-handed neutrinos.

Chapter 5

Explicit Leptoquark solutions to the B-physics anomalies

In this chapter, we will try to combine both the low-energy observables of Chapter 3 and the high-energy observables of Chapter 4 applied to models of leptoquarks, as defined in Sec. 2.2. We start by summarizing all those constraints on scenarios with a single leptoquark, and then consider a model with 2 scalar LQ: R_2 and S_3.

5.1 Collider constraints on Leptoquark scenarios

In addition to the study of the high-p_T tails of the $pp \to \ell\ell$ distributions discussed in Chapter 4 and in Refs. [185, 195, 227], search for LQs in hadron colliders can also be achieved through their direct pair production [228, 229]. While the study high-p_T tails can provide limits on the coupling of LQs to quarks and leptons, this is not the case for direct productions. Instead, it allows us to put powerful constraints on the LQ masses. The relevant diagrams are shown in Fig. 5.1

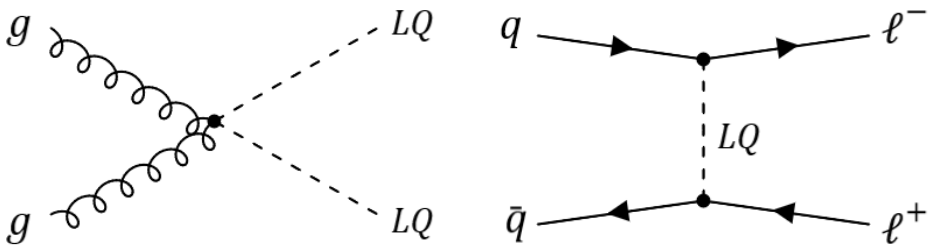

Figure 5.1: *Diagrams contributing the the LQ pair production (left) and high-p_T tails (right).*

5.1.1 Direct searches

The dominant mechanism for the LQ production at the LHC is $pp \to \mathrm{LQ}^\dagger\,\mathrm{LQ}$. Several searches for LQ pairs have been made at ATLAS and CMS for different final states, namely $(\bar{q}\ell)(q\bar{\ell})$, $(\bar{q}\nu)(q\bar{\nu})$ and $(\bar{q}_d\ell)(q_u\bar{\nu})$, where q_d and q_u stand for the generic down- and up-type quarks. From these searches it is possible to derive model independent bounds on a given LQ mass as a function of its branching fraction into a specific quark-lepton final state.

In Table 5.1 we present the limits on the LQ masses obtained from our recast of the latest $pp \to \mathrm{LQ}^\dagger\,\mathrm{LQ} \to (\bar{q}\ell)(q\bar{\ell})$ ATLAS and CMS searches. Previous limits were obtained in Ref. [28]. These limits are obtained as a function of the LQ branching fraction β, which we take to the benchmark values $\beta = 1$ and $\beta = 0.5$. Our main assumption is that the LQ production cross-section is dominated by QCD, which is true for the range of Yukawa couplings allowed by flavor constraints [28]. Furthermore, we assume that the vector LQ (V^μ) interaction with gluons ($G^{\mu\nu}$) is described by $\mathcal{L} \supset \kappa\, g_s V_\mu^\dagger G^{\mu\nu} V_\nu$, with $\kappa = 1$ (Yang-Mills case) [230], and we use the predictions from [229] in our recast. Compared to the previous study [28] with only $36\,\mathrm{fb}^{-1}$ of the LHC data, the limits on LQs masses have been considerably improved thanks to the increase in luminosity.

The LHC searches considered in Table 5.1 assume that pairs of LQs are produced and decay into the same quark-lepton final states. Recently, CMS performed a search for pair of LQs in the mixed channel $pp \to \mathrm{LQ}^\dagger\mathrm{LQ} \to b\tau t\nu$, with $140\ \mathrm{fb}^{-1}$ data [231]. This search was performed under the assumption that the LQs decay with equal branching fractions ($\beta = 0.5$) to the final states $\mathrm{LQ}^{(2/3)} \to b\bar{\tau}$, $t\bar{\nu}$, or $\mathrm{LQ}^{(-1/3)} \to t\tau\,, b\nu$, where the upper index denotes the LQ electric charge. Under this assumption the lower limits 1.0 TeV and 1.8 TeV have been obtained for the scalar and vector LQs, respectively. That search is particularly useful for the $U_1 = (\mathbf{3}, \mathbf{1}, 2/3)$ scenario, since the gauge invariance requirement implies that the couplings of U_1 to $t\bar{\nu}$ and to $b\bar{\tau}$ are equal. Note, however, that this search is very model dependent and, in particular, it does not generically apply to the models containing e.g. $S_1 = (\bar{\mathbf{3}}, \mathbf{1}, 1/3)$ or $R_2 = (\mathbf{3}, \mathbf{2}, 7/6)$.

Decays	Scalar LQ limits	Vector LQ limits	$\mathcal{L}_{\mathrm{int}}$ / Ref.
$jj\,\tau\bar{\tau}$	–	–	–
$b\bar{b}\,\tau\bar{\tau}$	1.0 (0.8) TeV	1.5 (1.3) TeV	36 fb^{-1} [232]
$t\bar{t}\,\tau\bar{\tau}$	1.4 (1.2) TeV	2.0 (1.8) TeV	140 fb^{-1} [233]
$jj\,\mu\bar{\mu}$	1.7 (1.4) TeV	2.3 (2.1) TeV	140 fb^{-1} [234]
$b\bar{b}\,\mu\bar{\mu}$	1.7 (1.5) TeV	2.3 (2.1) TeV	140 fb^{-1} [234]
$t\bar{t}\,\mu\bar{\mu}$	1.5 (1.3) TeV	2.0 (1.8) TeV	140 fb^{-1} [235]
$jj\,\nu\bar{\nu}$	1.0 (0.6) TeV	1.8 (1.5) TeV	36 fb^{-1} [236]
$b\bar{b}\,\nu\bar{\nu}$	1.1 (0.8) TeV	1.8 (1.5) TeV	36 fb^{-1} [236]
$t\bar{t}\,\nu\bar{\nu}$	1.2 (0.9) TeV	1.8 (1.6) TeV	140 fb^{-1} [237]

Table 5.1: *Summary of the current limits from searches for pair-produced LQs at the LHC for possible final states (first column). Limits on scalar and vector LQs are shown in the second and third column, respectively, for a branching fraction $\beta = 1$ ($\beta = 0.5$).*

5.1.2 Bounds from indirect high-p_T searches

Since the pioneering paper of Ref. [227] it is known that the high-energy tails of the invariant mass distribution of the processes $pp \to \ell\ell^{(\prime)}$ [185, 195] and $pp \to \ell\nu$ [160] are ideal probes for generic LQ models. These observables are particularly useful for setting upper bounds on complementary combinations of the couplings that cannot be constrained by flavor observables at low energies.

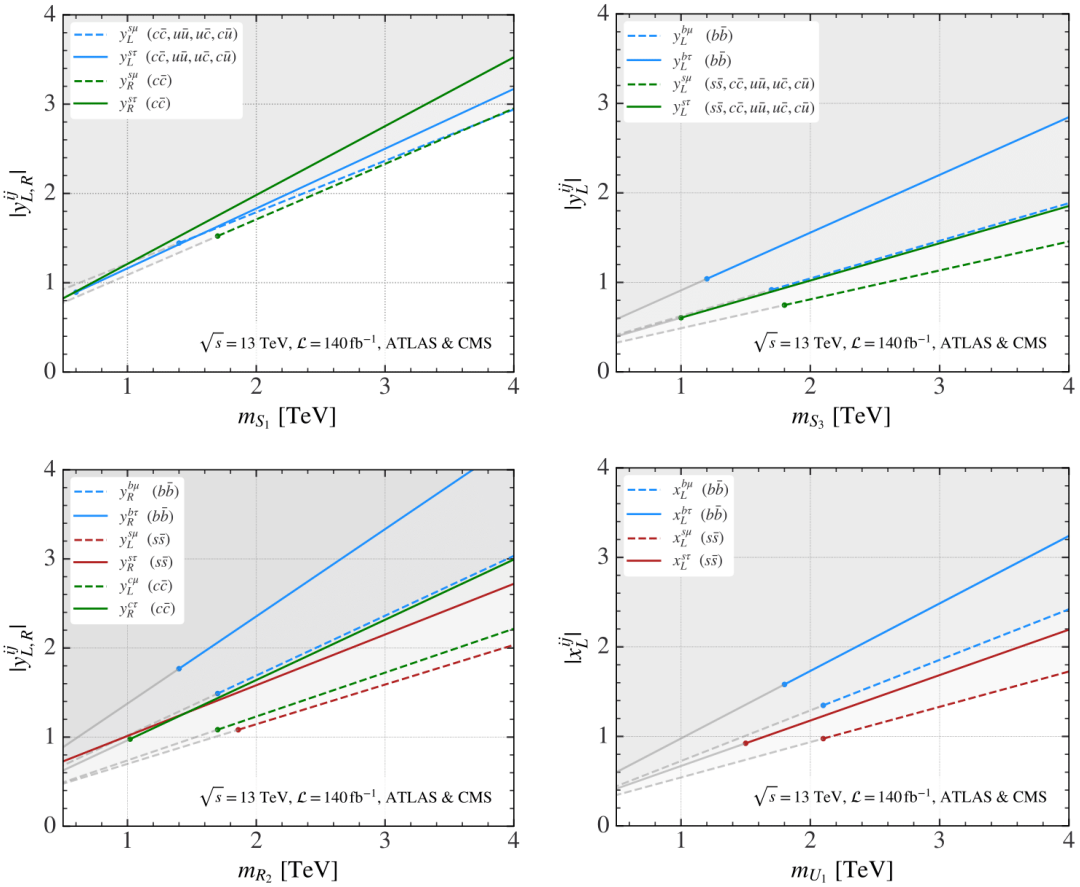

Figure 5.2: *Upper limits on the scalar (vector) LQ couplings y_L^{ij} (x_L^{ij}), as a function of the LQ masses, which have been obtained from the most recent LHC searches in the high-p_T bins of $pp \to \ell\ell$ at 13 TeV with $140\ \text{fb}^{-1}$ [210, 238]. The solid (dashed) lines represent limits arising from di-muon (di-tau) searches, by turning on a single LQ coupling in flavor space. In the plots we highlight the regions consistent with the lower bounds on the LQ masses given in Tab. 5.1 and discussed in Sec. 5.1.1. The $q\bar{q}$ pairs inside the parentheses indicate the combination of $q\bar{q} \to \ell\ell$ channels used to set the exclusion limits for each coupling. Notice that all $u\bar{u}$ transitions are Cabibbo suppressed.*

In Ref. [29], we obtained some constraints on the LQ couplings using LHC data by following a procedure already outlined in Ref. [28]. In particular, we used the most recent ATLAS and CMS searches for resonances in the dilepton channels:

- $pp \to \tau^+\tau^-$: We recast the ATLAS search for heavy Higgs boson decaying into the $\tau\tau$ channel, at $\sqrt{s} = 13\ \text{TeV}$ with $140\ \text{fb}^{-1}$ data [210]. We consider events with hadronic τ-leptons (τ_{had}) and we focus our analysis on the b-veto category.

- $pp \to \mu^+\mu^-$: We recast the CMS search for a heavy Z' boson decaying into the $\mu\mu$ channel, at $\sqrt{s} = 13$ TeV with 140 fb^{-1} data [238].

The constraints obtained from those two recasts already involve many flavor combinations, due to the flavor content of the proton. Other searches such as lepton flavor violating (LFV) and mono-lepton searches are related to di-lepton through $SU(2)$ invariance, and as such would improve the constraints, at the cost of even more flavor structure. The `HighPT` package was specifically designed to be able to disentangle the differing flavor structure.

In Fig. 5.2 we show the constraints on the LQ couplings obtained using only those two searches as a function of the LQ mass for the LQ models that are relevant for the B-physics anomalies, namely the scalars S_1, S_3 and R_2, and the vector U_1. In these plots, we only present limits for the vector LQ couplings to left-handed currents. [1] The 95% upper limits on the couplings are obtained as a function of the LQ masses by turning on one single flavor coupling at a time. The specific $q\bar{q} \to \ell\ell$ transitions contributing to each exclusion limit are displayed inside the parentheses $(q\bar{q})$. As shown in Fig. 5.2, these limits are typically more stringent than naive perturbative bounds on the couplings, namely $|y| \lesssim \sqrt{4\pi}$. The relevance of these constraints to the scenarios aiming to explain $R_{K^{(*)}}$ and $R_{D^{(*)}}$ will be discussed in Sec. 5.2.

As of the time of writing, `HighPT` only supports mediator mass of 2 TeV, and thus cannot produce graphs equivalent to Fig. 5.2 for combined searches. Instead, we provide the high-p_T constraints on the couplings of all leptoquark states, see Tab. 4.1, where we consider a single coupling at a time and Leptoquark propagation effects have been systematically included, which weaken the LHC limits in comparison to the ones derived via matching to the SMEFT. The effects of the propagation of mediators have been discussed in Sec. 4.5, with an explicit comparison between the constraints for concrete mediators and EFT for representative leptoquark scenarios.

Our results are collected in Fig. 5.3 for all leptoquark couplings that contribute to mono- and di-lepton tails. These results follow the same pattern of the SMEFT results presented in Fig. 4.4, with the strongest bounds corresponding to the lightest quark flavors, as they have the largest PDFs. Moreover, we find that bounds on the couplings to electrons and muons are comparable, whereas the ones on tauonic couplings turn out to be less stringent due to the weaker experimental sensitivity at the LHC. The only couplings that are not constrained by our observables are the ones that involve right-handed top-quarks.

Finally, we emphasize that there are non-negligible correlations between the limits on different leptoquark-couplings. These correlations are relevant for realistic scenarios where the couplings to different quarks and leptons are themselves correlated. The complete leptoquark likelihoods for the benchmark mass 2 TeV is fully implemented in the `HighPT` package [52].

[1] See Refs. [239, 240] for recent and updated high-p_T limits for right-handed couplings.

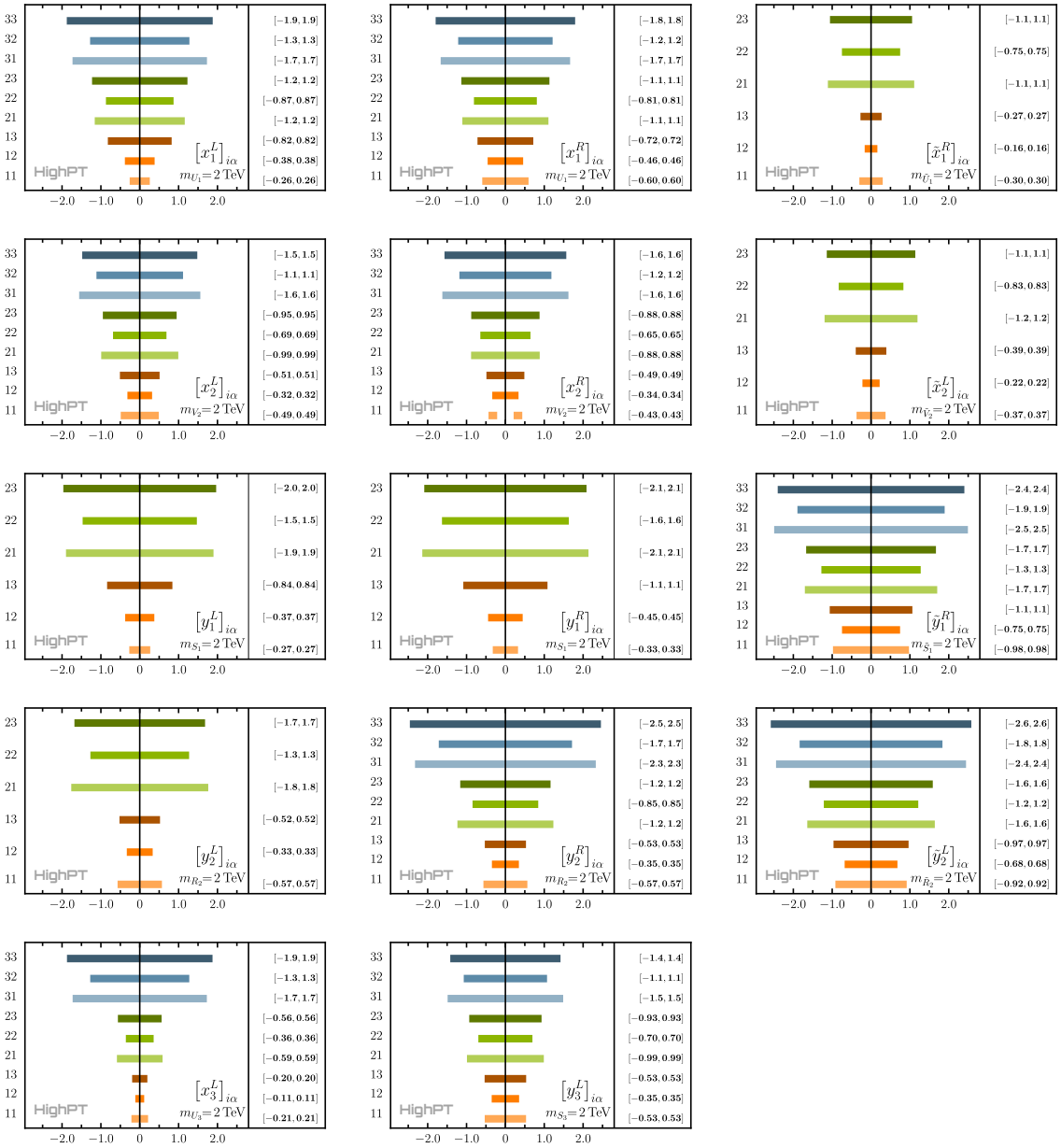

Figure 5.3: *LHC constraints on the coupling constants of all leptoquarks, where a single coupling is turned on at a time. The numbers on the left-hand side of each plot correspond to the respective flavor indices $i\alpha$. See Tab. 4.1 for the definition of the couplings. Note that these results, being obtained from a combination of all the searches in Tab. 4.2, are compatible, if not stronger, than those obtained in Fig. 5.2 for a mass of* 2 TeV.

5.2 Single Leptoquark solutions to the B-physics anomalies

Armed with the mass and coupling constraints from Sec. 5.1 and with the constraints on the EFT coefficients from Chapter 3 which can be related to LQ scenarios through the matching conditions defined in Sec. 2.2, we are now able to determine if any of the 5 individual LQ states we are considering can explain the B-anomalies.

5.2.1 S_3 and U_3

The matching of the S_3 and U_3 LQs to the neutral and charged EFT is given in Eq. 2.12-2.13 and Eq. 2.24-2.25 respectively. In both case, the following conditions are obtained:

$$\delta C_9 = -\delta C_{10} \text{ and } g_{V_L} < 0. \tag{5.1}$$

As seen in Fig. 3.1, $\delta C_9 = -\delta C_{10}$ is the correct combination to explain the neutral current anomalies $R^{\text{exp}}_{K^{(*)}} < R^{\text{SM}}_{K^{(*)}}$, whereas the charged current anomalies $R^{\text{exp}}_{D^{(*)}} > R^{\text{SM}}_{D^{(*)}}$ instead require $g_{V_L} > 0$, and thus cannot be accommodated by S_3 or U_3.

5.2.2 S_1

According to the matching Eq. (2.15), two different scenarios can lead to an explanation of the charged current anomalies. If we assume the minimalistic scenario with $[y_1^R]^{ij} = 0$, then we can have $g_{V_L} > 0$, which is enough to explain $R^{\text{exp}}_{D^{(*)}} > R^{\text{SM}}_{D^{(*)}}$. Alternatively, it is possible to turn on the right-handed coupling and use the second part of the matching 2.15, since $g_{S_L} = -4g_T$ is also a viable solution as shown in Fig. 3.2.

S_1, however, does not lead to a desired contribution to the $b \to s\mu\mu$. In the minimal ansatz for the Yukawa couplings, accommodating $R^{\text{exp}}_{K^{(*)}} < R^{\text{SM}}_{K^{(*)}}$ and Δm_{B_s} requires large LQ mass, $m_{S_1} \gtrsim 4$ TeV, and at least one of the Yukawa couplings to hit the perturbativity limit $\sqrt{4\pi}$ [28]. Therefore, one needs to turn on at least $[y_1^R]^{c\tau}$ and otherwise satisfy the condition $|[y_1^R]^{i\mu}| \ll |[y_1^L]^{i\mu}|$, for $i \in \{u, c, t\}$ to be consistent with data, cf. Fig. (3.1). However, requiring consistency with a number of measured flavor physics observables [28], including $R^{\mu/e}_{D^{(*)}} = \mathcal{B}(B \to D^{(*)}\mu\bar{\nu})/\mathcal{B}(B \to D^{(*)}e\bar{\nu})$, $\mathcal{B}(B \to K^{(*)}\nu\bar{\nu})$, $\mathcal{B}(K \to \mu\nu)/\mathcal{B}(K \to e\nu)$ and the experimental limit on $\mathcal{B}(\tau \to \mu\gamma)$, leads to a large m_{S_1} and very large couplings. This is why the S_1 scenario is considered as unacceptable for describing $R^{\text{exp}}_{K^{(*)}} < R^{\text{SM}}_{K^{(*)}}$, but fully acceptable for describing $R^{\text{exp}}_{D^{(*)}} > R^{\text{SM}}_{D^{(*)}}$. cf. Refs. [28, 241, 242].

5.2.3 R_2

As shown in Eq. 2.19, this LQ scenario generates the combination $g_{S_L} = 4\, g_T$ at the matching scale $\mu \simeq m_{R_2}$, which is consistent with data if g_{S_L} is mostly imaginary, cf. Fig. 3.2 and Refs. [34, 224, 243], it can therefore accommodate the observed excess in R_D and R_{D^*}, provided a large complex phase is present, and at least one $[y_2^R]^{ij}$ is non-zero, usually $[y_2^R]^{b\tau}$.

Like in the S_1 scenario, this LQ cannot generate the tree-level contribution consistent with $R_{K^{(*)}} < R^{\text{SM}}_{K^{(*)}}$, but it can do so through the box-diagrams [36]. The two essential couplings for this to be the case, $[y_2^L]^{c\mu}$ and $[y_2^L]^{t\mu}$, can now be quantitatively scrutinized. To that end it is enough to use two key constraints: the one arising from the well-measured $\mathcal{B}(Z \to \mu\mu)$ [56]

and another one, stemming from the high-p_T tail of the $pp \to \mu\mu$ differential cross-section. Note that the expression for the corresponding LQ contribution to $Z \to \mu\mu$ has been derived in Ref. [244], where the non-negligible finite terms $\propto x_Z \log x_t$ have been properly accounted for ($x_i = m_i^2/m_{R_2}^2$). As for the LQ mass, we use the bound given in Table 5.1 and set $m_{R_2} = 1.7$ TeV, while from Fig. 5.2 we can read off the constraints on the couplings as obtained from the large p_T considerations. The result is shown in Fig. 5.4 where we also draw the curves corresponding to three significant values of $R_{K^{(*)}}$, making it obvious that only $R_{K^{(*)}} \gtrsim 0.9$ is compatible with the two mentioned constraints. In other words, $R_{K^{(*)}}$ in this scenario is pushed to the edge of 1σ compatibility with $R_{K^{(*)}}^{(\text{exp})}$, cf. also Ref. [245].

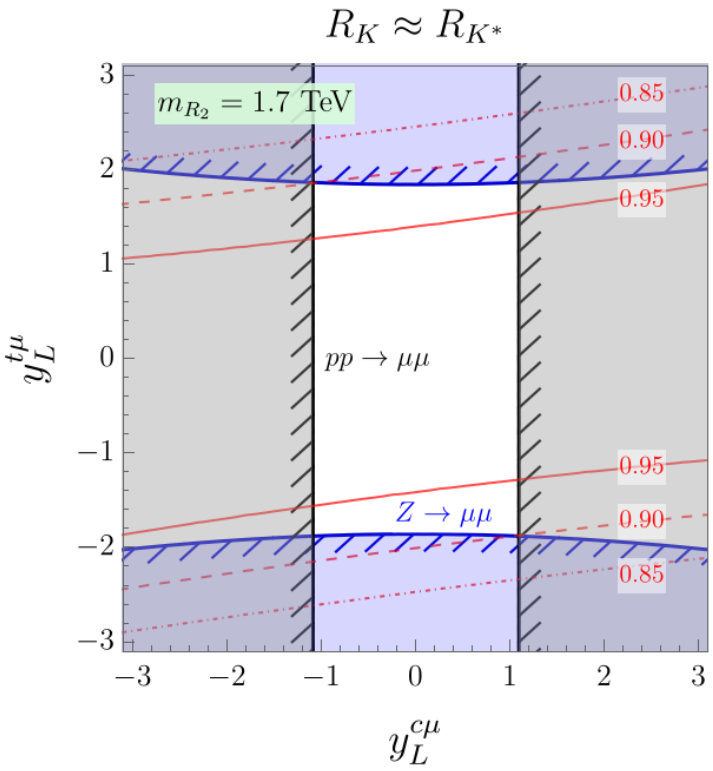

Figure 5.4: *The allowed regions for the couplings $y_L^{c\mu}$ and $y_L^{t\mu}$ are plotted in white for the $R_2 = (\mathbf{3}, \mathbf{2}, 7/6)$ LQ with mass $m_{R_2} = 1.7$ TeV. Predictions for $R_K \approx R_{K^*}$ in the bin $q^2 \in [1, 6]\,\text{GeV}^2$ are shown by the red contours. Excluded regions by Z-pole observables and $pp \to \mu\mu$ constraints are depicted in blue and gray, respectively.*

As discussed in [28], the simultaneous explanation of both $R_{K^{(*)}}$ and $R_{D^{(*)}}$ in this scenario is not possible even to 2σ because of the chiral enhancement by the top quark which leads to a prohibitively large $\mathcal{B}(\tau \to \mu\gamma)$, in conflict with the experimental bound [36].

5.2.4 U_1

In the minimal assumption where $x_1^R = 0$, this model predicts at the same time $\delta C_9 = -\delta C_{10}$ and $g_{V_L} > 0$. In other words, this state alone can simultaneously explain $R_{K^{(*)}}$ and $R_{D^{(*)}}$.

Owing to the fact that this LQ does not contribute to $B \to K^{(*)}\nu\bar{\nu}$ at tree-level, this is the only scenario that can satisfy both anomalies. The main drawback, however, is that the constraints derived from the loop-induced processes cannot be used unless a clear UV completion

is specified which in turn requires introducing several new parameters and new assumptions (model dependence) making the scenario less predictive. For that reason, we do not include, for example, the constraint arising from the frequency of oscillation of the $B_s - \bar{B}_s$ system (Δm_{B_s}) when dealing with vector leptoquarks. It has however been shown that this scenario can be significantly constrained by the tree-level processes alone [28, 246]. In particular, the model results in interesting correlations between the LFV processes $B \to K^{(*)}\mu\tau$ and $\tau \to \mu\phi$, and both upper and lower bounds for these modes can be derived. Setting the mass m_{U_1} to its lower bound of $1.8\,\mathrm{TeV}$ from Tab. 5.1, we then use the low energy flavor physics observables as in Ref. [28], combine them with the new constraints on couplings, as obtained from the high-p_T shapes of $pp \to \ell\ell$, shown in Fig. 5.2, and instead of plotting the couplings, we focus directly onto observables. Using the expressions for exclusive LFV $b \to s\ell_1\ell_2$ modes [241, 247] in the first panel of Fig. 5.5 we show how the region of $\mathcal{B}(B \to K\mu\tau)$ and $\mathcal{B}(\tau \to \mu\phi)$, allowed by the low-energy flavor physics constraints (gray points), gets reduced to the red region, once the current constraints coming from the high p_T considerations of $pp \to \ell\ell$ at the LHC are taken into account. We see that in both channels the current experimental bounds are already eliminating small sections of the parameter space. In the same plot we also show how that experimental bound on $\mathcal{B}(\tau \to \mu\phi)$ is expected to be lowered once the Belle II runs will be completed [129]. Concerning the experimental bound on $\mathcal{B}(B \to K\mu\tau)$, we note that the BaBar bound (4.8×10^{-5}) [248] has been recently confirmed and slightly improved by LHCb (3.9×10^{-5}) [249]. In the minimal U_1 scenario considered here, and with the current experimental constraints, we obtain

$$\mathcal{B}(B \to K\mu\tau) \gtrsim 0.7 \times 10^{-7}\,, \tag{5.2}$$

which could be tested experimentally. Note that this (lower) bound is not expected to increase significantly with the improved luminosity of the LHC data and with the projected $3\ \mathrm{ab}^{-1}$ of data we get only a factor of about 3 improvement, namely $\mathcal{B}(B \to K\mu\tau) \gtrsim 2.2 \times 10^{-7}$.

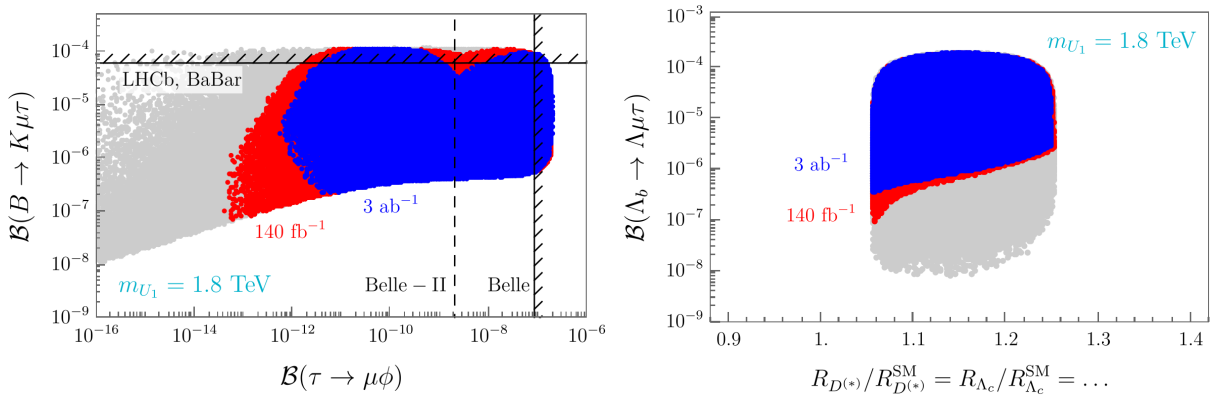

Figure 5.5: *Lower and upper bounds on the exclusive $b \to s\mu\tau$ processes as obtained in the minimal U_1 scenario from the constraints arising both from the low-energy observables (gray points) and those coming from the current direct searches at the LHC (red points), the subset of which (blue points) correspond to the projected integrated luminosity of $3\ \mathrm{ab}^{-1}$.*

We should also mention that, in this scenario, from the lower bound (5.2) and the experimental upper bound, one can derive the bounds on similar decay modes since $\mathcal{B}(B \to K^*\mu\tau)/\mathcal{B}(B \to K\mu\tau) \approx 1.8$, $\mathcal{B}(B_s \to \mu\tau)/\mathcal{B}(B \to K\mu\tau) \approx 0.9$, and $\mathcal{B}(\Lambda_b \to \Lambda\mu\tau)/\mathcal{B}(B \to K\mu\tau) \approx 1.7$ [247]. Furthermore, in this scenario the SM contribution to the $b \to c\tau\bar{\nu}$ decay modes gets only modified by and overall factor. For that reason, the predicted increase of R_X with respect to the SM is the

same for any $X \in \{D^{(*)}, D_s^{(*)}, J/\psi, \Lambda_c^{(*)}, \dots\}$. From the right panel of Fig. 5.5 we see that with the current experimental constraints we have

$$1.05 \lesssim \frac{R_X}{R_X^{\rm SM}} \lesssim 1.25\,, \tag{5.3}$$

the interval which remains as such even by projecting to $3\ \mathrm{ab}^{-1}$ of the LHC data (blue regions in Fig. 5.5).

We were able to check the robustness of the above findings by varying m_{U_1} and by imposing all of the constraints mentioned above, including the LHC bounds on the pair-produced leptoquarks decaying into various final states. The result is shown in Fig. 5.6 from which we see that the lower bound on $\mathcal{B}(B \to K\mu\tau)$ remains stable with respect to the variation of m_{U_1}. Notice that the lower bound on the mass is $m_{U_1} \gtrsim 1.35$ TeV, while the perturbativity limit on the couplings set an upper limit $m_{U_1} \lesssim 18$ TeV.

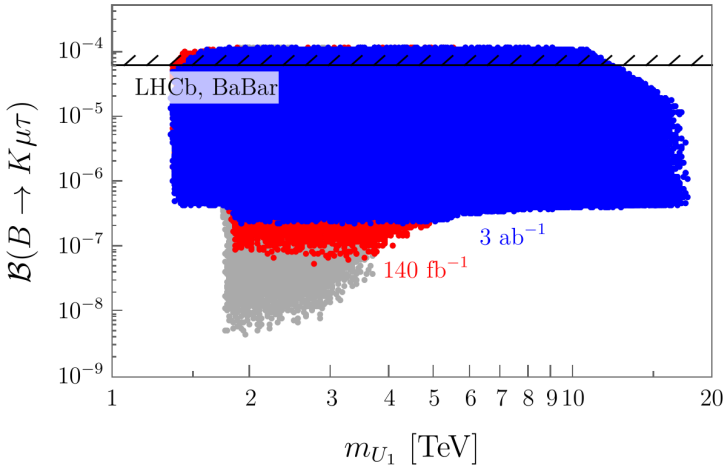

Figure 5.6: *Limits on $\mathcal{B}(B \to K\mu\tau)$ with respect to the variation of the mass of the U_1-leptoquark, and by keeping all of the constraints discussed in the text. Colors of the points are the same as in Fig. 5.5.*

Finally, we summarized the situation regarding the viability of a scenario in which the SM is extended by a single $\mathcal{O}(1\,\mathrm{TeV})$ LQ state in Tab. 5.2.

5.2.5 Summary

In this work, we revisited our previous phenomenological study and examined the viability of the scenarios in which the SM is extended by only one $\mathcal{O}(1\,\mathrm{TeV})$ LQ after comparing them to the most recent experimental results, in addition to those already discussed in Ref. [28]. In that respect the Belle measurement of $R_{D^{(*)}}$ [3] has been particularly important, as well as the new R_K and $\mathcal{B}(B_s \to \mu\mu)$ values reported by the LHCb Collaboration [1,12]. Besides the low-energy observables, we also exploit the most recent experimental improvements regarding the direct searches and the high p_T considerations of the $pp \to \ell\ell$ differential cross-section studied at the LHC.

Better experimental bounds on the LQ pair production, $pp \to \mathrm{LQ}^\dagger\,\mathrm{LQ}$, results in a larger lower bound on $m_{\rm LQ}$, now straddling 2 TeV and being higher for the vector LQs than that for the scalar ones. From the study of the large-p_T spectrum of the differential cross-section of

Model		$R_{K^{(*)}}$	$R_{D^{(*)}}$	$R_{K^{(*)}}$ & $R_{D^{(*)}}$
S_3	$(\bar{\mathbf{3}}, \mathbf{3}, 1/3)$	✓	✗	✗
S_1	$(\bar{\mathbf{3}}, \mathbf{1}, 1/3)$	✗	✓	✗
R_2	$(\mathbf{3}, \mathbf{2}, 7/6)$	✗	✓	✗
U_1	$(\mathbf{3}, \mathbf{1}, 2/3)$	✓	✓	✓
U_3	$(\mathbf{3}, \mathbf{3}, 2/3)$	✓	✗	✗

Table 5.2: *Summary of the LQ models which can accommodate $R_{K^{(*)}}$ (first column), $R_{D^{(*)}}$ (second column), and both $R_{K^{(*)}}$ and $R_{D^{(*)}}$ (third column), without being in conflict with existing constraints. See text for details.*

$pp \to \ell\ell$, we extract the upper bounds on Yukawa couplings which provide us with constraints complementary to those inferred from the low-energy observables.

Whenever available we use the improved theoretical expressions and improved hadronic inputs. On the basis of our results, which are summarized in Table 5.2, we confirm that none of the scalar LQs alone, with the mass $m_{\rm LQ} \lesssim 2$ TeV, can be a viable scenario of NP that captures both types of anomalies, $R^{\rm exp}_{K^{(*)}} < R^{\rm SM}_{K^{(*)}}$ and $R^{\rm exp}_{D^{(*)}} > R^{\rm SM}_{D^{(*)}}$. Instead, one can combine S_3 with either S_1 or R_2 [35, 177, 178, 180, 181] to get a model suitable for describing all of the data in a scenario requiring the least number of parameters. We investigate one such scenario in Sec. 5.3.

With the new experimental data we were able to better examine the model with R_2 scalar LQ, and check on the possibility of describing the $R^{\rm exp}_{K^{(*)}} < R^{\rm SM}_{K^{(*)}}$ anomaly through the loop process. We found that $\mathcal{B}(Z \to \mu\mu)$ and the constraint coming from the high p_T shape of the $pp \to \mu\mu$ cross-section at the LHC are complementary to each other and allow us to rule out the model (to 1σ) if $R_{K^{(*)}} \lesssim 0.9$.

Besides the scalar LQs we also considered the vector one, U_1, for which we could not account for the loop induced processes, such as Δm_{B_s}, but by focusing on the tree level observables alone we could confirm that this scenario, in its minimal setup ($x_R = 0$) can describe both $R^{\rm exp}_{D^{(*)}} > R^{\rm SM}_{D^{(*)}}$ and $R^{\rm exp}_{K^{(*)}} < R^{\rm SM}_{K^{(*)}}$. In this U_1 model all the exclusive processes based on $b \to c\tau\bar{\nu}$ are modified by the same multiplicative factor so that all the LFUV ratios are the same. In other words, and with the currently available experimental information, $1.05 \lesssim R_X/R^{\rm SM}_X \lesssim 1.25$, $X \in \{D^{(*)}, D_s^{(*)}, J/\psi, \Lambda_c^{(*)}, \dots\}$. Also interesting are the upper and lower bounds on the LFV $b \to s\mu\tau$ modes. While the upper bound is already superseded by the experimentally established one, this scenario provides us with the lower bound, which we found to be $\mathcal{B}(B \to K\mu\tau) \gtrsim 0.7 \times 10^{-7}$. In this study we also included baryons and obtain $1.2 \times 10^{-7} \lesssim \mathcal{B}(\Lambda_b \to \Lambda\mu\tau) \lesssim 6.6 \times 10^{-5}$, where the lower bound is a prediction of the U_1 model discussed here, and the upper bound is obtained by rescaling the experimental bound on $\mathcal{B}(B \to K\mu\tau)$.

5.3 R_2-S_3 combined model

5.3.1 Introduction

We established in Sec. 5.2 that the only viable scenario involving a single $\mathcal{O}(1\ \mathrm{TeV})$ LQ mediator that can accommodate the B-anomalies while remaining consistent with other measured low energy flavor observables, as well as with the bounds arising from collider searches at the LHC is the U_1 vector leptoquark. While the vector LQ is an appealing solution, it creates problems when building a particular model because the resulting effective theory is not renormalizable unless a particular ultra-violet (UV) completion to the theory is specified [167]. This, in turn, necessitates introducing more states, and more parameters, which require many assumptions to be made to make a predictive model. An alternative to that scenario is to combine two scalar LQs, such as $S_1 = (\overline{\mathbf{3}}, \mathbf{1}, 1/3)$ with $S_3 = (\overline{\mathbf{3}}, \mathbf{3}, 1/3)$ [250], or $R_2 = (\mathbf{3}, \mathbf{2}, 7/6)$ with S_3. The advantage of the two scalar LQ scenarios is that they remain renormalizable, the loop processes can be easily computed without the necessity of introducing a UV cutoff by hand, so that, once measured, such processes can be used as constraints. In Ref. [35] a model in which the R_2 leptoquark is combined with S_3 both with mass $\mathcal{O}(1\ \mathrm{TeV})$ has been proposed. To make it minimalistic we chose the structure of the NP couplings such that the matrices of left-handed couplings to R_2 and S_3 are related via $y_3^L = y_2^L$, a pattern that can provide a plausible embedding of the resulting effective theory in a $SU(5)$ unification scenario.

In this section, we update the analysis presented in Ref. [35] to show that the proposed scenario is still viable and consistent with the current experimental data. Furthermore, we discuss several new observables, including those relevant to the angular distributions of $B \to D^*(\to D\pi)\tau\bar{\nu}$ and $\Lambda_b \to \Lambda_c(\to \Lambda\pi)\tau\bar{\nu}$ that were discussed in Chapter 3, the measurement of which can help distinguishing this particular model from the other ones proposed in the literature. Another novelty is the analysis of the high-p_T tails both of the mono-τ and di-τ events for various leptoquark masses, which was not discussed in the first proposal of this model [35].

5.3.2 Model

As mentioned above, we combine R_2 with S_3 LQs to accommodate both kinds of B-anomalies. More specifically, as discussed in Sec. 5.2, the (partial) branching fractions of the exclusive $b \to s\mu\mu$ can be accurately described by a S_3 LQ, while a R_2 LQ is responsible for the excess of events based on the $b \to c\tau\bar{\nu}$ transition.

To be more specific, the interaction Lagrangian between the LQs and the SM fermions in this model reads:

$$\mathcal{L} \supset \mathcal{L}_{R_2} + \mathcal{L}_{S_3}, \tag{5.4}$$

In the mass eigenstate basis the above Lagrangian becomes:

$$\begin{aligned}
\mathcal{L} \supset &+ (V[y_2^R])^{ij} \bar{u}_{Li} \ell_{Rj} R_2^{\frac{5}{3}} + [y_2^R]^{ij} \bar{d}_{Li} \ell_{Rj} R_2^{\frac{2}{3}} \\
&- (V_R^{u\dagger}[y_2^L]U)^{ij} \bar{u}_{Ri} \nu_{Lj} R_2^{\frac{2}{3}} + (V_R^{u\dagger}[y_2^L])^{ij} \bar{u}_{Ri} \ell_{Lj} R_2^{\frac{5}{3}} \\
&- [y_3^L]^{ij} \bar{d}_{Li}^C \nu_{Lj} S_3^{\frac{1}{3}} + \sqrt{2}(V^*[y_3^L])^{ij} \bar{u}_{Li}^C \nu_{Lj} S_3^{-\frac{2}{3}} \\
&- \sqrt{2}[y_3^L]^{ij} \bar{d}_{Li}^C \ell_{Lj} S_3^{\frac{4}{3}} - (V^*[y_3^L])^{ij} \bar{u}_{Li}^C \ell_{Lj} S_3^{\frac{1}{3}} \\
&+ \text{h.c.},
\end{aligned} \tag{5.5}$$

where the superindices in R_2 and S_3 refer to the electric charge and V_R^u is the rotation matrix of the right-handed up quarks between the flavor and mass basis as defined in Eq. 1.19. We neglected the PMNS matrix. In what follows we will assume the components of the R_2 doublet and those of the S_3 triplet to be mass degenerate, respectively.

Concerning the coupling matrices, we assume their structure to be minimalistic and the non-zero values are:

$$[y_2^R] = \begin{pmatrix} 0 & 0 & 0 \\ 0 & 0 & 0 \\ 0 & 0 & y_R^{b\tau} \end{pmatrix}, \; V_R^{u\dagger}[y_2^L] = \begin{pmatrix} 0 & 0 & 0 \\ 0 & -y_L^{c\mu} & -y_L^{c\tau} \\ 0 & 0 & 0 \end{pmatrix}, \tag{5.6}$$

where, as mentioned above, we take $[y_3^L] = [y_2^L]$, namely,

$$[y_3^L] = -\begin{pmatrix} 1 & 0 & 0 \\ 0 & \cos\theta & \sin\theta \\ 0 & -\sin\theta & \cos\theta \end{pmatrix} \begin{pmatrix} 0 & 0 & 0 \\ 0 & -y_L^{c\mu} & -y_L^{c\tau} \\ 0 & 0 & 0 \end{pmatrix}. \tag{5.7}$$

In summary, the New Physics (NP) parameters in this model are: m_{R_2}, m_{S_3}, $y_R^{b\tau}$, $y_L^{c\mu}$, $y_L^{c\tau}$, and θ. All of the mentioned parameters are real except for $y_R^{b\tau}$ which we allow to be complex in order to accommodate for the complex phases mentioned in Sec. 5.2.3.

Matching to the EFT

Substituting the NP couplings in the matching equation of Sec. 2.2.1, we obtain

$$g_{S_L}(\Lambda) = 4\, g_T(\Lambda) = \frac{y_L^{c\tau}\; y_R^{b\tau\,*}}{4\sqrt{2} G_F V_{cb}\, m_{R_2}^2}, \tag{5.8}$$

at the scale $\mu = \Lambda \simeq m_{R_2}$. As explained in Sec. 2.1.2, that relation translates to $g_{S_L}(m_b) \approx 8.1 \times g_T(m_b)$ [25] due to the renormalization group running from $\Lambda \simeq 1\,\text{TeV}$ down to the low energy scale $\mu = m_b$. More specifically, since $g_{S_L}(m_b) = 1.56\, g_{S_L}(\Lambda)$, and $g_T(m_b) = 0.77\, g_T(\Lambda)$, one then obtains $g_{S_L}(m_b) \approx 8.1 \times g_T(m_b)$. The contribution to $b \to c\tau\bar{\nu}$ from S_3 is tiny [35] and will be neglected in the following discussion.

The matching to the neutral current Lagrangian Eq. 2.3 reads:

$$\begin{aligned} \delta C_9 = -\delta C_{10} &= \frac{\pi v^2}{V_{tb} V_{ts}^* \alpha_{\text{em}}} \frac{\left(Y_L^{(S_3)}\right)^{b\mu} \left(Y_L^{(S_3)}\right)^{s\mu\,*}}{m_{S_3}^2} \\ &= -\frac{\pi v^2}{V_{tb} V_{ts}^* \alpha_{\text{em}}} \frac{\sin 2\theta \, \left|y_L^{c\mu}\right|^2}{2\, m_{S_3}^2}. \end{aligned} \tag{5.9}$$

5.3.3 Phenomenological Analysis

$R_{D^{(*)}}$

From Fig. 5.7 we see that for all currently viable values of g_{S_L}, that are consistent with $R_{D^{(*)}}^{\text{exp}}$, one must have $\text{Im}[g_{S_L}] \neq 0$. That is why we emphasized after Eq. (5.7) that one of the couplings entering the expression for g_{S_L} in Eq. (5.8) should be complex, which we chose to be $y_R^{b\tau}$.

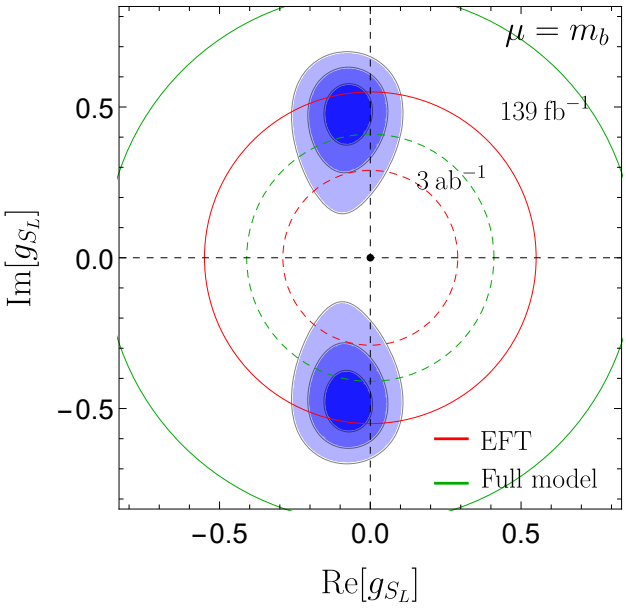

Figure 5.7: *1σ, 2σ and 3σ regions of complex values for $g_{S_L} \equiv g_{S_L}(m_b)$ allowed by $R^{\rm exp}_{D^{(*)}}$, cf. Eqs. (2.1,5.8). Red and green circles correspond to the constraints on this coupling obtained from analysis of the high-p_T tail of $pp \to \tau\nu$, as obtained from the LHC data [213, 251]. See text for more details.*

Constraints on g_{S_L} from high-p_T tails of $pp \to \tau\nu$

The previously obtained bounds on EFT coefficients from the high-p_T tail distribution of $pp \to \tau\nu$ events at LHC amounts to

$$|g_{S_L}| \leq 0.51\,, \tag{5.10}$$

which is obtained by recasting to our problem the bounds on W' obtained from 139 fb^{-1} by ATLAS [213], under the condition $g_{S_L} = 4g_T$, which upon evolving down to $\mu = m_b$ amounts to represented by the red circle in Fig. 5.7.

Since the LQ masses that we work with are quite light compared to the scale at which the EFT expansion converges properly for the study of high-p_T tails [157], one should also use the propagating LQ, and check on the difference with respect to the bounds on g_{S_L} obtained by treating LQ as static.

It is possible to adapt directly the results of Sec. 5.1 by noticing that the coupling structures factorizes out of the partonic cross-section. Indeed, using the Lagrangian specified in Sec. 5.3.2, for the partonic cross section we obtain:

$$\begin{aligned}\frac{\mathrm{d}\hat{\sigma}\left(c\bar{b} \to \tau^+\nu_\tau\right)}{\mathrm{d}\hat{t}} = \frac{1}{192\pi\hat{s}^2}\Bigg[&\frac{g^4\,|V_{cb}|^2\,\hat{t}^2}{\left(\hat{s}-m_W^2\right)^2} \\ &+ \frac{\sin^2\theta\,|V_{cs}\cos\theta - V_{cb}\sin\theta|^2\,\left|y^L_{c\tau}\right|^4\,\hat{t}^2}{4\left(\hat{t}-m^2_{S_3}\right)^2} + \frac{\left|y^L_{c\tau}\right|^2\left|y^R_{b\tau}\right|^2\,\hat{u}^2}{\left(\hat{u}-m^2_{R_2}\right)^2} \\ &+ \frac{g^2\sin\theta\,\mathrm{Re}\left[\left(V_{cs}\cos\theta - V_{cb}\sin\theta\right)V^*_{cb}\right]\left|y^L_{c\tau}\right|^2\,\hat{t}^2}{\left(\hat{s}-m_W^2\right)\left(\hat{t}-m^2_{S_3}\right)}\Bigg],\end{aligned} \tag{5.11}$$

with a similar expression for $b\bar{c} \to \tau^- \bar{\nu}_\tau$, where the first term within the brackets corresponds to the SM contribution, followed by the S_3 and R_2 contributions, and finally the last term is interference between S_3 and the SM contributions. Note that the fermion masses in the above expression have been neglected. It appears that, for our phenomenological application, the R_2 term indeed dominates because the S_3 term is suppressed with respect to R_2 by $V_{cs}\cos\theta - V_{cb}\sin\theta$, in which the first term is small due to a tiny $\cos\theta$ and the second one due to the smallness of V_{cb}. One can therefore write:

$$\hat{\sigma}(\hat{s}) \simeq \frac{|y^R_{b\tau}|^2\left(|y^L_{c\tau}|^2 + |y^L_{c\mu}|^2\right)}{192\pi m^2_{R_2}}\left[\frac{x+2}{x(1+x)} - \frac{2\log(1+x)}{x^2}\right], \tag{5.12}$$

where $x = \hat{s}/m^2_{R_2}$. Again, after recasting the results by ATLAS [213] and using the above expressions, we obtain

$$\left(\left|y^L_{c\tau}\right|^2 + \left|y^L_{c\mu}\right|^2\right)\left|y^R_{b\tau}\right|^2 < 5.95\,, \tag{5.13}$$

which then can be combined into g_{S_L} via Eq. (2.19), and evolved down to $\mu = m_b$. For the benchmark mass, $m_{R_2} = 1.3$ TeV, we then find,

$$|g_{S_L}| \leq 0.88\,, \tag{5.14}$$

shown by a green circle in Fig. 5.7. Note that this bound, obtained by including the propagating R_2, is far less stringent than the one deduced from the data after integrating out R_2, c.f. Eq. (5.10) as discussed in Sec. 4.5.

In summary, from the current data by ATLAS regarding the mono-tau high-p_T tails, and by including the propagation of the R_2 LQ of $m_{R_2} = 1.3$ TeV, one cannot obtain a very useful constraint on the NP couplings appearing in Eq. (2.1). However, by assuming the data to be Gaussian in each bin, one can make a simple projection to an integrated $3\ \text{ab}^{-1}$ of the LHC data and arrive at $|g_{S_L}| \leq 0.41$, which would indeed be a powerful constraint. In Fig. 5.7 the dashed circles correspond to the projected bounds both by using the effective and propagating R_2 of $m_{R_2} = 1.3$ TeV.

$R_{K^{(*)}}$

In order to accommodate the neutral current anomaly $\delta C_9 = -\delta C_{10} = -0.41 \pm 0.09$ [28], and knowing that $V_{tb}V^*_{ts} < 0$, one should have $\sin 2\theta < 0$. The factor $\sin 2\theta$ provides a desired suppression of the $b \to s\mu\mu$ decays with respect to $b \to c\tau\bar{\nu}$. Indeed, from the fit with data we obtain $|\theta| \approx \pi/2$, i.e. slightly larger than but close to $\pm\pi/2$. The contribution of this model to the $B_s - \bar{B}_s$ mixing amplitude comes from the S_3 box-diagram and it is proportional to $\sin^2(2\theta)$, thus again bringing a desired suppression since we know that the SM contribution saturates the measured Δm_{B_s}. More precisely, the S_3 contribution to Δm_{B_s} is $\propto \sin^2 2\theta \left[\left(y^{c\mu}_L\right)^2 + \left(y^{c\tau}_L\right)^2\right]^2 / m^2_{S_3}$.

Parameter space of the R_2-S_3 model

Besides $R_{D^{(*)}}$, $R_{K^{(*)}}$ and $\mathcal{B}(B_s \to \mu\mu)$ discussed so far in this section, and which are the most important constraints on the parameters of this model, the following quantities are used as further constraints:

- The $B_s - \bar{B}_s$ mixing is included by considering $R(\Delta m_{B_s}) = \Delta m_{B_s}/\Delta m_{B_s}^{\rm SM}$. We combine the improved experimental value with the lattice QCD result by HPQCD [252] and obtain $R(\Delta m_{B_s})^{\rm exp} = 1.027(68)$. We also performed the full scan of parameter space using the FLAG value for the corresponding hadronic matrix element as computed with $N_f = 2+1$ dynamical quark flavors, which corresponds to $R(\Delta m_{B_s})^{\rm exp} = 0.897(69)$ [62], and found no significant impact to the selected parameter space, except for the slightly different value of $\chi^2_{\rm min}$.

- We require the results to be consistent with $R_{D^{(*)}}^{(\mu/e)\,\rm exp} = 0.977(43)$ [31], which is obtained by combining $R_D^{(\mu/e)\,\rm exp} = 0.995(45)$ [103] with $R_{D^*}^{(\mu/e)\,\rm exp} = 1.04(5)$ [253]. Note that in this model only S_3 can contribute to $R_{D^{(*)}}^{(\mu/e)} = \mathcal{B}(B \to D^{(*)}\mu\bar{\nu})/\mathcal{B}(B \to D^{(*)}e\bar{\nu})$.

- We also impose the measured $\mathcal{B}(B \to \tau\nu) = 1.09(24) \times 10^{-4}$ [56] as a constraint, where we use $f_B = 190.0 \pm 1.3$ MeV [62]. When needed we take the CKM couplings from Ref. [254].

- Tests of LFUV in the kaon leptonic decays can also be used as constraints to the S_3 LQ. We consider $r_K^{(e/\mu)} = \Gamma(K \to e\bar{\nu})/\Gamma(K \to \mu\bar{\nu})$ and $r_K^{(\tau/\mu)} = \Gamma(\tau \to K\bar{\nu})/\Gamma(K \to \mu\bar{\nu})$, the measured values of which [56] are compared to the SM values, $r_K^{(e/\mu)\,\rm exp}/r_K^{(e/\mu)\,\rm SM} = 1.004(4)$, $r_K^{(\tau/\mu)\,\rm exp}/r_K^{(\tau/\mu)\,\rm SM} = 0.972(14)$, and represent a rather powerful constraint, cf. Ref. [31]. Similarly, the ratio $r_{D_s}^{(\tau/\mu)} = \mathcal{B}(D_s \to \tau\bar{\nu})/\mathcal{B}(D_s \to \mu\bar{\nu})$, is converted to a constraint when comparing to $r_{D_s}^{(\tau/\mu)\,\rm exp}/r_{D_s}^{(\tau/\mu)\,\rm SM} = 1.027(52)$ [56].

- Experimental bounds on the lepton flavor violating (LFV) decay modes $\mathcal{B}(\tau \to \mu\gamma) < 4.4 \times 10^{-8}$, $\mathcal{B}(\tau \to \phi\mu) < 8.4 \times 10^{-8}$ [56] provide the significant constraints too. Note that both R_2 and S_3 contribute to the latter mode, cf. Ref. [32], while the expression for the LQ contribution to $\mathcal{B}(\tau \to \phi\mu)$ can be found in [241]. We also use $\mathcal{B}(B \to K\mu^-\tau^+) < 2.8 \times 10^{-5}$ [56, 255] in our scan of the parameter space.

- In Ref. [35] we provided the expressions for $R_{\nu\nu}^{(*)} = \mathcal{B}(B \to K^{(*)}\nu\bar{\nu})/\mathcal{B}(B \to K^{(*)}\nu\bar{\nu})^{\rm SM}$, which should respect the experimental bounds $R_{\nu\nu} < 3.9$ and $R_{\nu\nu}^* < 2.7$ [256].

- The complete expressions for the scalar LQ contributions to $\mathcal{B}(Z \to \ell\ell)$ have been derived in Ref. [244] and they are used in this analysis, together with the experimental values for the branching fractions given in Ref. [56].

- Finally, we take into account the bounds on the couplings derived from the high-p_T tails after recasting the bounds on heavy Higgs decaying to two τ-leptons obtained from $139\,\text{fb}^{-1}$ of data by ATLAS, reported in Ref. [210]. By focusing on the region of $m_{\tau\tau} \geq 700$ GeV, and by using the propagating R_2 of $m_{R_2} = 1.3$ TeV, we obtain rather stringent bounds on the couplings, which can be conveniently written as

$$1.75(y_R^{b\tau})^4 + 0.29(y_R^{b\tau})^2 + 7.96(y_L^{c\tau})^4 + 3.43(y_L^{c\tau})^2 \leq 25.9. \tag{5.15}$$

  Notice that in obtaining this result we use the experimental bounds from Ref. [210] to 2σ.

A careful reader would notice that with respect to Ref. [35], where $m_{R_2} = 0.8$ TeV has been used to present the results, here we take $m_{R_2} = 1.3$ TeV. This choice is made in order to be consistent with the most recent bounds regarding the LQ production processes in the direct searches at the LHC, as discussed in Ref. [28]. For the same reason we take $m_{S_3} = 2$ TeV and

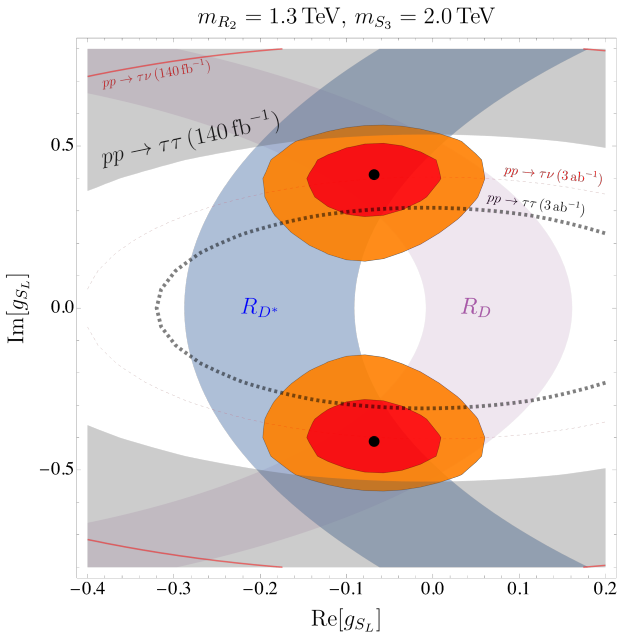

Figure 5.8: *Results of the flavor fit in the g_{S_L} plane, as defined in Eq. (2.1) for the transition $b \to c\tau\bar{\nu}_\tau$. The allowed $1\,\sigma(2\,\sigma)$ regions are shown in red (orange). Separate constraints from R_D and R_{D^*} to $2\,\sigma$ accuracy are shown by the purple and blue regions, respectively. The current LHC exclusions are depicted by the gray regions. We also show the projected bounds expected to be obtained from the high p_T mono-tau (red curve) and di-tau tails (dashed curve) with $3\ \text{ab}^{-1}$ of data.*

perform a scan over the remaining parameters of the model, $y_R^{b\tau}$, $y_L^{c\mu}$, $y_L^{c\tau}$ and $\theta \in (\pi/2, \pi) \cup (-\pi/2, 0)$, by imposing all of the constraints discussed so far. In Fig. 5.8 we show the result of such a scan in the $g_{S_L} \equiv g_{S_L}(m_b)$ plane. We obtain $\chi^2_{\text{min}} = 13.5$, and for the best fit values we get (to 1σ)

$$\text{Re}[g_{S_L}] = -0.07(14),\ |\text{Im}[g_{S_L}]| = 0.44\,\left(^{+0.09}_{-0.12}\right)\ . \tag{5.16}$$

If we did not use the experimental bounds on the LFV modes as constraints, our flavor fit would have given two solutions: one corresponding to a small angle $\theta \sim 0$, and another one corresponding to $|\theta| \sim \pi/2$. In fact, $\mathcal{B}(\tau \to \mu\phi) \propto \cos^4\theta$, and the corresponding experimental bound help us select a viable solution, i.e. the one with $|\theta| \approx \pi/2$.

In Fig. 5.8 we also plot the current constraint, $|g_{S_L}| < 0.55$, obtained from the study of the high-p_T di-tau tails. In the same plot, we also show the projected bound from $3\ \text{ab}^{-1}$ of data, a constraint that based on current information should be much stronger than the one based on the high-p_T mono-tau tails.

Before closing this Section we also provide the ranges for the couplings we obtain after imposing all of the constraints discussed so far:

$$\begin{aligned}
y_L^{c\mu} &\in (0.16, 0.33)_{1\sigma}, (0.11, 0.40)_{2\sigma}, \\
y_L^{c\tau} &\in (0.87, 1.40)_{1\sigma}, (0.64, 1.54)_{2\sigma}, \\
\text{Re}\left[y_R^{b\tau}\right] &\in (-0.37, 0.02)_{1\sigma}, (-0.58, 0.15)_{2\sigma}, \\
\left|\text{Im}\left[y_R^{b\tau}\right]\right| &\in (0.83, 1.53)_{1\sigma}, (0.61, 1.87)_{2\sigma}, \\
\theta &\in \frac{\pi}{2}(1.01, 1.06)_{1\sigma}, \frac{\pi}{2}(1.01, 1.12)_{2\sigma},
\end{aligned} \tag{5.17}$$

where $\mathrm{Im}\left[y_R^{b\tau}\right]$ has two symmetric solutions (positive and negative).

5.3.4 More Observables

Contribution to the electric dipole moment of the neutron

From fit to the data we saw that we obtain $\mathrm{Im}[g_{S_L}] \gg \mathrm{Re}[g_{S_L}]$ when accommodating $R_{D^{(*)}}^{\mathrm{exp}} > R_{D^{(*)}}^{\mathrm{SM}}$. In other words we get a large $|\mathrm{Im}\left[y_R^{b\tau}\right]|$, which then calls for a careful analysis of the observables in which such a complex phase may play a significant role. We first check whether or not this phase might be in conflict with the current bound on the electric dipole moment of the neutron, $|d_n| < 1.8 \times 10^{-26}\ e$cm [257]. That issue has recently been addressed in Ref. [258] in the scenarios in which the SM is extended by one or more scalar leptoquarks. For our purpose it is important to note that the charm quark contribution to d_n can be written as $d_n = g_T^c\, d_c$, where the tensor charge g_T^c, defined as

$$\langle N|\bar{c}\sigma^{\mu\nu}\gamma_5 c|N\rangle = g_T^c\, \bar{u}_N \sigma^{\mu\nu}\gamma_5 u_N\,, \tag{5.18}$$

has been recently computed by means of numerical simulations of QCD on the lattice with $N_{\mathrm{f}} = 2+1+1$ dynamical quark flavors [259]. The reported result at $\mu = 2$ GeV, in the $\overline{\mathrm{MS}}$ renormalization scheme is $g_T^c = -(2.4 \pm 1.6) \times 10^{-4}$. We translate the notation of Ref. [258] to the one used here and write:

$$\begin{aligned} d_c &= 0.1 \times Q_c\, e\, m_c\, \frac{1}{m_{R_2}^2}\, \mathrm{Im}\left[V_{cb}^*\, y_R^{b\tau\,*}\, y_L^{c\tau}\right] \\ &\simeq 0.1 \times Q_c\, e\, m_c\, \frac{4\sqrt{2} G_F V_{cb}^2}{1.7}\, \mathrm{Im}\left[g_{S_L}\right], \end{aligned} \tag{5.19}$$

where in the second line we employed Eq. (5.8). In the denominator 1.7 accounts for the running of g_{S_L} to the low energy scale. By using the charm quark mass value from Ref. [62], the central value for g_T^c, and the experimental bound on $|d_n|$, we arrive at

$$|\mathrm{Im}\left[g_{S_L}\right]| < 0.76\,, \tag{5.20}$$

which is obviously in good agreement with what we obtain in Fig. 5.8 and in Eq. (5.16). However, we should note that if instead of the central value we take $g_T^c = -4 \times 10^{-4}$ then this constraint translates to $|\mathrm{Im}\left[g_{S_L}\right]| < 0.46$, which would eliminate a fraction of the allowed g_{S_L} regions in Fig. 5.8. This shows why a more precise lattice QCD value of g_T^c would be highly beneficial for checking the validity of the model proposed in Ref. [35] and further discussed here.

Contribution to Δa_{CP}

The difference in the time-integrated CP asymmetries of $D^0 \to K^+K^-$ and $D^0 \to \pi^+\pi^-$ has been measured by LHCb. Their recent result $\Delta A_{\mathrm{CP}} = (-15.4 \pm 2.9) \times 10^{-4}$ [260] has been corrected for the effects of $D^0 - \overline{D}^0$ mixing so that the result for the difference of direct CP asymmetries becomes $\Delta a_{\mathrm{CP}}^{\mathrm{dir}} = (-15.7 \pm 2.9) \times 10^{-4}$ [261]. The interpretation of this result is still unclear. In the SM picture, the effect could be attributed to the (nonperturbative) rescattering of light mesons in the final state. Otherwise, one would need a NP contribution to accommodate the measured value [262].

In Ref. [263] the NP contribution to $\Delta a_{\rm CP}$ has been estimated under the assumption of the maximal strong phases. It was found that $|\Delta a_{\rm CP}| \lesssim 1.8|{\rm Im}C_8^{\rm NP}(m_c) + {\rm Im}C_{8'}^{\rm NP}(m_c)|$, where $C_{8,8'}$ are the Wilson coefficients of the chromomagnetic operators:

$$\mathcal{H} = \frac{G_F}{\sqrt{2}} \frac{g_s m_c}{4\pi^2} \bar{u}_L \sigma_{\mu\nu} \left[C_8 P_R + C_{8'} P_L\right] c \, T^a G_a^{\mu\nu}. \tag{5.21}$$

In our model R_2 will contribute to $c_R \to u_L g$ and to one-loop we get

$$C_8^{\rm NP} = \frac{m_\tau V_{ub} y_R^{b\tau} y_L^{c\tau *}}{4\sqrt{2} G_F m_c} B_0'(0, m_{R_2}^2, m_\tau^2)\,. \tag{5.22}$$

With the structure of couplings chosen in our model, cf. Eq. (5.6), there is no one-loop contribution to $c_L \to u_R g$, i.e. $C_{8'} = 0$. By taking $m_\tau/m_{R_2} \to 0$, we have $B_0'(0, m_{R_2}^2, 0) \to 1/(2m_{R_2}^2)$, which then leads to $|\Delta a_{CP}| \lesssim 10^{-4}$, thus a very small effect.

Contribution to $B \to K\nu\nu$ and $K \to \pi\nu\nu$

It is well known that a contribution of the left-handed current to $b \to s\ell\ell$ implies a similar contribution to $B \to K^{(*)}\nu\nu$ decays. In our case that means

$$R_{\nu\nu}^{(*)} = \frac{\mathcal{B}(B \to K^{(*)}\nu\nu)}{\mathcal{B}(B \to K^{(*)}\nu\nu)^{\rm SM}} = \frac{\sum_{ij} |\delta_{ij} C_L^{SM} + \delta C_L^{ij}|^2}{3|C_L^{\rm SM}|^2}, \tag{5.23}$$

where $C_L^{\rm SM} = -6.38(6)$ [264] and the tree-level contribution arising from S_3 amounts to [31]

$$\begin{aligned} \sum_{ii} \delta C_L^{ii} &= \sum_i \frac{\pi v^2}{2\alpha_{\rm em}\lambda_t} \frac{\left(Y_L^{(S_3)}\right)^{b\,i} \left(Y_L^{(S_3)}\right)^{s\,i\,*}}{m_{S_3}^2} \\ &= -\frac{\pi v^2}{2\alpha_{\rm em}\lambda_t} \frac{\sin 2\theta \, \left(y_L^{c\mu\,2} + y_L^{c\tau\,2}\right)}{m_{S_3}^2}\,, \end{aligned} \tag{5.24}$$

thus also negative, and therefore the net effect in the present model is that $R_{\nu\nu}^{(*)} > 1$. We get

$$R_{\nu\nu}^{(*)} \in (1.3, 2.5)_{1\sigma}, (1.1, 3.4)_{2\sigma}, \tag{5.25}$$

the result which is likely to be probed experimentally at Belle II [265].

The expressions relevant to the S_3 contribution to $\mathcal{B}(K \to \pi\nu\nu)$ have been derived in Ref. [266]. With our choice of couplings, together with values given in Eq. (5.17), that contribution turns out to be very small. We checked that the same conclusion holds for the R_2 contribution as well.

$B \to K\mu\tau$ and its correlation with $\tau \to \mu\gamma$ and $R_{\nu\nu}^{(*)}$

Most of the models that can accommodate the LFUV also predict a non-zero branching fraction of the associated LFV decay modes [267]. Even more interesting is that in our model we get both the lower and the upper bounds, namely and to 1σ,

$$0.6 \times 10^{-7} \lesssim \mathcal{B}(B \to K\mu^\pm\tau^\mp) \lesssim 3.1 \times 10^{-7}\,, \tag{5.26}$$

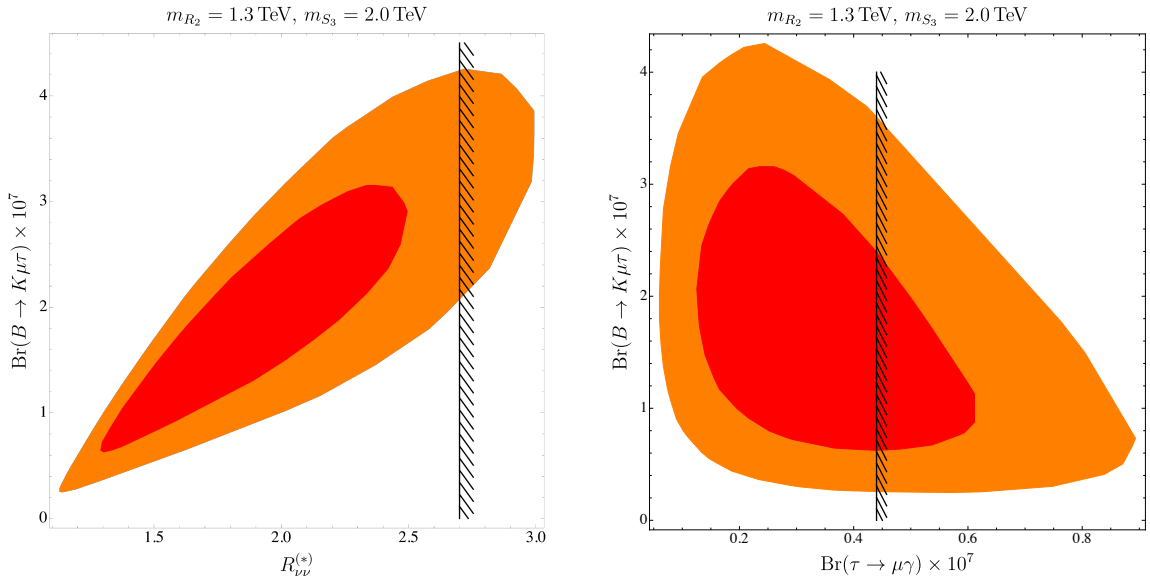

Figure 5.9: *$\mathcal{B}(B \to K\mu\tau)$ is plotted against $R^{(*)}_{\nu\nu} = \mathcal{B}(B \to K^{(*)}\nu\bar{\nu})/\mathcal{B}(B \to K^{(*)}\nu\bar{\nu})^{\text{SM}}$ for the $1\,\sigma$ (red) and $2\,\sigma$ (orange) regions of Fig. 5.8. The black line denotes the current experimental limit, $R^*_{\nu\nu} < 2.7$ [256]. We also show the similar correlation between $\mathcal{B}(B \to K\mu\tau)$ and $\mathcal{B}(\tau \to \mu\gamma)$ obtained in this model.*

currently, however, two orders of magnitude lower than the experimental limit [255]. This prediction can be translated into similar modes via relations $\mathcal{B}(B \to K^*\mu\tau) \approx 1.9 \times \mathcal{B}(B \to K\mu\tau)$, $\mathcal{B}(B_s \to \mu\tau) \approx 0.9 \times \mathcal{B}(B \to K\mu\tau)$, and $\mathcal{B}(\Lambda_b \to \Lambda\mu\tau) \approx 1.7 \times \mathcal{B}(B \to K\mu\tau)$ [268]. It is interesting to note that $\mathcal{B}(B \to K\mu\tau)$ is linearly correlated with $R^{(*)}_{\nu\nu}$, as show in Fig. 5.9.

Another interesting LFV mode is $\tau \to \mu\gamma$, because in order to accommodate both types of B-anomalies we needed to switch on the NP couplings to both τ and μ. Indeed, in this model we obtain a lower bound which to 1σ is

$$\mathcal{B}(\tau \to \mu\gamma) \gtrsim 1.2 \times 10^{-8}\,, \tag{5.27}$$

and its correlation with $\mathcal{B}(B \to K\mu\tau)$, also shown in Fig. 5.9, is less pronounced than the one between $\mathcal{B}(B \to K\mu\tau)$ and $R^{(*)}_{\nu\nu}$.

Angular observables in $B \to D^*(\to D\pi)\tau\nu$ and in $\Lambda_b \to \Lambda_c(\to \Lambda\pi)\tau\nu$

The angular analysis of the exclusive $b \to c\tau\bar{\nu}$ modes can help identify several new observables, the measurement of which could help disentangle the situation and select among the currently viable scenarios. As an example we write the full angular distribution of the baryon decay as [61]

$$\begin{aligned}\frac{d^4\mathcal{B}}{dq^2 d\cos\theta_\tau d\cos\theta d\phi} = 8\pi \Big[&\mathcal{A}_1 + \mathcal{A}_2\cos\theta \\ &+ (\mathcal{B}_1 + \mathcal{B}_2\cos\theta)\cos\theta_\tau + (\mathcal{C}_1 + \mathcal{C}_2\cos\theta)\cos^2\theta_\tau \\ &+ (\mathcal{D}_3\sin\theta\cos\phi + \mathcal{D}_4\sin\theta\sin\phi)\sin\theta_\tau \\ &+ (\mathcal{E}_3\sin\theta\cos\phi + \mathcal{E}_4\sin\theta\sin\phi)\sin\theta_\tau\cos\theta_\tau\Big],\end{aligned} \tag{5.28}$$

where the angles θ and θ_τ are defined with respect to the direction of flight of Λ_c: θ being the angle of Λ in the $\Lambda\pi$ rest frame, and θ_τ is the angle of τ in the $\tau\bar{\nu}$-rest frame. ϕ is the angle between the $\tau\bar{\nu}$ and the $\Lambda\pi$ planes. In the above expression the q^2-dependent coefficient functions, $\mathcal{A}_{1,2}$, $\mathcal{B}_{1,2}$, $\mathcal{C}_{1,2}$, $\mathcal{D}_{3,4}$, $\mathcal{E}_{3,4}$, are given in terms of kinematical quantities and hadronic form factors [61]. Notice that all of the form factors relevant to any BSM discussion are already available, as they have all been computed in lattice QCD away from the zero-recoil point [154]. Forward-backward asymmetry is defined as

$$A_{\rm fb}(q^2) = \frac{1}{2}\,\frac{\mathcal{B}_1(q^2)}{\Gamma(\Lambda_b \to \Lambda_c \tau\bar{\nu})}\,, \tag{5.29}$$

where the full decay width is given by

$$\Gamma(\Lambda_b \to \Lambda_c \tau\bar{\nu}) = \int\limits_{m_\tau^2}^{(m_{\Lambda_b}-m_{\Lambda_c})^2} dq^2 \,\left[\mathcal{A}_1(q^2) + \frac{1}{3}\mathcal{C}_1(q^2)\right]\,. \tag{5.30}$$

We find that for all of the available g_{S_L} values discussed in the previous section, the shape of $A_{\rm fb}(q^2)$ becomes different with respect to that found in the SM. In particular, the point q_0^2, at which this asymmetry is zero, $A_{\rm fb}(q_0^2) = 0$, is larger than the one found in the SM. Another quantity that one can use to monitor the viability of this model is

$$D_4(q^2) = \frac{\mathcal{D}_4(q^2)}{\Gamma(\Lambda_b \to \Lambda_c \tau\bar{\nu})}\,, \tag{5.31}$$

which is strictly zero in the SM and becomes non-zero only if the NP coupling can take a complex value, such as the case with our model, $\mathrm{Im}\,[g_{S_L}] \neq 0$. In Fig. 3.16 we illustrate the change in shape of $A_{\rm fb}(q^2)$ and of $D_4(q^2)$ once $g_{S_L} = 8.1 \times g_T$ is switched to a plausible $g_{S_L} \simeq 0.5i$.

We repeated the same exercise with $B \to D^*\tau\nu$ [63, 147–150, 178] and found that the corresponding $A_{\rm fb}(q^2)$ changes only slightly. In order to support our observations by numerical values, we compute

$$\langle O \rangle = \int\limits_{m_\tau^2}^{(M_{\Lambda_b}-M_{\Lambda_c})^2} O\; dq^2, \tag{5.32}$$

for $O \in \{A_{\rm fb}, D_4\}$, and collect the results in Tab. 5.3 where we also give the values for q_0^2 at which $A_{\rm fb}(q_0^2) = 0$ and the results for the LFUV ratio

$$R_{\Lambda_c} = \frac{\mathcal{B}(\Lambda_b \to \Lambda_c \tau\bar{\nu})}{\mathcal{B}(\Lambda_b \to \Lambda_c \mu\bar{\nu})}. \tag{5.33}$$

From Tab. 5.3 we see that R_{Λ_c} follows the pattern and $R_{\Lambda_c} > R_{\Lambda_c}^{\rm SM}$. This can be tested with a more precise measurement of R_{Λ_c}. Furthermore, in this model we clearly observe that

$$\langle A_{\rm fb}\rangle > \langle A_{\rm fb}\rangle^{\rm SM}, \qquad |\langle D_4\rangle| > |\langle D_4\rangle|^{\rm SM}\,, \tag{5.34}$$

which is in stark contrast with the models based on accommodating the B-anomalies by couplings to a U_1 vector LQ in which $\langle A_{\rm fb}\rangle = \langle A_{\rm fb}\rangle^{\rm SM}$, and $\langle D_4\rangle = 0$. It is important to emphasize that these quantities can be used to discriminate among various scenarios proposed to explain B-anomalies.

$g_{S_L}(m_b)$	0	$-0.07\,\binom{+0.14}{-0.14} + 0.44\,\binom{+0.09}{-0.12}\,i$
R_{Λ_c}	$0.333(14)$	$0.366(15)\,\binom{-0.002}{+0.009}\,\binom{+0.015}{-0.014}$
$\langle A_{\rm fb}\rangle$	$0.049(8)$	$0.085(7)\,\binom{+0.002}{+0.004}\,\binom{+0.014}{-0.016}$
$q_0^2\,[\mathrm{GeV}^2]$	$7.97(7)$	$8.49(8)\,\binom{+0.00}{+0.13}\,\binom{+0.27}{-0.25}$
$\langle D_4\rangle$	0	$0.102(1)\,\binom{+0.001}{-0.002}\,\binom{+0.016}{-0.025}$

Table 5.3: *Values of the observables relevant to $\Lambda_b \to \Lambda_c(\to \Lambda\pi)\tau\nu$, discussed in the text and computed in the SM ($g_{S_L} = 0$) and for $g_{S_L} \neq 0$, as obtained from our scan, cf. Eq. (5.16). Second and third uncertainties correspond to the variation of the central value with respect to the variation of the real and of the imaginary part of g_{S_L}, respectively.*

5.3.5 Mass range for this scenario to remain valid

So far in this section, we chose as a benchmark point the leptoquark masses $m_{R_2} = 1.3$ TeV and $m_{S_3} = 2$ TeV, consistent with the lower bounds deduced from the direct searches at the LHC, as discussed in Ref. [28]. From the low energy flavor physics observables, we then obtained the constraints on the couplings of the model, and we pointed out that the very stringent constraints on the couplings can also be obtained from the analysis of the high-p_T di-tau tails at the LHC. To monitor the range of masses preferred by this scenario we varied m_{R_2} and m_{S_3} and applied the same constraints on the couplings as before. We find that the model is highly sensitive to m_{R_2}, while it is only slightly sensitive to the variation of m_{S_3}. The result is shown in Fig. 5.10 where we see that the current setup of Yukawa matrices, cf. Eqs. (5.6,5.7), remain consistent with the constraints to 2σ if $m_{R_2} \lesssim 4.3$ TeV. In other words, if the flavor constraints remain unchanged, this scenario can be tested at the LHC. It is also interesting to note from Fig. 5.10 that the effective coupling $y_{\rm eff} = \sqrt{|y_L^{c\tau} y_R^{b\tau\,*}|}$ always remains well below the perturbativity limit, $y_{\rm eff} \leq \sqrt{4\pi}$.

5.3.6 Conclusion

We update the parameter space of the model in which the SM is extended by $\mathcal{O}(1\,\mathrm{TeV})$ two scalar LQs, R_2 and S_3, and show that this model is still a plausible framework to accommodate the B-anomalies while remaining consistent both with a number of experimental constraints arising from the low energy observables, as well as with those deduced from the LHC measurements relevant to the high-p_T tails of $pp \to \tau\tau$ and $pp \to \tau\nu$. A peculiarity of this R_2-S_3 scenario is that there is a complex coupling. We find that the size of the corresponding imaginary part of the model parameter $y_R^{b\tau} \propto g_{S_L}$ results in: (i) a value of the electric dipole moment of the neutron consistent with the experimental bound, (ii) too small a contribution to $\Delta a_{\rm CP}$, the difference of the CP-asymmetries between $D^0 \to K^+K^-$ and $D^0 \to \pi^+\pi^-$, (iii) a significant change in the observables that can be deduced from the angular distribution of $B \to D^*(\to D\pi)\tau\nu$ and $\Lambda_b \to \Lambda_c(\to \Lambda\pi)\tau\nu$ and which are zero in the SM and in scenarios in which the NP couplings are real. We also find that the forward-backward asymmetry in the case of $\Lambda_b \to \Lambda_c\tau\nu$

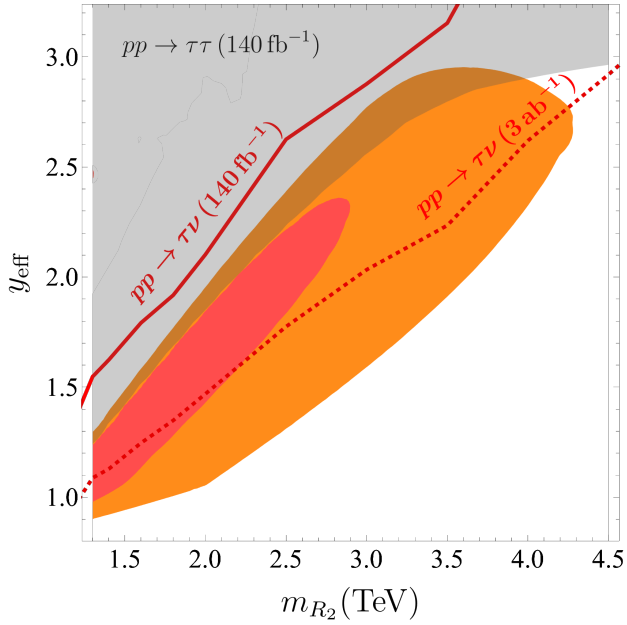

Figure 5.10: *We plot the dependence of the effective coupling* $y_{\mathrm{eff}} = \sqrt{|y_L^{c\tau} y_R^{b\tau\,*}|}$ *on the variation of the leptoquark mass* m_{R_2}*. The orange regions are allowed by the low energy flavor physics constraints to* 1σ *and* 2σ*. The gray area is excluded by the* 2σ *limits arising from the study of the high-*p_T *tails of* $pp \to \tau\tau$*, as obtained from the currently available LHC data. We also plot the limit from the case of mono-tau in the final state.*

becomes significantly different from its SM value. Like in the other models built to accommodate B-anomalies and involving LQs, we establish the upper and lower bounds to the exclusive LFV decay modes based on $b \to s\mu^{\pm}\tau^{\mp}$. We also checked that the model gives a negligible contribution to $\mathcal{B}(K \to \pi\nu\nu)$, but it significantly enhances $\mathcal{B}(B \to K^{(*)}\nu\nu)$, cf. (5.25), which will soon be experimentally scrutinized at Belle-II. We also find a clear correlation between $\mathcal{B}(B \to K^{(*)}\nu\nu)$ and the LFV decays such as $\mathcal{B}(B \to K\mu\tau)$. Importantly, the model remains consistent with the current experimental upper bound on $\mathcal{B}(\tau \to \mu\gamma)$.

Chapter 6

Synthèse en français

6.1 Le Modèle Standard

Le Modèle Standard (MS) de la physique des particules figure parmi les théories les plus prédictives de la Nature. Sa validité a été continuellement testée expérimentalement avec une précision inégalée, aboutissant à la découverte en 2012 au LHC de la dernière pierre du Modèle Standard : le boson de Higgs.

Cependant, le Modèle Standard ne peut pas être la théorie finale de la Nature. En effet, malgré tous ses succès, il existe des observations que le MS ne peut expliquer. Celles-ci comprennent :

- L'absence de mécanisme pour la génération de la masse des neutrinos. Les valeurs absolues de ces masses n'ont pas encore été mesurées, mais l'observation des oscillations des neutrinos et la cosmologie prouvent qu'elle sont non-nulles.

- L'absence de candidat pour une particule de matière noire. La matière noire est nécessaire pour expliquer le comportement des structures à très grande échelle, telle que la vitesse de rotation des galaxies. Le Modèle Standard ne contient aucune particule suffisamment massive et aux interactions suffisamment faibles pour jouer ce rôle.

- Le problème de hiérarchie. Le boson de Higgs est une particule scalaire, les corrections quantiques à sa masse sont donc proportionnelles à l'échelle maximale de la théorie, l'échelle de Planck, de l'ordre de 10^{19} GeV. Une annulation anormalement exacte est alors nécessaire pour obtenir un Higgs léger de seulement 125 geV.

- Le problème de la saveur. Les masses des fermions dans la théorie sont organisées suivant des motifs fortement organisés. Chaque famille est plus lourde que la précédente : au total 6 ordres de grandeurs séparent le fermion le plus lourd (quark top, 173 geV) et le plus léger (électron, 511 keV). De même, la matrice de Cabibbo-Kobayashi-Maskawa (CKM) qui régit le mélange des quarks présente également une structure très hiérarchisée. Tous ces paramètres ne dépendent que des couplages de Yukawa, qui n'obéissent pourtant aucune symétrie dans le Modèle Standard. Le secteur de la saveur a également reçu un regain d'attention durant la dernière décennie grâce à la découverte des "anomalies du B",

Pour toutes ces raisons, le MS doit nécessite d'être complété par de la Nouvelle Physique (NP). Dans cette thèse, nous explorons en particulier le dernier point, en construisant de nou-

velles observables de saveurs, dans le but d'élucider la structure sous-jacente au secteur de Yukawa du MS.

6.2 Possibles Extensions du Modèle Standard

Les motivations présentées précédemment ne nous donnent que peu d'informations concernant la nature de la Nouvelle Physique. Il est donc important de travailler dans un cadre indépendant du modèle considéré. Cela est rendu possible grâce à une approche de théorie effective des champs (EFT), à une échelle de quelques TeV [15].

Ainsi, pour encapsuler toutes les dynamiques possibles à basses énergies, il suffit d'étendre le Lagrangien du Modèle Standard par tous les opérateurs satisfaisant les mêmes symétries que le MS. Explicitement, le Lagrangien effectif pour les transitions semi-leptoniques chargées fait intervenir 5 opérateurs:

$$\begin{aligned}\mathcal{L}_{\text{eff}}^{CC} = -2\sqrt{2}G_F V_{ij}\Big[&(1+g_{V_L}^{ij\,\ell})\,(\bar{u}_{Li}\gamma_\mu d_{Lj})\,(\bar{\ell}_L\gamma^\mu\nu_L) + g_{V_R}^{ij\,\ell}\,(\bar{u}_{Ri}\gamma_\mu d_{Rj})\,(\bar{\ell}_L\gamma^\mu\nu_L) \\ &+ g_{S_L}^{ij\,\ell}(\mu)\,(\bar{u}_{Ri}d_{Lj})\,(\bar{\ell}_R\nu_L) + g_{S_R}^{ij\,\ell}\,(\bar{u}_{Li}d_{Rj})\,(\bar{\ell}_R\nu_L) + g_T^{ij\,\ell}(\mu)\,(\bar{u}_{Ri}\sigma_{\mu\nu}d_{Lj})\,(\bar{\ell}_R\sigma^{\mu\nu}\nu_L)\Big] + \text{h.c.}\,,\end{aligned} \tag{6.1}$$

généralisant l'interaction de Fermi. De la même manière pour les courants neutres, on considère le Lagrangien suivant :

$$\mathcal{L}_{\text{eff}}^{NC} = \frac{4G_F}{\sqrt{2}}V_{t\alpha}V_{t\beta}^*\sum_i C_i\,\mathcal{O}_i + \text{h.c.}\,, \tag{6.2}$$

où tous les opérateurs sont définis Eq. (2.4). Au dessus de l'échelle électrofaible, il est nécessaire de tenir compte de la propagation des bosons de jauge. Nous préférerons donc utiliser la Théorie Effective du Modèle Standard (SMEFT), faisant intervenir tous les champs présents dans le MS :

$$\mathcal{L}_{\text{SMEFT}} \;=\; \mathcal{L}_{\text{SM}} \;+\; \sum_{d,k}\frac{\mathcal{C}_k^{(d)}}{\Lambda^{d-4}}\,\mathcal{O}_k^{(d)} \;+\; \sum_{d,k}\left[\frac{\mathcal{C}_k^{(d)}}{\Lambda^{d-4}}\,\widetilde{\mathcal{O}}_k^{(d)} \;+\; \text{h.c.}\right]. \tag{6.3}$$

La liste complète des opérateurs pertinents pour la physique de la saveur est détaillée en appendice E. La correspondance entre les coefficients de la SMEFT et de l'EFT à basse énergie est donnée Eq. (2.7).

Dans certains cas, il peut également être intéressant de tester des scénarios explicites de nouvelle physique, afin par exemple de mesurer la validité de l'approche effective. Dans cette thèse, nous avons choisi de travailler avec des scénarios faisant intervenir un ou plusieurs état de leptoquarks. Les leptoquarks sont des bosons hypothétiques pouvant coupler directement à un quark et un lepton. Ils sont particulièrement étudiés dans le cadre de la physique de la saveur, car ils permettent d'expliquer les anomalies du B au niveau des arbres. la liste des leptoquarks considérés, ainsi que leur correspondance avec la théorie effective, sont explicitées Section 2.2.

6.3 Observables de Saveur à basses énergies

Les observables de saveur les plus souvent considérées à basses énergies sont les rapports d'universalité leptoniques. Pour les courants chargés, la transition semileptonique $b\bar{c} \to \tau\bar{\nu}$

peut par exemple être sondée grâce au rapport

$$R_{D^{(*)}} = \left. \frac{\mathcal{B}(B \to D^{(*)}\tau\bar{\nu})}{\mathcal{B}(B \to D^{(*)}\ell\bar{\nu})} \right|_{\ell \in \{e,\mu\}} , \tag{6.4}$$

dans lequel une majorité des incertitudes théoriques (provenant de la matrice CKM et des facteurs de forme hadroniques) s'annulent. Expérimentalement, les valeurs mesurées sont en tension avec le Modèle Standard, comme illustré Figure 3.2.

Nous avons étudié la phénoménologie des désintégrations leptoniques et semileptoniques des mésons pseudoscalaires pour toutes les combinaisons de saveur expérimentalement accessibles, en prêtant une attention toute particulière au traitement des incertitudes hadroniques. Les contraintes obtenues sont résumées Table 6.1.

$u_i\, d_j\, \ell$	$\mathrm{Re}(g_V^{ij\,\ell})$	$\mathrm{Re}(g_A^{ij\,\ell})$	$\mathrm{Re}(g_S^{ij\,\ell})$	$\mathrm{Re}(g_P^{ij\,\ell})$	$\mathrm{Re}(g_T^{ij\,\ell})$
$u\,s\,\mu$	$(0 \pm 2) \times 10^{-3}$	$(2.2 \pm 1.8) \times 10^{-3}$	$(-2 \pm 9) \times 10^{-4}$	$(-9 \pm 8) \times 10^{-5}$	$(-2 \pm 9) \times 10^{-3}$
$u\,s\,\tau$	–	$(2.2 \pm 1.7) \times 10^{-2}$	–	$(1.6 \pm 1.1) \times 10^{-2}$	–
$c\,d\,\mu$	$(-3.0 \pm 1.6) \times 10^{-2}$	$(7 \pm 4) \times 10^{-2}$	$(-9 \pm 7) \times 10^{-2}$	$(-2.6 \pm 1.3) \times 10^{-3}$	$(-2.0 \pm 1.4) \times 10^{-1}$
$c\,d\,\tau$	–	$(-0.1 \pm 1.1) \times 10^{-1}$	–	$(1 \pm 7) \times 10^{-2}$	–
$c\,s\,\mu$	$(3 \pm 6) \times 10^{-3}$	$(-2 \pm 4) \times 10^{-2}$	$(-1 \pm 2) \times 10^{-2}$	$(0.7 \pm 1.4) \times 10^{-3}$	$(1.2 \pm 1.8) \times 10^{-2}$
$c\,s\,\tau$	–	$(-3 \pm 4) \times 10^{-2}$	–	$(2 \pm 2) \times 10^{-2}$	–
$u\,b\,\mu$	–	–	–	–	–
$u\,b\,\tau$	-1 ± 2	$(-1 \pm 2) \times 10^{-1}$	-0.3 ± 1.5	$(3 \pm 7) \times 10^{-2}$	-0.3 ± 1.1
$c\,b\,\mu$	$(0 \pm 2) \times 10^{-2}$	–	$(1 \pm 2) \times 10^{-1}$	$(0 \pm 8) \times 10^{-1}$	$(-1 \pm 3) \times 10^{-1}$
$c\,b\,\tau$	$(7 \pm 5) \times 10^{-2}$	1 ± 4	$(9 \pm 6) \times 10^{-2}$	$(-2 \pm 8) \times 10^{-1}$	$(1.2 \pm 0.8) \times 10^{-1}$

Table 6.1: *Contraintes à 1σ sur la partie réelle des coefficients $g_\alpha^{ij\,\ell} = g_\alpha^{ij\,\ell}(\mu)$, avec $\alpha \in \{V, A, S, P, T\}$), obtenues à partir des observables de la Table 3.4. L'échelle μ est prise à $\mu = 2$ GeV pour les mésons K et D, et $\mu = m_b$ pour les mésons B.*

En plus de ces observables, nous étudions la phénoménologie des observables angulaires pour les désintégrations semileptoniques. Nous montrons que même en présence de nouvelle physique, seules 4 observables linéairement indépendantes sont suffisantes pour totalement caractériser la distribution angulaire : le rapport de branchement (seule observables actuellement considéré expérimentalement), l'asymétrie avant/arrière, l'asymétrie de polarisation leptonique et la convexité de la distribution.

L'étude de ces trois dernières observables, encore non mesurées, offre d'excellentes perspectives pour démêler les différentes contributions de la Nouvelle Physique.

En plus des désintégrations des mésons, nous étudions les désintégrations exclusives des baryons lourds, pour lesquelles les facteurs de formes hadroniques ont également été calculés avec une grande précision [154, 161]. La collaboration LHCb a récemment publié la première mesure du rapport R_{Λ_c} :

$$R_{\Lambda_c} = \frac{\mathcal{B}(\Lambda_b \to \Lambda_c \tau\bar{\nu})}{\mathcal{B}(\Lambda_b \to \Lambda_c \mu\bar{\nu})} = 0.242 \pm 0.076\,, \tag{6.5}$$

compatible avec la prédiction du Modèle Standard. La désintégration $\Lambda_b \to \Lambda_c \tau \bar{\nu}$ est particulièrement intéressante, puisque la désintégration secondaire $\Lambda_c \to \Lambda \pi$ peut également apporter de l'information sur la nouvelle physique. Au total, 18 observables linéairement indépendantes sont accessibles.

En particulier, l'asymétrie avant/arrière exhibe une quasi-annulation accidentelle dans le cas du Modèle Standard, ce qui la rend particulièrement sensible à la Nouvelle Physique. Enfin, nous trouvons des observables, dénommées D_4 et E_4, proportionnelles uniquement à la partie imaginaire des couplages de la NP, qui seraient donc indicateurs d'une nouvelle violation de la symétrie CP. Ces deux observables sont illustrées Figure 6.1 pour un scénario de NP faisant intervenir la combinaison $g_{S_L} = 4g_T$, qui sera motivé dans la suite.

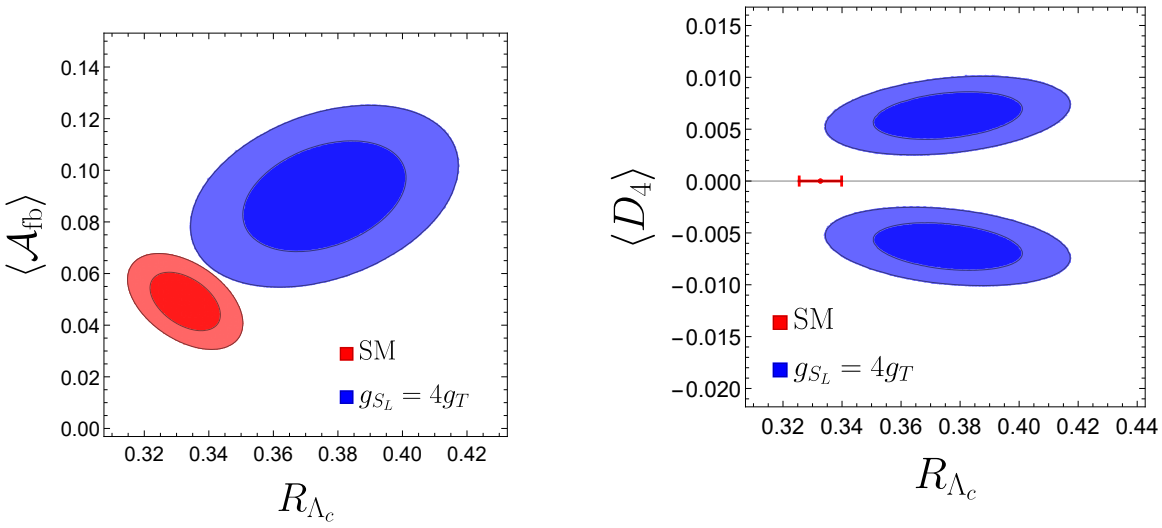

Figure 6.1: *Valeurs prédites pour les observables R_{Λ_c}, $\langle \mathcal{A}_{\rm fb} \rangle$ et $\langle D_4 \rangle$ dans le Modèle Standard (rouge) et par les valeurs mesurées de R_D et R_{D^*} dans un scénario de NP avec $g_{S_L} = +4g_T$ (bleu). Puisque les valeurs sont incompatibles, la mesure de ces observables pourrait invalider complètement ce scénario.*

6.4 Observables de Saveur aux hautes énergies

En plus des observables à basses énergies basées sur la désintégration des hadrons, l'étude des processus semileptoniques au LHC peut également servir à contraindre le secteur de la saveur. En effet, toutes les saveurs de quarks (sauf le top) contribuent à la section efficace proton-proton :

$$\sigma\left(pp \to \ell_\alpha \bar{\ell}'_\beta\right) = \sum_{ij} \int \frac{\mathrm{d}\hat{s}}{s} \mathcal{L}_{ij}\left(\hat{s}\right) \hat{\sigma}(\bar{q}_i q_j \to \ell_\alpha \bar{\ell}'_\beta)\,, \tag{6.6}$$

où $\mathcal{L}_{ij}$ désigne les fonctions de luminosité partoniques, et $\hat{\sigma}(\bar{q}_i q_j \to \ell_\alpha \bar{\ell}'_\beta)$ la section efficace partonique. Bien que les fonctions $\mathcal{L}_{ij}$ soient très hiérarchisées, avec une contribution bien plus faible des quarks lourds par rapport aux quarks de valence, la section efficace partonique augmente généralement avec l'énergie pour de nombreux scénarios de Nouvelle Physique.

Ainsi, chercher des excès d'événements dans la queue de distribution à haute énergie permet de contraindre les coefficients de la NP.

Pour démêler les différentes contributions, nous écrivons l'amplitude partonique en termes de facteurs de formes :

$$\begin{aligned}\mathcal{A}(\bar{q}_i q_j \to \ell_\alpha^- \ell_\beta^+) \;=\; \frac{1}{v^2}\sum_{XY}\Big\{ & \left(\bar{\ell}_\alpha \gamma^\mu \mathbb{P}_X \ell_\beta\right)\left(\bar{q}_i \gamma_\mu \mathbb{P}_Y q_j\right)\, [\mathcal{F}_V^{XY,\,qq}(\hat{s},\hat{t})]_{ij}^{\alpha\beta} \\ & + \left(\bar{\ell}_\alpha \mathbb{P}_X \ell_\beta\right)\left(\bar{q}_i \mathbb{P}_Y q_j\right)\, [\mathcal{F}_S^{XY,\,qq}(\hat{s},\hat{t})]_{ij}^{\alpha\beta} \\ & + \left(\bar{\ell}_\alpha \sigma_{\mu\nu} \mathbb{P}_X \ell_\beta\right)\left(\bar{q}_i \sigma^{\mu\nu} \mathbb{P}_X q_j\right)\, [\mathcal{F}_T^{X,\,qq}(\hat{s},\hat{t})]_{ij}^{\alpha\beta} \\ & + \left(\bar{\ell}_\alpha \gamma_\mu \mathbb{P}_X \ell_\beta\right)\left(\bar{q}_i \sigma^{\mu\nu} \mathbb{P}_Y q_j\right)\, \frac{ik_\nu}{v}\, [\mathcal{F}_{D_q}^{XY,\,qq}(\hat{s},\hat{t})]_{ij}^{\alpha\beta} \\ & + \left(\bar{\ell}_\alpha \sigma^{\mu\nu} \mathbb{P}_X \ell_\beta\right)\left(\bar{q}_i \gamma_\mu \mathbb{P}_Y q_j\right)\, \frac{ik_\nu}{v}\, [\mathcal{F}_{D_\ell}^{XY,\,qq}(\hat{s},\hat{t})]_{ij}^{\alpha\beta} \Big\}\,,\end{aligned} \tag{6.7}$$

où $X, Y \in \{L, R\}$, $\mathbb{P}_{R,L} = (1 \pm \gamma^5)/2$, et $v = (\sqrt{2}G_F)^{-1/2}$. $\hat{s} = k^2$, $\hat{t}$ et $\hat{u} = -\hat{s} - \hat{t}$ sont les variables de Mandelstam. Ces facteurs de formes sont ensuite décomposés en une partie régulière, correspondant aux interaction de théories effective à 4 fermions, et un nombre fini de pôles, correspondant aux médiateurs (MS et NP).

Pour extraire une limite des observations au LHC par rapport à la section efficace hadronique calculée, il est nécessaire de prendre en compte la réponse du détecteur. Cette réponse peut être encodée dans un noyau K défini par

$$\frac{\mathrm{d}\sigma}{\mathrm{d}x_{\mathrm{obs}}} \;=\; \int \mathrm{d}x\; K(x_{\mathrm{obs}}|x)\, \frac{\mathrm{d}\sigma}{\mathrm{d}x}\,. \tag{6.8}$$

Après discrétisation, le nombre d'événements attendu s'exprime

$$\mathcal{N}_A \;=\; \sum_{B\,\in\,\mathcal{B}} \mathcal{L}_{\mathrm{int}} \cdot K_{AB} \cdot \sigma_B\,, \tag{6.9}$$

où $\mathcal{L}_{\mathrm{int}}$ est la luminosité intégrée de la recherche expérimentale. La matrice K est extraite par Monte-Carlo grâce aux programmes `Madgraph5` [219], `Pythia8` [220], et `Delphes3` [221], en reproduisant du mieux possible les sélections expérimentales.

Les contraintes finales sont obtenues en comparant les distributions d'événements pour chaque recherche expérimentale avec le résultat théorique Equation (6.9). La Figure 6.2 montre un exemple de contrainte obtenu dans le cadre d'un scénario explicite, montrant le bon accord avec la théorie effective pour des masses supérieures à $3\ \mathrm{TeV}$, mais une sous-estimation des contraintes en deçà.

6.5 Les Leptoquarks comme solutions aux anomalies du B

Dans cette Section, nous étudions les extensions du Modèle Standard faisant intervenir les états de leptoquarks. Pour les théories à un seul leptoquark, nous obtenons que :

- S_3 et U_3 résultent en $g_{V_L} < 0$, alors que $R_{D^{(*)}}$ nécessite $g_{V_L} > 0$.
- S_1 peut expliquer $R_{D^{(*)}}$ mais pas $R_{K^{(*)}}$ [28, 241, 242].

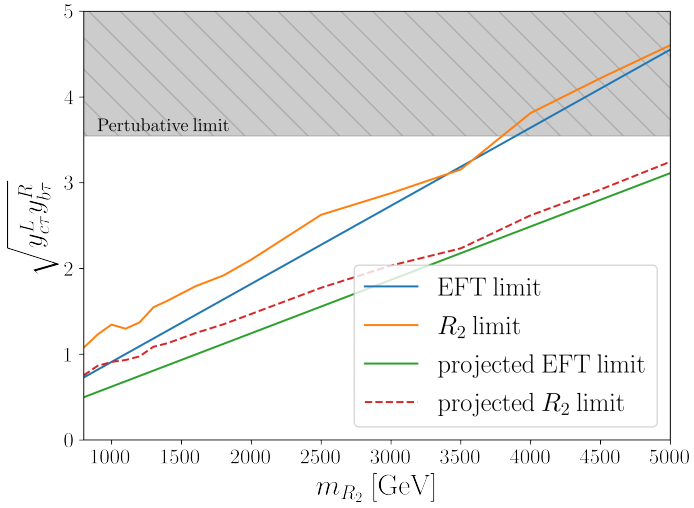

Figure 6.2: *Limites à $p < 0.05$ sur $\sqrt{y^L_{c\tau} y^R_{b\tau}}$ en fonction de la masse du leptoquark R_2 (orange). La contrainte obtenue par théorie effective est montrée en bleu.*

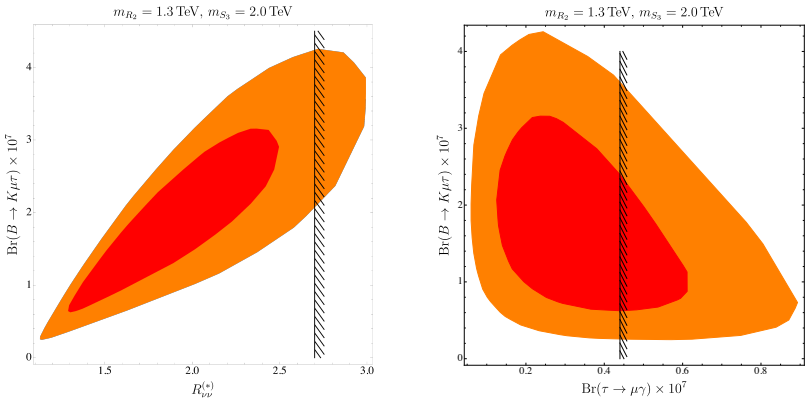

Figure 6.3: *Contours à 1 et 2σ de $\mathcal{B}(B \to K\mu\tau)$, $R^{(*)}_{\nu\nu} = \mathcal{B}(B \to K^{(*)}\nu\bar{\nu})/\mathcal{B}(B \to K^{(*)}\nu\bar{\nu})^{\mathrm{SM}}$ et $\mathcal{B}(\tau \to \mu\gamma)$ autorisés dans le modèle $R_2 - S_3$. La ligne noire montre la limite expérimentale actuelle.*

- R_2 produit la combinaison $g_{S_L} = 4g_T$ mentionnée plus haut, qui peut expliquer $R_{D^{(*)}}$, mais ne peut pas accommoder les anomalies pour les courants neutres [28, 36, 245].
- U_1 est le seul leptoquark pouvant expliquer les deux anomalies en même temps [28, 246].

Cependant, le leptoquark U_1 étant un boson vecteur, il est impossible de calculer les observables à boucle sans introduire de complétion ultraviolette, nécessitant de nombreuses hypothèses supplémentaires. Dans une optique de minimalité, nous proposons à la place un scénario de nouvelle physique faisant intervenir deux leptoquarks scalaires : R_2 et S_3. L'ensemble des contraintes phénoménologiques réduit fortement l'espace des paramètres de la théorie, et nous permet de faire des prédictions concernant des modes accessibles expérimentalement, y compris ceux violant la saveur leptonique, montré Figure 6.3.

Publication list

- D. Bečirević, F. Jaffredo, A. Peñuelas and O. Sumensari, New Physics effects in leptonic and semileptonic decays, JHEP **05** (2021), 175 doi:10.1007/JHEP05(2021)175 [arXiv:2012.09872 [hep-ph]].
- A. Angelescu, D. Bečirević, D. A. Faroughy, F. Jaffredo and O. Sumensari, Single leptoquark solutions to the B-physics anomalies, Phys. Rev. D **104** (2021) no.5, 055017 doi:10.1103/PhysRevD.104.055017 [arXiv:2103.12504 [hep-ph]].
- F. Jaffredo, Revisiting mono-tau tails at the LHC, Eur. Phys. J. C **82** (2022) no.6, 541 doi:10.1140/epjc/s10052-022-10504-9 [arXiv:2112.14604 [hep-ph]].
- D. Bečirević, I. Doršner, S. Fajfer, D. A. Faroughy, F. Jaffredo, N. Košnik and O. Sumensari, On a model with two scalar leptoquarks –R_2 and S_3, [arXiv:2206.09717 [hep-ph]].
- L. Allwicher, D. A. Faroughy, F. Jaffredo, O. Sumensari and F. Wilsch, Drell-Yan Tails Beyond the Standard Model, [arXiv:2207.10714 [hep-ph]].
- L. Allwicher, D. A. Faroughy, F. Jaffredo, O. Sumensari and F. Wilsch, HighPT: A Tool for high-p_T Drell-Yan Tails Beyond the Standard Model, [arXiv:2207.10756 [hep-ph]].
- D. Bečirević and F. Jaffredo, Looking for the effects of New Physics in the $\Lambda_b \longrightarrow \Lambda_c(\to \Lambda\pi)\ell\nu$ decay mode, [arXiv:2209.13409 [hep-ph]].

Appendix

A SMEFT conventions

For Hermitian semi-leptonic operators, we define the Hermitian conjugate $\mathcal{C}^\dagger$ of a Wilson coefficients $\mathcal{C}$ that can be a two-tensor or four-tensor in quark/lepton flavor space as:

$$[\mathcal{C}^\dagger]^{\alpha\beta} \equiv [\mathcal{C}^*]^{\beta\alpha}\,, \tag{A.1}$$

$$[\mathcal{C}^\dagger]_{ij} \equiv [\mathcal{C}^*]_{ji}\,, \tag{A.2}$$

$$[\mathcal{C}^\dagger]_{ij}^{\alpha\beta} \equiv [\mathcal{C}^*]_{ji}^{\beta\alpha}\,. \tag{A.3}$$

These coefficients have a redundancy under the flavor index swappings $\alpha \leftrightarrow \beta$ and/or $i \leftrightarrow j$. One can remove this redundancy by adopting the following convention: For four-tensors, we fix the lepton indices to $\alpha \leq \beta$, which also determines the ordering of the quark flavor indices of the semileptonic four fermion operators if $\alpha < \beta$. For the case $\alpha = \beta$ we adopt the ordering $i \leq j$.[1] coefficients

In order to keep expressions compact, it is useful to introduce the following notation for the signed sums of Wilson coefficients associated to operators with the same field content, but different gauge/Lorentz structure:

$$\mathcal{C}^{(i\pm j\pm k\pm\ldots)} \;\equiv\; \mathcal{C}^{(i)} \pm \mathcal{C}^{(j)} \pm \mathcal{C}^{(k)} \pm \ldots \tag{A.4}$$

B Form-factor rotations from the weak basis to the mass basis

Here we provide the rotations needed to go from the form-factors expressed in the mass basis to the ones in the weak basis, for which all the matching conditions to the SMEFT and the mediators are provided in Appendix C and D. Everything is expressed in terms of the matrices V_u and V_d, which are the left-handed rotations to the mass basis for up-type and down-type quarks, respectively. The CKM matrix can then be expressed as $V = V_u^\dagger V_d$.

$$\mathcal{F}_V^{XL,ud} \to V_u^\dagger \mathcal{F}_V^{XL,ud} V_d\,, \qquad \mathcal{F}_{I\neq V}^{XL,ud} \to \mathcal{F}_{I\neq V}^{XL,ud} V_d\,, \qquad \mathcal{F}_{I\neq V}^{XR,ud} \to V_u^\dagger \mathcal{F}_{I\neq V}^{XR,ud}\,, \tag{B.1}$$

$$\mathcal{F}_V^{XL,uu} \to V_u^\dagger \mathcal{F}_V^{XL,uu} V_u\,, \qquad \mathcal{F}_{I\neq V}^{XL,uu} \to \mathcal{F}_{I\neq V}^{XL,uu} V_u\,, \tag{B.2}$$

$$\mathcal{F}_V^{XL,dd} \to V_d^\dagger \mathcal{F}_V^{XL,dd} V_d\,, \qquad \mathcal{F}_{I\neq V}^{XL,dd} \to \mathcal{F}_{I\neq V}^{XL,dd} V_d\,. \tag{B.3}$$

[1] This choice agrees with the conventions adapted by `DsixTools` [269] and `WCxf` [270] with the exception of the $C_{\substack{qe\\ij\alpha\beta}}$ operator in the original Warsaw basis that we dub $C_{\substack{eq\\ \alpha\beta ij}}$.

The rotation to the down-aligned basis can be obtained from the above by setting $V_u = V^\dagger$ and $V_d = \mathbb{1}$, while the up-aligned one with $V_u = \mathbb{1}$ and $V_d = V$. Notice that the rotations for all the remaining form-factors can be obtained by noticing that

$$\left[\mathcal{F}_V^{XY,\,ud}\right] = \left[\mathcal{F}_V^{XY,\,du}\right]^\dagger , \tag{B.4}$$

$$\left[\mathcal{F}_{I=S,T}^{LL,\,ud}\right] = \left[\mathcal{F}_{I=S,T}^{RR,\,du}\right]^\dagger , \qquad \left[\mathcal{F}_{I=S,T}^{RR,\,ud}\right] = \left[\mathcal{F}_{I=S,T}^{LL,\,du}\right]^\dagger , \tag{B.5}$$

$$\left[\mathcal{F}_S^{RL,\,ud}\right] = \left[\mathcal{F}_S^{LR,\,du}\right]^\dagger , \qquad \left[\mathcal{F}_S^{LR,\,ud}\right] = \left[\mathcal{F}_S^{RL,\,du}\right]^\dagger , \tag{B.6}$$

$$\left[\mathcal{F}_{D_\ell}^{RX,\,ud}\right] = -\left[\mathcal{F}_{D_\ell}^{LX,\,du}\right]^\dagger , \qquad \left[\mathcal{F}_{D_\ell}^{LX,\,ud}\right] = -\left[\mathcal{F}_{D_\ell}^{RX,\,du}\right]^\dagger , \tag{B.7}$$

$$\left[\mathcal{F}_{D_q}^{XL,\,ud}\right] = -\left[\mathcal{F}_{D_q}^{XR,\,du}\right]^\dagger , \qquad \left[\mathcal{F}_{D_q}^{XR,\,ud}\right] = -\left[\mathcal{F}_{D_q}^{XL,\,du}\right]^\dagger , \tag{B.8}$$

$$\left[\mathcal{F}_{I=S,T}^{LL,\,qq}\right] = \left[\mathcal{F}_{I=S,T}^{RR,\,qq}\right]^\dagger , \qquad \left[\mathcal{F}_S^{RL,\,qq}\right] = \left[\mathcal{F}_S^{LR,\,qq}\right]^\dagger , \tag{B.9}$$

$$\left[\mathcal{F}_{D_\ell}^{RX,\,qq}\right] = -\left[\mathcal{F}_{D_\ell}^{LX,\,qq}\right]^\dagger , \qquad \left[\mathcal{F}_{D_q}^{XL,\,qq}\right] = -\left[\mathcal{F}_{D_q}^{XR,\,qq}\right]^\dagger . \tag{B.10}$$

C Form-factors in the SMEFT

C.1 Scalar and tensor form-factors

In this appendix, we provide the full matching between the form-factor coefficients in Eq. 4.29-4.33 and the SMEFT Wilson coefficients. These results are consistent with the vertex parametrizations in Ref. [196].

Neutral currents. The matching to the SMEFT Wilson coefficients depend if the process is up-quark or down-quark initiated, $\bar{u}_i u_j \to \ell_\alpha^- \ell_\beta^+$ and $\bar{d}_i d_j \to \ell_\alpha^- \ell_\beta^+$. This is then given by:

$$\mathcal{F}_{S\,(0,0)}^{RR,\,uu} = -\frac{v^2}{\Lambda^2}\,\mathcal{C}_{lequ}^{(1)}\,, \qquad \mathcal{F}_{S\,(0,0)}^{RL,\,dd} = \frac{v^2}{\Lambda^2}\,\mathcal{C}_{ledq}\,, \tag{C.1}$$

$$\mathcal{F}_{T\,(0,0)}^{RR,\,uu} = -\frac{v^2}{\Lambda^2}\,\mathcal{C}_{lequ}^{(3)}\,. \tag{C.2}$$

Charged currents. For the mono-lepton processes $\bar{u}_i d_j \to \ell_\alpha^- \nu_\beta$ (and their conjugates), the matching reads:

$$\mathcal{F}_{S\,(0,0)}^{RR,\,du} = \frac{v^2}{\Lambda^2}\,\mathcal{C}_{lequ}^{(1)}\,, \qquad \mathcal{F}_{S\,(0,0)}^{RL,\,du} = \frac{v^2}{\Lambda^2}\,\mathcal{C}_{ledq}\,, \tag{C.3}$$

$$\mathcal{F}_{T\,(0,0)}^{RR,\,du} = \frac{v^2}{\Lambda^2}\,\mathcal{C}_{lequ}^{(3)}\,. \tag{C.4}$$

C.2 Vector form-factors

Neutral currents $\bar{u}_i u_j \to l_\alpha^- l_\beta^+$: The matching of the coefficients $\mathcal{F}_{V\,(0,0)}^{XY}$ to the SMEFT for up-quark initiated processes is given by:

$$\mathcal{F}_{V\,(0,0)}^{LL,\,uu} = \frac{v^2}{\Lambda^2}\,\mathcal{C}_{lq}^{(1-3)} + \frac{v^4}{2\Lambda^4}\,\mathcal{C}_{l^2q^2H^2}^{(1+2-3-4)} + \frac{v^2 m_Z^2}{2\Lambda^4}\left[g_l^L\,\mathcal{C}_{q^2H^2D^3}^{(1-2-3+4)} + g_u^L\,\mathcal{C}_{l^2H^2D^3}^{(1-2+3-4)}\right], \tag{C.5}$$

$$\mathcal{F}^{LR,\,uu}_{V\,(0,0)} = \frac{v^2}{\Lambda^2}\,\mathcal{C}_{lu} + \frac{v^4}{2\Lambda^4}\,\mathcal{C}^{(1+2)}_{l^2u^2H^2} + \frac{v^2m_Z^2}{2\Lambda^4}\left[g_l^L\,\mathcal{C}^{(1-2)}_{u^2H^2D^3} + g_u^L\,\mathcal{C}^{(1-2+3-4)}_{l^2H^2D^3}\right], \tag{C.6}$$

$$\mathcal{F}^{RL,\,uu}_{V\,(0,0)} = \frac{v^2}{\Lambda^2}\,\mathcal{C}_{qe} + \frac{v^4}{2\Lambda^4}\,\mathcal{C}^{(1-2)}_{q^2e^2H^2} + \frac{v^2m_Z^2}{2\Lambda^4}\left[g_l^R\,\mathcal{C}^{(1-2-3+4)}_{q^2H^2D^3} + g_u^L\,\mathcal{C}^{(1-2)}_{e^2H^2D^3}\right], \tag{C.7}$$

$$\mathcal{F}^{RR,\,uu}_{V\,(0,0)} = \frac{v^2}{\Lambda^2}\,\mathcal{C}_{eu} + \frac{v^4}{2\Lambda^4}\,\mathcal{C}_{e^2u^2H^2} + \frac{v^2m_Z^2}{2\Lambda^4}\left[g_l^R\,\mathcal{C}^{(1-2)}_{u^2H^2D^3} + g_u^R\,\mathcal{C}^{(1-2)}_{e^2H^2D^3}\right]. \tag{C.8}$$

The higher order coefficients $\mathcal{F}^{XY}_{V\,(1,0)}$ and $\mathcal{F}^{XY}_{V\,(0,1)}$ are generated in the SMEFT at $d = 8$ from momentum-dependent contact operators in the class $\boldsymbol{\psi^4 D^2}$. These read:

$$\mathcal{F}^{LL,\,uu}_{V\,(1,0)} = \frac{v^4}{\Lambda^4}\,\mathcal{C}^{(1+2-3-4)}_{l^2Q^2D^2}\,, \qquad \mathcal{F}^{LL,\,uu}_{V\,(0,1)} = 2\frac{v^4}{\Lambda^4}\,\mathcal{C}^{(2-4)}_{l^2Q^2D^2}\,, \tag{C.9}$$

$$\mathcal{F}^{LR,\,uu}_{V\,(1,0)} = \frac{v^4}{\Lambda^4}\,\mathcal{C}^{(1+2)}_{l^2u^2D^2}\,, \qquad \mathcal{F}^{LR,\,uu}_{V\,(0,1)} = 2\frac{v^4}{\Lambda^4}\,\mathcal{C}^{(2)}_{l^2u^2D^2}\,, \tag{C.10}$$

$$\mathcal{F}^{RL,\,uu}_{V\,(1,0)} = \frac{v^4}{\Lambda^4}\,\mathcal{C}^{(1+2)}_{q^2e^2D^2}\,, \qquad \mathcal{F}^{RL,\,uu}_{V\,(0,1)} = 2\frac{v^4}{\Lambda^4}\,\mathcal{C}^{(2)}_{q^2e^2D^2}\,, \tag{C.11}$$

$$\mathcal{F}^{RR,\,uu}_{V\,(1,0)} = \frac{v^4}{\Lambda^4}\,\mathcal{C}^{(1+2)}_{e^2u^2D^2}\,, \qquad \mathcal{F}^{RR,\,uu}_{V\,(0,1)} = 2\frac{v^4}{\Lambda^4}\,\mathcal{C}^{(2)}_{e^2u^2D^2}\,. \tag{C.12}$$

The matching of the pole residues to the SMEFT is given by:

$$\begin{aligned}
\delta\mathcal{S}^{LL,\,uu}_{(Z)} =& -2\frac{m_Z^2}{\Lambda^2}\left[g_l^L\,\mathcal{C}^{(1-3)}_{Hq} + g_u^L\,\mathcal{C}^{(1+3)}_{Hl}\right] + \frac{v^2m_Z^2}{\Lambda^4}\mathcal{C}^{(1+3)}_{Hl}\mathcal{C}^{(1-3)}_{Hq} \\
&- \frac{v^2m_Z^2}{\Lambda^4}\left[g_l^L\left(\mathcal{C}^{(1)}_{q^2H^4D} - 2\mathcal{C}^{(2)}_{q^2H^4D}\right) + g_u^L\left(\mathcal{C}^{(1)}_{l^2H^4D} + 2\mathcal{C}^{(2)}_{l^2H^4D}\right)\right] \\
&+ \frac{m_Z^4}{2\Lambda^4}\left[g_l^L\,\mathcal{C}^{(1-2-3+4)}_{q^2H^2D^3} + g_u^L\,\mathcal{C}^{(1-2+3-4)}_{l^2H^2D^3}\right], \\
\delta\mathcal{S}^{LR,\,uu}_{(Z)} =& -2\frac{m_Z^2}{\Lambda^2}\left[g_l^L\,\mathcal{C}_{Hu} + g_u^R\,\mathcal{C}^{(1+3)}_{Hl}\right] + \frac{v^2m_Z^2}{\Lambda^4}\mathcal{C}^{(1+3)}_{Hl}\mathcal{C}_{Hu} \\
&- \frac{v^2m_Z^2}{\Lambda^4}\left[g_l^L\mathcal{C}_{u^2H^4D} + g_u^R\left(\mathcal{C}^{(1)}_{l^2H^4D} + 2\mathcal{C}^{(2)}_{l^2H^4D}\right)\right] \\
&+ \frac{m_Z^4}{2\Lambda^4}\left[g_l^L\,\mathcal{C}^{(1-2)}_{u^2H^2D^3} + g_u^R\,\mathcal{C}^{(1-2+3-4)}_{l^2H^2D^3}\right], \\
\delta\mathcal{S}^{RL,\,uu}_{(Z)} =& -2\frac{m_Z^2}{\Lambda^2}\left[g_l^R\,\mathcal{C}^{(1-3)}_{Hq} + g_u^L\,\mathcal{C}_{He}\right] + \frac{v^2m_Z^2}{\Lambda^4}\,\mathcal{C}_{He}\,\mathcal{C}^{(1-3)}_{Hq} \\
&- \frac{v^2m_Z^2}{\Lambda^4}\left[g_l^R\left(\mathcal{C}^{(1)}_{q^2H^4D} - 2\mathcal{C}^{(2)}_{q^2H^4D}\right) + g_u^L\mathcal{C}_{e^2H^4D}\right] \\
&+ \frac{m_Z^4}{2\Lambda^4}\left[g_l^R\,\mathcal{C}^{(1-2-3+4)}_{q^2H^2D^3} + g_u^L\,\mathcal{C}^{(1-2)}_{e^2H^2D^3}\right], \\
\delta\mathcal{S}^{RR,\,uu}_{(Z)} =& -2\frac{m_Z^2}{\Lambda^2}\left[g_l^R\,\mathcal{C}_{Hu} + g_u^R\,\mathcal{C}_{He}\right] + \frac{v^2m_Z^2}{\Lambda^4}\left[\mathcal{C}_{He}\,\mathcal{C}_{Hu} - g_L^R\mathcal{C}_{u^2H^4D} - g_u^R\mathcal{C}_{e^2H^4D}\right] \\
&+ \frac{m_Z^4}{2\Lambda^4}\left[g_l^R\,\mathcal{C}^{(1-2)}_{u^2H^2D^3} + g_u^R\,\mathcal{C}^{(1-2)}_{e^2H^2D^3}\right].
\end{aligned} \tag{C.13}$$

Neutral currents $\boldsymbol{\bar{d}_i d_j \to \ell^-_\alpha \ell^+_\beta}$: For down-quark initiated processes the matching for the leading coefficient $\mathcal{F}^{XY}_{V\,(0,0)}$ is given by:

$$\mathcal{F}^{LL,\,dd}_{V\,(0,0)} = \frac{v^2}{\Lambda^2}\,\mathcal{C}^{(1+3)}_{lq} + \frac{v^4}{2\Lambda^4}\,\mathcal{C}^{(1+2+3+4)}_{l^2q^2H^2} + \frac{v^2m_Z^2}{2\Lambda^4}\left[g_l^L\,\mathcal{C}^{(1-2+3-4)\,\dagger}_{q^2H^2D^3} + g_d^L\,\mathcal{C}^{(1-2+3-4)}_{l^2H^2D^3}\right], \tag{C.14}$$

$$\mathcal{F}^{LR,\,dd}_{V\,(0,0)} = \frac{v^2}{\Lambda^2}\,\mathcal{C}_{ld} + \frac{v^4}{2\Lambda^4}\,\mathcal{C}^{(1+2)}_{l^2d^2H^2} + \frac{v^2m_Z^2}{2\Lambda^4}\left[g_l^L\,\mathcal{C}^{(1-2)\,\dagger}_{d^2H^2D^3} + g_d^R\,\mathcal{C}^{(1-2+3-4)}_{l^2H^2D^3}\right], \tag{C.15}$$

$$\mathcal{F}^{RL,\,dd}_{V\,(0,0)} = \frac{v^2}{\Lambda^2}\,\mathcal{C}_{qe} + \frac{v^4}{2\Lambda^4}\,\mathcal{C}^{(1+2)}_{q^2e^2H^2} + \frac{v^2m_Z^2}{2\Lambda^4}\left[g_l^R\,\mathcal{C}^{(1-2+3-4)\,\dagger}_{q^2H^2D^3} + g_d^L\,\mathcal{C}^{(1-2)}_{e^2H^2D^3}\right], \tag{C.16}$$

$$\mathcal{F}^{RR,\,dd}_{V\,(0,0)} = \frac{v^2}{\Lambda^2}\,\mathcal{C}_{ed} + \frac{v^4}{2\Lambda^4}\,\mathcal{C}_{e^2d^2H^2} + \frac{v^2m_Z^2}{2\Lambda^4}\left[g_l^R\,\mathcal{C}^{(1-2)\,\dagger}_{d^2H^2D^3} + g_d^R\,\mathcal{C}^{(1-2)}_{e^2H^2D^3}\right]. \tag{C.17}$$

The higher order coefficients $\mathcal{F}^{XY}_{V\,(1,0)}$ and $\mathcal{F}^{XY}_{V\,(0,1)}$ read:

$$\mathcal{F}^{LL,\,dd}_{V\,(1,0)} = \frac{v^4}{\Lambda^4}\,\mathcal{C}^{(1+2+3+4)}_{l^2q^2D^2}\ , \qquad \mathcal{F}^{LL,\,dd}_{V\,(0,1)} = 2\frac{v^4}{\Lambda^4}\,\mathcal{C}^{(2+4)}_{l^2q^2D^2}\,, \tag{C.18}$$

$$\mathcal{F}^{LR,\,dd}_{V\,(1,0)} = \frac{v^4}{\Lambda^4}\,\mathcal{C}^{(1+2)}_{l^2d^2D^2}\ , \qquad \mathcal{F}^{LR,\,dd}_{V\,(0,1)} = 2\frac{v^4}{\Lambda^4}\,\mathcal{C}^{(2)}_{l^2d^2D^2}\,, \tag{C.19}$$

$$\mathcal{F}^{RL,\,dd}_{V\,(1,0)} = \frac{v^4}{\Lambda^4}\,\mathcal{C}^{(1+2)}_{q^2e^2D^2}\ , \qquad \mathcal{F}^{RL,\,dd}_{V\,(0,1)} = 2\frac{v^4}{\Lambda^4}\,\mathcal{C}^{(2)}_{q^2e^2D^2}\,, \tag{C.20}$$

$$\mathcal{F}^{RR,\,dd}_{V\,(1,0)} = \frac{v^4}{\Lambda^4}\,\mathcal{C}^{(1+2)}_{e^2d^2D^2}\ , \qquad \mathcal{F}^{RR,\,dd}_{V\,(0,1)} = 2\frac{v^4}{\Lambda^4}\,\mathcal{C}^{(2)}_{e^2d^2D^2}\,. \tag{C.21}$$

and the pole residues are given by:

$$\begin{aligned}
\delta\mathcal{S}^{LL,\,dd}_{(Z)} =& -2\frac{m_Z^2}{\Lambda^2}\left[g_l^L\,\mathcal{C}^{(1+3)}_{Hq} + g_d^L\,\mathcal{C}^{(1+3)}_{Hl}\right] + \frac{v^2m_Z^2}{\Lambda^4}\mathcal{C}^{(1+3)}_{Hl}\mathcal{C}^{(1+3)}_{Hq} \\
&- \frac{v^2m_Z^2}{\Lambda^4}\left[g_l^L\left(\mathcal{C}^{(1)}_{q^2H^4D} + 2\mathcal{C}^{(2)}_{q^2H^4D}\right) + g_d^L\left(\mathcal{C}^{(1)}_{l^2H^4D} + 2\mathcal{C}^{(2)}_{l^2H^4D}\right)\right] \\
&+ \frac{m_Z^4}{2\Lambda^4}\left[g_l^L\,\mathcal{C}^{(1-2+3-4)}_{q^2H^2D^3} + g_d^L\,\mathcal{C}^{(1-2+3-4)}_{l^2H^2D^3}\right], \\
\delta\mathcal{S}^{LR,\,dd}_{(Z)} =& -2\frac{m_Z^2}{\Lambda^2}\left[g_l^L\,\mathcal{C}_{Hd} + g_d^R\,\mathcal{C}^{(1+3)}_{Hl}\right] + \frac{v^2m_Z^2}{\Lambda^4}\mathcal{C}^{(1+3)}_{Hl}\mathcal{C}_{Hd} \\
&- \frac{v^2m_Z^2}{\Lambda^4}\left[g_l^L\mathcal{C}_{d^2H^4D} + g_d^R\left(\mathcal{C}^{(1)}_{l^2H^4D} + 2\mathcal{C}^{(2)}_{l^2H^4D}\right)\right] \\
&+ \frac{m_Z^4}{2\Lambda^4}\left[g_l^L\,\mathcal{C}^{(1-2)}_{d^2H^2D^3} + g_d^R\,\mathcal{C}^{(1-2+3-4)}_{l^2H^2D^3}\right], \\
\delta\mathcal{S}^{RL,\,dd}_{(Z)} =& -2\frac{m_Z^2}{\Lambda^2}\left[g_l^R\,\mathcal{C}^{(1+3)}_{Hq} + g_d^L\,\mathcal{C}_{He}\right] + \frac{v^2m_Z^2}{\Lambda^4}\,\mathcal{C}_{He}\,\mathcal{C}^{(1+3)}_{Hq} \\
&- \frac{v^2m_Z^2}{\Lambda^4}\left[g_l^R\left(\mathcal{C}^{(1)}_{q^2H^4D} + 2\mathcal{C}^{(2)}_{q^2H^4D}\right) + g_d^L\mathcal{C}_{e^2H^4D}\right] \\
&+ \frac{m_Z^4}{2\Lambda^4}\left[g_l^R\,\mathcal{C}^{(1-2+3-4)}_{q^2H^2D^3} + g_d^L\,\mathcal{C}^{(1-2)}_{e^2H^2D^3}\right], \\
\delta\mathcal{S}^{RR,\,dd}_{(Z)} =& -2\frac{m_Z^2}{\Lambda^2}\left[g_l^R\,\mathcal{C}_{Hd} + g_d^R\,\mathcal{C}_{He}\right] + \frac{v^2m_Z^2}{\Lambda^4}\left[\mathcal{C}_{He}\,\mathcal{C}_{Hd} - g_L^R\mathcal{C}_{d^2H^4D} - g_d^R\mathcal{C}_{e^2H^4D}\right] \\
&+ \frac{m_Z^4}{2\Lambda^4}\left[g_l^R\,\mathcal{C}^{(1-2)}_{d^2H^2D^3} + g_d^R\,\mathcal{C}^{(1-2)}_{e^2H^2D^3}\right].
\end{aligned} \tag{C.22}$$

Charged currents $\bar{u}_i d_j \to \ell^-_\alpha \bar{\nu}_\beta$: The matching of the leading form-factor coefficients $\mathcal{F}^{LL(LR)}_{V\,(0,0)}$ is given by:

$$\begin{aligned}
\left[\mathcal{F}^{LL,\,ud}_{V\,(0,0)}\right]^{\alpha\beta}_{ij} =\ & 2\frac{v^2}{\Lambda^2}\left[\mathcal{C}^{(3)}_{lq}\right]^{\alpha\beta}_{ij} + \frac{v^4}{\Lambda^4}\left(\left[\mathcal{C}^{(3)}_{l^2q^2H^2}\right]^{\alpha\beta}_{ij} + i\left[\mathcal{C}^{(5)}_{l^2q^2H^2}\right]^{\alpha\beta}_{i\neq j}\right) + \\
&- \frac{g^2}{2}\frac{v^4}{2\Lambda^4}\left[\left(\mathcal{C}^{(3)}_{l^2H^2D^3} - \mathcal{C}^{(4)\,\dagger}_{l^2H^2D^3}\right)\mathbb{1}_q + \left(\mathcal{C}^{(3)\,\dagger}_{q^2H^2D^3} - \mathcal{C}^{(4)}_{q^2H^2D^3}\right)\mathbb{1}_l\right]^{\alpha\beta}_{ij}.
\end{aligned} \tag{C.23}$$

Notice that the $d = 8$ operator $\mathcal{O}^{(5)}_{l^2q^2H^2} = \epsilon^{IJK}$... only contributes to flavor violating processes and therefore does not enter into neutral currents, but does affect charged currents like e.g.

$u\bar{s} \to \ell^{\pm}\nu$ at order $\mathcal{O}(1/\Lambda^4)$. The effects of this operator are small because they only interfere with CKM suppressed transitions in the SM. For the higher-order regular coefficients we obtain the following matching to the SMEFT:

$$\mathcal{F}^{LL,\,ud}_{V\,(1,0)} = 2\frac{v^4}{\Lambda^4}\,\mathcal{C}^{(3+4)}_{l^2q^2D^2}\,, \qquad\qquad \mathcal{F}^{LL,\,ud}_{V\,(0,1)} = 4\frac{v^4}{\Lambda^4}\,\mathcal{C}^{(4)}_{l^2q^2D^2}\,. \tag{C.24}$$

The matching of the pole residues is given by:

$$\begin{aligned}
\delta\mathcal{S}^{LL,\,ud}_{(W)} =& \frac{g^2}{2}\frac{v^2}{\Lambda^2}\left[\mathcal{C}^{(3)\,\dagger}_{Hl}\,\mathbb{1}_q + \mathcal{C}^{(3)}_{Hl}\,\mathbb{1}_\ell\right] + \frac{g^2}{2}\frac{v^4}{\Lambda^4}\,\mathcal{C}^{(3)\,\dagger}_{Hl}\,\mathcal{C}^{(3)}_{Hq} \\
&+ \frac{g^2}{2}\frac{v^4}{2\Lambda^4}\left[\mathcal{C}^{(2^\dagger-3^\dagger+4)}_{l^2H^4D}\mathbb{1}_q + \mathcal{C}^{(2-3+4^\dagger)}_{q^2H^4D}\mathbb{1}_l\right] \\
&- \frac{g^2}{2}\frac{v^2m_W^2}{2\Lambda^4}\left[\left(\mathcal{C}^{(3)}_{l^2H^2D^3} - \mathcal{C}^{(4)\,\dagger}_{l^2H^2D^3}\right)\mathbb{1}_q + \left(\mathcal{C}^{(3)\,\dagger}_{q^2H^2D^3} - \mathcal{C}^{(4)}_{q^2H^2D^3}\right)\mathbb{1}_l\right]\,, \\
\delta\mathcal{S}^{LR,\,ud}_{(W)} =& \frac{g^2}{4}\frac{v^2}{\Lambda^2}\,\mathcal{C}_{Hud}\,\mathbb{1}_l
\end{aligned} \tag{C.25}$$

and $\delta\mathcal{S}^{LL,\,du}_{(W)} = \delta\mathcal{S}^{LL,\,ud}_{(W)}$ and $\delta\mathcal{S}^{LR,\,du}_{(W)} = \delta\mathcal{S}^{LR,\,ud\,\dagger}_{(W)}$.

C.3 Dipole form-factors

Neutral currents. The matching conditions for the Z boson and photon pole coefficients are given by:

$$\mathcal{S}^{RR,qq}_{D_l\,(\gamma)} = \mathcal{P}^{RL,qq}_{D_l\,(\gamma)} = -\sqrt{2}eQ_q\frac{v^2}{\Lambda^2}\left(s_wC_{eW} - c_wC_{eB}\right)\mathbb{1}_q\,, \tag{C.26}$$

$$\mathcal{S}^{LR,qq}_{D_l\,(\gamma)} = \mathcal{P}^{LL,qq}_{D_l\,(\gamma)} = \sqrt{2}eQ_q\frac{v^2}{\Lambda^2}\left(s_wC^\dagger_{eW} - c_wC^\dagger_{eB}\right)\mathbb{1}_q\,, \tag{C.27}$$

$$\mathcal{P}^{RR,qq}_{D_l\,(Z)} = \mathcal{P}^{RL,qq}_{D_l\,(Z)} = -\sqrt{2}g_q^{R/L}\frac{v^2}{\Lambda^2}\left(c_wC_{eW} + s_wC_{eB}\right)\mathbb{1}_q\,, \tag{C.28}$$

$$\mathcal{S}^{LR,qq}_{D_l\,(Z)} = \mathcal{P}^{LL,qq}_{D_l\,(Z)} = \sqrt{2}g_q^{R/L}\frac{v^2}{\Lambda^2}\left(c_wC^\dagger_{eW} + s_wC^\dagger_{eB}\right)\mathbb{1}_q\,, \tag{C.29}$$

$$\mathcal{P}^{RR,dd}_{D_q\,(\gamma)} = \mathcal{P}^{LR,dd}_{D_q\,(\gamma)} = \sqrt{2}eQ_e\frac{v^2}{\Lambda^2}\left(s_wC_{dW} - c_wC_{dB}\right)\mathbb{1}_\ell\,, \tag{C.30}$$

$$\mathcal{S}^{RL,dd}_{D_q\,(\gamma)} = \mathcal{P}^{LL,dd}_{D_q\,(\gamma)} = -\sqrt{2}eQ_e\frac{v^2}{\Lambda^2}\left(s_wC^\dagger_{dW} - c_wC^\dagger_{dB}\right)\mathbb{1}_\ell\,, \tag{C.31}$$

$$\mathcal{S}^{RR,dd}_{D_q\,(Z)} = \mathcal{P}^{LR,dd}_{D_q\,(Z)} = \sqrt{2}g_l^{R/L}\frac{v^2}{\Lambda^2}\left(c_wC_{dW} + s_wC_{dB}\right)\mathbb{1}_\ell\,, \tag{C.32}$$

$$\mathcal{S}^{RL,dd}_{D_q\,(Z)} = \mathcal{P}^{LL,dd}_{D_q\,(Z)} = -\sqrt{2}g_l^{R/L}\frac{v^2}{\Lambda^2}\left(c_wC^\dagger_{dW} + s_wC^\dagger_{dB}\right)\mathbb{1}_\ell\,. \tag{C.33}$$

$$\mathcal{P}^{RR,uu}_{D_q\,(\gamma)} = \mathcal{P}^{LR,uu}_{D_q\,(\gamma)} = -\sqrt{2}eQ_e\frac{v^2}{\Lambda^2}\left(s_wC_{uW} + c_wC_{uB}\right)\mathbb{1}_\ell\,, \tag{C.34}$$

$$\mathcal{P}^{RL,uu}_{D_q\,(\gamma)} = \mathcal{P}^{LL,uu}_{D_q\,(\gamma)} = \sqrt{2}eQ_e\frac{v^2}{\Lambda^2}\left(s_wC^\dagger_{uW} + c_wC^\dagger_{uB}\right)\mathbb{1}_\ell\,, \tag{C.35}$$

$$\mathcal{P}^{RR,uu}_{D_q\,(Z)} = \mathcal{P}^{LR,uu}_{D_q\,(Z)} = -\sqrt{2}g_l^{R/L}\frac{v^2}{\Lambda^2}\left(c_wC_{uW} - s_wC_{uB}\right)\mathbb{1}_\ell\,, \tag{C.36}$$

$$\mathcal{P}^{RL,uu}_{D_q\,(Z)} = \mathcal{P}^{LL,uu}_{D_q\,(Z)} = \sqrt{2}g_l^{R/L}\frac{v^2}{\Lambda^2}\left(c_wC^\dagger_{uW} - s_wC^\dagger_{uB}\right)\mathbb{1}_\ell\,. \tag{C.37}$$

Charged currents. The W boson pole coefficients read:

$$\mathcal{P}^{RL,ud}_{D_l\,(W)} = \sqrt{2}g\frac{v^2}{\Lambda^2}C_{eW}\mathbb{1}_q\,, \qquad \mathcal{P}^{LL,du}_{D_l\,(W)} = -\sqrt{2}g\frac{v^2}{\Lambda^2}C^\dagger_{eW}\mathbb{1}_q\,, \tag{C.38}$$

$$\mathcal{P}^{LR,ud}_{D_q\,(W)} = -\sqrt{2}g\frac{v^2}{\Lambda^2}C_{dW}\mathbb{1}_\ell\,, \qquad \mathcal{P}^{LL,du}_{D_q\,(W)} = \sqrt{2}g\frac{v^2}{\Lambda^2}C^\dagger_{dW}\mathbb{1}_\ell\,, \tag{C.39}$$

$$\mathcal{P}^{LR,du}_{D_q\,(W)} = -\sqrt{2}g\frac{v^2}{\Lambda^2}C_{uW}\mathbb{1}_\ell\,, \qquad \mathcal{P}^{LL,ud}_{D_q\,(W)} = \sqrt{2}g\frac{v^2}{\Lambda^2}C^\dagger_{uW}\mathbb{1}_\ell\,. \tag{C.40}$$

D Form-factors in concrete UV models

We now give the matching of every tree-level mediator in Tab. 4.1 to the pole form factors.

D.1 Scalar form-factors

Neutral currents $\bar{u}_i u_j \to \ell^-_\alpha \ell^+_\beta$:

$$\frac{1}{v^2}\left[\mathcal{F}^{LL,\,uu}_{S,\,\text{Poles}}\right]^{\alpha\beta}_{ij} = \frac{\frac{1}{2}[y_1^L]^{j\beta}[y_1^R]^{i\alpha *}}{\hat{u}-\Omega_{S_1}} - \frac{\frac{1}{2}[y_2^L]^{i\beta}[y_2^R]^{j\alpha *}}{\hat{t}-\Omega_{R_2^{(5/3)}}}\,, \tag{D.1}$$

$$\frac{1}{v^2}\left[\mathcal{F}^{LR,\,uu}_{S,\,\text{Poles}}\right]^{\alpha\beta}_{ij} = 0\,. \tag{D.2}$$

Neutral currents $\bar{d}_i d_j \to \ell^-_\alpha \ell^+_\beta$:

$$\frac{1}{v^2}\left[\mathcal{F}^{LL,\,dd}_{S,\,\text{Poles}}\right]^{\alpha\beta}_{ij} = 0, \tag{D.3}$$

$$\frac{1}{v^2}\left[\mathcal{F}^{LR,\,dd}_{S,\,\text{Poles}}\right]^{\alpha\beta}_{ij} = -\frac{2[x_1^L]^{i\beta}[x_1^R]^{j\alpha *}}{\hat{t}-\Omega_{U_1}} + \frac{2[x_2^R]^{i\alpha *}[x_2^L]^{j\beta}}{\hat{u}-\Omega_{V_2^{(4/3)}}}\,. \tag{D.4}$$

Charged currents $\bar{u}_i d_j \to \ell^-_\alpha \bar{\nu}_\beta$:

$$\frac{1}{v^2}\left[\mathcal{F}^{LL,\,ud}_{S,\,\text{Poles}}\right]^{\alpha\beta}_{ij} = \frac{\frac{1}{2}\,[y_2^L]^{i\beta}[y_2^R]^{j\alpha *}}{\hat{t}-\Omega_{R_2^{(2/3)}}} - \frac{\frac{1}{2}\,[y_1^L]^{j\beta}[y_1^R]^{i\alpha *}}{\hat{u}-\Omega_{S_1}}\,, \tag{D.5}$$

$$\frac{1}{v^2}\left[\mathcal{F}^{LR,\,ud}_{S,\,\text{Poles}}\right]^{\alpha\beta}_{ij} = -\frac{2\,[x_1^L]^{i\beta}[x_1^R]^{j\alpha *}}{\hat{t}-\Omega_{U_1}} + \frac{2\,[x_2^L]^{j\beta}[x_2^R]^{i\alpha *}}{\hat{u}-\Omega_{V_2^{(1/3)}}}\,, \tag{D.6}$$

$$\frac{1}{v^2}\left[\mathcal{F}^{RL,\,ud}_{S,\,\text{Poles}}\right]^{\alpha\beta}_{ij} = -\frac{2\,[x_1^L]^{j\alpha *}[\bar{x}_1^R]^{i\beta}}{\hat{t}-\Omega_{U_1}} + \frac{[\widetilde{x}_2^R]^{j\beta}[\widetilde{x}_2^L]^{i\alpha *}}{\hat{u}-\Omega_{\widetilde{V}_2^{(1/3)}}}\,, \tag{D.7}$$

$$\frac{1}{v^2}\left[\mathcal{F}^{RR,\,ud}_{S,\,\text{Poles}}\right]^{\alpha\beta}_{ij} = \frac{\frac{1}{2}\,[\widetilde{y}_2^R]^{i\beta}[\widetilde{y}_2^L]^{j\alpha *}}{\hat{u}-\Omega_{\widetilde{R}_2^{(2/3)}}} + \frac{\frac{1}{2}\,[\bar{y}_1^R]^{j\beta}[y_1^L]^{i\alpha *}}{\hat{u}-\Omega_{S_1}}\,. \tag{D.8}$$

D.2 Vector form-factors

Neutral currents $\bar{u}_i u_j \to \ell^-_\alpha \ell^+_\beta$:

$$\frac{1}{v^2}\left[\mathcal{F}^{LL,\,uu}_{V,\,\text{Poles}}\right]^{\alpha\beta}_{ij} = \frac{[g_1^l]^{\alpha\beta}[g_1^q]^{ij}}{\hat{s}-\Omega_{Z'}} - \frac{[g_3^l]^{\alpha\beta}[g_3^q]^{ij}}{\hat{s}-\Omega_{W'}} - \frac{\frac{1}{2}\,[y_3^L]^{j\beta}[y_3^L]^{i\alpha *}}{\hat{u}-\Omega_{S_3^{(1/3)}}}$$

$$- \frac{\frac{1}{2}\,[y_1^L]^{j\beta}[y_1^L]^{i\alpha *}}{\hat{u}-\Omega_{S_1}} + \frac{2\,[x_3^L]^{i\beta}[x_3^L]^{j\alpha *}}{\hat{t}-\Omega_{U_3}^{(5/3)}}, \tag{D.9}$$

$$\frac{1}{v^2}\left[\mathcal{F}_{V,\,\text{Poles}}^{LR,\,uu}\right]_{ij}^{\alpha\beta} = \frac{[g_1^l]^{\alpha\beta}[g_1^u]^{ij}}{\hat{s}-\Omega_{Z'}} + \frac{[\widetilde{x}_2^L]^{i\beta}[\widetilde{x}_2^L]^{i\alpha *}}{\hat{u}-\Omega_{\widetilde{V}_2^{(1/3)}}} + \frac{\frac{1}{2}\,[y_2^L]^{i\beta}[y_2^L]^{j\alpha *}}{\hat{t}-\Omega_{R_2^{(5/3)}}}, \tag{D.10}$$

$$\frac{1}{v^2}\left[\mathcal{F}_{V,\,\text{Poles}}^{RL,\,uu}\right]_{ij}^{\alpha\beta} = \frac{[g_1^e]^{\alpha\beta}[g_1^q]^{ij}}{\hat{s}-\Omega_{Z'}} - \frac{[x_2^R]^{j\beta}[x_2^R]^{i\alpha *}}{\hat{u}-\Omega_{V_2^{(1/3)}}} + \frac{\frac{1}{2}\,[y_2^R]^{i\beta}[y_2^R]^{j\alpha *}}{\hat{t}-\Omega_{R_2^{(5/3)}}}, \tag{D.11}$$

$$\frac{1}{v^2}\left[\mathcal{F}_{V,\,\text{Poles}}^{RR,\,uu}\right]_{ij}^{\alpha\beta} = \frac{[g_1^e]^{\alpha\beta}[g_1^u]^{ij}}{\hat{s}-\Omega_{Z'}} + \frac{[\widetilde{x}_1^R]^{i\beta}[\widetilde{x}_1^R]^{j\alpha *}}{\hat{t}-\Omega_{\widetilde{U}_1}} - \frac{\frac{1}{2}\,[y_1^R]^{j\beta}[y_1^R]^{i\alpha *}}{\hat{u}-\Omega_{S_1}}, \tag{D.12}$$

Neutral currents $\bar{d}_i d_j \to \ell_\alpha^- \ell_\beta^+$:

$$\frac{1}{v^2}\left[\mathcal{F}_{V,\,\text{Poles}}^{LL,\,dd}\right]_{ij}^{\alpha\beta} = \frac{[g_1^l]^{\alpha\beta}[g_1^q]^{ij}}{\hat{s}-\Omega_{Z'}} + \frac{[g_3^l]^{\alpha\beta}[g_3^q]^{ij}}{\hat{s}-\Omega_{W'}} + \frac{[x_1^L]^{i\beta}[x_1^L]^{j\alpha *}}{\hat{t}-\Omega_{U_1}} + \frac{[x_3^L]^{i\beta}[x_3^L]^{j\alpha *}}{\hat{t}-\Omega_{U_3^{(2/3)}}} - \frac{[y_3^L]^{j\beta}[y_3^L]^{i\alpha *}}{\hat{u}-\Omega_{S_3^{(4/3)}}}, \tag{D.13}$$

$$\frac{1}{v^2}\left[\mathcal{F}_{V\,\text{Poles}}^{LR,\,dd}\right]_{ij}^{\alpha\beta} = \frac{[g_1^l]^{\alpha\beta}[g_1^d]^{ij}}{\hat{s}-\Omega_{Z'}} + \frac{\frac{1}{2}\,[\widetilde{y}_2^L]^{i\beta}[\widetilde{y}_2^L]^{j\alpha *}}{\hat{t}-\Omega_{\widetilde{R}_2^{(2/3)}}} - \frac{[x_2^L]^{j\beta}[x_2^L]^{i\alpha *}}{\hat{u}-\Omega_{V_2^{(4/3)}}}, \tag{D.14}$$

$$\frac{1}{v^2}\left[\mathcal{F}_{V,\,\text{Poles}}^{RL,\,dd}\right]_{ij}^{\alpha\beta} = \frac{[g_1^e]^{\alpha\beta}[g_1^q]^{ij}}{\hat{s}-m_{Z'}^2} + \frac{\frac{1}{2}[y_2^R]^{i\beta}[y_2^R]^{j\alpha *}}{\hat{t}-\Omega_{R_2^{(2/3)}}} - \frac{[x_2^R]^{j\beta}[x_2^R]^{i\alpha *}}{\hat{u}-\Omega_{V_2^{(4/3)}}}, \tag{D.15}$$

$$\frac{1}{v^2}\left[\mathcal{F}_{V,\,\text{Poles}}^{RR,\,dd}\right]_{ij}^{\alpha\beta} = \frac{[g_1^e]^{\alpha\beta}[g_1^d]^{ij}}{\hat{s}-\Omega_{Z'}} + \frac{[x_1^R]^{i\beta}[x_1^R]^{j\alpha *}}{\hat{t}-\Omega_{U_1}} + \frac{\frac{1}{2}\,[\widetilde{y}_1^R]^{j\beta}[\widetilde{y}_1^R]^{i\alpha *}}{\hat{u}-\Omega_{\widetilde{S}_1}}. \tag{D.16}$$

Charged currents $\bar{u}_i d_j \to \ell_\alpha^- \bar{\nu}_\beta$:

$$\frac{1}{v^2}\left[\mathcal{F}_{V,\,\text{Poles}}^{LL,\,ud}\right]_{ij}^{\alpha\beta} = \frac{2\,[g_3^l]^{\alpha\beta}[g_3^q]^{ij}}{\hat{s}-\Omega_{W'}} + \frac{[x_1^L]^{i\beta}[x_1^L]^{j\alpha *}}{\hat{t}-\Omega_{U_1}} - \frac{[x_3^L]^{i\beta}[x_3^L]^{j\alpha *}}{\hat{t}-\Omega_{U_3^{(2/3)}}} + \frac{\frac{1}{2}\,[y_1^L]^{j\beta}[y_1^L]^{i\alpha *}}{\hat{u}-\Omega_{S_1}} - \frac{\frac{1}{2}\,[y_3^L]^{j\beta}[y_3^L]^{i\alpha *}}{\hat{u}-\Omega_{S_3^{(1/3)}}}, \tag{D.17}$$

$$\frac{1}{v^2}\left[\mathcal{F}_{V,\,\text{Poles}}^{LR,\,ud}\right]_{ij}^{\alpha\beta} = 0\,, \tag{D.18}$$

$$\frac{1}{v^2}\left[\mathcal{F}_{V,\,\text{Poles}}^{RL,\,ud}\right]_{ij}^{\alpha\beta} = 0\,, \tag{D.19}$$

$$\frac{1}{v^2}\left[\mathcal{F}_{V,\,\text{Poles}}^{RR,\,ud}\right]_{ij}^{\alpha\beta} = \frac{[\bar{x}_1^R]^{j\alpha *}[\bar{x}_1^R]^{i\beta}}{\hat{t}-\Omega_{U_1}} + \frac{[\widetilde{g}_1^l]^{\alpha\beta}[\widetilde{g}_1^q]^{ij}}{\hat{s}-\Omega_{\widetilde{Z}}} - \frac{\frac{1}{2}[\bar{y}_1^R]^{j\beta}[y_1^R]^{i\alpha *}}{\hat{u}-\Omega_{S_1}}\,. \tag{D.20}$$

D.3 Tensor form-factors

Neutral currents $\bar{u}_i u_j \to \ell_\alpha^- \ell_\beta^+$:

$$\frac{1}{v^2}\left[\mathcal{F}_{T,\,\text{Poles}}^{LL,\,uu}\right]_{ij}^{\alpha\beta} = -\frac{\frac{1}{8}\,[y_1^L]^{j\beta}[y_1^R]^{i\alpha *}}{\hat{u}-\Omega_{S_1}} - \frac{\frac{1}{8}\,[y_2^L]^{i\beta}[y_2^R]^{j\alpha *}}{\hat{t}-\Omega_{R_2^{(5/3)}}}. \tag{D.21}$$

Charged currents $\bar{u}_i d_j \to \ell_\alpha^- \bar{\nu}_\beta$:

$$\frac{1}{v^2}\left[\mathcal{F}_{T,\,\text{Poles}}^{LL,\,ud}\right]_{ij}^{\alpha\beta} = \frac{\frac{1}{8}\,[y_2^L]^{i\beta}[y_2^R]^{j\alpha *}}{\hat{t}-\Omega_{R_2^{(2/3)}}} + \frac{\frac{1}{8}\,[y_1^L]^{j\beta}[y_1^R]^{i\alpha *}}{\hat{u}-\Omega_{S_1}}\,, \tag{D.22}$$

$$\frac{1}{v^2}\left[\mathcal{F}_{T,\,\text{Poles}}^{RR,\,ud}\right]_{ij}^{\alpha\beta} = \frac{\frac{1}{8}\,[\widetilde{y}_2^R]^{i\beta}[\widetilde{y}_2^L]^{j\alpha *}}{\hat{t}-\Omega_{\widetilde{R}_2^{(2/3)}}} - \frac{\frac{1}{8}\,[\bar{y}_1^R]^{j\beta}[y_1^L]^{i\alpha *}}{\hat{u}-\Omega_{S_1}}\,. \tag{D.23}$$

E $d \leq 8$ semi-leptonic SMEFT operators

$d=6$	ψ^4	$pp\to\ell\ell$	$pp\to\ell\nu$
$\mathcal{O}_{lq}^{(1)}$	$(\bar{l}_\alpha\gamma^\mu l_\beta)(\bar{q}_i\gamma_\mu q_j)$	✓	–
$\mathcal{O}_{lq}^{(3)}$	$(\bar{l}_\alpha\gamma^\mu\tau^I l_\beta)(\bar{q}_i\gamma_\mu\tau^I q_j)$	✓	✓
$\mathcal{O}_{lu}$	$(l_\alpha\gamma^\mu l_\beta)(\bar{u}_i\gamma_\mu u_j)$	✓	–
$\mathcal{O}_{ld}$	$(\bar{l}_\alpha\gamma^\mu l_\beta)(\bar{d}_i\gamma_\mu d_j)$	✓	–
$\mathcal{O}_{eq}$	$(\bar{e}_\alpha\gamma^\mu e_\beta)(\bar{q}_i\gamma_\mu q_j)$	✓	–
$\mathcal{O}_{eu}$	$(\bar{e}_\alpha\gamma^\mu e_\beta)(\bar{u}_i\gamma_\mu u_j)$	✓	–
$\mathcal{O}_{ed}$	$(\bar{e}_\alpha\gamma^\mu e_\beta)(\bar{d}_i\gamma_\mu d_j)$	✓	–
$\mathcal{O}_{ledq}$ + h.c.	$(\bar{l}_\alpha e_\beta)(\bar{d}_i q_j)$	✓	✓
$\mathcal{O}_{lequ}^{(1)}$ + h.c.	$(\bar{l}_\alpha e_\beta)\varepsilon(\bar{q}_i u_j)$	✓	✓
$\mathcal{O}_{lequ}^{(3)}$ + h.c.	$(\bar{l}_\alpha\sigma^{\mu\nu} e_\beta)\varepsilon(\bar{q}_i\sigma_{\mu\nu} u_j)$	✓	✓

$d=6$	ψ^2H^2D	$pp\to\ell\ell$	$pp\to\ell\nu$
$\mathcal{O}_{Hl}^{(1)}$	$(\bar{l}_\alpha\gamma^\mu l_\beta)(H^\dagger i\overleftrightarrow{D}_\mu H)$	✓	–
$\mathcal{O}_{Hl}^{(3)}$	$(\bar{l}_\alpha\gamma^\mu\tau^I l_\beta)(H^\dagger i\overleftrightarrow{D}^I_\mu H)$	✓	✓
$\mathcal{O}_{Hq}^{(1)}$	$(\bar{q}_i\gamma^\mu q_j)(H^\dagger i\overleftrightarrow{D}_\mu H)$	✓	–
$\mathcal{O}_{Hq}^{(3)}$	$(\bar{q}_i\gamma^\mu\tau^I q_j)(H^\dagger i\overleftrightarrow{D}^I_\mu H)$	✓	✓
$\mathcal{O}_{He}$	$(\bar{e}_\alpha\gamma^\mu e_\beta)(H^\dagger i\overleftrightarrow{D}_\mu H)$	✓	–
$\mathcal{O}_{Hu}$	$(\bar{u}_i\gamma^\mu u_j)(H^\dagger i\overleftrightarrow{D}_\mu H)$	✓	–
$\mathcal{O}_{Hd}$	$(\bar{d}_i\gamma^\mu d_j)(H^\dagger i\overleftrightarrow{D}_\mu H)$	✓	–
$\mathcal{O}_{Hud}$ + h.c.	$(\bar{u}_i\gamma^\mu d_j)(\widetilde{H}^\dagger i D_\mu H)$	–	✓

$d=6$	ψ^2XH + h.c.	$pp\to\ell\ell$	$pp\to\ell\nu$
$\mathcal{O}_{eW}$	$(l_\alpha\sigma^{\mu\nu}e_\beta)\,\tau^I H W^I_{\mu\nu}$	✓	✓
$\mathcal{O}_{eB}$	$(\bar{l}_\alpha\sigma^{\mu\nu}e_\beta)\,H B_{\mu\nu}$	✓	–
$\mathcal{O}_{uW}$	$(\bar{q}_i\sigma^{\mu\nu}u_j)\,\tau^I\widetilde{H}W^I_{\mu\nu}$	✓	✓
$\mathcal{O}_{uB}$	$(\bar{q}_i\sigma^{\mu\nu}u_j)\,\widetilde{H}B_{\mu\nu}$	✓	–
$\mathcal{O}_{dW}$	$(\bar{q}_i\sigma^{\mu\nu}d_j)\,\tau^I H W^I_{\mu\nu}$	✓	✓
$\mathcal{O}_{dB}$	$(\bar{q}_i\sigma^{\mu\nu}\,d_j)H B_{\mu\nu}$	✓	–

Table 2: *Dimension-*6 *operators contributing to the* $\bar{q}q'\to\bar{\ell}\ell'$ *transition at tree-level. A "*$+\mathrm{h.c.}$*" in the first column indicates that the operator is not hermitian, and as such the SMEFT Lagrangian contains the operator and its hermitian conjugate. The last two columns indicate if the operators contribute to neutral or charged current transitions.*

$d=8$	$\psi^4 H^2$	$pp \to \ell\ell$	$pp \to \ell\nu$
$\mathcal{O}^{(1)}_{l^2q^2H^2}$	$(\bar{l}_\alpha\gamma^\mu l_\beta)(\bar{q}_i\gamma_\mu q_j)(H^\dagger H)$	✓	–
$\mathcal{O}^{(2)}_{l^2q^2H^2}$	$(\bar{l}_\alpha\gamma^\mu\tau^I l_\beta)(\bar{q}_i\gamma_\mu q_j)(H^\dagger\tau^I H)$	✓	–
$\mathcal{O}^{(3)}_{l^2q^2H^2}$	$(\bar{l}_\alpha\gamma^\mu\tau^I l_\beta)(\bar{q}_i\gamma_\mu\tau^I q_j)(H^\dagger H)$	✓	✓
$\mathcal{O}^{(4)}_{l^2q^2H^2}$	$(\bar{l}_\alpha\gamma^\mu l_\beta)(\bar{q}_i\gamma_\mu\tau^I q_j)(H^\dagger\tau^I H)$	✓	–
$\mathcal{O}^{(5)}_{l^2q^2H^2}$	$\epsilon^{IJK}(\bar{l}_\alpha\gamma^\mu\tau^I l_\beta)(\bar{q}_i\gamma_\mu\tau^J q_j)(H^\dagger\tau^K H)$	–	✓
$\mathcal{O}^{(1)}_{l^2u^2H^2}$	$(\bar{l}_\alpha\gamma^\mu l_\beta)(\bar{u}_i\gamma_\mu u_j)(H^\dagger H)$	✓	–
$\mathcal{O}^{(2)}_{l^2u^2H^2}$	$(\bar{l}_\alpha\gamma^\mu\tau^I l_\beta)(\bar{u}_i\gamma_\mu u_j)(H^\dagger\tau^I H)$	✓	–
$\mathcal{O}^{(1)}_{l^2d^2H^2}$	$(\bar{l}_\alpha\gamma^\mu l_\beta)(\bar{d}_i\gamma_\mu d_j)(H^\dagger H)$	✓	–
$\mathcal{O}^{(2)}_{l^2d^2H^2}$	$(\bar{l}_\alpha\gamma^\mu\tau^I l_\beta)(\bar{d}_i\gamma_\mu d_j)(H^\dagger\tau^I H)$	✓	–
$\mathcal{O}^{(1)}_{q^2e^2H^2}$	$(\bar{q}_i\gamma^\mu q_j)(\bar{e}_\alpha\gamma_\mu e_\beta)(H^\dagger H)$	✓	–
$\mathcal{O}^{(2)}_{q^2e^2H^2}$	$(\bar{q}_i\gamma^\mu\tau^I q_j)(\bar{e}_\alpha\gamma_\mu e_\beta)(H^\dagger\tau^I H)$	✓	–
$\mathcal{O}_{e^2u^2H^2}$	$(\bar{e}_\alpha\gamma^\mu e_\beta)(\bar{u}_i\gamma_\mu u_j)(H^\dagger H)$	✓	–
$\mathcal{O}_{e^2d^2H^2}$	$(\bar{e}_\alpha\gamma^\mu e_\beta)(\bar{d}_i\gamma_\mu d_j)(H^\dagger H)$	✓	–

$d=8$	$\psi^4 D^2$	$pp \to \ell\ell$	$pp \to \ell\nu$
$\mathcal{O}^{(1)}_{l^2q^2D^2}$	$D^\nu(\bar{l}_\alpha\gamma^\mu l_\beta)D_\nu(\bar{q}_i\gamma_\mu q_j)$	✓	–
$\mathcal{O}^{(2)}_{l^2q^2D^2}$	$(\bar{l}_\alpha\gamma^\mu \overleftrightarrow{D}^\nu l_\beta)(\bar{q}_i\gamma_\mu \overleftrightarrow{D}_\nu q_j)$	✓	–
$\mathcal{O}^{(3)}_{l^2q^2D^2}$	$D^\nu(\bar{l}_\alpha\gamma^\mu\tau^I l_\beta)D_\nu(\bar{q}_i\gamma_\mu\tau^I q_j)$	✓	✓
$\mathcal{O}^{(4)}_{l^2q^2D^2}$	$(\bar{l}_\alpha\gamma^\mu \overleftrightarrow{D}^{I\nu} l_\beta)(\bar{q}_i\gamma_\mu \overleftrightarrow{D}^I_\nu q_j)$	✓	✓
$\mathcal{O}^{(1)}_{l^2u^2D^2}$	$D^\nu(\bar{l}_\alpha\gamma^\mu l_\beta)D_\nu(\bar{u}_i\gamma_\mu u_j)$	✓	–
$\mathcal{O}^{(2)}_{l^2u^2D^2}$	$(\bar{l}_\alpha\gamma^\mu \overleftrightarrow{D}^\nu l_\beta)(\bar{u}_i\gamma_\mu \overleftrightarrow{D}_\nu u_j)$	✓	–
$\mathcal{O}^{(1)}_{l^2d^2D^2}$	$D^\nu(\bar{l}_\alpha\gamma^\mu l_\beta)D_\nu(\bar{d}_i\gamma_\mu d_j)$	✓	–
$\mathcal{O}^{(2)}_{l^2d^2D^2}$	$(\bar{l}_\alpha\gamma^\mu \overleftrightarrow{D}^\nu l_\beta)(\bar{d}_i\gamma_\mu \overleftrightarrow{D}_\nu d_j)$	✓	–
$\mathcal{O}^{(1)}_{q^2e^2D^2}$	$D^\nu(\bar{q}_i\gamma^\mu q_j)D_\nu(\bar{e}_\alpha\gamma_\mu e_\beta)$	✓	–
$\mathcal{O}^{(2)}_{q^2e^2D^2}$	$(\bar{q}_i\gamma^\mu \overleftrightarrow{D}^\nu q_j)(\bar{e}_\alpha\gamma_\mu \overleftrightarrow{D}_\nu e_\beta)$	✓	–
$\mathcal{O}^{(1)}_{e^2u^2D^2}$	$D^\nu(\bar{e}_\alpha\gamma^\mu e_\beta)D_\nu(\bar{u}_i\gamma_\mu u_j)$	✓	–
$\mathcal{O}^{(2)}_{e^2u^2D^2}$	$(\bar{e}_\alpha\gamma^\mu \overleftrightarrow{D}^\nu e_\beta)(\bar{u}_i\gamma_\mu \overleftrightarrow{D}_\nu u_j)$	✓	–
$\mathcal{O}^{(1)}_{e^2d^2D^2}$	$D^\nu(\bar{e}_\alpha\gamma^\mu e_\beta)D_\nu(\bar{d}_i\gamma_\mu d_j)$	✓	–
$\mathcal{O}^{(2)}_{e^2d^2D^2}$	$(\bar{e}_\alpha\gamma^\mu \overleftrightarrow{D}^\nu e_\beta)(\bar{d}_i\gamma_\mu \overleftrightarrow{D}_\nu d_j)$	✓	–

Table 3: *Same as 2 but with dimension-8 operators involving 4 fermions.*

$d=8$	$\psi^2 H^4 D$	$pp \to \ell\ell$	$pp \to \ell\nu$
$\mathcal{O}^{(1)}_{l^2H^4D}$	$i(\bar{l}_\alpha \gamma^\mu l_\beta)(H^\dagger \overleftrightarrow{D}_\mu H)(H^\dagger H)$	✓	–
$\mathcal{O}^{(2)}_{l^2H^4D}$	$i(\bar{l}_\alpha \gamma^\mu \tau^I l_\beta)[(H^\dagger \overleftrightarrow{D}^I_\mu H)(H^\dagger H) + (H^\dagger \overleftrightarrow{D}_\mu H)(H^\dagger \tau^I H)]$	✓	✓
$\mathcal{O}^{(3)}_{l^2H^4D}$	$\epsilon^{IJK}(\bar{l}_\alpha \gamma^\mu \tau^I l_\beta)(H^\dagger \overleftrightarrow{D}^J_\mu H)(H^\dagger \tau^K H)$	–	✓
$\mathcal{O}^{(4)}_{l^2H^4D}$	$\epsilon^{IJK}(\bar{l}_\alpha \gamma^\mu \tau^I l_\beta)(H^\dagger \tau^J H)(D_\mu H)^\dagger \tau^K H$	–	✓
$\mathcal{O}^{(1)}_{q^2H^4D}$	$i(\bar{q}_i \gamma^\mu q_j)(H^\dagger \overleftrightarrow{D}_\mu H)(H^\dagger H)$	✓	–
$\mathcal{O}^{(2)}_{q^2H^4D}$	$i(\bar{q}_i \gamma^\mu \tau^I q_j)[(H^\dagger \overleftrightarrow{D}^I_\mu H)(H^\dagger H) + (H^\dagger \overleftrightarrow{D}_\mu H)(H^\dagger \tau^I H)]$	✓	✓
$\mathcal{O}^{(3)}_{q^2H^4D}$	$i\epsilon^{IJK}(\bar{q}_i \gamma^\mu \tau^I q_j)(H^\dagger \overleftrightarrow{D}^J_\mu H)(H^\dagger \tau^K H)$	–	✓
$\mathcal{O}^{(4)}_{q^2H^4D}$	$\epsilon^{IJK}(\bar{q}_i \gamma^\mu \tau^I q_j)(H^\dagger \tau^J H)(D_\mu H)^\dagger \tau^K H$	–	✓
$\mathcal{O}_{e^2H^4D}$	$i(\bar{e}_\alpha \gamma^\mu e_\beta)(H^\dagger \overleftrightarrow{D}_\mu H)(H^\dagger H)$	✓	–
$\mathcal{O}_{u^2H^4D}$	$i(\bar{u}_i \gamma^\mu u_j)(H^\dagger \overleftrightarrow{D}_\mu H)(H^\dagger H)$	✓	–
$\mathcal{O}_{d^2H^4D}$	$i(\bar{d}_i \gamma^\mu d_j)(H^\dagger \overleftrightarrow{D}_\mu H)(H^\dagger H)$	✓	–

$d=8$	$\psi^2 H^2 D^3$	$pp \to \ell\ell$	$pp \to \ell\nu$
$\mathcal{O}^{(1)}_{l^2H^2D^3}$	$i(\bar{l}_\alpha \gamma^\mu D^\nu l_\beta)\,(D_{(\mu}D_{\nu)}H)^\dagger H$	✓	–
$\mathcal{O}^{(2)}_{l^2H^2D^3}$	$i(\bar{l}_\alpha \gamma^\mu D^\nu l_\beta)\,H^\dagger (D_{(\mu}D_{\nu)}H)$	✓	–
$\mathcal{O}^{(3)}_{l^2H^2D^3}$	$i(\bar{l}_\alpha \gamma^\mu \tau^I D^\nu l_\beta)\,(D_{(\mu}D_{\nu)}H)^\dagger \tau^I H)$	✓	✓
$\mathcal{O}^{(4)}_{l^2H^2D^3}$	$i(\bar{l}_\alpha \gamma^\mu \tau^I D^\nu l_\beta)\,H^\dagger \tau^I (D_{(\mu}D_{\nu)}H)$	✓	✓
$\mathcal{O}^{(1)}_{e^2H^2D^3}$	$i(\bar{e}_\alpha \gamma^\mu D^\nu e_\beta)\,(D_{(\mu}D_{\nu)}H)^\dagger H)$	✓	–
$\mathcal{O}^{(2)}_{e^2H^2D^3}$	$i(\bar{e}_\alpha \gamma^\mu D^\nu e_\beta)\,H^\dagger (D_{(\mu}D_{\nu)}H)$	✓	–
$\mathcal{O}^{(1)}_{q^2H^2D^3}$	$i(\bar{q}_i \gamma^\mu D^\nu q_j)\,(D_{(\mu}D_{\nu)}H)^\dagger H$	✓	–
$\mathcal{O}^{(2)}_{q^2H^2D^3}$	$i(\bar{q}_i \gamma^\mu D^\nu q_j)\,H^\dagger (D_{(\mu}D_{\nu)}H)$	✓	–
$\mathcal{O}^{(3)}_{q^2H^2D^3}$	$i(\bar{q}_i \gamma^\mu \tau^I D^\nu q_j)\,(D_{(\mu}D_{\nu)}H)^\dagger \tau^I H$	✓	✓
$\mathcal{O}^{(4)}_{q^2H^2D^3}$	$i(\bar{q}_i \gamma^\mu \tau^I D^\nu q_j)\,H^\dagger \tau^I (D_{(\mu}D_{\nu)}H)$	✓	✓
$\mathcal{O}^{(1)}_{u^2H^2D^3}$	$i(\bar{u}_i \gamma^\mu D^\nu u_j)\,(D_{(\mu}D_{\nu)}H)^\dagger H$	✓	–
$\mathcal{O}^{(2)}_{u^2H^2D^3}$	$i(\bar{u}_i \gamma^\mu D^\nu u_j)\,H^\dagger (D_{(\mu}D_{\nu)}H)$	✓	–
$\mathcal{O}^{(1)}_{d^2H^2D^3}$	$i(\bar{d}_i \gamma^\mu D^\nu d_j)\,(D_{(\mu}D_{\nu)}H)^\dagger H$	✓	–
$\mathcal{O}^{(2)}_{d^2H^2D^3}$	$i(\bar{d}_i \gamma^\mu D^\nu d_j)\,H^\dagger (D_{(\mu}D_{\nu)}H)$	✓	–

Table 4: *Same as 2 but with dimension-8 operators involving 2 fermions.*

Bibliography

[1] Roel Aaij et al. Test of lepton universality in beauty-quark decays. *Nature Phys.*, 18(3):277–282, 2022.

[2] R. Aaij et al. Test of lepton universality with $B^0 \to K^{*0}\ell^+\ell^-$ decays. *JHEP*, 08:055, 2017.

[3] A. Abdesselam et al. Measurement of $\mathcal{R}(D)$ and $\mathcal{R}(D^*)$ with a semileptonic tagging method. 4 2019.

[4] Yasmine Sara Amhis et al. Averages of b-hadron, c-hadron, and τ-lepton properties as of 2018. *Eur. Phys. J. C*, 81(3):226, 2021.

[5] S. Schael et al. Precision electroweak measurements on the Z resonance. *Phys. Rept.*, 427:257–454, 2006.

[6] S. Schael et al. Electroweak Measurements in Electron-Positron Collisions at W-Boson-Pair Energies at LEP. *Phys. Rept.*, 532:119–244, 2013.

[7] Morad Aaboud et al. Measurement of the Higgs boson mass in the $H \to ZZ^* \to 4\ell$ and $H \to \gamma\gamma$ channels with $\sqrt{s} = 13$ TeV pp collisions using the ATLAS detector. *Phys. Lett. B*, 784:345–366, 2018.

[8] Albert M Sirunyan et al. A measurement of the Higgs boson mass in the diphoton decay channel. *Phys. Lett. B*, 805:135425, 2020.

[9] Marzia Bordone, Gino Isidori, and Andrea Pattori. On the Standard Model predictions for R_K and R_{K^*}. *Eur. Phys. J. C*, 76(8):440, 2016.

[10] Roel Aaij et al. Test of lepton universality with $\Lambda_b^0 \to pK^-\ell^+\ell^-$ decays. *JHEP*, 05:040, 2020.

[11] Combination of the ATLAS, CMS and LHCb results on the $B^0_{(s)} \to \mu^+\mu^-$ decays. 2020.

[12] A. Khodjamirian, Th. Mannel, and Y. M. Wang. $B \to K\ell^+\ell^-$ decay at large hadronic recoil. *JHEP*, 02:010, 2013.

[13] Roger Barlow. Asymmetric statistical errors. In *PHYSTAT (2005): Statistical Problems in Particle Physics, Astrophysics and Cosmology*, pages 56–59, 6 2004.

[14] Martin Beneke, Christoph Bobeth, and Robert Szafron. Power-enhanced leading-logarithmic QED corrections to $B_q \to \mu^+\mu^-$. *JHEP*, 10:232, 2019.

[15] Luca Di Luzio and Marco Nardecchia. What is the scale of new physics behind the b-flavour anomalies? *The European Physical Journal C*, 77(8), aug 2017.

[16] R. Aaij et al. Measurement of the ratio of branching fractions $\mathcal{B}(B_c^+ \to J/\psi\tau^+\nu_\tau)/\mathcal{B}(B_c^+ \to J/\psi\mu^+\nu_\mu)$. *Phys. Rev. Lett.*, 120(12):121801, 2018.

[17] Elizabeth E. Jenkins, Aneesh V. Manohar, and Peter Stoffer. Low-Energy Effective Field Theory below the Electroweak Scale: Anomalous Dimensions. *JHEP*, 01:084, 2018.

[18] B. Grzadkowski, M. Iskrzynski, M. Misiak, and J. Rosiek. Dimension-Six Terms in the Standard Model Lagrangian. *JHEP*, 10:085, 2010.

[19] W. Buchmuller and D. Wyler. Effective Lagrangian Analysis of New Interactions and Flavor Conservation. *Nucl. Phys. B*, 268:621–653, 1986.

[20] Elizabeth E. Jenkins, Aneesh V. Manohar, and Michael Trott. Renormalization Group Evolution of the Standard Model Dimension Six Operators I: Formalism and lambda Dependence. *JHEP*, 10:087, 2013.

[21] Hao-Lin Li, Zhe Ren, Jing Shu, Ming-Lei Xiao, Jiang-Hao Yu, and Yu-Hui Zheng. Complete set of dimension-eight operators in the standard model effective field theory. *Phys. Rev. D*, 104(1):015026, 2021.

[22] Christopher W. Murphy. Dimension-8 operators in the Standard Model Eective Field Theory. *JHEP*, 10:174, 2020.

[23] Ilaria Brivio, Sally Dawson, Jorge de Blas, Gauthier Durieux, Pierre Savard, Ansgar Denner, Ayres Freitas, Chris Hays, Ben Pecjak, and Alessandro Vicini. Electroweak input parameters. 11 2021.

[24] Sébastien Descotes-Genon, Adam Falkowski, Marco Fedele, Martín González-Alonso, and Javier Virto. The CKM parameters in the SMEFT. *JHEP*, 05:172, 2019.

[25] Martín González-Alonso, Jorge Martin Camalich, and Kin Mimouni. Renormalization-group evolution of new physics contributions to (semi)leptonic meson decays. *Phys. Lett. B*, 772:777–785, 2017.

[26] Ferruccio Feruglio, Paride Paradisi, and Andrea Pattori. Revisiting Lepton Flavor Universality in B Decays. *Phys. Rev. Lett.*, 118(1):011801, 2017.

[27] Ferruccio Feruglio, Paride Paradisi, and Olcyr Sumensari. Implications of scalar and tensor explanations of $R_{D^{(*)}}$. *JHEP*, 11:191, 2018.

[28] A. Angelescu, Damir Bečirević, D. A. Faroughy, and O. Sumensari. Closing the window on single leptoquark solutions to the B-physics anomalies. *JHEP*, 10:183, 2018.

[29] Andrei Angelescu, Damir Bečirević, Darius A. Faroughy, Florentin Jaffredo, and Olcyr Sumensari. Single leptoquark solutions to the B-physics anomalies. *Phys. Rev. D*, 104(5):055017, 2021.

[30] Gudrun Hiller and Martin Schmaltz. R_K and future $b \to s\ell\ell$ physics beyond the standard model opportunities. *Phys. Rev. D*, 90:054014, 2014.

[31] Ilja Doršner, Svjetlana Fajfer, Darius A. Faroughy, and Nejc Košnik. The role of the S_3 GUT leptoquark in flavor universality and collider searches. *JHEP*, 10:188, 2017.

[32] I. Doršner, S. Fajfer, A. Greljo, J. F. Kamenik, and N. Košnik. Physics of leptoquarks in precision experiments and at particle colliders. *Phys. Rept.*, 641:1–68, 2016.

[33] Martin Bauer and Matthias Neubert. Minimal Leptoquark Explanation for the $R_{D^{(*)}}$, R_K , and $(g-2)_\mu$ Anomalies. *Phys. Rev. Lett.*, 116(14):141802, 2016.

[34] Yasuhito Sakaki, Minoru Tanaka, Andrey Tayduganov, and Ryoutaro Watanabe. Testing leptoquark models in $\bar{B} \to D^{(*)}\tau\bar{\nu}$. *Phys. Rev. D*, 88(9):094012, 2013.

[35] Damir Bečirević, Ilja Doršner, Svjetlana Fajfer, Nejc Košnik, Darius A. Faroughy, and Olcyr Sumensari. Scalar leptoquarks from grand unified theories to accommodate the B-physics anomalies. *Phys. Rev. D*, 98(5):055003, 2018.

[36] Damir Bečirević and Olcyr Sumensari. A leptoquark model to accommodate $R_K^{\rm exp} < R_K^{\rm SM}$ and $R_{K^*}^{\rm exp} < R_{K^*}^{\rm SM}$. *JHEP*, 08:104, 2017.

[37] Nima Assad, Bartosz Fornal, and Benjamin Grinstein. Baryon Number and Lepton Universality Violation in Leptoquark and Diquark Models. *Phys. Lett. B*, 777:324–331, 2018.

[38] Lorenzo Calibbi, Andreas Crivellin, and Toshihiko Ota. Effective Field Theory Approach to $b \to s\ell\ell^{(')}$, $B \to K^{(*)}\nu\overline{\nu}$ and $B \to D^{(*)}\tau\nu$ with Third Generation Couplings. *Phys. Rev. Lett.*, 115:181801, 2015.

[39] Dario Buttazzo, Admir Greljo, Gino Isidori, and David Marzocca. B-physics anomalies: a guide to combined explanations. *JHEP*, 11:044, 2017.

[40] Jacky Kumar, David London, and Ryoutaro Watanabe. Combined Explanations of the $b \to s\mu^+\mu^-$ and $b \to c\tau^-\bar{\nu}$ Anomalies: a General Model Analysis. *Phys. Rev. D*, 99(1):015007, 2019.

[41] Svjetlana Fajfer and Nejc Košnik. Vector leptoquark resolution of R_K and $R_{D^{(*)}}$ puzzles. *Phys. Lett. B*, 755:270–274, 2016.

[42] Andrzej J. Buras, Jennifer Girrbach-Noe, Christoph Niehoff, and David M. Straub. $B \to K^{(*)}\nu\overline{\nu}$ decays in the Standard Model and beyond. *JHEP*, 02:184, 2015.

[43] Gerhard Buchalla and Andrzej J. Buras. QCD corrections to rare K and B decays for arbitrary top quark mass. *Nucl. Phys. B*, 400:225–239, 1993.

[44] Gerhard Buchalla and Andrzej J. Buras. The rare decays $K \to \pi\nu\bar{\nu}$, $B \to X\nu\bar{\nu}$ and $B \to l^+l^-$: An Update. *Nucl. Phys. B*, 548:309–327, 1999.

[45] Mikolaj Misiak and Jorg Urban. QCD corrections to FCNC decays mediated by Z penguins and W boxes. *Phys. Lett. B*, 451:161–169, 1999.

[46] Joachim Brod, Martin Gorbahn, and Emmanuel Stamou. Two-Loop Electroweak Corrections for the $K \to \pi\nu\bar{\nu}$ Decays. *Phys. Rev. D*, 83:034030, 2011.

[47] Elizabeth E. Jenkins, Aneesh V. Manohar, and Michael Trott. Renormalization Group Evolution of the Standard Model Dimension Six Operators II: Yukawa Dependence. *JHEP*, 01:035, 2014.

[48] Rodrigo Alonso, Elizabeth E. Jenkins, Aneesh V. Manohar, and Michael Trott. Renormalization Group Evolution of the Standard Model Dimension Six Operators III: Gauge Coupling Dependence and Phenomenology. *JHEP*, 04:159, 2014.

[49] J. P. Lees et al. Search for $B \to K^{(*)}\nu\overline{\nu}$ and invisible quarkonium decays. *Phys. Rev. D*, 87(11):112005, 2013.

[50] J. Grygier et al. Search for $\boldsymbol{B \to h\nu\bar{\nu}}$ decays with semileptonic tagging at Belle. *Phys. Rev. D*, 96(9):091101, 2017. [Addendum: Phys.Rev.D 97, 099902 (2018)].

[51] F. Abudinén et al. Search for B+→K+$\nu\nu^{-}$ Decays Using an Inclusive Tagging Method at Belle II. *Phys. Rev. Lett.*, 127(18):181802, 2021.

[52] Lukas Allwicher, Darius Faroughy, Florentin Jaffredo, Olcyr Sumensari, and Felix Wilsch. In preparation. 2022.

[53] Ferruccio Feruglio, Paride Paradisi, and Andrea Pattori. On the Importance of Electroweak Corrections for B Anomalies. *JHEP*, 09:061, 2017.

[54] Claudia Cornella, Ferruccio Feruglio, and Paride Paradisi. Low-energy Effects of Lepton Flavour Universality Violation. *JHEP*, 11:012, 2018.

[55] Víctor Bresó-Pla, Adam Falkowski, and Martín González-Alonso. A_{FB} in the SMEFT: precision Z physics at the LHC. *JHEP*, 08:021, 2021.

[56] P. A. Zyla et al. Review of Particle Physics. *PTEP*, 2020(8):083C01, 2020.

[57] Rodrigo Alonso, Benjamín Grinstein, and Jorge Martin Camalich. Lifetime of B_c^- Constrains Explanations for Anomalies in $B \to D^{(*)}\tau\nu$. *Phys. Rev. Lett.*, 118(8):081802, 2017.

[58] A. Bazavov et al. Semileptonic form factors for $B \to D^*\ell\nu$ at nonzero recoil from 2 + 1-flavor lattice QCD. 5 2021.

[59] Florian U. Bernlochner, Zoltan Ligeti, Michele Papucci, and Dean J. Robinson. Combined analysis of semileptonic B decays to D and D^*: $R(D^{(*)})$, $|V_{cb}|$, and new physics. *Phys. Rev. D*, 95(11):115008, 2017. [Erratum: Phys.Rev.D 97, 059902 (2018)].

[60] Sabine Crepe-Renaudin. The start of Tevatron and D0 in Run 2. *Frascati Phys. Ser.*, 27:727–741, 2002.

[61] Philipp Böer, Ahmet Kokulu, Jan-Niklas Toelstede, and Danny van Dyk. Angular Analysis of \boldmath $\Lambda_b \to \Lambda_c(\to \Lambda\pi)\ell\bar{\nu}$. *JHEP*, 12:082, 2019.

[62] S. Aoki et al. FLAG Review 2019: Flavour Lattice Averaging Group (FLAG). *Eur. Phys. J. C*, 80(2):113, 2020.

[63] Damir Bečirević, Marco Fedele, Ivan Nišandžić, and Andrey Tayduganov. Lepton Flavor Universality tests through angular observables of $\overline{B} \to D^{(*)}\ell\overline{\nu}$ decay modes. 7 2019.

[64] G. C. Donald, C. T. H. Davies, J. Koponen, and G. P. Lepage. V_{cs} from $D_s \to \phi\ell\nu$ semileptonic decay and full lattice QCD. *Phys. Rev. D*, 90(7):074506, 2014.

[65] Judd Harrison, Christine T. H. Davies, and Andrew Lytle. $B_c \to J/\psi$ form factors for the full q^2 range from lattice QCD. *Phys. Rev. D*, 102(9):094518, 2020.

[66] J. Charles et al. Current status of the Standard Model CKM fit and constraints on $\Delta F = 2$ New Physics. *Phys. Rev. D*, 91(7):073007, 2015.

[67] M. Bona et al. The Unitarity Triangle Fit in the Standard Model and Hadronic Parameters from Lattice QCD: A Reappraisal after the Measurements of Delta m(s) and BR(B —> tau nu(tau)). *JHEP*, 10:081, 2006.

[68] Simone Bifani, Sébastien Descotes-Genon, Antonio Romero Vidal, and Marie-Hélène Schune. Review of Lepton Universality tests in B decays. *J. Phys. G*, 46(2):023001, 2019.

[69] Giovanni Banelli, Robert Fleischer, Ruben Jaarsma, and Gilberto Tetlalmatzi-Xolocotzi. Decoding (Pseudo)-Scalar Operators in Leptonic and Semileptonic B Decays. *Eur. Phys. J. C*, 78(11):911, 2018.

[70] B. Colquhoun, C. T. H. Davies, R. J. Dowdall, J. Kettle, J. Koponen, G. P. Lepage, and A. T. Lytle. B-meson decay constants: a more complete picture from full lattice QCD. *Phys. Rev. D*, 91(11):114509, 2015.

[71] N. Carrasco, P. Lami, V. Lubicz, L. Riggio, S. Simula, and C. Tarantino. $K \to \pi$ semileptonic form factors with $N_f = 2{+}1{+}1$ twisted mass fermions. *Phys. Rev. D*, 93(11):114512, 2016.

[72] Junpei Kakazu, Ken-ichi Ishikawa, Naruhito Ishizuka, Yoshinobu Kuramashi, Yoshifumi Nakamura, Yusuke Namekawa, Yusuke Taniguchi, Naoya Ukita, Takeshi Yamazaki, and Tomoteru Yoshié. K_{l3} form factors at the physical point on a $(10.9fm)^3$ volume. *Phys. Rev. D*, 101(9):094504, 2020.

[73] A. Bazavov et al. Determination of $|V_{us}|$ from a Lattice-QCD Calculation of the $K \to \pi\ell\nu$ Semileptonic Form Factor with Physical Quark Masses. *Phys. Rev. Lett.*, 112(11):112001, 2014.

[74] I. Baum, V. Lubicz, G. Martinelli, L. Orifici, and S. Simula. Matrix elements of the electromagnetic operator between kaon and pion states. *Phys. Rev. D*, 84:074503, 2011.

[75] V. Lubicz, L. Riggio, G. Salerno, S. Simula, and C. Tarantino. Scalar and vector form factors of $D \to \pi(K)\ell\nu$ decays with $N_f = 2 + 1 + 1$ twisted fermions. *Phys. Rev. D*, 96(5):054514, 2017. [Erratum: Phys.Rev.D 99, 099902 (2019), Erratum: Phys.Rev.D 100, 079901 (2019)].

[76] V. Lubicz, L. Riggio, G. Salerno, S. Simula, and C. Tarantino. Tensor form factor of $D \to \pi(K)\ell\nu$ and $D \to \pi(K)\ell\ell$ decays with $N_f = 2 + 1 + 1$ twisted-mass fermions. *Phys. Rev. D*, 98(1):014516, 2018.

[77] Jon A. Bailey et al. B→D$\ell\nu$ form factors at nonzero recoil and |V_{cb}| from 2+1-flavor lattice QCD. *Phys. Rev. D*, 92(3):034506, 2015.

[78] Heechang Na, Chris M. Bouchard, G. Peter Lepage, Chris Monahan, and Junko Shigemitsu. $B \to Dl\nu$ form factors at nonzero recoil and extraction of $|V_{cb}|$. *Phys. Rev. D*, 92(5):054510, 2015. [Erratum: Phys.Rev.D 93, 119906 (2016)].

[79] Mariam Atoui, Vincent Morénas, Damir Bečirevic, and Francesco Sanfilippo. $B_s \to D_s \ell \nu_\ell$ near zero recoil in and beyond the Standard Model. *Eur. Phys. J. C*, 74(5):2861, 2014.

[80] Jon A. Bailey et al. $|V_{ub}|$ from $B \to \pi \ell \nu$ decays and (2+1)-flavor lattice QCD. *Phys. Rev. D*, 92(1):014024, 2015.

[81] J. M. Flynn, T. Izubuchi, T. Kawanai, C. Lehner, A. Soni, R. S. Van de Water, and O. Witzel. $B \to \pi \ell \nu$ and $B_s \to K \ell \nu$ form factors and $|V_{ub}|$ from 2+1-flavor lattice QCD with domain-wall light quarks and relativistic heavy quarks. *Phys. Rev. D*, 91(7):074510, 2015.

[82] Jon A. Bailey et al. $B \to \pi \ell \ell$ form factors for new-physics searches from lattice QCD. *Phys. Rev. Lett.*, 115(15):152002, 2015.

[83] Alexei Bazavov et al. $B_s \to K \ell \nu$ decay from lattice QCD. *Phys. Rev. D*, 100(3):034501, 2019.

[84] M. Antonelli et al. An Evaluation of $|V_{us}|$ and precise tests of the Standard Model from world data on leptonic and semileptonic kaon decays. *Eur. Phys. J. C*, 69:399–424, 2010.

[85] William J. Marciano and A. Sirlin. Radiative corrections to pi(lepton 2) decays. *Phys. Rev. Lett.*, 71:3629–3632, 1993.

[86] A. Sirlin. Current Algebra Formulation of Radiative Corrections in Gauge Theories and the Universality of the Weak Interactions. *Rev. Mod. Phys.*, 50:573, 1978. [Erratum: Rev.Mod.Phys. 50, 905 (1978)].

[87] Vincenzo Cirigliano and Ignasi Rosell. pi/K —> e anti-nu(e) branching ratios to O(e**2 p**4) in Chiral Perturbation Theory. *JHEP*, 10:005, 2007.

[88] M. Di Carlo, D. Giusti, V. Lubicz, G. Martinelli, C. T. Sachrajda, F. Sanfilippo, S. Simula, and N. Tantalo. Light-meson leptonic decay rates in lattice QCD+QED. *Phys. Rev. D*, 100(3):034514, 2019.

[89] William J. Marciano. Precise determination of |V(us)| from lattice calculations of pseudoscalar decay constants. *Phys. Rev. Lett.*, 93:231803, 2004.

[90] Vincenzo Cirigliano, Gerhard Ecker, Helmut Neufeld, Antonio Pich, and Jorge Portoles. Kaon Decays in the Standard Model. *Rev. Mod. Phys.*, 84:399, 2012.

[91] Jonathan L. Rosner, Sheldon Stone, and Ruth S. Van de Water. Leptonic Decays of Charged Pseudoscalar Mesons - 2015. 9 2015.

[92] Antonio Pich. Precision Tau Physics. *Prog. Part. Nucl. Phys.*, 75:41–85, 2014.

[93] Roger Decker and Markus Finkemeier. Short and long distance effects in the decay tau —> pi tau-neutrino (gamma). *Nucl. Phys. B*, 438:17–53, 1995.

[94] Stefan de Boer, Teppei Kitahara, and Ivan Nisandzic. Soft-Photon Corrections to $\bar{B} \to D\tau^-\bar{\nu}_\tau$ Relative to $\bar{B} \to D\mu^-\bar{\nu}_\mu$. *Phys. Rev. Lett.*, 120(26):261804, 2018.

[95] Gino Isidori, Saad Nabeebaccus, and Roman Zwicky. QED corrections in $\overline{B} \to \overline{K}\ell^+\ell^-$ at the double-differential level. *JHEP*, 12:104, 2020.

[96] Damir Becirevic and Nejc Kosnik. Soft photons in semileptonic B —> D decays. *Acta Phys. Polon. Supp.*, 3:207–214, 2010.

[97] D. Besson et al. Improved measurements of D meson semileptonic decays to pi and K mesons. *Phys. Rev. D*, 80:032005, 2009.

[98] M. Ablikim et al. Analysis of $D^+ \to \bar{K}^0 e^+ \nu_e$ and $D^+ \to \pi^0 e^+ \nu_e$ semileptonic decays. *Phys. Rev. D*, 96(1):012002, 2017.

[99] M. Ablikim et al. Measurement of the branching fraction for the semi-leptonic decay $D^{0(+)} \to \pi^{-(0)} \mu^+ \nu_\mu$ and test of lepton universality. *Phys. Rev. Lett.*, 121(17):171803, 2018.

[100] Medina Ablikim et al. Observation of the leptonic decay $D^+ \to \tau^+ \nu_\tau$. *Phys. Rev. Lett.*, 123(21):211802, 2019.

[101] M. Ablikim et al. Measurement of the absolute branching fractions for purely leptonic D_s^+ decays. *Phys. Rev. D*, 104(5):052009, 2021.

[102] A. Sibidanov et al. Search for $B^- \to \mu^- \bar{\nu}_\mu$ Decays at the Belle Experiment. *Phys. Rev. Lett.*, 121(3):031801, 2018.

[103] R. Glattauer et al. Measurement of the decay $B \to D \ell \nu_\ell$ in fully reconstructed events and determination of the Cabibbo-Kobayashi-Maskawa matrix element $|V_{cb}|$. *Phys. Rev. D*, 93(3):032006, 2016.

[104] Matthew Moulson. Experimental determination of V_{us} from kaon decays. *PoS*, CKM2016:033, 2017.

[105] D. Giusti, V. Lubicz, G. Martinelli, C. T. Sachrajda, F. Sanfilippo, S. Simula, N. Tantalo, and C. Tarantino. First lattice calculation of the QED corrections to leptonic decay rates. *Phys. Rev. Lett.*, 120(7):072001, 2018.

[106] Andrzej Czarnecki, William J. Marciano, and Alberto Sirlin. Radiative Corrections to Neutron and Nuclear Beta Decays Revisited. *Phys. Rev. D*, 100(7):073008, 2019.

[107] William J. Marciano and Alberto Sirlin. Improved calculation of electroweak radiative corrections and the value of V(ud). *Phys. Rev. Lett.*, 96:032002, 2006.

[108] Chien-Yeah Seng, Mikhail Gorchtein, Hiren H. Patel, and Michael J. Ramsey-Musolf. Reduced Hadronic Uncertainty in the Determination of V_{ud}. *Phys. Rev. Lett.*, 121(24):241804, 2018.

[109] Chien-Yeah Seng, Xu Feng, Mikhail Gorchtein, and Lu-Chang Jin. Joint lattice QCD–dispersion theory analysis confirms the quark-mixing top-row unitarity deficit. *Phys. Rev. D*, 101(11):111301, 2020.

[110] Andreas Crivellin and Martin Hoferichter. β Decays as Sensitive Probes of Lepton Flavor Universality. *Phys. Rev. Lett.*, 125(11):111801, 2020.

[111] F. Ambrosino et al. Measurement of the absolute branching ratios for semileptonic $K^\pm$ decays with the KLOE detector. *JHEP*, 02:098, 2008.

[112] M. Ablikim et al. Study of Dynamics of $D^0 \to K^- e^+ \nu_e$ and $D^0 \to \pi^- e^+ \nu_e$ Decays. *Phys. Rev. D*, 92(7):072012, 2015.

[113] L. Riggio, G. Salerno, and S. Simula. Extraction of $|V_{cd}|$ and $|V_{cs}|$ from experimental decay rates using lattice QCD $D \to \pi(K)\ell\nu$ form factors. *Eur. Phys. J. C*, 78(6):501, 2018.

[114] Robert Fleischer, Ruben Jaarsma, and Gabriël Koole. Testing Lepton Flavour Universality with (Semi)-Leptonic $D_{(s)}$ Decays. *Eur. Phys. J. C*, 80(2):153, 2020.

[115] Xue Leng, Xiao-Long Mu, Zhi-Tian Zou, and Ying Li. Investigation on effects of new physics in $c \to (s,d)\ell^+\nu_\ell$ transitions. *Chin. Phys. C*, 45(6):063107, 2021.

[116] Svjetlana Fajfer, Ivan Nisandzic, and Ursa Rojec. Discerning new physics in charm meson leptonic and semileptonic decays. *Phys. Rev. D*, 91(9):094009, 2015.

[117] Medina Ablikim et al. Study of the $D^0 \to K^- \mu^+ \nu_\mu$ dynamics and test of lepton flavor universality with $D^0 \to K^- \ell^+ \nu_\ell$ decays. *Phys. Rev. Lett.*, 122(1):011804, 2019.

[118] Medina Ablikim et al. Improved measurement of the absolute branching fraction of $D^+ \to \bar{K}^0 \mu^+ \nu_\mu$. *Eur. Phys. J. C*, 76(7):369, 2016.

[119] J. P. Lees et al. Evidence for an excess of $\bar{B} \to D^{(*)} \tau^- \bar{\nu}_\tau$ decays. *Phys. Rev. Lett.*, 109:101802, 2012.

[120] M. Huschle et al. Measurement of the branching ratio of $\bar{B} \to D^{(*)} \tau^- \bar{\nu}_\tau$ relative to $\bar{B} \to D^{(*)} \ell^- \bar{\nu}_\ell$ decays with hadronic tagging at Belle. *Phys. Rev. D*, 92(7):072014, 2015.

[121] S. Hirose et al. Measurement of the τ lepton polarization and $R(D^*)$ in the decay $\bar{B} \to D^* \tau^- \bar{\nu}_\tau$. *Phys. Rev. Lett.*, 118(21):211801, 2017.

[122] Roel Aaij et al. Measurement of the ratio of branching fractions $\mathcal{B}(\bar{B}^0 \to D^{*+} \tau^- \bar{\nu}_\tau)/\mathcal{B}(\bar{B}^0 \to D^{*+} \mu^- \bar{\nu}_\mu)$. *Phys. Rev. Lett.*, 115(11):111803, 2015. [Erratum: Phys.Rev.Lett. 115, 159901 (2015)].

[123] P. Gambino et al. Challenges in semileptonic B decays. *Eur. Phys. J. C*, 80(10):966, 2020.

[124] Judd Harrison, Christine T. H. Davies, and Andrew Lytle. $R(J/\psi)$ and $B_c^- \to J/\psi \ell^- \bar{\nu}_\ell$ Lepton Flavor Universality Violating Observables from Lattice QCD. *Phys. Rev. Lett.*, 125(22):222003, 2020.

[125] Gino Isidori and Olcyr Sumensari. Optimized lepton universality tests in $B \to V \ell \bar{\nu}$ decays. *Eur. Phys. J. C*, 80(11):1078, 2020.

[126] J. P. Lees et al. Branching fraction and form-factor shape measurements of exclusive charmless semileptonic B decays, and determination of $|V_{ub}|$. *Phys. Rev. D*, 86:092004, 2012.

[127] A. Sibidanov et al. Study of Exclusive $B \to X_u \ell \nu$ Decays and Extraction of $\|V_{ub}\|$ using Full Reconstruction Tagging at the Belle Experiment. *Phys. Rev. D*, 88(3):032005, 2013.

[128] P. Hamer et al. Search for $B^0 \to \pi^- \tau^+ \nu_\tau$ with hadronic tagging at Belle. *Phys. Rev. D*, 93(3):032007, 2016.

[129] W. Altmannshofer et al. The Belle II Physics Book. *PTEP*, 2019(12):123C01, 2019. [Erratum: PTEP 2020, 029201 (2020)].

[130] Christopher J. Monahan, Chris M. Bouchard, G. Peter Lepage, Heechang Na, and Junko Shigemitsu. Form factor ratios for $B_s \to K\,\ell\,\nu$ and $B_s \to D_s\,\ell\,\nu$ semileptonic decays and $|V_{ub}/V_{cb}|$. *Phys. Rev. D*, 98(11):114509, 2018.

[131] Roel Aaij et al. First observation of the decay $B_s^0 \to K^-\mu^+\nu_\mu$ and Measurement of $|V_{ub}|/|V_{cb}|$. *Phys. Rev. Lett.*, 126(8):081804, 2021.

[132] Riccardo Barbieri, Gino Isidori, Joel Jones-Perez, Paolo Lodone, and David M. Straub. $U(2)$ and Minimal Flavour Violation in Supersymmetry. *Eur. Phys. J. C*, 71:1725, 2011.

[133] Javier Fuentes-Martín, Gino Isidori, Julie Pagès, and Kei Yamamoto. With or without U(2)? Probing non-standard flavor and helicity structures in semileptonic B decays. *Phys. Lett. B*, 800:135080, 2020.

[134] N. Carrasco et al. Up, down, strange and charm quark masses with N_f = 2+1+1 twisted mass lattice QCD. *Nucl. Phys. B*, 887:19–68, 2014.

[135] Pouya Asadi, Anna Hallin, Jorge Martin Camalich, David Shih, and Susanne Westhoff. Complete framework for tau polarimetry in $B \to D^{(*)}\tau\nu$ decays. *Phys. Rev. D*, 102(9):095028, 2020.

[136] Rodrigo Alonso, Jorge Martin Camalich, and Susanne Westhoff. Tau properties in $B \to D\tau\nu$ from visible final-state kinematics. *Phys. Rev. D*, 95(9):093006, 2017.

[137] R. Frezzotti, M. Garofalo, V. Lubicz, G. Martinelli, C. T. Sachrajda, F. Sanfilippo, S. Simula, and N. Tantalo. Comparison of lattice QCD+QED predictions for radiative leptonic decays of light mesons with experimental data. *Phys. Rev. D*, 103(5):053005, 2021.

[138] J. P. Lees et al. Measurement of an Excess of $\bar{B} \to D^{(*)}\tau^-\bar{\nu}_\tau$ Decays and Implications for Charged Higgs Bosons. *Phys. Rev. D*, 88(7):072012, 2013.

[139] Y. Aoki et al. FLAG Review 2021. 11 2021.

[140] Judd Harrison and Christine T. H. Davies. $B_s \to D_s^*$form factors for the full q^2 range from lattice QCD. *Phys. Rev. D*, 105(9):094506, 2022.

[141] T. Kaneko, Y. Aoki, G. Bailas, B. Colquhoun, H. Fukaya, S. Hashimoto, and J. Koponen. $B \to D^{(*)}\ell\nu$ form factors from lattice QCD with relativistic heavy quarks. *PoS*, LATTICE2019:139, 2019.

[142] M. Huschle et al. Measurement of the branching ratio of $\bar{B} \to D^{(*)}\tau^-\bar{\nu}_\tau$ relative to $\bar{B} \to D^{(*)}\ell^-\bar{\nu}_\ell$ decays with hadronic tagging at Belle. *Phys. Rev. D*, 92(7):072014, 2015.

[143] Y. Sato et al. Measurement of the branching ratio of $\bar{B}^0 \to D^{*+}\tau^-\bar{\nu}_\tau$ relative to $\bar{B}^0 \to D^{*+}\ell^-\bar{\nu}_\ell$ decays with a semileptonic tagging method. *Phys. Rev. D*, 94(7):072007, 2016.

[144] G. Caria et al. Measurement of $\mathcal{R}(D)$ and $\mathcal{R}(D^*)$ with a semileptonic tagging method. *Phys. Rev. Lett.*, 124(16):161803, 2020.

[145] Y. Amhis et al. Averages of b-hadron, c-hadron, and τ-lepton properties as of 2021. 6 2022.

[146] Damir Becirevic, Svjetlana Fajfer, Ivan Nisandzic, and Andrey Tayduganov. Angular distributions of $\bar{B} \to D^{(*)}\ell\bar{\nu}_\ell$ decays and search of New Physics. *Nucl. Phys. B*, 946:114707, 2019.

[147] Christoph Bobeth, Marzia Bordone, Nico Gubernari, Martin Jung, and Danny van Dyk. Lepton-flavour non-universality of $\bar{B} \to D^*\ell\bar{\nu}$ angular distributions in and beyond the Standard Model. *Eur. Phys. J. C*, 81(11):984, 2021.

[148] Alexandre Carvunis, Andreas Crivellin, Diego Guadagnoli, and Shireen Gangal. The Forward-Backward Asymmetry in $B \to D^*\ell\nu$: One more hint for Scalar Leptoquarks? *Phys. Rev. D*, 105(3):L031701, 2022.

[149] C. P. Burgess, Serge Hamoudou, Jacky Kumar, and David London. Beyond the standard model effective field theory with $B \to c\tau^-\overline{\nu}$. *Phys. Rev. D*, 105(7):073008, 2022.

[150] Bhubanjyoti Bhattacharya, Alakabha Datta, Saeed Kamali, and David London. A measurable angular distribution for $\overline{B} \to D^*\tau^-\overline{v}_\tau$ decays. *JHEP*, 07(07):194, 2020.

[151] Alejandro Celis, Martin Jung, Xin-Qiang Li, and Antonio Pich. Scalar contributions to $b \to c(u)\tau\nu$ transitions. *Phys. Lett. B*, 771:168–179, 2017.

[152] Roel Aaij et al. Measurement of the shape of the $\Lambda_b^0 \to \Lambda_c^+\mu^-\overline{\nu}_\mu$ differential decay rate. *Phys. Rev. D*, 96(11):112005, 2017.

[153] Roel Aaij et al. Observation of the decay $\Lambda_b^0 \to \Lambda_c^+\tau^-\overline{\nu}_\tau$. *Phys. Rev. Lett.*, 128(19):191803, 2022.

[154] William Detmold, Christoph Lehner, and Stefan Meinel. $\Lambda_b \to p\ell^-\bar{\nu}_\ell$ and $\Lambda_b \to \Lambda_c\ell^-\bar{\nu}_\ell$ form factors from lattice QCD with relativistic heavy quarks. *Phys. Rev. D*, 92(3):034503, 2015.

[155] Lukas Allwicher, Darius A. Faroughy, Florentin Jaffredo, Olcyr Sumensari, and Felix Wilsch. Drell-Yan Tails Beyond the Standard Model. 7 2022.

[156] Lukas Allwicher, Darius. A. Faroughy, Florentin Jaffredo, Olcyr Sumensari, and Felix Wilsch. HighPT: A Tool for high-p_T Drell-Yan Tails Beyond the Standard Model. 7 2022.

[157] Florentin Jaffredo. Revisiting mono-τ tails at the LHC. *Eur. Phys. J. C*, 82(6):541, 12 2021.

[158] Syuhei Iguro, Michihisa Takeuchi, and Ryoutaro Watanabe. Testing leptoquark/EFT in $\bar{B} \to D^{(*)}l\bar{\nu}$ at the LHC. *Eur. Phys. J. C*, 81(5):406, 2021.

[159] David Marzocca, Ui Min, and Minho Son. Bottom-Flavored Mono-Tau Tails at the LHC. *JHEP*, 12:035, 2020.

[160] Admir Greljo, Jorge Martin Camalich, and José David Ruiz-Álvarez. Mono-τ Signatures at the LHC Constrain Explanations of B-decay Anomalies. *Phys. Rev. Lett.*, 122(13):131803, 2019.

[161] Alakabha Datta, Saeed Kamali, Stefan Meinel, and Ahmed Rashed. Phenomenology of $\Lambda_b \to \Lambda_c\tau\overline{\nu}_\tau$ using lattice QCD calculations. *JHEP*, 08:131, 2017.

[162] Medina Ablikim et al. Measurements of Weak Decay Asymmetries of $\Lambda_c^+ \to pK_S^0$, $\Lambda\pi^+$, $\Sigma^+\pi^0$, and $\Sigma^0\pi^+$. *Phys. Rev. D*, 100(7):072004, 2019.

[163] Thomas Gutsche, Mikhail A. Ivanov, Jürgen G. Körner, Valery E. Lyubovitskij, Pietro Santorelli, and Nurgul Habyl. Semileptonic decay $\Lambda_b \to \Lambda_c + \tau^- + \bar{\nu_\tau}$ in the covariant confined quark model. *Phys. Rev. D*, 91(7):074001, 2015. [Erratum: Phys.Rev.D 91, 119907 (2015)].

[164] Xiao-Long Mu, Ying Li, Zhi-Tian Zou, and Bin Zhu. Investigation of effects of new physics in $\Lambda_b \to \Lambda_c \tau \bar{\nu}_\tau$ decay. *Phys. Rev. D*, 100(11):113004, 2019.

[165] Quan-Yi Hu, Xin-Qiang Li, Ya-Dong Yang, and Dong-Hui Zheng. The measurable angular distribution of $\Lambda_b^0 \to \Lambda_c^+ \left(\to \Lambda^0\pi^+\right) \tau^- \left(\to \pi^- v_\tau\right) \bar{v}_\tau$ decay. *JHEP*, 02:183, 2021.

[166] Neus Penalva, Eliecer Hernández, and Juan Nieves. Further tests of lepton flavour universality from the charged lepton energy distribution in $b \to c$ semileptonic decays: The case of $\Lambda_b \to \Lambda_c \ell \bar{\nu}_\ell$. *Phys. Rev. D*, 100(11):113007, 2019.

[167] Luca Di Luzio, Admir Greljo, and Marco Nardecchia. Gauge leptoquark as the origin of B-physics anomalies. *Phys. Rev. D*, 96(11):115011, 2017.

[168] Marzia Bordone, Claudia Cornella, Javier Fuentes-Martín, and Gino Isidori. Low-energy signatures of the PS^3 model: from B-physics anomalies to LFV. *JHEP*, 10:148, 2018.

[169] Javier Fuentes-Martín, Gino Isidori, Matthias König, and Nudžeim Selimović. Vector Leptoquarks Beyond Tree Level. *Phys. Rev. D*, 101(3):035024, 2020.

[170] Monika Blanke and Andreas Crivellin. B Meson Anomalies in a Pati-Salam Model within the Randall-Sundrum Background. *Phys. Rev. Lett.*, 121(1):011801, 2018.

[171] Javier Fuentes-Martin, Gino Isidori, Javier M. Lizana, Nudzeim Selimovic, and Ben A. Stefanek. Flavor hierarchies, flavor anomalies, and Higgs mass from a warped extra dimension. 3 2022.

[172] Rodrigo Alonso, Benjamin Grinstein, and Jorge Martin Camalich. $SU(2) \times U(1)$ gauge invariance and the shape of new physics in rare B decays. *Phys. Rev. Lett.*, 113:241802, 2014.

[173] Rodrigo Alonso, Benjamín Grinstein, and Jorge Martin Camalich. Lepton universality violation and lepton flavor conservation in B-meson decays. *JHEP*, 10:184, 2015.

[174] B. Grinstein, S. Pokorski, and G. G. Ross. Lepton non-universality in B decays and fermion mass structure. *JHEP*, 12:079, 2018.

[175] Svjetlana Fajfer, Jernej F. Kamenik, Ivan Nisandzic, and Jure Zupan. Implications of Lepton Flavor Universality Violations in B Decays. *Phys. Rev. Lett.*, 109:161801, 2012.

[176] Alejandro Celis, Martin Jung, Xin-Qiang Li, and Antonio Pich. Sensitivity to charged scalars in $\boldsymbol{B \to D^{(*)}\tau\nu_\tau}$ and $\boldsymbol{B \to \tau\nu_\tau}$ decays. *JHEP*, 01:054, 2013.

[177] Shaikh Saad and Anil Thapa. Common origin of neutrino masses and $R_{D^{(*)}}$, $R_{K^{(*)}}$ anomalies. *Phys. Rev. D*, 102(1):015014, 2020.

[178] Damir Bečirević, Ilja Doršner, Svjetlana Fajfer, Darius A. Faroughy, Florentin Jaffredo, Nejc Košnik, and Olcyr Sumensari. On a model with two scalar leptoquarks – r_2 and s_3. 2022.

[179] Andreas Crivellin, Benjamin Fuks, and Luc Schnell. Explaining the hints for lepton flavour universality violation with three S_2 leptoquark generations. *JHEP*, 06:169, 2022.

[180] Valerio Gherardi, David Marzocca, and Elena Venturini. Low-energy phenomenology of scalar leptoquarks at one-loop accuracy. *JHEP*, 01:138, 2021.

[181] Andreas Crivellin, Dario Müller, and Toshihiko Ota. Simultaneous explanation of R(D$^{()}$) and b$\to$sμ^+ μ: the last scalar leptoquarks standing. *JHEP*, 09:040, 2017.

[182] Andreas Crivellin, Dario Müller, and Francesco Saturnino. Flavor Phenomenology of the Leptoquark Singlet-Triplet Model. *JHEP*, 06:020, 2020.

[183] G. D'Ambrosio, G. F. Giudice, G. Isidori, and A. Strumia. Minimal flavor violation: An Effective field theory approach. *Nucl. Phys. B*, 645:155–187, 2002.

[184] Marco Farina, Giuliano Panico, Duccio Pappadopulo, Joshua T. Ruderman, Riccardo Torre, and Andrea Wulzer. Energy helps accuracy: electroweak precision tests at hadron colliders. *Phys. Lett. B*, 772:210–215, 2017.

[185] Darius A. Faroughy, Admir Greljo, and Jernej F. Kamenik. Confronting lepton flavor universality violation in B decays with high-p_T tau lepton searches at LHC. *Phys. Lett. B*, 764:126–134, 2017.

[186] Jorge de Blas, Mikael Chala, and Jose Santiago. Global Constraints on Lepton-Quark Contact Interactions. *Phys. Rev. D*, 88:095011, 2013.

[187] Sacha Davidson, Sebastien Descotes-Genon, and Patrice Verdier. Of Contact Interactions and Colliders. *Phys. Rev. D*, 91(5):055031, 2015.

[188] S. Dawson, P. P. Giardino, and A. Ismail. Standard model EFT and the Drell-Yan process at high energy. *Phys. Rev. D*, 99(3):035044, 2019.

[189] Vincenzo Cirigliano, Martin Gonzalez-Alonso, and Michael L. Graesser. Non-standard Charged Current Interactions: beta decays versus the LHC. *JHEP*, 02:046, 2013.

[190] Admir Greljo and David Marzocca. High-p_T dilepton tails and flavor physics. *Eur. Phys. J. C*, 77(8):548, 2017.

[191] Javier Fuentes-Martin, Admir Greljo, Jorge Martin Camalich, and José David Ruiz-Alvarez. Charm physics confronts high-p$_T$ lepton tails. *JHEP*, 11:080, 2020.

[192] Hsi-Ming Chang, Martin González-Alonso, and Jorge Martin Camalich. Nonstandard Semileptonic Hyperon Decays. *Phys. Rev. Lett.*, 114(16):161802, 2015.

[193] Vincenzo Cirigliano, Adam Falkowski, Martín González-Alonso, and Antonio Rodríguez-Sánchez. Hadronic τ Decays as New Physics Probes in the LHC Era. *Phys. Rev. Lett.*, 122(22):221801, 2019.

[194] Motoi Endo, Syuhei Iguro, Teppei Kitahara, Michihisa Takeuchi, and Ryoutaro Watanabe. Non-resonant new physics search at the LHC for the b $\to$ c$\tau\nu$ anomalies. *JHEP*, 02:106, 2022.

[195] Andrei Angelescu, Darius A. Faroughy, and Olcyr Sumensari. Lepton Flavor Violation and Dilepton Tails at the LHC. *Eur. Phys. J. C*, 80(7):641, 2020.

[196] Radja Boughezal, Emanuele Mereghetti, and Frank Petriello. Dilepton production in the SMEFT at O(1/Λ4). *Phys. Rev. D*, 104(9):095022, 2021.

[197] Lukas Allwicher, Darius Faroughy, Florentin Jaffredo, Olcyr Sumensari, and Felix Wilsch. HighPT: A Tool for High-pT Collider Studies Beyond the Standard Model. 2022.

[198] David M. Straub. flavio: a Python package for flavour and precision phenomenology in the Standard Model and beyond. 10 2018.

[199] Jason Aebischer, Jacky Kumar, Peter Stangl, and David M. Straub. A Global Likelihood for Precision Constraints and Flavour Anomalies. *Eur. Phys. J. C*, 79(6):509, 2019.

[200] Adam Falkowski and David Straub. Flavourful SMEFT likelihood for Higgs and electroweak data. *JHEP*, 04:066, 2020.

[201] W. Buchmuller, R. Ruckl, and D. Wyler. Leptoquarks in Lepton - Quark Collisions. *Phys. Lett. B*, 191:442–448, 1987. [Erratum: Phys.Lett.B 448, 320–320 (1999)].

[202] Luca Buonocore, Paolo Nason, Francesco Tramontano, and Giulia Zanderighi. Photon and leptons induced processes at the LHC. *JHEP*, 12:073, 2021.

[203] John M. Campbell, J. W. Huston, and W. J. Stirling. Hard Interactions of Quarks and Gluons: A Primer for LHC Physics. *Rept. Prog. Phys.*, 70:89, 2007.

[204] C. Buttar et al. Les houches physics at TeV colliders 2005, standard model and Higgs working group: Summary report. In *4th Les Houches Workshop on Physics at TeV Colliders*, 4 2006.

[205] Assia Bessaa and Sacha Davidson. Constraints on t -channel leptoquark exchange from LHC contact interaction searches. *Eur. Phys. J. C*, 75(2):97, 2015.

[206] J. Ohnemus, S. Rudaz, T. F. Walsh, and P. M. Zerwas. Single leptoquark production at hadron colliders. *Phys. Lett. B*, 334:203–207, 1994.

[207] Luca Buonocore, Ulrich Haisch, Paolo Nason, Francesco Tramontano, and Giulia Zanderighi. Lepton-Quark Collisions at the Large Hadron Collider. *Phys. Rev. Lett.*, 125(23):231804, 2020.

[208] Admir Greljo and Nudzeim Selimovic. Lepton-Quark Fusion at Hadron Colliders, precisely. *JHEP*, 03:279, 2021.

[209] Herbi K. Dreiner, Victor Martin Lozano, Saurabh Nangia, and Toby Opferkuch. Lepton PDFs and Multipurpose Single Lepton Searches at the LHC. 12 2021.

[210] Georges Aad et al. Search for heavy Higgs bosons decaying into two tau leptons with the ATLAS detector using pp collisions at $\sqrt{s} = 13$ TeV. *Phys. Rev. Lett.*, 125(5):051801, 2020.

[211] V. Blobel. Unfolding Methods in High-energy Physics Experiments. In *1984 CERN School of Computing*, 12 1984.

[212] Albert M Sirunyan et al. Search for resonant and nonresonant new phenomena in high-mass dilepton final states at $\sqrt{s}$ = 13 TeV. *JHEP*, 07:208, 2021.

[213] Search for high-mass resonances in final states with a tau lepton and missing transverse momentum with the ATLAS detector. 6 2021.

[214] Georges Aad et al. Search for a heavy charged boson in events with a charged lepton and missing transverse momentum from pp collisions at $\sqrt{s} = 13$ TeV with the ATLAS detector. *Phys. Rev. D*, 100(5):052013, 2019.

[215] Search for heavy resonances and quantum black holes in eμ, eτ, and $\mu\tau$ final states in proton-proton collisions at $\sqrt{s}$ = 13 TeV. 5 2022.

[216] Jon Butterworth et al. PDF4LHC recommendations for LHC Run II. *J. Phys. G*, 43:023001, 2016.

[217] Adam Alloul, Neil D. Christensen, Céline Degrande, Claude Duhr, and Benjamin Fuks. FeynRules 2.0 - A complete toolbox for tree-level phenomenology. *Comput. Phys. Commun.*, 185:2250–2300, 2014.

[218] Celine Degrande, Claude Duhr, Benjamin Fuks, David Grellscheid, Olivier Mattelaer, and Thomas Reiter. UFO - The Universal FeynRules Output. *Comput. Phys. Commun.*, 183:1201–1214, 2012.

[219] J. Alwall, R. Frederix, S. Frixione, V. Hirschi, F. Maltoni, O. Mattelaer, H. S. Shao, T. Stelzer, P. Torrielli, and M. Zaro. The automated computation of tree-level and next-to-leading order differential cross sections, and their matching to parton shower simulations. *JHEP*, 07:079, 2014.

[220] Torbjörn Sjöstrand, Stefan Ask, Jesper R. Christiansen, Richard Corke, Nishita Desai, Philip Ilten, Stephen Mrenna, Stefan Prestel, Christine O. Rasmussen, and Peter Z. Skands. An introduction to PYTHIA 8.2. *Comput. Phys. Commun.*, 191:159–177, 2015.

[221] J. de Favereau, C. Delaere, P. Demin, A. Giammanco, V. Lemaître, A. Mertens, and M. Selvaggi. DELPHES 3, A modular framework for fast simulation of a generic collider experiment. *JHEP*, 02:057, 2014.

[222] Lukas Allwicher, Darius Faroughy, Florentin Jaffredo, Olcyr Sumensari, and Felix Wilsch. Drell-yan tails beyond the standard model, in preparation. 2022.

[223] Claudia Cornella, Darius A. Faroughy, Javier Fuentes-Martin, Gino Isidori, and Matthias Neubert. Reading the footprints of the B-meson flavor anomalies. *JHEP*, 08:050, 2021.

[224] Damir Bečirević, Boris Panes, Olcyr Sumensari, and Renata Zukanovich Funchal. Seeking leptoquarks in IceCube. *JHEP*, 06:032, 2018.

[225] Ilaria Brivio et al. Truncation, validity, uncertainties. 1 2022.

[226] Glen Cowan, Kyle Cranmer, Eilam Gross, and Ofer Vitells. Asymptotic formulae for likelihood-based tests of new physics. *Eur. Phys. J. C*, 71:1554, 2011. [Erratum: Eur.Phys.J.C 73, 2501 (2013)].

[227] Oscar J. P. Eboli and Angela V. Olinto. Composite Leptoquarks in Hadronic Colliders. *Phys. Rev. D*, 38:3461, 1988.

[228] Bastian Diaz, Martin Schmaltz, and Yi-Ming Zhong. The leptoquark Hunter's guide: Pair production. *JHEP*, 10:097, 2017.

[229] Ilja Doršner and Admir Greljo. Leptoquark toolbox for precision collider studies. *JHEP*, 05:126, 2018.

[230] Johannes Blumlein, Edward Boos, and Alexander Kryukov. Leptoquark pair production in hadronic interactions. *Z. Phys. C*, 76:137–153, 1997.

[231] Albert M Sirunyan et al. Search for singly and pair-produced leptoquarks coupling to third-generation fermions in proton-proton collisions at s=13 TeV. *Phys. Lett. B*, 819:136446, 2021.

[232] Morad Aaboud et al. Searches for third-generation scalar leptoquarks in $\sqrt{s}$ = 13 TeV pp collisions with the ATLAS detector. *JHEP*, 06:144, 2019.

[233] Georges Aad et al. Search for pair production of third-generation scalar leptoquarks decaying into a top quark and a τ-lepton in pp collisions at $\sqrt{s}$ = 13 TeV with the ATLAS detector. *JHEP*, 06:179, 2021.

[234] Georges Aad et al. Search for pairs of scalar leptoquarks decaying into quarks and electrons or muons in $\sqrt{s}$ = 13 TeV pp collisions with the ATLAS detector. *JHEP*, 10:112, 2020.

[235] Georges Aad et al. Search for pair production of scalar leptoquarks decaying into first- or second-generation leptons and top quarks in proton–proton collisions at $\sqrt{s}$ = 13 TeV with the ATLAS detector. *Eur. Phys. J. C*, 81(4):313, 2021.

[236] Constraints on models of scalar and vector leptoquarks decaying to a quark and a neutrino at $\sqrt{s} = 13$ TeV. 2018.

[237] Georges Aad et al. Search for a scalar partner of the top quark in the all-hadronic $t\bar{t}$ plus missing transverse momentum final state at $\sqrt{s} = 13$ TeV with the ATLAS detector. *Eur. Phys. J. C*, 80(8):737, 2020.

[238] Search for a narrow resonance in high-mass dilepton final states in proton-proton collisions using 140 fb^{-1} of data at $\sqrt{s} = 13$ TeV. 2019.

[239] Michael J. Baker, Javier Fuentes-Martín, Gino Isidori, and Matthias König. High- p_T signatures in vector–leptoquark models. *Eur. Phys. J. C*, 79(4):334, 2019.

[240] Marzia Bordone, Claudia Cornella, Gino Isidori, and Matthias König. The LFU ratio R_π in the Standard Model and beyond. *Eur. Phys. J. C*, 81(9):850, 2021.

[241] Damir Bečirević, Nejc Košnik, Olcyr Sumensari, and Renata Zukanovich Funchal. Palatable Leptoquark Scenarios for Lepton Flavor Violation in Exclusive $b \to s\ell_1\ell_2$ modes. *JHEP*, 11:035, 2016.

[242] Yi Cai, John Gargalionis, Michael A. Schmidt, and Raymond R. Volkas. Reconsidering the One Leptoquark solution: flavor anomalies and neutrino mass. *JHEP*, 10:047, 2017.

[243] Gudrun Hiller, Dennis Loose, and Kay Schönwald. Leptoquark Flavor Patterns & B Decay Anomalies. *JHEP*, 12:027, 2016.

[244] P. Arnan, D. Becirevic, F. Mescia, and O. Sumensari. Probing low energy scalar leptoquarks by the leptonic W and Z couplings. *JHEP*, 02:109, 2019.

[245] José Eliel Camargo-Molina, Alejandro Celis, and Darius A. Faroughy. Anomalies in Bottom from new physics in Top. *Phys. Lett. B*, 784:284–293, 2018.

[246] Claudia Cornella, Javier Fuentes-Martin, and Gino Isidori. Revisiting the vector leptoquark explanation of the B-physics anomalies. *JHEP*, 07:168, 2019.

[247] Florentin Jaffredo and Damir Becirevic. Flavor physics of heavy baryons, in preparation. 2022.

[248] J. P. Lees et al. A search for the decay modes $B^{+-} \to h^{+-}\tau^{+-}l$. *Phys. Rev. D*, 86:012004, 2012.

[249] Roel Aaij et al. Search for the lepton flavour violating decay $B^+ \to K^+\mu^-\tau^+$ using B^{*0}_{s2} decays. *JHEP*, 06:129, 2020.

[250] K. Marko and A. Rich. Search for orthopositronium decay into four photons as a test of charge-conjugation invariance. *Phys. Rev. Lett.*, 33:980–983, 1974.

[251] Morad Aaboud et al. Search for High-Mass Resonances Decaying to $\tau\nu$ in pp Collisions at $\sqrt{s}$=13 TeV with the ATLAS Detector. *Phys. Rev. Lett.*, 120(16):161802, 2018.

[252] R. J. Dowdall, C. T. H. Davies, R. R. Horgan, G. P. Lepage, C. J. Monahan, J. Shigemitsu, and M. Wingate. Neutral B-meson mixing from full lattice QCD at the physical point. *Phys. Rev. D*, 100(9):094508, 2019.

[253] A. Abdesselam et al. Precise determination of the CKM matrix element $|V_{cb}|$ with $\bar{B}^0 \to D^{*+}\,\ell^-\,\bar{\nu}_\ell$ decays with hadronic tagging at Belle. 2 2017.

[254] J. Charles, Andreas Hocker, H. Lacker, S. Laplace, F. R. Le Diberder, J. Malcles, J. Ocariz, M. Pivk, and L. Roos. CP violation and the CKM matrix: Assessing the impact of the asymmetric B factories. *Eur. Phys. J. C*, 41(1):1–131, 2005.

[255] Roel Aaij et al. Search for the lepton flavour violating decay $B^+ \to K^+\mu^-\tau^+$ using B^{*0}_{s2} decays. *JHEP*, 06:129, 2020.

[256] J. Grygier et al. Search for $\boldsymbol{B \to h\nu\bar{\nu}}$ decays with semileptonic tagging at Belle. *Phys. Rev. D*, 96(9):091101, 2017. [Addendum: Phys.Rev.D 97, 099902 (2018)].

[257] C. Abel et al. Measurement of the Permanent Electric Dipole Moment of the Neutron. *Phys. Rev. Lett.*, 124(8):081803, 2020.

[258] W. Dekens, J. de Vries, M. Jung, and K. K. Vos. The phenomenology of electric dipole moments in models of scalar leptoquarks. *JHEP*, 01:069, 2019.

[259] C. Alexandrou, S. Bacchio, M. Constantinou, J. Finkenrath, K. Hadjiyiannakou, K. Jansen, G. Koutsou, and A. Vaquero Aviles-Casco. Nucleon axial, tensor, and scalar charges and σ-terms in lattice QCD. *Phys. Rev. D*, 102(5):054517, 2020.

[260] Roel Aaij et al. Observation of CP Violation in Charm Decays. *Phys. Rev. Lett.*, 122(21):211803, 2019.

[261] Alexander Lenz and Guy Wilkinson. Mixing and CP Violation in the Charm System. *Ann. Rev. Nucl. Part. Sci.*, 71:59–85, 2021.

[262] Yuval Grossman and Stefan Schacht. The emergence of the $\Delta U = 0$ rule in charm physics. *JHEP*, 07:020, 2019.

[263] Gian Francesco Giudice, Gino Isidori, and Paride Paradisi. Direct CP violation in charm and flavor mixing beyond the SM. *JHEP*, 04:060, 2012.

[264] Wolfgang Altmannshofer, Andrzej J. Buras, David M. Straub, and Michael Wick. New strategies for New Physics search in $B \to K^* \nu\bar{\nu}$, $B \to K \nu\bar{\nu}$ and $B \to X_s \nu\bar{\nu}$ decays. *JHEP*, 04:022, 2009.

[265] Filippo Dattola. Search for $B^+ \to K^+ \nu\bar{\nu}$ decays with an inclusive tagging method at the Belle II experiment. In *55th Rencontres de Moriond on Electroweak Interactions and Unified Theories*, 5 2021.

[266] S. Fajfer, N. Košnik, and L. Vale Silva. Footprints of leptoquarks: from $R_{K^{(*)}}$ to $K \to \pi\nu\bar{\nu}$. *Eur. Phys. J. C*, 78(4):275, 2018.

[267] Sheldon L. Glashow, Diego Guadagnoli, and Kenneth Lane. Lepton Flavor Violation in B Decays? *Phys. Rev. Lett.*, 114:091801, 2015.

[268] Damir Bečirević, Olcyr Sumensari, and Renata Zukanovich Funchal. Lepton flavor violation in exclusive $b \to s$ decays. *Eur. Phys. J. C*, 76(3):134, 2016.

[269] Alejandro Celis, Javier Fuentes-Martin, Avelino Vicente, and Javier Virto. DsixTools: The Standard Model Effective Field Theory Toolkit. *Eur. Phys. J. C*, 77(6):405, 2017.

[270] Jason Aebischer et al. WCxf: an exchange format for Wilson coefficients beyond the Standard Model. *Comput. Phys. Commun.*, 232:71–83, 2018.